Thermische breuk van glas

Thermal Fracture of Glass

Marc Vandebroek

Promotoren:
prof. dr. ir. -architect J. Belis, prof. dr. G. Van Tendeloo, prof. ir.-architect L. Denissen
Proefschrift ingediend tot het behalen van de graden van
Doctor in de Ingenieurswetenschappen: Bouwkunde (Universiteit Gent) en
Doctor in de Architectuur (Universiteit Antwerpen)

Vakgroep Bouwkundige Constructies
Voorzitter: prof. dr. ir. L. Taerwe
Faculteit Ingenieurswetenschappen en Architectuur

UNIVERSITEIT GENT

Departement Fysica
Voorzitter: prof. dr. J. Dirckx
Faculteit Wetenschappen

Universiteit Antwerpen

Opleiding Architectuur
Faculteit Ontwerpwetenschappen

Academiejaar 2014 - 2015

ISBN 978-90-8578-738-9
NUR 955, 950
Wettelijk depot: D/2014/10.500/84

Examination committee

Prof. L. Schrijver, PhD (chairman), Fac. of Design Sciences, UA, Belgium

Prof. P. De Baets, PhD (co-chairman), FEA, Soete Laboratory, UGent, Belgium

Prof. J. Belis, PhD (supervisor), FEA, LMO, UGent, Belgium

Prof. G. Van Tendeloo, PhD (supervisor), Fac. of Sciences, EMAT, UA, Belgium

Prof. L. Denissen (supervisor), Fac. of Design Sciences, UA, Belgium

Dr C. Louter, ICOM, EPFL, Switzerland

Dr M. Overend, Dep. Of Eng., SRG, University of Cambridge, UK

Prof. B. Partoens, PhD, Fac. Of Sciences, CMT, UA, Belgium

Prof. L. Taerwe, PhD (secretary), FEA, Magnel Laboratory, UGent, Belgium

Research institutes

Ghent University, Department of Structural Engineering

Laboratory for Research on Structural Models

Technologiepark-Zwijnaarde 904, Ghent B-9052, Belgium

University of Antwerp, Department of Physics

Electron Microscopy for Materials Science

Groenenborgerlaan 171, Antwerp B-2020, Belgium

Funding

University of Antwerp, Fac. of Design Sciences

Mutsaardstraat 31, Antwerp B-2000, Belgium

Preface

Glass is known for both its transparent and brittle nature. The latter still arouses a certain reserve amongst designers to use glass as a load bearing structural element. However, for windows in façades, the longer experience of using glass in this setting has taught designers to better cope with its brittleness, especially when thermal actions are involved. Simplified thermal fracture verifications for common façade configurations are provided in the literature. The need for an accurate thermal fracture calculation method has increased over the past decades, as designers have proposed to use glass in more complicated façade configurations (e.g. double skin façades) as well as situations for which tempering the panes is not an option. As thermal fracture is determined by multiple environmental, geometrical, material and usage conditions, the thermal fracture verification is not simple.

This study investigates thermal fracture in a theoretical, experimental and numerical manner. The goal is to provide a solid basis for a more extensive parametrical study in the future.

Acknowledgements

Fascinated by the idea of better understanding principles behind the fundamental behaviour of nature or of man-made artefacts, I started this work several years ago. This would not have been possible without the seemingly endless support of, above all, my family as well as all the other people who helped and encouraged me.

Hereby, I would like to thank my wife Greet, my children Laurens, Anne-Cécile and Vincent, my parents, family, friends and colleagues at the various institutions and companies with whom I have interacted.

In particular, I would like to acknowledge the support of:

- my supervisors: prof. J. Belis, prof. G. Van Tendeloo and prof. L. Denissen, who have taught and inspired me during the past five years and with whom I have had a very open and trustful collaboration
- the members of the Laboratory for research on Structural Models, in particular em. prof. R. Van Impe, em. prof. G. Lagae, prof. R. Caspeele, dr D. Callewaert, dr D. Sonck, dr D. Delincé, ir. J. Dispersyn, ing. B. De Waele, ms. C. Malfait, mr. D. Elias, mr. E. Vonck, ir. M. Vandenpoel, ir. B. Bobelyn, ir. D. Feryn, ir. D. Vansteenbrugge and ir. N. Balcaen
- the members of Magnel Laboratory, in particular prof. L. Taerwe, chairman of the Department of Structural Engineering
- the members of the Laboratory of Textile at Ghent University, in particular ing. J. Louwagie
- the members of the Faculty of Design Sciences at the University of Antwerp
- the members of EMAT and CMT at the Faculty of Sciences of the University of Antwerp, in particular mr. L. Rossou
- the members of ICOM (EPFL), in particular, dr C. Louter, dr M. Lindqvist and prof. J.P. Lebet
- the members of the Glass and Façade Technology Research Group at the department of Engineering at the University of Cambridge, in particular Dr M. Overend and ingegnere M. Zaccaria
- the members of the department of Material Science at the Delft University of Technology, in particular dr F. Veer

- the members of the Department Civil Engineering and Geodesy-Institute of Materials and Mechanics in Civil Engineering at the TU Darmstadt, in particular Prof. J. Schneider, Dr.-Ing. P. Hof, Dr.-Ing. S. Schula and Dipl.-Ing. J. Kleuderlein
- the members of the Department of Structural Design and Building Physics at the University of the German Federal Armed Forces in Munich, in particular Prof. G. Siebert
- the members of the 'Fachverband Konstruktiever Glasbau', in particular Dr.-Ing. F. Ensslen and Dr.-Ing. F. Schneider
- the COST Action TU0905, European Research Network on Structural Glass, and all its members
- the experts of the companies Scheldebouw, Permasteelisa, Lerobel and Saint-Gobain, in particular ir. H. De Bleecker, ir.-arch. M. Berckmoes, mr. M. Joosten and ing. F. Serruys
- the experts I met at different conferences
- my brother in law Shawn for reading the manuscript

and all the people who supported me and whom I did not mention.

Finally, I would like to encourage everybody and in particular my family to enjoy and to take advantage of learning opportunities throughout your life. Although it required many sacrifices, I would not hesitate to do it again.

Marc Vandebroek

Sint-Niklaas, Belgium, October 2014

Summary

The use of glass has been limited to windows for a long period of time. However, since the nineties of the 20th century, façades became more complex to cope with energy efficiency and also the use of structural glass became popular amongst designers. In both cases, thermal fracture of glass elements imply considerable costs and safety risks. In general, thermal fracture is caused by a temperature gradient in the glass pane. For example, the latter may appear because the part concealed within the surrounding frame remains colder, while the temperature of the central part increases due to solar radiation. Consequently, the edges are subjected to tensile stresses, which cause failure when exceeding the edge strength. For simple window configurations, the application of the existing empirical verification method is sufficient to avoid thermal fracture. However, these rules do not provide an accurate probability of failure, and are not applicable to the more complex façade constructions of today. Also, for structural elements, the combination of thermal actions and other actions must be considered. Therefore, a general and accurate method according to the safety principles of the Eurocodes should be developed.

The safety against thermal fracture is determined by on the one hand the magnitude of the edge stresses caused by the climate actions and on the other by the glass edge strength. The latter is highly dependent on the defects, induced by the edge finishing process, including cutting, arrissing, grinding and polishing. Furthermore, humidity has a significant influence on the strength of glass when the edge is stressed during a long period of time; this phenomenon is known as stress corrosion. To estimate the edge strength of glass and the influence of humidity, a large experimental campaign was launched in the current study. Hereby, the influence of stress corrosion, load duration and load history, size and stress distribution on the edge strength was estimated. Next, a complex double skin façade (DSF) was simulated with real climate data at two locations in the Netherlands to investigate the environmental influence on the stresses at the edge. During the lifetime of the façade, the stress history was computed. From this, the distribution of the maximum yearly stresses was evaluated. Finally, the verification according to the Eurocodes was performed to estimate the safety against thermal fracture. This verification was performed with the distribution of the maximum values, but also with an equivalent lifetime stress, derived from the complete stress history. The latter method involves damage accumulation caused by reloading.

The state of the art about thermal fracture is mostly empirically based, on the action side as well as on the resistance side. The theory of linear elastic fracture mechanics and stress corrosion describes well the edge strength of glass as it is strongly dependent on the damage caused by cutting and processing the edge and on the environmental environment. The approach in this theory can be either explicit or stochastic. However, the strength values in the different existing empirical verification rules vary a lot. At the action side, only a peak solar radiation is considered, without accounting for damage accumulation. Finally, the state of the art only provides rules for simple façade configurations.

In the current study, as-received glass was experimentally investigated, applying the stochastic approach. This means that the damage which caused the failure was not quantified. Indeed, the results were analysed statistically and theoretical laws concerning linear elastic fracture mechanics and stress corrosion were validated. First, a correlation was found between temperature testing and mechanical (four-point bending) testing. Next, the stress corrosion parameters which resulted from mechanical testing corresponded well to those provided in the literature. Also, the characteristic edge strength values, determined by the Coverage method, were comparable to those in the literature. The strength values varied significantly depending on the type of edge finishing (cut, arrissed, ground or smooth ground). However, the strength values for a specific edge finishing were mostly independent of the failure location. Furthermore, the influence of the load history was investigated. It was found that the results of testing at a constant stress were very well predicted by the theoretical approach in literature. However, for a cyclic loading, the theory was about 6% too conservative, because of crack healing due to hysteresis effects. Finally, the influence of the size and stress distribution effect was estimated by means of testing. The size effect approach in literature was unsafe compared to the experiments (up to 14 %). Also, a reliable favourable stress distribution effect was not observed, contrary to the theory.
With the knowledge of the theory and the experimental validations, a double skin façade was simulated over a twenty-year period (1991-2010). First, a south orientation was computed and it was found that the verification with maximum yearly stresses or with the equivalent lifetime stress resulted in a comparable safety. During another twenty-year period (1971-1990), the results were very similar. However, 320 km direction north, the thermal stresses decreased considerably. Next, the same façade configuration was computed for an east orientation. Then, the equivalent lifetime stress verification was 22 % more conservative compared to the maximum stress verification.

It is concluded that the existing methods to evaluate thermal fracture vary considerably amongst the different standards and guidelines. Also, they do not consider damage accumulation and the safety margin is not quantified. This study provided a better insight in the mechanisms of failure caused by thermal actions and applied the semi-probabilistic approach according to the Eurocodes. The proposed method accounts for stress corrosion and damage accumulation. Stress corrosion and crack healing effects were quantified in a very accurate manner by testing at different stress rates and different load histories in a four-point bending setup. Also, the size effect and stress distribution effect was thoroughly examined by testing. All these effects were not yet quantified for the edge strength of glass.

Future work could focus on performing a parameter study, varying the geometrical and material properties of the façade configuration and estimating the influence of ventilation in a double skin façade. Also, the cutting and processing parameters (cutting wheel, cutting pressure, cutting speed, grinding discs,…) can be optimized, resulting in higher edge strength values, which must be controlled by an appropriate conformity system.

Samenvatting

Het gebruik van glas beperkte zich geruime tijd tot glasramen. Omwille van energiebesparing werden echter sinds de jaren ’90 van de vorige eeuw de façades complexer in ontwerp en uitvoering. Ook het gebruik van structureel glas nam aanzienlijk toe. In beide gevallen brengt eventuele thermische breuk grote kosten en risico’s met zich mee. Thermische breuk wordt veroorzaakt door temperatuursgradiënten in de glasplaat. Deze ontstaan bijvoorbeeld wanneer het gedeelte van de glasplaat dat in het raamkader zit kouder blijft dan het centrale gedeelte dat door zonnestraling wordt opgewarmd. Bijgevolg is de rand van de glasplaat aan trekspanning onderhevig, waarbij breuk ontstaat indien de lokale sterkte wordt overschreden. Voor de eenvoudige glasraamconfiguraties voldoet het nazicht volgens de bestaande empirische methodes meestal om thermische breuk te vermijden. Nochtans bieden deze regels geen bezwijkkans en zijn ze niet toepasbaar op hedendaagse complexere gevelconstructies. Ook voor structurele elementen dient de combinatie van thermische belastingen met andere optredende belastingen beschouwd te worden. Bijgevolg zou er een algemene nauwkeurige methode volgens de veiligheidsprincipes van de Eurocodes moeten ontwikkeld worden.

De veiligheid tegen thermische breuk wordt enerzijds bepaald door de grootte van de optredende spanningen, veroorzaakt door klimaatbelasting en anderzijds door de glasrandsterkte. Deze laatste is sterk afhankelijk van defecten die door het verwerken van het glas worden geïnduceerd. Het verwerken omvat o.a. het snijden, kanten, schuren of polijsten van het glas. Bovendien heeft de vochtigheid in de lucht een aanzienlijke invloed op de sterkte van glas wanneer dit gedurende lange tijd aan spanning onderhevig is. Dit fenomeen noemt men spanningscorrosie. Om de glasrandsterkte en de invloed van de vochtigheid te schatten werd in dit onderzoek een groot experimenteel proefprogramma opgezet. Hierin is de invloed van de spanningscorrosie, de belastingsduur en belastingsgeschiedenis, het schaaleffect en het spanningsverdelingseffect op de glasrandsterkte onderzocht. Vervolgens werd een dubbele huidgevel gesimuleerd met werkelijke klimaatgegevens van twee locaties in Nederland om de invloed van de omgeving op de spanningen aan de rand te begroten. Na de bepaling van de spanningsgeschiedenis gedurende de levensduur van de glasplaten, werd de distributie van de jaarlijkse maximale spanningen afgeleid. Tenslotte kon de veiligheid tegen thermische breuk volgens de Eurocodes bepaald worden. Deze verificatie gebeurde zowel met de distributie van de jaarlijkse maximale spanningen als met een equivalente spanning gedurende de levensduur van de glasplaat. Deze laatste houdt rekening met schadeaccumulatie bij herhaalde belasting.

De bestaande methodes betreffende thermische breuk steunen vooral op empirische regels, zowel langs de belastingszijde als langs de weerstandbiedende zijde. De lineair elastische breuktheorie en de theorie i.v.m. spanningscorrosie geven een goed inzicht in de glasrandsterkte, gezien deze sterkte afhangt van de schade ten gevolge van het verwerken van de rand en van de klimaatcondities. De theoretische aanpak kan zowel op expliciete als op stochastische wijze gebeuren. Ondanks deze grondige theoretische inzichten is er een groot verschil tussen de verschillende empirische methodes betreffende de sterktewaarden die worden aangehouden. Bovendien wordt er in de bestaande methodes aan de belastingszijde enkel een maximale thermische belasting beschouwd, zonder rekening te houden met schadeaccumulatie. Tenslotte zijn de bestaande methodes enkel toepasbaar op eenvoudige gevelconfiguraties.

In het huidig onderzoek is glas beproefd en op stochastische wijze geanalyseerd, waarbij de defecten die de breuk veroorzaakten niet werden opgemeten. De sterkteresultaten werden statistisch geanalyseerd en op basis hiervan de theoretische inzichten betreffende de lineair elastisch breuktheorie en de theorie van de spanningscorrosie gevalideerd. Eerst werd de correlatie aangetoond tussen thermische belasting en mechanische belasting met behulp van de vierpuntsbuigproef. Vervolgens werden de spanningscorrosieparameters experimenteel bepaald en deze correspondeerden met de waarden uit de literatuur. Ook de karakteristieke sterktewaarden, rekening houdend met betrouwbaarheidintervallen, zijn conform met de literatuur en de normen. Een aanzienlijke variatie was waarneembaar in functie van de randafwerking (gebroken, gekant, op maat geschuurd met blinkende delen of geschuurd zonder blinkende delen op de oppervlakte van de rand). De locatie waar de breuk startte had echter voor een bepaalde randafwerking weinig invloed op de sterktewaarde. Vervolgens werd de invloed van de belastingsgeschiedenis onderzocht. De theorie voorspelt hierbij zeer goed de testresultaten onder constante belasting maar voor cyclisch constante belasting is de theorie ongeveer 6 % te conservatief, toe te schrijven aan een helingseffect bij herhaalde belasting. Tenslotte werd het schaaleffect en het spanningsdistributie effect experimenteel begroot. De theoretische benadering van het schaaleffect is onveilig vergeleken met de testresultaten van dit onderzoek (tot 14 %) en een betrouwbaar voordelig effect van de spanningsverdeling volgens de theorie was niet waarneembaar in het proefprogramma.

Met de opgedane kennis uit de theorie en het proefprogramma, werd een dubbele huidgevel gesimuleerd over een tijdsperiode van 20 jaar (1991-2010). Eerst werd de zuidelijke oriëntatie beschouwd en hieruit bleek dat de jaarlijkse

maximale spanningen ongeveer dezelfde veiligheid vertoonden als de equivalente spanning gedurende de ganse levensduur van de glasplaat. Vervolgens werd dezelfde configuratie berekend over een andere periode van 20 jaar (1971-1990) en dit resulteerde in analoge resultaten. Echter, 320 km meer naar het noorden werden aanzienlijk lagere spanningen gesimuleerd. Ook de oostelijke oriëntatie werd met de zuidelijke vergeleken over de periode 1991-2010. Voor deze oriëntatie bedroeg de equivalente spanning gedurende de levensduur 22 % meer dan de jaarlijkse maximale spanning. In dit geval zou een ontwerp op basis van enkel maximale spanningen niet veilig genoeg zijn.

Tot besluit kan men stellen dat de bestaande methodes om thermische breuk te evalueren sterk verschillen van document tot document. Ook beschouwen ze geen schadeaccumulatie en de veiligheid wordt niet begroot. Deze studie biedt een beter inzicht in de mechanismes die thermische breuk veroorzaken en past de semi-probabilistische methode volgens de principes van de Eurocodes toe. De voorgestelde methode houdt rekening met spanningscorrosie en schadeaccumulatie. Spanningscorrosie en helingseffecten werden zeer accuraat gekwantificeerd door middel van vierpuntsbuigproeven, waarbij met verschillende belastingssnelheden en belastingsgeschiedenissen werd getest. Ook het schaaleffect en het spanningsdistributieeffect werden grondig getest. Deze effecten werden nog niet uitvoerig getest voor de glasrandsterkte onder een actief gecontroleerde klimaatomgeving in het laboratorium op zulke grote schaal (3220 proefresultaten).

Toekomstig werk kan zich nog toespitsen op een parameterstudie die de invloed van de geometrische karakteristieken en de materiaaleigenschappen van de façadeconfiguratie kan inschatten, alsook de gunstige invloed van ventilatie in een dubbele huidgevel kan begroten. Ook kan nog verder onderzocht worden hoe de snijparameters (snijwieltje, snijdruk, snelheid,…) en randafwerkings-parameters (schuurschijven, schuursnelheid,…) geoptimaliseerd kunnen worden om te resulteren in hogere sterktes. Deze kunnen dan door middel van een gepast conformiteitssysteem gegarandeerd worden.

Table of contents

List of symbols and abbreviations

symbol	description
A	stressed area of the element
E	module of elasticity
$F_a(a)$	cumulative distribution function (Pareto distribution)
F_i	empirical failure probability assigned to the i^{th} strength value
K_I	stress intensity factor in mode I
K_{Ic}	fracture toughness of modern soda-lime silica glass
K_{th}	crack growth threshold
L	nominal support span of the specimen
L_s	nominal load span of the specimen
L_t	nominal specimen length
M	actual number of flaws in a glass element
P	total load
$P(M)$	probability of an element containing exactly M flaws
P_f	experimental failure load
P_b	probability of failure
$P_{f,inert}$	failure probability of a random glass element
$P_{s,inert}$	survival probability of a random glass element
$P^{(1)}_{f,inert}$	failure probability of one flaw, in inert conditions
$P^{(1)}_{s,inert}$	survival probability of one flaw, in inert conditions
$P^{(M)}_{s,inert}$	survival probability of a glass element with exactly M flaws, in inert conditions
S_0	unit surface
S_s	surface of the glass element which is subjected to a stress larger than the threshold strength
T	temperature
V	variation coefficient
Y	geometry factor
Z	average number of flaws in a glass element
Z_0	number of flaws in the unit surface S_0
a	flaw depth perpendicular to the surface
a_0	lower limit for the flaw depth a
a_{ci}	initial critical flaw depth
$a_{ci,dom}$	initial critical depth of the dominant flaw
$a_c(t)$	critical flaw depth at time t

a_{3PB}	correcting factor for the Hertzian line contact effect in the 3PB test
a_{4PB}	correcting factor for the Hertzian line contact effect in the 4PB test
b	thickness of the specimen
b'	developed thickness of the specimen
$b(n_s)$	unbiasing factor
c	sample variation coefficient
c_f	distance between the support and the failure origin
c_{prob}	correction factor for the lifetime of the element
d	distance between the load and the support
f	tensile strength corresponding to a constant stress rate
f_{NF}	allowable stress according to NF P 78-201-1/A1(DTU39) (1998)
$f_{g;k}$	5% characteristic surface tensile strength with a 95% confidence level of Annealed Glass equal to 45 MPa according to the standards
$f_{b;k}$	5% characteristic surface tensile strength with a 95% confidence level of Heath Strengthened Glass or Fully Tempered Glass equal to 70 MPa or 120 MPa, respectively, according to the standards
$f_{eg;k}$	5% characteristic tensile edge strength with a 95% confidence level of Annealed Glass according to the standards
f_{eg}	experimental tensile edge strength corresponding to a constant stress rate in 4PB
f'_{eg}	corrected experimental tensile edge strength corresponding to a constant stress rate (Hertzian line contact effect) in 4PB
$f'_{eg,60}$	corrected experimental tensile edge strength corresponding to a reference period of 60 s and to a constant stress rate (Hertzian line contact effect) in 4PB
$f'_{eg,k}$	5% characteristic edge strength value with a 75% confidence level
$f'_{eg,m}$	mean edge strength value
$f_{eg,3PB}$	experimental tensile edge strength corresponding to a constant stress rate in 3PB
$f'_{eg,3PB}$	corrected experimental tensile edge strength corresponding to a constant stress rate (Hertzian line contact effect) in 3PB
$f_{eg,4PB}$	experimental tensile edge strength corresponding to a constant stress rate in 4PB
$f'_{eg,4PB}$	corrected experimental tensile edge strength corresponding to a constant stress rate (Hertzian line contact effect) in 4PB

f_{ct}	tensile strength corresponding to a constant loading
f_{cycl}	tensile strength corresponding to a cyclic loading
$f_{ct,inert}$	inert tensile strength corresponding to a constant loading
$f_{ct,threshold}$	threshold strength corresponding to a constant loading
f_d	design strength value without crack healing
f'_d	design strength value with crack healing
f_{inert}	inert tensile strength corresponding to a constant stress rate
$f_a(a)$	probability density function (Pareto distribution)
h	height of the specimen
h_e	external heat transfer coefficient
h_i	internal heat transfer coefficient
k_A	correction factor for the size effect
k_{mod}	correction factor for the load duration
k_s	coefficient derived from the noncentral *t*-distribution
k_t	frame coefficient according to NF P 78-201-1/A1(DTU39) (1998)
m_0	shape parameter of the 2-parameter Weibull distribution in inert conditions
m'_0	shape parameter of the 2-parameter Weibull distribution in ambient conditions
m_{corr}	corrected Weibull shape parameter
n	crack velocity parameter
n_s	specimen number of the series
r	power coefficient of the Pareto distribution
r^2	coefficient of determination (least-squares method)
s	sample standard deviation
t	time
t_f	time period during which the flaw can resist the stress history or failure time or load duration before failure
$t_{f,threshold}$	load duration corresponding to the threshold strength
t_{load}	load duration of the action
t_{test}	load duration of the test
t_{th}	moment where the stress equals the threshold stress
v	crack propagation speed
v_0	crack propagation speed, when $K_I = K_{Ic}$
z	flaw density
$\bar{x}$	sample mean
ΔT	temperature gradient
Φ	cumulative distribution function of the standardised normal distribution

α	expansion coefficient
α_c	cutting angle
β	reliability index
γ	confidence level
γ_F	partial safety factor for the actions
γ_M	partial safety factor for material property
ε	coefficient of emissivity
ε_s	strain measured by a strain-gauge
ϑ	scale parameter of the 2-parameter Weibull distribution in inert conditions, depending on the mean number of flaws of the stressed surface of the element
ϑ_0	scale parameter of the 2-parameter Weibull distribution in inert conditions
ϑ'_0	scale parameter of the 2-parameter Weibull distribution in ambient conditions
ρ_s	coefficient of reflectance
σ	standard deviation
σ_c	critical stress (strength)
$\sigma_{d,eq,lifetime}$	equivalent lifetime constant design stress
$\sigma_{d,eq,yearly}$	yearly maximum equivalent constant design stress
$\sigma_{d,eq,NF}$	maximum equivalent constant stress calculated with the climate data according to NF P 78-201-1/A1(DTU39) (1998)
$\sigma_{d,th}$	threshold design stress
$\sigma_{d,5\%,eq,yearly}$	5% maximum value of the distribution of $\sigma_{d,eq,yearly}$
σ_e	calculated stress at the edge
$\sigma_{eq,lifetime}$	the equivalent lifetime constant stress
$\sigma_{eq,yearly}$	yearly maximum equivalent constant stress
σ_n	tensile stress normal to the flaws plane
$\sigma_n(t)$	tensile stress normal to the plane of the flaw at time t
σ_{4PB}	calculated stress in the 4PB test
σ_{3PB}	calculated stress in the 3PB test
$\sigma_{\Delta T,NF}$	calculated stress according to NF P 78-201-1/A1(DTU39) (1998)
τ_s	coefficient of transmittance

abbreviation	description
ANG	Annealed Glass
CCF	Closed Cavity Façade
CDF	Cumulative Distribution Function
FE	Finite Element
FTG	Fully Tempered Glass
HSG	Heat Strengthened Glass
IGU	Insulating Glass Unit
LEFM	Linear Elastic Fracture Mechanics
LSM	Least-Squares Method
MLE	Maximum Likelihood Estimate
NF	French standard NF P 78-201-1/A1(DTU39) (1998)
PVB	Polyvinylbutyral
RC	Reliability Class
SLSG	Soda Lime Silica Glass
TP	Test Programme
3PB	Three-Point Bending
4PB	Four-Point Bending

1. Introduction to the research

I have not been able to discover the cause of those properties of gravity from phenomena, and I frame no hypotheses; for whatever is not deduced from the phenomena is to be called a hypothesis, and hypotheses, whether metaphysical or physical, whether of occult qualities or mechanical, have no place in experimental philosophy.

Isaac Newton (1643-1727)

1.1 Introduction

In this chapter, the research topic is introduced, the problem is defined and the method is explained. Also, the objectives and the outline of the dissertation are provided. This chapter introduces the chapters 2, 3 and 4, where the topic is investigated.

1.2 Problem definition

Since the nineties of the 20th century there has been a growing interest among architects to design buildings with glazed single or double skin façades. Compared to the single skin façade, the double skin façade has several advantages concerning energy efficiency (see chapter 2). Usually, the inner part of the double skin façade or the single skin façade consists of an insulating glass unit (IGU). Due to the solar radiation, the temperature of the central part of a glass pane increases considerably compared to the colder part concealed within the surrounding frame (see Figure 1.1). The difference in temperature between different parts of the glass pane induces temperature gradients, leading to a simultaneous and contradictory mechanical action of warm parts trying to expand and cold parts trying to withstand this expansion (see Figure 1.1). Thus, these temperature gradients induce high tensile stresses at the cold part, which is in general the edge of the pane (Sglavo 2007). Glass fracture will occur when these stresses exceed the local glass edge strength.

On the one hand, the edge strength of glass is currently not very well known (see chapter 2). As thermal fracture is always initiated at the edge, a good estimation of the edge strength is crucial to determine the safety against thermal fracture. The edge strength is mainly determined by the scoring and eventually the processing of the edge. The most common edge finishings are simply cut, arrissed, ground or polished (see chapter 2). Processing the edge of a pane induces defects, i.e. flaws. The edge strength depends on the size and distribution of these edge flaws. Thus, multiple parameters influence the edge quality, e.g. the cutting wheel, the cutting oil, the cutting pressure and speed, the type of grinding or polishing discs, the speed of grinding or polishing, etc. (see chapter 2).

On the other hand, the stresses at the edge depend on a large number of parameters, e.g. the climate conditions combined with the façade orientation,

the geometry and composition of the façade, the presence of shade on a part of the glazing, the presence of sun shades or curtains, etc. (see chapter 2).

Over the past decades, buildings have become considerably taller. Consequently, thermal fracture of glazed façade elements imply significant replacement costs and safety risks. Therefore, compared to the existing methods, a more precise estimation of the safety against thermal fracture is needed. Also, as the existing methods are not very accurate, the designer often applies heat strengthened glass (HSG) or fully tempered glass (FTG) where annealed glass should satisfy. However, HSG and FTG are more expensive and result in optical distortions. Finally, the existing methods are not applicable to complex façade configurations. Therefore, a general method according to the principles of EN 1990 (2002) should be developed.

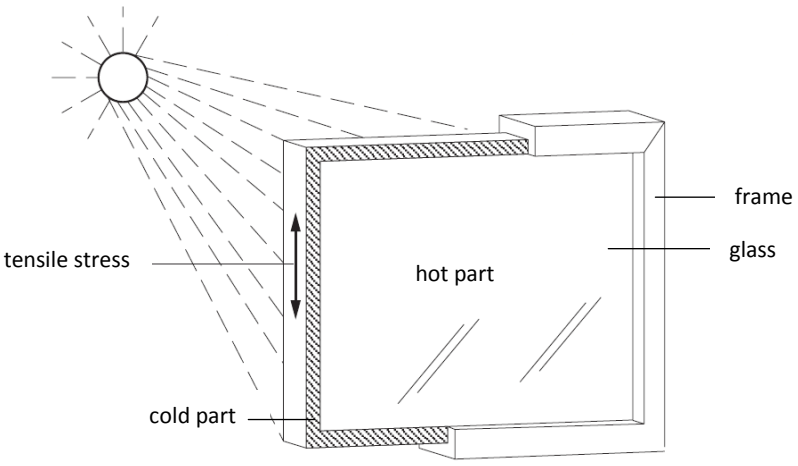

Figure 1.1: Principle of thermal fracture (TV 214 1999).

1.3 Methodology

The evaluation of thermal fracture, described in the literature and the existing standards is mainly an empirical one (see chapter 2). Consequently, the safety margin against thermal fracture is not quantified. According to Feldmann *et al.* (2014), Eurocode Outlook No. 20 states: 'A calculation method for the load case "thermal stresses" should be established in the Eurocode. The existing methods should be analysed and adjusted to fit with the Eurocode safety framework

(mean value, standard deviation and design value). This means that also the loads from other Eurocodes have to be adopted to the specific need in glass design.' The current research aims at proposing a methodology for estimating the safety according to the principles of the semi-probabilistic approach of EN 1990 (2002). To do so, first, the edge strength was estimated by experimental investigations (see chapter 3). Then, the thermal stresses were simulated by means of finite element software. Finally, the stresses and the strength were compared in the ultimate limit state method (see chapter 4).

1.3.1 Experimental investigations

The glass edge strength is not well documented in the literature and in the existing standards. In the literature, different testing setups and specimen sizes are used to estimate the glass edge strength. In the existing standards, characteristic values of the edge strength are presented, but the testing conditions, the setup and the evaluation of the results are not well described or lacking. For that reason, the edge strength was explored profoundly in this study (3220 test results).

1.3.2 Numerical investigations

To estimate the thermal stresses in a pane, finite element software was used. Stresses were calculated on the basis of real climate data at two locations of the Netherlands during a twenty-year period. First, the temperature gradients and then the stresses induced by these gradients were computed. This resulted in the stress history during the lifetime of the pane.

1.3.3 Ultimate limit state

From the stress history (see section 1.3.2), the yearly maximum stresses were evaluated statistically. Also, the complete stress history was transformed into an equivalent constant stress value. Finally, the characteristic maximum stress value was compared to the edge strength, but also the equivalent stress value was compared to the edge strength (see chapter 4).

1.4 Objectives

The general goal of this research consists of formulating a methodology for a semi-probabilistic approach to thermal fracture in glass panels.

To do so, important questions had to be addressed:

- how to determine the characteristic or design value of the edge strength
- how to quantify the influence of stress corrosion and crack healing on the structural resistance against thermal fracture of glass
- how to assess the safety margin in function of the climate data being applied for the calculation of the thermal stresses

1.5 Outline

The dissertation consists of 5 chapters (see Figure 1.2):

Chapter 1 provides an introduction to the work. In this chapter, the research topic is introduced, the problem is defined (section 1.2) and the method is explained (section 1.3). Also, the objectives (section 1.4) and the outline (section1.5) of the dissertation are provided.

Chapter 2 presents the state of the art concerning thermal fracture. First, an introduction about façade constructions in modern architecture is presented (section 2.2). Then, the existing knowledge about the strength of glass is summarized (section 2.3). Next, the most important environmental parameters which influence the thermal stresses at the edge are described (section 2.4). Finally, the methods to assess the risk of thermal fracture in the existing literature and the standards are compiled (section 2.5).

Chapter 3 focuses on the experimental investigations. First, the temperature test setup and the bending test setup are presented (section 3.2). Next, the correlation between temperature testing and four-point bending (4PB) testing is provided (section 3.3). Finally, the influence of stress corrosion, load history, size and stress distribution on the edge strength is demonstrated (sections 3.4 to 3.8).

Chapter 4 provides the numerical investigations. First, the action model, the structural model and the verification method are presented (section 4.2). A double skin façade was analyzed and the ultimate limit state verification was performed (sections 4.3 to 4.6).

Chapter 5 summarizes the conclusions (section 5.1) and recommendations for future research (section 5.2).

1.6 Highlights of this chapter

- Today, thermal fracture of glazed façade elements imply significant replacement costs and safety risks
- Thermal fracture is caused by thermal gradients, mostly induced by solar irradiance
- This work combines experimental and numerical investigations into a verification method for thermal fracture
- The aim of the work is to better understand the mechanisms behind the problem of thermal fracture

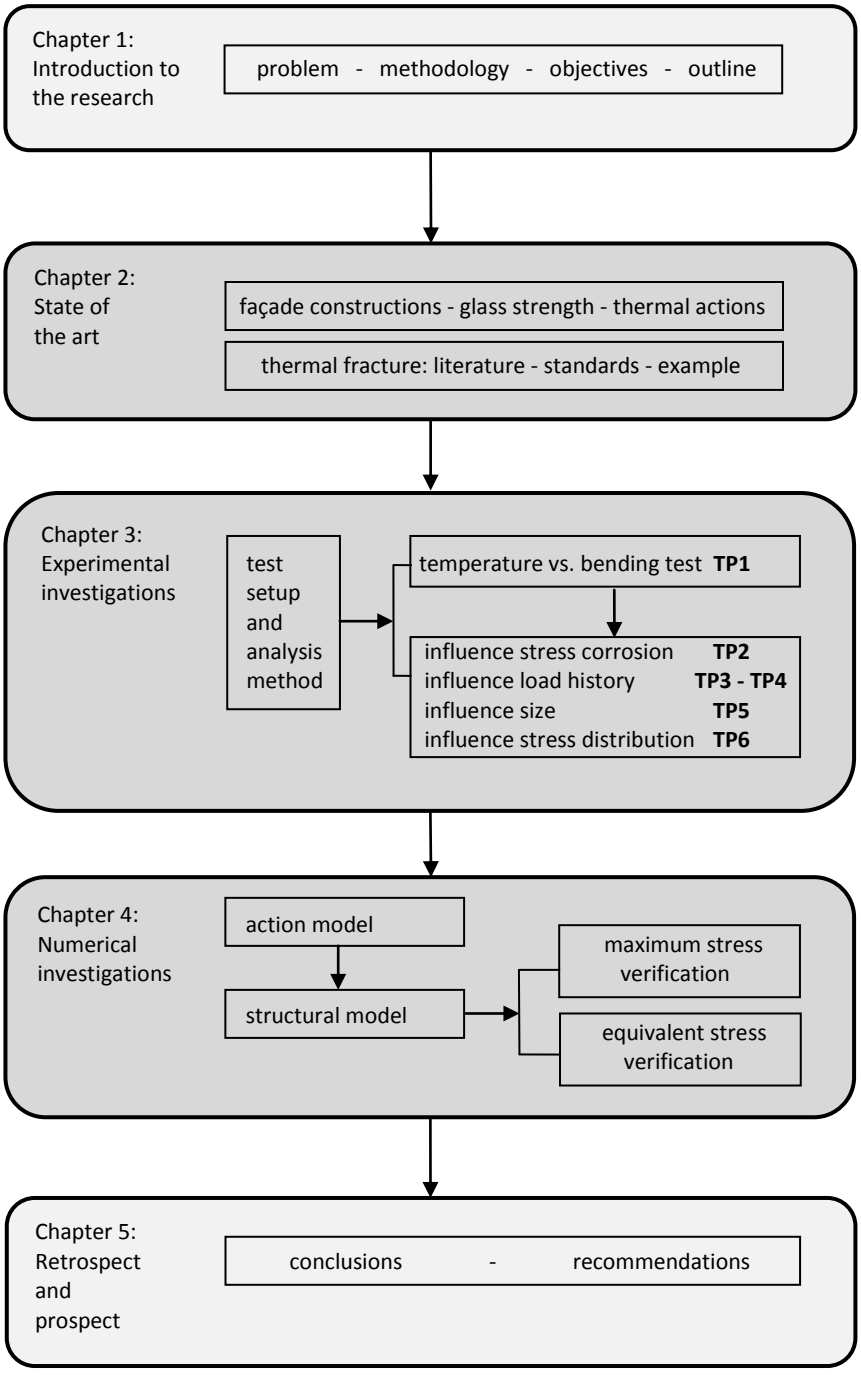

Figure 1.2: Outline of the dissertation (TP: test programme, see chapter 3).

2. State of the art

A human being is a part of a whole, called by us universe, a part limited in time and space. He experiences himself, his thoughts and feelings as something separated from the rest... a kind of optical delusion of his consciousness. This delusion is a kind of prison for us, restricting us to our personal desires and to affection for a few persons nearest to us. Our task must be to free ourselves from this prison by widening our circle of compassion to embrace all living creatures and the whole of nature in its beauty.

Albert Einstein (1879-1955)

2.1 Introduction

In this chapter, the state of the art concerning the thermal fracture verification is presented. As most of the thermal fracture failures occur when the panes are concealed within a frame, an introduction about façades is provided. Then, the available knowledge about glass strength, resisting thermal stresses and the thermal actions, inducing thermal stresses, is listed. Finally, the existing approaches to estimate the risk for thermal fracture are provided. Then, it becomes clear that certain issues (see chapter 3 and 4) still need more research in order to do a precise evaluation of thermal fracture during design.

2.2 Façade constructions

During the last two decades, many office buildings were designed with highly glazed façades. Transparency and daylight became important design requirements. However, to reduce energy loss, more and more glazed office buildings were built with double skin façades (Blomsterberg 2007).

While windows are constructed in the building openings, curtain walls are built in front of the building structure, consisting of vertical and horizontal profiles. Mostly, the curtain wall has no structural function. Most curtain walls are made with extruded aluminium profiles because of the low weight. When the single façade is doubled inside or outside by a second glazed façade, with a cavity of 0.1 m to 2 m, a ventilated (or non-ventilated) double skin façade is created. The possible ventilation can be natural, mechanical or hybrid. In case of a façade ventilated with outdoor air, the inner skin is mostly a double-glazed unit and the outer skin a single pane. In case of a façade ventilated with indoor air, the opposite is commonly applied. Shading devices are usually placed in the cavity and need no maintenance (Saelens 2002, Blomsterberg 2007).

Double skin façades can provide some improvements such as energy savings, wind protection, fire protection, sound reduction and others. In most existing office buildings, air conditioning systems have to compensate for summer overheating. However, only a well-designed and manufactured double skin façade can result in a lower operating cost, compared to a glazed single skin façade (Saelens 2002, Blomsterberg 2007). Further, it is necessary to perform a whole building energy analysis, instead of only analyzing the transmission losses and gains (Saelens 2002).

Most methods in the literature and the standards to estimate the resistance to thermal fracture concentrate on windows (see section 2.5). A general method for all kinds of glazed skins, including double skin façades would be useful. However, the estimation of the thermal stresses for a double skin façade is very complex. Finite element analyses which include ventilation are very time-consuming and, consequently, thermal stress calculations over a long time period are not yet possible (see section 2.5).

It is important to determine the period during which the thermal stress calculation should be performed and which climate data should be considered. In the current study, thermal stresses were calculated on a double skin façade without ventilation (Closed Cavity Façade or CCF). In the cavity of the CCF, a dry air supply prevents condensation. These thermal stresses were compared to the strength values found in the standards (see section 2.3) or determined by testing (see chapter 3).

2.3 Glass strength

2.3.1 Introduction

Glass is a brittle material with an almost perfectly linear elastic behaviour. Most of the glass used in buildings is soda lime silica glass (SLSG) manufactured in a float process. The theoretical tensile strength based on molecular forces is very high and may reach 32 GPa (Haldimann *et al.* 2008).

However, already when manufacturing and processing glass, defects are induced to the glass surface. These defects occur as mechanical flaws, almost invisible to the naked eye. Most of these flaws have dimensions between 30 µm and 300 µm (Haldimann *et al.* 2008). During the float process the glass surface is damaged by the rollers of the annealing lehr, and the strength is determined by the induced mechanical flaws. At the end of the float line, the Annealed Glass (ANG) is cut into large 6.00 m * 3.21 m standard size float glass panels.

Next, these large panes are cut on large cutting tables into the desired sizes or further processed to produce glass products of the required shape, performance or appearance (Haldimann *et al.* 2008). The pane is first scored with a cutting wheel (see Figure 2.2, above) with a certain angle α_c (between 130° for thin panes to 160° for thick panes), while using an appropriate cutting oil. The pressure (between 0.5 bar for thin panes to 2.5 bar for thick panes) and the cutting speed (between 100 m/min and 150 m/min) of the cutting wheel are chosen in function of the thickness of the pane. Then, the plate is broken. In most cases, the cut edges are then arrissed (seamed), grinded, smooth grinded or polished according to EN 12150-1 (2000) or EN 1863-1 (2000), shown in Figures 2.1, 2.2, 2.3 and 2.4. For a pane concealed within a frame, an arrissed edge will satisfy most often, as the craftsman will not hurt himself. However, for elements of which the edge stays visible, a more esthetic finishing is required, i.e. smooth ground or polished. The arrissed edge can be achieved by a grinding disc or occasionally by a belt. If the arrissed edge is dressed to size, the edge finishing is called 'ground' instead of 'arrissed'. The ground edge has several blank spots at the edge surface, whereas the arrissed edge has a totally blank edge surface (see Figures 2.1 and 2.2). However, if no blank spots are left at the edge surface, the edge is called 'smooth ground'. Finally, for a polished edge, a supplementary polishing disc is used in the second, third and fourth grinding operation (see Figure 2.3).

In most cases, the arrissed, ground, smooth ground and polished edges have two small bevels (approximately 0.9 to 1.4 mm) at an angle of approximately 45°. Each company may perform the operations with a certain variation compared to the principle of Figure 2.3. During these grinding operations, mechanical flaws are induced at the edges or at the surfaces between the edges (see Figure 2.4). These flaws will be studied in detail in chapter 3.

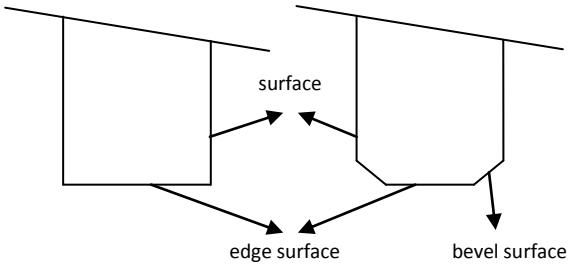

Figure 2.1: Terminology of the surface.

cutting wheel and cutting angle α_c (oaklanddiamondtools.com)

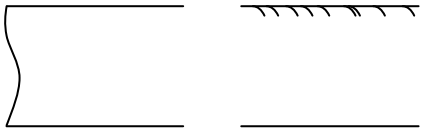

cut edge (KG)

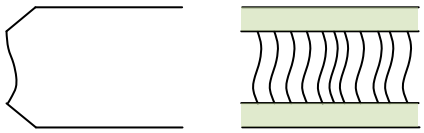

arrissed edge (KGS)

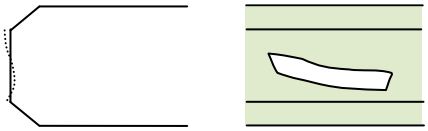

ground edge (KMG)

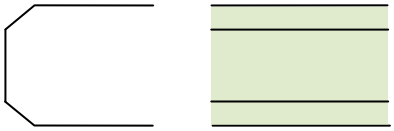

smooth ground edge, no blank spots at the edge surface (KGN)

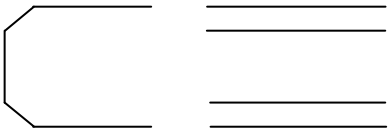

polished edge (KPO)

Figure 2.2a: Terminology of the edge finishing (EN 12150-1 2000; EN 1863-1 2000), the German terminology between brackets (DIN 1249-11 1986).

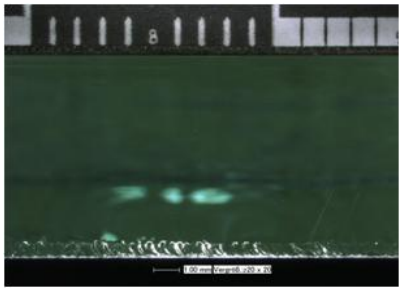

cut edge finishing

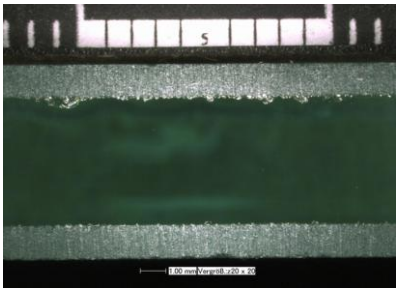

arrissed edge finishing

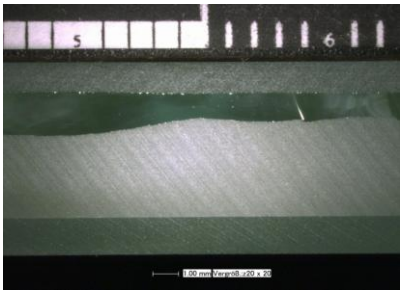

ground edge finishing

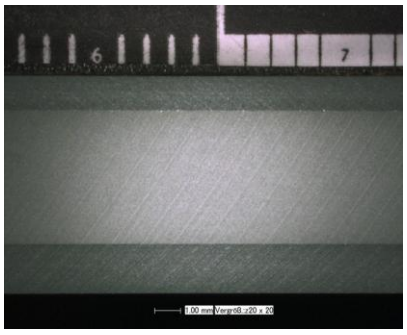

smooth ground edge finishing

Figure 2.2b: Pictures of cut, arrissed, gound and smooth ground edge finishing (FKG, J. Kleuderlein, TU Darmstadt).

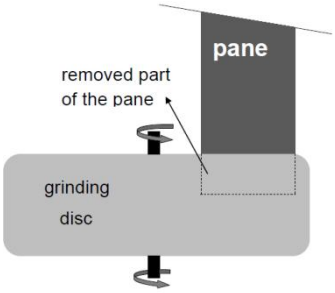

first grinding operation (diamond discs): bottom surface (removal: about 2 mm for smooth ground and less for ground)

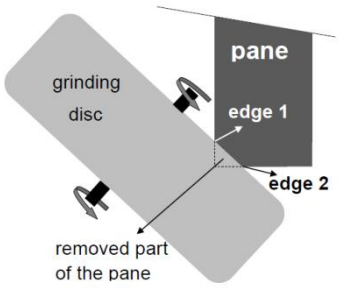

second grinding operation (diamond discs): first bevel surface

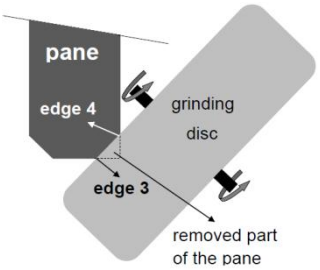

third grinding operation (diamond discs): second bevel surface

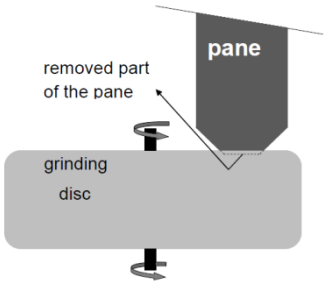

fourth grinding operation (final grinding discs): bottom surface (removal: about 0.1 mm)

Figure 2.3: Principle of processing the edge.

For structural applications, tempering of glass is common practice. For applications in buildings, thermal tempering is more applied than chemical tempering. Due to this treatment, compressive stresses are induced at the surface. Two levels of residual stress are applied, resulting in Heat Strengthened Glass (HSG) or Fully Tempered Glass (FTG) (EN 12150-1 2000; EN 1863-1 2000).

In standards and literature, the 5% characteristic surface tensile strength with a 95% confidence level amounts to $f_{g;k}$ = 45 MPa for ANG, to $f_{b;k}$ = 70 MPa for HSG and to $f_{b;k}$ = 120 MPa for FTG (EN 12150-1 2000; EN 1863-1 2000).

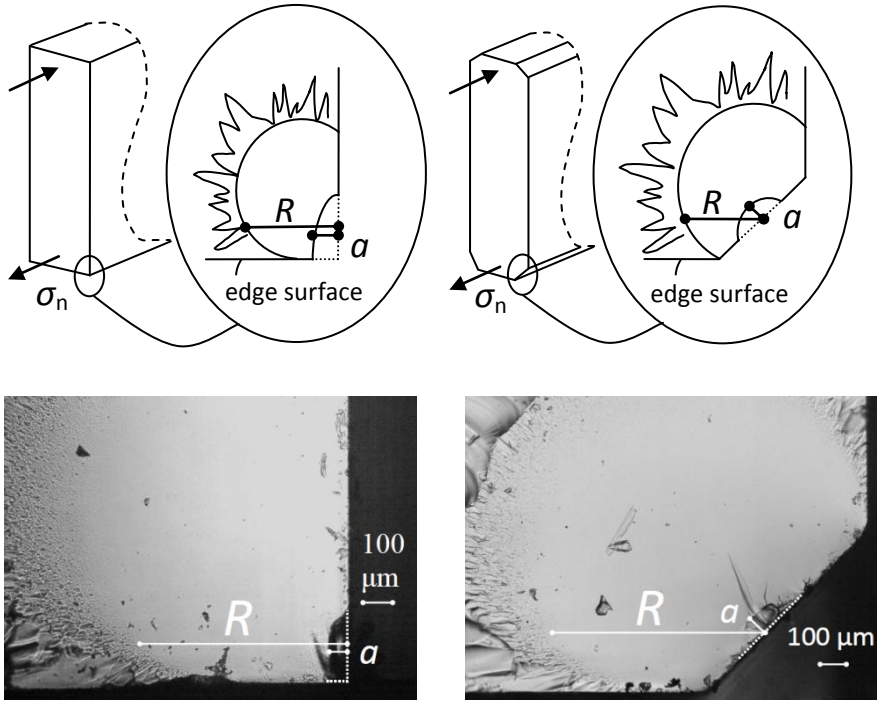

cut edge arrissed or (smooth) ground edge

Figure 2.4: Schematic (above) and microscopic view of edge flaws, σ_n denotes the tensile stress normal to the flaws plane, a the flaw depth perpendicular to the surface and R the mirror zone depth.

The edge strength for ANG is documented in the literature and the standards:

- NEN 2608+C1 (2012) proposes $f_{eg;k}$ = 0.8 * 45 MPa = 36 MPa for a load perpendicular to the pane and $f_{eg;k}$ = 0.62 * 45 MPa = 27.9 MPa for an in-plane load, both applicable for every edge finishing.
- Siebert (2011) provides a value of $f_{eg;k}$ = 0.8 * 45 MPa = 36 MPa, applicable for every edge finishing.

Little information is given about the determination of these strength values. Also, the testing method is not provided in these documents.

Furthermore, Güsgen (1998), Hess (2000), Belis (2005), Sglavo *et al.* (2007), Veer and Riemslag (2009), Veer and Rodichev (2011) and Lindqvist (2013) presented test results for the edge strength of glass. These researchers used different specimen sizes and number of specimens in a series, and tested in different environmental conditions with different loading rates.

In chapter 3 of the current study, the edge strength of ANG is tested extensively under controlled test conditions and the test results of different edge finishings are presented. These strength results vary considerably depending on the particular edge finishing.

2.3.2 Fracture mechanics and stress corrosion

The theory of linear elastic fracture mechanics (LEFM) describes the relation between the tensile strength and the flaw parameters, i.e. the flaw geometry and the flaw depth.

Since Griffith (1920) demonstrated that flaws determine the strength of glass, and because glass shows a perfectly elastic behaviour up till failure, the linear elastic fracture mechanics (LEFM) theory is generally accepted in glass design.
There are three types of fracture to be considered, as illustrated in Figure 2.5 (Lawn 1993). Mode I is crack opening, mode II is in-plane crack shearing or sliding and mode III is anti-plane crack shearing or tearing (Lawn 1993).

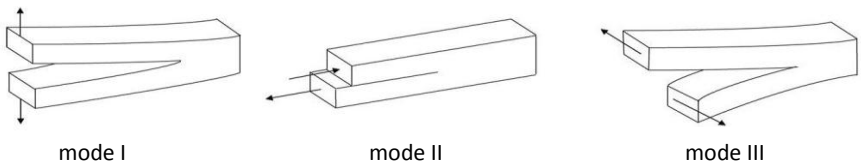

Figure 2.5: Fracture in modes I, II and III (Lawn 1993).

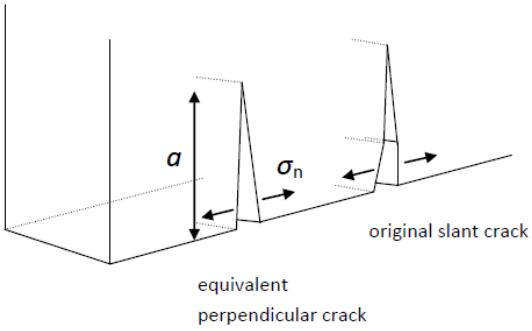

Figure 2.6: The slant edge crack and its perpendicular equivalent, σ_n denotes the tensile stress normal to the flaws plane, a the flaw depth perpendicular to the surface (Porter 2001).

In this research, only mode I is considered. The stress field induced by thermal or mechanical loading (4PB of 3PB test) is uniaxial in this study. Furthermore, according to the literature (Lawn 1993), the action of the imposed shear deflects the crack away from plane geometry and moreover, tends toward the orientation of minimum shear.

According to the theory of LEFM, at inert conditions, i.e. when no water vapour affects the flaws, the mode I stress intensity factor K_I [MPa $m^{1/2}$] is given by (Irwin 1957):

$$K_I = Y \cdot \sigma_n \cdot (\pi . a)^{1/2} \qquad (2.1)$$

where Y [-] is the geometry factor which depends mainly on the crack geometry and the element geometry; σ_n [MPa] is the tensile stress normal to the flaw's plane (see Figure 2.4) and a [m] is the flaw depth (the flaw depth a is measured perpendicularly to the edge which contains the longest flaw length, in case the flaw spreads over two edges: see Figure 2.4).

In many publications Y is used as a synonym for $Y.(\pi)^{1/2}$. If a crack is not perpendicular to the surface, the geometry factor Y varies (Porter 2001). However, under the tensile stress σ_n, an inclined crack grows with a kink which results in a crack in mode I (Figure 2.6; Lawn 1993; Porter 2001). Yingzhi and Hills (1990) reported that such a crack orientation could accurately be modelled by an equivalent perpendicular edge crack (see Figure 2.6).

Furthermore, according to LEFM, the critical stress intensity factor or fracture toughness is the stress intensity factor which leads to instantaneous failure (i.e. corresponding to the inert or short-term strength) thus (Griffith 1920; Irwin 1957; Haldimann *et al.* 2008):

$$K_{Ic} = Y.f_{ct,inert}.(\pi.a_{ci})^{1/2} \tag{2.2}$$

where K_{Ic} = 0.75 MPa.m$^{1/2}$ is a good practical value for the fracture toughness of modern soda-lime silica glass (Haldimann *et al.* 2008; Overend and Zammit 2012); $f_{ct,inert}$ [MPa] is the inert strength (strength under inert conditions) corresponding to a constant loading and a_{ci} [m] is the initial critical flaw depth, i.e. the depth of the flaw which caused failure but measured before loading the specimen. The location of the critical flaw can be found easily by looking at the mirror zone after failure. The critical flaw is located at the centre of the mirror zone (see Figure 2.4). The mirror zone depth R can be measured according to ASTM C1678 (2010) and is about 10 times larger than the critical flaw depth (Rodichev *et al.* 2007). An empirical relationship was found between the strength and the square root of the mirror zone depth, independent of the loading rate (ASTM C1678-10 2010; Zaccaria and Overend 2012).

Under the combined influence of water vapour and an applied load, small surface flaws grow continuously till failure. This phenomenon is called stress corrosion.
The relation between the crack propagation speed v and the stress intensity factor K_I in region I (see Figure 2.7) is given by (Wiederhorn and Bolz 1970; Lawn 1993; Haldimann *et al.* 2008):

$$v = v_0.(K_I/K_{Ic})^n \tag{2.3}$$

where v [m/s] is the crack propagation speed and v_0 [m/s] is the crack propagation speed when $K_I = K_{Ic}$.
Since structural elements are generally expected to be in service for several years, only region I (Figure 2.7) is taken into account.
Haldimann (2006) assumes that in laboratory conditions, a value of v_0 = 0.01 mm/s is an appropriate value for a surface strength model.

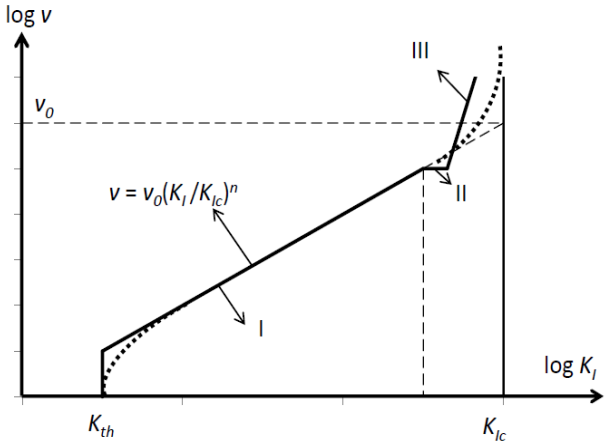

Figure 2.7: Relationship between crack propagation speed and stress intensity (Wiederhorn and Bolz 1970; Lawn 1993; Haldimann *et al.* 2008).

Further, in the framework of the current research, a load duration dependent formula for the edge strength is necessary. This can be obtained by considering the following differential equation of crack growth (Porter 2001; Haldimann *et al.* 2008):

$$v = \mathrm{d}a/\mathrm{d}t = v_0.(K_I/K_{Ic})^n \tag{2.4}$$

where t [s] is the time.
Using Eq. (2.1), integration of Eq. (2.4) yields (Porter 2001; Haldimann *et al.* 2008):

$$\int_{a_{ci}}^{a_c(t)} (1/a^{n/2}).\mathrm{d}a = \int_0^t v_0.(Y.\sqrt{\pi}/K_{Ic})^n.\sigma_n^n(t).\mathrm{d}t \tag{2.5}$$

where a_{ci} [m] is the initial critical flaw depth; $a_c(t)$ [m] is the critical flaw depth at time t and $\sigma_n(t)$ [MPa] is the tensile stress normal to the plane of the flaw at time t.

Thus, with n being constant, Eq. (2.5) yields (Vandebroek *et al.* 2013):

$$\int_0^t \sigma_n^n(t).dt = \frac{2}{(n-2).v_0.(Y.\sqrt{\pi}/K_{Ic})^n.a_{ci}^{(n-2)/2}} (1-(a_{ci}/a_c(t))^{(n-2)/2}) \tag{2.6}$$

With $\sigma_n(t)$ being constant, Eq. (2.6) yields (Vandebroek *et al.* 2012):

$$t.(\sigma_n)^n = \frac{2}{(n-2).v_0.(Y.\sqrt{\pi}/K_{Ic})^n.a_{ci}^{(n-2)/2}}(1-(a_{ci}/a_c(t))^{(n-2)/2}) \tag{2.7}$$

At failure time t_f (or lifetime of the flaw under consideration or load duration before failure), σ_n equals f_{ct} and $a_c(t)$ equals $a_c(t_f)$, which leads to:

$$t_f.(f_{ct})^n = \frac{2}{(n-2).v_0.(Y.\sqrt{\pi}/K_{Ic})^n.a_{ci}^{(n-2)/2}}(1-(a_{ci}/a_c(t_f))^{(n-2)/2}) \tag{2.8}$$

where f_{ct} [MPa] is the strength corresponding to a constant loading; t_f [s] is the load duration, i.e. the time period during which the flaw can resist the constant stress equal to f_{ct}.

As n is large and assuming $a_c(t_f) >> a_{ci}$, Eq. (2.10) yields (Porter 2001; Haldimann *et al.* 2008; Overend and Zammit 2012; Vandebroek *et al.* 2012; Wachtman *et al.* 2009):

$$t_f.(f_{ct})^n = \frac{2}{(n-2).v_0.(Y.\sqrt{\pi}/K_{Ic})^n.a_{ci}^{(n-2)/2}} \tag{2.9}$$

At failure time t_f (or lifetime of the flaw under consideration or load duration), $a_c(t)$ equals $a_c(t_f)$ and Eq. (2.8) leads to (Vandebroek *et al.* 2013):

$$\int_0^{t_f}\sigma_n^n(t).dt = \frac{2}{(n-2).v_0.(Y.\sqrt{\pi}/K_{Ic})^n.a_{ci}^{(n-2)/2}}(1-(a_{ci}/a_c(t_f))^{(n-2)/2}) \tag{2.10}$$

where t_f [s] is the time period during which the flaw can resist the stress history.

As n is large and assuming $a_c(t_f) >> a_{ci}$, Eq. (2.10) yields (Porter 2001; Haldimann *et al.* 2008; Overend and Zammit 2012):

$$\int_0^{t_f}\sigma_n^n(t).dt = \frac{2}{(n-2).v_0.(Y.\sqrt{\pi}/K_{Ic})^n.a_{ci}^{(n-2)/2}} \tag{2.11}$$

Eq. (2.11) means that two stress histories $\sigma_{n1}(t)$, $t \in [0,t_{f1}]$ and $\sigma_{n2}(t)$, $t \in [0,t_{f2}]$ cause the same crack growth if:

$$\int_0^{t_{f1}} \sigma_{n1}^n(t).dt = \int_0^{t_{f2}} \sigma_{n2}^n(t).dt \tag{2.12}$$

on condition that the two stress histories are applied on specimens with the same material properties and flaw characteristics under the same environmental conditions.

The value of these integrals increases from 0 at the beginning of the loading to the value of Eq. (2.9) at failure (Haldimann 2006). The integration will be performed for values of $K_I > K_{th}$, K_{th} being the crack growth threshold (Fink 2000; Haldimann 2006; Haldimann *et al.* 2008). In the literature (Simmons and Freiman 1981; Gehrke *et al.* 1987), the value of the crack growth threshold in air K_{th} = 0.27 MPa.m$^{1/2}$ is provided. For the crack growth threshold in water K_{th} = 0.20 MPa.m$^{1/2}$ is provided by Wiederhorn and Bolz (1970).

Comparing the strength values of two specimens tested at a different constant stress i.e. assuming a constant value of $\sigma_{n1}(t) = f_{ct,1}$ and $\sigma_{n2}(t) = f_{ct,2}$, Eq (2.12) yields:

$$f_{ct,1}/f_{ct,2} = (t_{f,ct,2}/t_{f,ct,1})^{1/n} \tag{2.13}$$

As the load during a test is linearly increasing, instead of being constant, a correction factor has to be applied when comparing the experimental strength value f to the strength value f_{ct} in Eq. (2.9) (Mencik 1992):

$$f_{ct} = (t_f/(n+1).t_{f,ct})^{1/n}.f \tag{2.14}$$

where f [MPa] is the experimental strength value corresponding to a linearly increasing loading and n [-] is the crack velocity parameter (constant value between 16 for 100% RH and 18.1 for 50% RH) (Charles 1958; Blank 1993; Shen 1997; Fink 2000; Wörner 2001).

Using Eq. (2.14), Eq. (2.13) yields:

$$f_1/f_2 = (t_{f,2}/t_{f,1})^{1/n} \tag{2.15}$$

Eq. (2.15) and (2.14) are verified experimentally for the edge strength and are presented in sections 3.4 and 3.5, respectively.

2.3.3 Explicit approach

As described in section 2.3.1, the edge strength of glass depends on the size and distribution of flaws at the edge, caused by scoring and eventually processing the edge. However, in some cases one flaw is substantially larger than the other flaws in the population, for instance because of vandalism or damage during handling or other causes. If the depth of the dominant flaw is known, the explicit approach can be applied to estimate the edge strength. However, these cases are rather rare and most often the stochastic approach is more appropriate to apply (see 2.3.4).

If the initial critical depth of the dominant flaw $a_{ci,dom}$, as well as the geometry factor Y is known, the inert strength $f_{ct,inert}$ (corresponding to constant loading) can be derived from Eq. (2.2):

$$f_{ct,inert} = \frac{K_{Ic}}{Y.(\pi.a_{ci,dom})^{1/2}} \tag{2.16}$$

Similarly, if the stress corrosion parameters n and v_0 are known, the ambient strength f_{ct} (corresponding to constant loading) in function of the load duration t_f can be derived from Eq. (2.9):

$$f_{ct} = \left(\frac{2}{t_f.(n-2).v_0.(Y.\sqrt{\pi}/K_{Ic})^n.a_{ci,\mathrm{dom}}^{(n-2)/2}} \right)^{1/n} \tag{2.17}$$

For a certain dominant flaw with initial critical depth $a_{ci,dom}$, the relation between the strength f_{ct} and the load duration t_f is given by Eq. (2.17) and depicted in Figure 2.8 by the dotted line. The real curve (continuous line) deviates

corresponding to the two asymptotes (Overend and Zammit 2012), with which the dotted lines in Figure 2.7 merge. In Figure 2.7, one asymptote corresponds to the inert strength $f_{ct,inert}$ (K_{Ic} = 0.75 MPa.m$^{1/2}$) and the other asymptote corresponds to the threshold strength $f_{ct,threshold}$ (K_{th} = 0.27 MPa.m$^{1/2}$). Consequently, the real curve deviates from the dotted line to the inert strength $f_{ct,inert}$ at the vertical axis and to the horizontal part at the right side in Figure 2.8.

The load duration $t_{f,threshold}$ corresponding to the threshold strength $f_{ct,threshold}$ (corresponding to constant loading) can be derived from Eq. (2.9):

$$t_{f,threshold} = \frac{2}{(\frac{K_{th}}{K_{Ic}}.f_{ct,inert})^n.(n-2).v_0.(Y.\sqrt{\pi}/K_{Ic})^n.a_{ci,\mathrm{dom}}^{(n-2)/2}} \tag{2.18}$$

where $f_{ct,threshold} = (K_{th}/ K_{Ic}).\ f_{ct,inert}$ is the threshold strength.

A larger dominant flaw corresponds to a lower strength curve as shown in Figure 2.9.

In most cases, the initial critical flaw depth $a_{ci,dom}$ is unknown. Some values are provided by Fink (2000) for damage at the surface of glazing. A similar value could be determined for handling damage at the edge by deliberately causing the damage and then measuring the flaw depth.

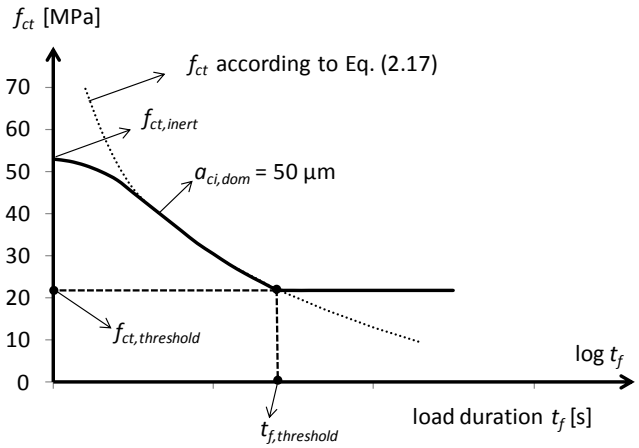

Figure 2.8: Relationship between the strength f_{ct} and the load duration t_f for one critical flaw depth.

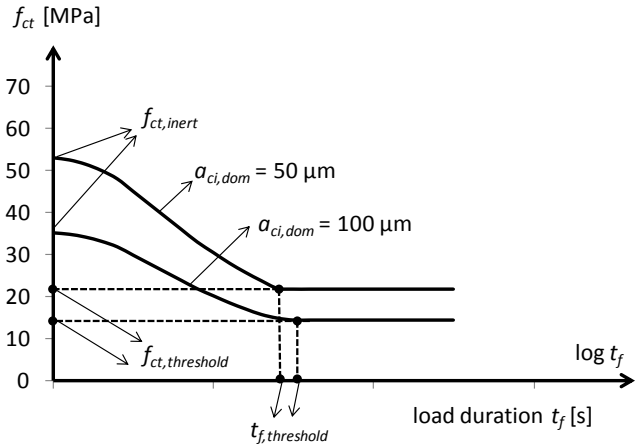

Figure 2.9: Relationship between the strength f_{ct} and the load duration t_f for two different critical flaw depths.

2.3.4 Stochastic approach

Apart from possible damage caused e.g. by handling or transport, the size and distribution of flaws at the edge, caused by scoring and processing the edge are considered in this approach. Multiple parameters influence these defects at the edge, e.g. the cutting wheel, the cutting oil, the cutting pressure and speed, the type of grinding or polishing discs, the speed of grinding or polishing, etc. Normally, the edge surface does not contain any flaws that are much larger than others. This surface condition can be presented by a random surface flaw population (Haldimann 2006; Haldimann *et al.* 2008).

In this section, the derivation of the interrelation between the scatter of the flaw size and the scatter of the strength is based on the following hypotheses and assumptions (Haldimann 2006; Haldimann *et al.* 2008):

- the edge surface contains a large number of mechanical flaws of variable depth - the depth of the flaws is a random variable
- the flaws do not influence each other, which is a conservative assumption (Auradou *et al.* 2001)
- the element fails when the first flaw fails
- the orientation of the flaws is perpendicular to the stress σ_n (mode I, see Figures 2.5 and 2.6)
- there is no subcritical crack growth (from Eq. (2.39) onwards, stress corrosion is considered again)
- the stress is considered to be constant

For a more general derivation, the literature provides more information about the relation between the flaw size and the strength (Haldimann 2006; Haldimann *et al.* 2008).

In literature (Munz and Fett 1999; Haldimann 2006; Haldimann *et al.* 2008), the distribution of the flaw depth and the distribution of the number of flaws are in general described by a Pareto (power law) distribution and a Poisson distribution, respectively.

Assuming a large mean number of flaws, the probability density function $f_a(a)$ is proportional to the power law $1/a^r$. The cumulative distribution function (CDF) of the flaw depth a is then given by:

$$\begin{aligned} F_a(a) &= 0 && \text{for } a < a_0 \\ F_a(a) &= 1 - (a_0/a)^{r-1} && \text{for } a \geq a_0 \end{aligned} \tag{2.19}$$

For normalisation reasons of the cumulative distribution function, a lower limit a_0 for the flaw depth a has to be introduced. The value of a_0 is not of importance (Munz and Fett 1999; Haldimann 2006; Haldimann *et al.* 2008).

The flaw density z is defined as the number of flaws Z_0 in the unit surface S_0. Thus the average number of flaws in a glass element is equal to:

$$Z = z.S_s = \frac{Z_0}{S_0}.S_s \tag{2.20}$$

where S_s is the surface of the glass element which is subjected to a stress larger than the threshold strength $f_{ct,threshold} = (K_{th}/ K_{Ic}).\ f_{ct,inert}$.

A glass element fails if any of the flaws fail or it survives if all the flaws survive. The survival probability of one flaw is equal to:

$$P_{s,inert}^{(1)} = 1 - P_{f,inert}^{(1)} \tag{2.21}$$

Thus, the survival probability of a glass element with exactly M flaws equals:

$$P_{s,inert}^{(M)} = (1 - P_{f,inert}^{(1)})^M \tag{2.22}$$

In a real glass element, the total number of flaws is a random variable itself and M remains unknown. Only the mean number of flaws Z shall be considered as a known variable.

The actual number of flaws M in a glass element (as defined above) may be larger or smaller than Z . If the actual number of flaws M follows a Poisson distribution, then the probability of an element containing exactly M flaws is given by:

$$P(M) = \frac{\exp(-Z).Z^M}{M!} \tag{2.23}$$

The survival probability of a random glass element is obtained by multiplying the probability *P(M)* of an element with surface S_s (i.e. the surface of the glass element which is subjected to a stress larger than the threshold strength $f_{ct,threshold}$) having exactly *M* flaws by the corresponding survival probability and summing up over all possible number of flaws:

$$P_{s,inert} = \sum_{M=0}^{\infty} P(M).P_{s,inert}^{(M)} \tag{2.24}$$

or

$$P_{s,inert} = \sum_{M=0}^{\infty} \frac{\exp(-Z).Z^M}{M!}.(1-P_{f,inert}^{(1)})^M \tag{2.25}$$

Using the definition of the exponential function as an infinite series:

$$\exp(x) = \sum_{M=0}^{\infty} \frac{x^M}{M!} \tag{2.26}$$

yields:

$$P_{s,inert} = \exp(-Z.P_{f,inert}^{(1)}) \tag{2.27}$$

Thus, the failure probability equals:

$$P_{f,inert} = 1 - P_{s,inert} = 1 - \exp(-Z.P_{f,inert}^{(1)}) \tag{2.28}$$

With the failure probability of a flaw being the probability that its random size *a* is larger than the critical flaw size a_{ci}:

$$P_{f,inert}^{(1)}(a) = \int_{a_{ci}}^{\infty} f_a(a)da = 1 - F_a(a_{ci}) \tag{2.29}$$

and inserting Eq. (2.19) into Eq. (2.29) the failure probability is given by:

$$P_{f,inert}(a) = 1 - \exp(-Z.(a_0/a_{ci})^{r-1}) \tag{2.30}$$

The relation between a_{ci} and the inert strength $f_{ct,inert}$ (corresponding to a constant loading) follows from Eq. (2.2):

$$a_{ci} = \left(\frac{K_{Ic}}{f_{ct,inert}.Y.(\pi)^{1/2}}\right)^2 \tag{2.31}$$

Thus,

$$P_{f,inert}\,(f_{ct,inert}) = 1 - \exp\left(-Z.(a_0)^{r-1}.\left(\frac{f_{ct,inert}.Y.\sqrt{\pi}}{K_{Ic}}\right)^{2(r-1)}\right) \tag{2.32}$$

or

$$P_{f,inert}\,(f_{ct,inert}) = F\,(f_{ct,inert}) = 1 - \exp\left(-\left(\frac{f_{ct,inert}}{\vartheta}\right)^{m_0}\right) \tag{2.33}$$

This is a 2-parameter Weibull distribution with parameters:

$$\vartheta = \frac{K_{Ic}}{Z^{1/m_0}.Y.\sqrt{\pi}.\sqrt{a_0}} \quad \text{and} \quad m_0 = 2.(r-1) \tag{2.34}$$

The parameter ϑ depends on the mean number of flaws Z of the stressed surface S_s of the element (see Eq. 2.20). To avoid this, substitution of Eq. (2.20) into Eq. (2.33) yields:

$$P_{f,inert}\,(f_{ct,inert}) = F\,(f_{ct,inert}) = 1 - \exp\left(-\frac{S_s}{S_0}\left(\frac{f_{ct,inert}}{\vartheta_0}\right)^{m_0}\right) \tag{2.35}$$

with the Weibull scale parameter ϑ_0 and the Weibull shape parameter m_0 only depending on the surface flaw population and thus being true material parameters:

$$\vartheta_0 = \frac{K_{Ic}}{Z_0^{1/m_0}.Y.\sqrt{\pi}.\sqrt{a_0}} \quad \text{and} \quad m_0 = 2.(r-1) \tag{2.36}$$

From Eq. (2.34) and Eq. (2.36):

$$\vartheta = \vartheta_0.\left(\frac{Z_0}{Z}\right)^{1/m_0} \tag{2.37}$$

For two elements with stressed surfaces $S_{s,1}$ and $S_{s,2}$ (which are subjected to stresses larger than the threshold strength $f_{ct,threshold}$), the ratio of the scale parameters is:

$$\frac{\vartheta_1}{\vartheta_2} = \left(\frac{S_{s,2}}{S_{s,1}}\right)^{1/m_0} \tag{2.38}$$

This ratio is referred to as the size effect (Munz and Fett 1999; Haldimann 2006; Haldimann *et al.* 2008).

For the determination of the Weibull parameters, ϑ_0 and m_0, Eq. (2.36) supposes the knowledge of the values of *r, Z_0, Y and a_0.* This means that the distribution of the flaw depth, the distribution of the number of flaws and the geometry of the flaws has to be estimated. This can be achieved by an extensive microscopic research, which is rather time-consuming in practice. However, the Weibull parameters can be determined more easily by testing (see chapter 3).

When stress corrosion is involved, substitution of Eq. (2.17) into Eq. (2.30) leads to a similar 2-parameter Weibull distribution:

$$P_f(f_{ct}) = F(f_{ct}) = 1 - \exp\left(-\frac{S_s}{S_0}\left(\frac{f_{ct}}{\vartheta_0'}\right)^{m_0'}\right) \tag{2.39}$$

with the Weibull scale parameter ϑ'_0 and the Weibull shape parameter m'_0.

Similarly, for two elements with stressed surfaces $S_{s,1}$ and $S_{s,2}$ (which are subjected to stresses larger than the threshold strength $f_{ct,threshold}$), the ratio of the scale parameters is:

$$\frac{\vartheta'_1}{\vartheta'_2} = \left(\frac{S_{s,2}}{S_{s,1}}\right)^{1/m'_0} \tag{2.40}$$

Eq. (2.38) is valid, on condition that the two series are tested on specimens with the same flaw population, while Eq. (2.40) is valid, on condition that the two series are tested in identical laboratory conditions (the same stress corrosion parameters) and on specimens with the same flaw population. In section 3.7, the corresponding series of small and large specimens, which are compared to each other, were tested in identical laboratory conditions and had the same flaw population.

If two series with different sizes but with the same thickness are compared (see section 3.7), the surface S in Eq. (2.40) can be replaced by the stressed length L_s:

$$\frac{\vartheta'_1}{\vartheta'_2} = \left(\frac{S_{s,2}}{S_{s,1}}\right)^{1/m'0} = \left(\frac{b'L_{s,2}}{b'L_{s,1}}\right)^{1/m'0} = \left(\frac{L_{s,2}}{L_{s,1}}\right)^{1/m'0} \tag{2.41}$$

where the value of b' is the same for two specimens with the same thickness and the same edge finishing (see Fig. 2.10), but with a different size. However, the value of b' is different for the cut and arrissed or (smooth) ground specimens because of the anris for the latter (see Fig. 2.10), but Eq. (2.41) is not used to compare specimens with different edge finishings in the current study. Also, for different thicknesses of the same edge finishing, the value of b' is different, but in the current study, different thicknesses are not compared to each other.

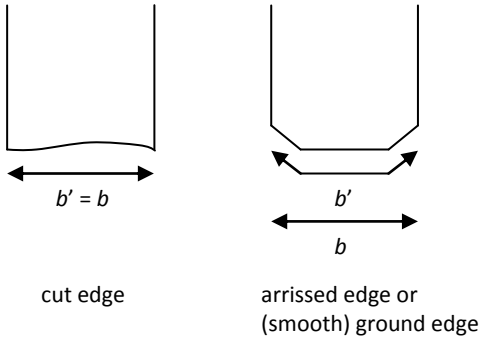

Figure 2.10: Schematic view of a cut, arrissed and (smooth) ground specimen edge (cross-section).

The Weibull parameters can be estimated by the least-squares method (LSM) or the method of maximum likelihood (MLE or maximum likelihood estimates). Linear regression is commonly used when all experimental data of one series result from one testing method (e.g. the 4PB test at 2 MPa/s, see section 3.2.3) and one specimen size.

However, if more than one testing method and/or more than one specimen size is pooled in one series, the method of maximum likelihood is more appropriate (Wachtman *et al.* 2009). The latter method is required in the ASTM C 1239-07 (2007). In the current study, one series is performed with one testing method, and all specimens of one series have the same thickness, load span and edge

finishing. Thus, both methods, the least-squares method and the method of maximum likelihood, are appropriate to use.
For the least-squares method, the empirical failure probability usually assigned to the i^{th} strength value (of n_s values) (Munz and Fett 1999; ASTM C 1239-07) can be calculated as:

$$F_i = \frac{i - 0.5}{n_s} \tag{2.42}$$

while Makkonen (2008) proposes the following estimator function:

$$F_i = \frac{i}{n_s + 1} \tag{2.43}$$

For the method of maximum likelihood, the Weibull parameters are estimated after solving the non-linear Equations (2.44) and (2.45):

$$\frac{1}{m_0'} = \frac{\Sigma f_{eg,i}^{m_0'} . \ln f_{eg,i}}{\Sigma f_{eg,i}^{m_0'}} - \frac{1}{n_s} \Sigma \ln f_{eg,i} \tag{2.44}$$

$$\vartheta'^{m_0'}_0 = \frac{1}{n_s} \Sigma f_{eg,i}^{m_0'} \tag{2.45}$$

with $f_{eg,i}$ the tensile strength of the i^{th} specimen of the series.

Thoman et al (1969) used Monte Carlo methods to characterize the bias and provided tabulated unbiasing factors $b(n_s)$ which depend only on n_s. The corrected Weibull shape parameter is:

$$m_{corr} = m_0' . b(n_s) \tag{2.46}$$

with:

$$b(n_s) \approx \tanh^{1.87}\left(\left(\frac{n_s - 3.855}{0.678}\right)^{0.21375}\right) \tag{2.47}$$

2.3.5 Residual stress

According to the literature (Conway and Mecholsky 1989; Overend *et al.* 2007; Zaccaria and Overend 2012), residual compressive stresses are common in as-received annealed glass. The residual stress amounts from 5 MPa to 10 MPa. However, the reliability of the method to determine the residual stress is quite low and indeed has to be validated by photo-elastic measurements (Zaccaria and Overend 2012). For annealed soda lime silicate glass, only the residual stress at the surface is investigated by Zaccaria and Overend (2012) and not the residual stress at the edge. However, the latter residual stress may be quite different from the residual stress at the surface. It can be concluded that more investigations are required to determine the residual stresses of annealed glass specimens, at the surface or at the edge.

2.4 Thermal actions

The temperature difference in a pane which induces thermal stresses is mainly caused by the solar radiation and the daily variation of the outdoor temperature (diurnal range of the temperature). In Europe, the solar radiation on a vertical pane amounts from 750 W/m² to 1000 W/m² and the daily variation of the outdoor temperature ranges between 6 °C and 20 °C (prEN thstr 2004; NF P 78-201-1/A1(DTU39) 1998). The radiation has a larger influence on the temperature difference in a pane than the diurnal range.

Only the French standard NF P 78-201-1/A1(DTU39) (1998) provides more detailed information about the global solar radiation and the diurnal range of the temperature, but only for a specific location in France. The global solar radiation consists of the direct and the diffuse radiation. The latter is caused by the clouds and ranges between 10% and 20% of the global solar radiation.

According to the French standard NF P 78-201-1/A1(DTU39) (1998), thermal fracture must be estimated by using the climate data of 4 characteristic days (one for every season). However, these climate data are only given for a specific location in France. Figures 2.11 shows the diurnal range of the outdoor temperature for every season. Figure 2.12 depicts the solar radiation on a vertical pane for every façade orientation and every season (for locations of 0 to 500 m above sea-level). For other inclinations of the pane or elevation levels of more than 500 m above sea-level corrections are provided (NF P 78-201-1/A1(DTU39) 1998). Finally, Figure 2.12 also gives information about the diffuse solar radiation for every season.

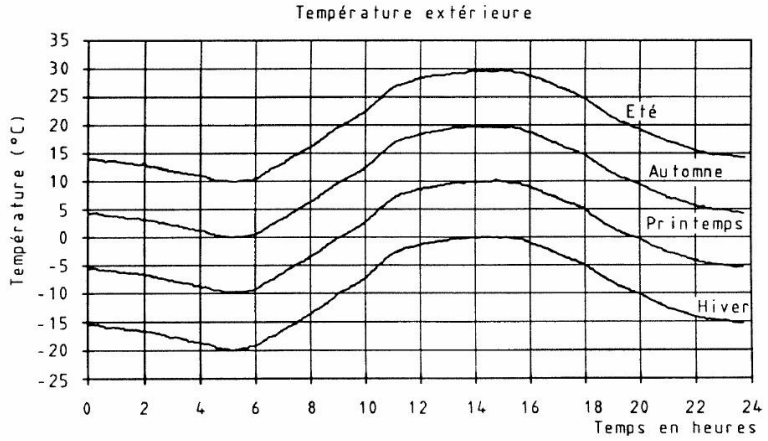

Figure 2.11: Diurnal range (NF P 78-201-1/A1(DTU39) 1998).

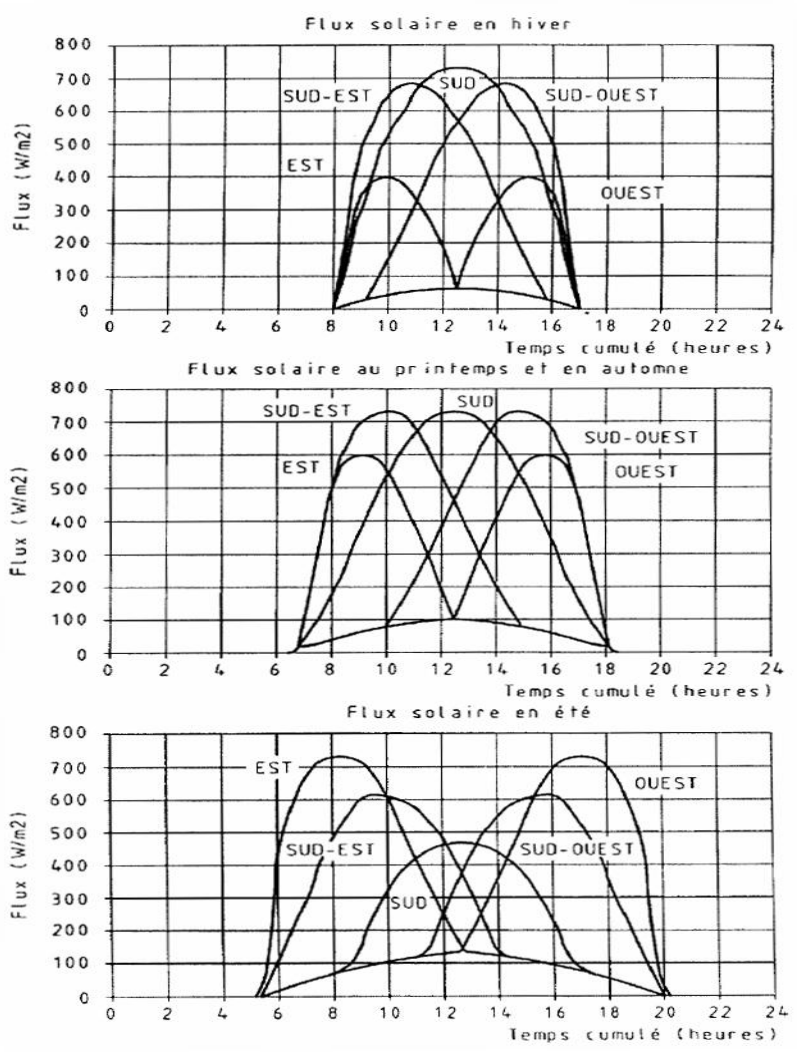

Figure 2.12: Global solar radiation on a vertical pane and diffuse solar radiation (NF P 78-201-1/A1(DTU39) 1998).

2.5 Thermal fracture

In the first section, two documents of interest are discussed. The first document, i.e. 'Evaluation des contraintes thermiques dans les vitrages' (Belgian Glass 1997, a document of the 'Fédération de l'industrie du Verre') is the most important input document for the preliminary European standard prEN thstr (2004), which is still under development. The second document delivers a very good overview of the topic. The literature of Beason and Lingnell (2002, 2003) is discussed in section 2.5.2, as the standard E2431-12 (2012) is based on these articles. Then, in the second section (2.5.2), the most important standards are addressed. In the last section, an example points out the pending difficulties.

2.5.1 Literature

2.5.1.1 Belgian Glass (1997)

Basically, the temperature difference between the part subjected to solar radiation and the part concealed within the frame has to stay below an allowable value for the particular glass product. A basic temperature difference accounts for the environmental influences. Then, the calculated temperature difference modifies this basic temperature difference.

The basic temperature difference depends on the solar radiation intensity, the solar energy absorption of the glazing, the heat transfer coefficients and the diurnal temperature range.
The calculated temperature difference additionally accounts for the influence of blinds, possible shadow on a part of the pane and the frame characteristics. The ventilation between the blinds and the glazing is taken into account. Finally, the shadow on a part of the window and the frame characteristics have an influence on the temperature difference.

The described method is a deterministic one which does not mention stresses or safety coefficients. Moreover, the unknown safety margin is identical for structural elements, secondary elements or infill panels.

Concerning the influence of solar radiation, the altitude of the site and the orientation of the glazing, the influence of haze and ground reflectance and the time of the year are important. However, the 'Belgian Glass' document simplifies

these influences by assuming a maximum intensity which has to be taken into account during the lifetime of the glazing, regardless of the aforementioned influences on the solar radiation. Thus, only an instantaneous temperature difference is considered, assuming this maximum difference to be determinative for the complete lifetime of the glazing unit. Also, stress corrosion (see section 2.3.2) is not considered in this method.

2.5.1.2 Thermal stresses in double-glazed windows (Pilette and Taylor 1988)

In this article, a detailed study about some parameters which influence thermal fracture is presented. Two steady-state heat transfer analyses were performed on three different types of sealed double-glazed windows. In steady-state condition of heat transfer, there is no temperature variation with time. The first analysis simulated night conditions without solar radiation and the second with a specific solar heat flow. Then, the influence of the exterior air film conductance, the outdoor temperature, the heat flux, the inner pane absorption and the frame absorption was examined. Additionally the influence of shadow was estimated.

The conclusions of this study were:

- a steady-state analysis gives almost the same results as a transient analysis, in which a temperature variation with time is considered
- the temperature gradient in the outer pane is greatest for a low exterior air film conductance h_e, a mild outdoor temperature and a high solar radiation
- the temperature gradient in the inner pane is greatest for a high exterior air film conductance h_e, a low outdoor temperature, a high solar radiation and interior blinds
- temperature gradients through the glass thickness are small and can be neglected
- thermal stresses can be calculated separately for each pane of the insulating glass unit
- thermal stresses do not depend on the aspect ratios (between 1 and 2) of the window and the area (between 2 m² and 4 m²) of the window
- in case of shadow, the maximum stresses occur where the shadow line intersects the edges and the stresses rise as the portion of area shaded increases to about 1/3 of the total area.

This document does not provide a value of the solar radiation which needs to be applied, and no edge strength values are mentioned. Consequently, the probability of failure is not known for the treated examples in this document.

2.5.2 Standards

2.5.2.1 Preliminary European standard (prEN thstr 2004)

The same method compared to section 2.5.1.1 is provided in the preliminary standard prEN thstr (2004). However, some additional influences are accounted for.

The basic temperature difference depends on the solar radiation intensity, the solar energy absorption of the glazing, the possible heating from radiant heaters, the heat transfer coefficients, the diurnal temperature range and the eventual internal temperature rise. The latter can be caused by the air in the vicinity of the window not being ventilated, and thus being different from the ambient room temperature.

The calculated temperature difference additionally accounts for the influence of blinds, backups, possible shadow on a part of the pane and the frame characteristics. The color of the blinds is important, as well as the ventilation between the blinds and the glazing. Also, backup walls or ceilings can cause an accumulation of hot air and thus influence the temperature of the pane. Shadow can be static (present for more than 3 hours) or transient.

The described method has the same drawbacks as the 'Belgian Glass' (1997) document on which it is strongly based.

2.5.2.2 French standard (NF P 78-201-1/A1(DTU39) 1998)

In the French standard NF P 78-201-1/A1(DTU39) (1998), three levels of verification are presented.

The first method provides tables with solutions for annealed glazing which need no verification. A second method uses tables indicating the energy absorption coefficient which may not be exceeded.

Finally, the most precise but most time-consuming method consists of calculating the temperature difference between different areas of the glazing unit. This method is described in annex E of the standard NF P 78-201-1/A1(DTU39) (1998). The calculation of the temperature differences can be carried out in steady-state regime, and is only applicable on frames with a low thermal inertia. For other frames, these temperature differences must be calculated transient over a period of one day (depending on the season and the orientation of the glazing, see section 2.4). Then, the maximum temperature difference between two parts of the glazing unit is used to compute the stress which has to stay below an allowable stress. The calculated stress depends on the inertia of the frame and the shadow on the glazing. The allowable stress depends on the type of glass, the sensibility of the edge to thermal fracture (cut or ground, monolith glass or insulating glass unit), the inclination and the support conditions of the glazing.

Also this method is a deterministic one although stresses are calculated. However, no safety coefficients are mentioned. Again, the unknown safety margin is identical for structural elements, secondary elements or infill panels.

Using this method accounts for the influence of the latitude and the altitude of the site, the orientation and the slope of the glazing and finally the time of the year by calculating during one day per season. However, only an instantaneous stress is considered, assuming this maximum stress to be determinative for the complete lifetime of the glazing unit. Again, stress corrosion (section 2.3.2) is not considered in this method.

2.5.2.3 American standard (E2431-12 2012)

According to the standard E2431-12 (2012), the calculated stress due to the thermal loadings has to stay below the allowable stress corresponding to a certain probability of failure. The calculated stress depends on the incident solar irradiance, the glass thickness, the solar absorption, the frame type and the edge bite (part concealed within the frame), exterior shading conditions and interior shading devices. The standard provides curves to determine the calculated stress. The allowable stress depends on the desired probability of failure and the perimeter of the pane.

The use of this standard assumes that (E2431-12 2012):

- the glass edges shall be free of damage,
- the glass shall be properly glazed,
- the glass shall not have been subjected to abuse, and
- the glass edge support allows in-plane movement of the glass due to thermal expansion and contraction

The proposed method is a probabilistic one, concerning the resistance side. On the action side, the authority shall provide the incident solar irradiance. In the end, the designer is responsible for the choice of the probability of failure. In the two examples, presented in the standard, a probability of failure of 0.001 is provided for a commercial building and 0.008 for a residential building (E2431-12 2012). In literature, a smaller probability of failure of 0.0001 is proposed (Beason and Lingnell 2003) for thermal stress design. Also, the size effect is considered, as the allowable stress depends on the perimeter of the glass (see section 3.7). Finally, stress corrosion (sections 2.3.2 and 3.4) is considered in this method by assuming a load duration of 60 minutes (Beason and Lingnell 2003).
However, the standard does not address a transient influence by considering the diurnal temperature change. Nor does it address the influence of HVAC registers, thermally insulating window coverings, drop ceilings and other heat traps, increased solar irradiance caused by exterior reflections, variations in heat transfer coefficients other than assumed for the steady state analysis and stresses induced by thermal sources other than the sun.
Consequently, only an instantaneous stress is estimated, assuming this maximum stress to be determinative for the complete lifetime of the glazing unit.

2.5.3 Illustrative example

With a very simple example, the difference between the methods is demonstrated.

A single vertical window pane with dimensions of 1000 mm by 2000 mm by 4 mm with a solar absorption factor of 0.5 is considered. The pane is subjected to a solar irradiance of 750 W/m² and the diurnal temperature change amounts to 11 °C. The pane is not subjected to shadow and there are no blinds or internal backups. The glass has an edge bite of 20 mm and is supported in a conventional aluminum frame (light color with thermal barrier: frame factor of 0.7 according to the 'Belgian Glass' document (1997).

The module of elasticity is taken 73 GPa and the expansion coefficient α is taken 9.10^{-6} °C^{-1} (Belgian Glass 1997). The value of 73 GPa is a maximum characteristic value, not a mean value which is normally taken equal to 70 GPa according to DIN 18008-1 (2010) or prEN 16612 (2013).

'Belgian Glass' method (1997):

With the external heat transfer coefficient h_e = 16 W/m²°C, the internal heat transfer coefficient h_i = 8 W/m²°C and the module of elasticity E = 73000 MPa the calculated temperature difference equals to:

$$\Delta T = \left(\frac{0.5 * 750\,\text{W/m}^2 + 11\,°\text{C} * h_e}{h_e + h_i}\right) * 0.7 = 16.1\,°\text{C} \quad < 30\,°\text{C}$$

or in terms of stresses:

$$\sigma_e = \left(\frac{0.5 * 750\,\text{W/m}^2 + 11\,°\text{C} * h_e}{h_e + h_i}\right) * 0.7 * E * \alpha = 10.6\,\text{MPa} \quad < 19.7\,\text{MPa} \qquad (2.48)$$

Draft European Standard (prEN thstr 2004):

With the external heat transfer coefficient h_e = 12 W/m²°C and the internal heat transfer coefficient h_i = 8 W/m²°C the calculated temperature differences are equal to:

a) for a cut or arrissed edge:

$$\Delta T = \left(\frac{0.5 * 750\text{W/m}^2 + 11\text{°C} * h_e}{h_e + h_i}\right) * 0.7 = 17.8\,\text{°C} \quad < 35.0\,\text{°C}$$

or in terms of stresses (to compare with the other methods):

$$\sigma_e = \left(\frac{0.5 * 750\text{W/m}^2 + 11\text{°C} * h_e}{h_e + h_i}\right) * 0.7 * E * \alpha = 11.7\,\text{MPa} \quad < 23.0\,\text{MPa} \qquad (2.49)$$

b) for a smooth ground edge:

$$\Delta T = \left(\frac{0.5 * 750\text{W/m}^2 + 11\text{°C} * h_e}{h_e + h_i}\right) * 0.7 = 17.8\,\text{°C} \quad < 40.0\,\text{°C}$$

or in terms of stresses (to compare with the other methods):

$$\sigma_e = \left(\frac{0.5 * 750\text{W/m}^2 + 11\text{°C} * h_e}{h_e + h_i}\right) * 0.7 * E * \alpha = 11.7\,\text{MPa} \quad < 26.3\,\text{MPa} \qquad (2.50)$$

c) for a polished edge:

$$\Delta T = \left(\frac{0.5 * 750\text{W/m}^2 + 11\text{°C} * h_e}{h_e + h_i}\right) * 0.7 = 17.8\,\text{°C} \quad < 45.0\,\text{°C}$$

or in terms of stresses (to compare with the other methods):

$$\sigma_e = \left(\frac{0.5 * 750\text{W/m}^2 + 11\text{°C} * h_e}{h_e + h_i}\right) * 0.7 * E * \alpha = 11.7\,\text{MPa} \quad < 29.6\,\text{MPa} \qquad (2.51)$$

French Standard (NF P 78-201-1/A1(DTU39) 1998):

No calculation is needed when the coefficient of absorption is less than 0.56 (if not fixed immediately to a wall), regardless the edge finishing. If a calculation should be made, the allowable stress to apply should be 20 MPa for a cut edge and 24 MPa for an arrissed (with a disc, not with a belt) or a (smooth) ground edge, if the support is on the four edges. In other support conditions, the allowable stresses are 16 MPa and 19 MPa, respectively.

ASTM Standard (E2431-12 2012):

With a desired probability of failure of 0.008:

$$\sigma_e = 26\ \text{kPa} * 0.5 * 750\text{W/m}^2 = 9.8\ \text{MPa} \quad < 11.8\ \text{MPa} \tag{2.52}$$

With a desired probability of failure of 0.001:

$$\sigma_e = 26\ \text{kPa} * 0.5 * 750\text{W/m}^2 = 9.8\ \text{MPa} \quad > 8.7\ \text{MPa} \tag{2.53}$$

With a desired probability of failure of 0.0001:

$$\sigma_e = 26\ \text{kPa} * 0.5 * 750\text{W/m}^2 = 9.8\ \text{MPa} \quad > 6.3\ \text{MPa} \tag{2.54}$$

Comparison of the different methods:

It can be noticed that the calculated stresses vary in a small range between 9.8 MPa and 11.7 MPa, depending on the applied method, while the allowable stresses range between 11.8 MPa and 29.6 MPa.

Table 2.1 provides the ratio of the calculated stress and the allowable stress for the different methods. It can be concluded that the ASTM method is much more conservative compared to the Belgian Glass method and the European standard, certainly with the probability of failure of 0.0001 which is proposed by Beason and Lingnell (2003).

Table 2.1: Safety margin for the different methods.

method	calculated stress [MPa]	allowable stress [MPa]	calculated stress/ allowable stress [-]
Belgian Glass method	10.6	19.7	0.54
European standard			
cut or arrissed	11.7	23.0	0.51
smooth ground	11.7	26.3	0.44
polished	11.7	29.6	0.39
ASTM method			
P_b = 0.008	9.8	11.8	0.83
P_b = 0.001	9.8	8.8	1.11
P_b = 0.0001	9.8	6.4	1.53

From the comparison of the methods, it can be stressed that:

- the calculated stresses are quite similar in all methods applied to the example
- the allowable stresses vary considerably depending on the method
- this example shows clearly that testing the edge strength is necessary to clarify the considerable scatter in strength values amongst the different methods

2.6 Highlights of this chapter

- The edge strength of glass strongly depends on the edge flaws (defects)
- The theories of linear elastic fracture mechanics and stress corrosion allow to describe the strength behaviour of glass
- In this study the stochastic approach is applied as the geometry and depth of the individual flaws (defects) are not quantified (i.e. not measured)
- Models for thermal actions are simplified in the literature and the standards
- The existing methods to evaluate thermal fracture vary significantly, especially the specified values of the allowable stresses (strength values)
- These methods only consider simplified façade configurations
- Finally, they do not account for the complete lifetime stress history

Consequently, there is a need for a more detailed look at the edge strength as well as the thermal actions, to be able to propose a general method applicable to every façade configuration, including the complicated double skin façade. Moreover, this method should be able to predict the probability of failure according to the principles of EN 1990 (2002), which not all the existing methods do.

Indeed, the existing methods are not very accurate, which implies that the designer often applies heat strengthened glass or fully tempered glass as the strength values are much higher than for annealed glass. However, this solution is more expensive and results in optical deformations.

3. Experimental investigations

It seems to be one of the fundamental features of nature that fundamental physical laws are described in terms of a mathematical theory of great beauty and power, needing quite a high standard of mathematics for one to understand it. You may wonder: Why is nature constructed along these lines? One can only answer that our present knowledge seems to show that nature is so constructed. We simply have to accept it. One could perhaps describe the situation by saying that God is a mathematician of a very high order, and He used very advanced mathematics in constructing the universe. Our feeble attempts at mathematics enable us to understand a bit of the universe, and as we proceed to develop higher and higher mathematics we can hope to understand the universe better.

Paul Dirac (1902-1984)

3.1 Introduction

In this chapter, the different experimental investigations on as-received annealed glass are divided into six test programmes. The subsequent programmes are founded on the conclusions of the previous ones. For the programmes, the knowledge presented in chapter 2 was used frequently. The outcome of the programmes was used for the numerical simulations, provided in chapter 4. The testing was only performed with as-received glass, not with weathered glass or glass damaged during handling or transport or other in-service events that induce further flaws on the glass edge surface.

A first test programme (TP 1) was set up in order to evaluate the correlation between stresses induced by temperature loading and by mechanical loading (see Figures 3.1 to 3.6). First, panes were subjected to a temperature loading. Infrared-heaters induced a temperature gradient in panes of 500 mm * 500 mm * 8 mm (20 test results). Next, beams (550 mm * 50 mm * 8 mm) were cut out of identical panes and were subjected to in-plane 4PB until failure (20 test results). Finally, these two series were compared.

In a second test programme (TP 2: 960 test results), several in-plane 4PB tests were performed. Different edge finishings from different suppliers, with two different nominal glass thicknesses (4 mm and 8 mm), were tested. Three different loading rates were applied to investigate the influence of stress corrosion (see section 2.3.2) on the edge strength.

In a third and fourth test programme (TP 3: 1300 test results, TP 4: 320 test results), the influence of the load history on the edge strength was explored. Thus, the influence of crack healing was estimated.

Finally, in a fifth and sixth test programme, the influence of the size (TP 5: 360 test results) and the stress distribution (TP 6: 240 test results) on the edge strength was examined. Indeed, actual thermal stresses have a different distribution over a different stressed area compared to the stress distribution and the stressed area during common testing. The stress distribution effect was investigated by means of the in-plane three-point bending test (3PB test).

The specimen name of all series (TP 2 to TP 6) follows the same structure:

- the first letter indicates the edge finishing: N for smooth ground, G for ground, A for arrissed and C for cut
- then the figure indicates the supplier: from 1 to 5
- after the hyphen follows a small letter indicating the geometry type of the specimen: from a to h (see Table 3.1)
- and finally, the last figure provides the load history: from 1 to 8 (see Table 3.2)

For example: **N2-b1** stands for a series with specimens which have a smooth ground edge, from supplier 2 with dimensions of 550 mm * 62.5 mm * 4 mm tested at a constant stress rate of 50 MPa/s.

Table 3.1: overview of the specimen sizes of TP 2 to TP 6.

specimen geometry type	nominal thickness b [mm]	nominal height h [mm]	nominal specimen length L_t [mm]	nominal support span L [mm]	nominal load span L_s [mm]
a	4	12.5	110	100	40
b	4	62.5	550	500	200
c	8	18.8	170	150	60
d	8	62.5	550	500	200
e	4	62.5	550	500	250
f	4	125	1100	1000	500
g	8	62.5	550	500	250
h	8	125	1100	1000	500

Table 3.2: overview of the load history of TP 2 to TP 6 .

load history	type	value
1	constant stress rate	50 MPa/s
2	constant stress rate	2 MPa/s
3	constant stress rate	0.08 MPa/s
4	constant stress rate	1 MPa/s
5	constant stress	-
6	cyclic constant stress	5 s between cycles
7	cyclic constant stress	20 s between cycles
8	cyclic constant stress	1 week between cycles

3.2 Method

3.2.1 Introduction

Veer and Riemslag (2009) conclude that strength is not a material property alone. Specimens with other dimensions seem to fail differently. Also, other shapes might fail differently or the loading type, mechanical force or temperature load may influence the strength of glass.

For that reason, a comparison was made between a square pane of 500 mm by 500 mm which was loaded thermally and a beam of 550 mm by 50 mm loaded in an in-plane 4PB setup. If the results of the temperature test and the bending test corresponded, the further testing could be performed with the bending test setup. The bending test takes 60 times less time compared to the temperature test and is much more controllable.

3.2.2 Temperature test setup

A square pane of 500 mm was heated by IR-heaters from a distance of about 100 mm. The panes were cut without secondary processing (see section 2.3). The pane was installed with the score upwards in a bottom frame which consisted of fire resistant insulation. A top frame in the same material covered the edge of the pane, to avoid direct radiation on the edges of the pane, simulating the bite of a real frame (see Figure 3.1).

At every edge, three strain gauges were fixed on the top of the pane near the scored edge. The strain gauges of type FAE-12S-35-S6E-J had an accuracy of 1%. Supplementary, 16 thermo-couples were glued with thermal adhesive (Zalman) at the bottom of the pane (see Figure 3.1). The thermo-couples were calibrated with ice water at 0 °C and boiling water at 100 °C. The accuracy of the thermo-couples glued with the thermal adhesive was 2.5% in the range of 0 °C to 100 °C, instead of 5% with normal adhesive (Feryn 2012).

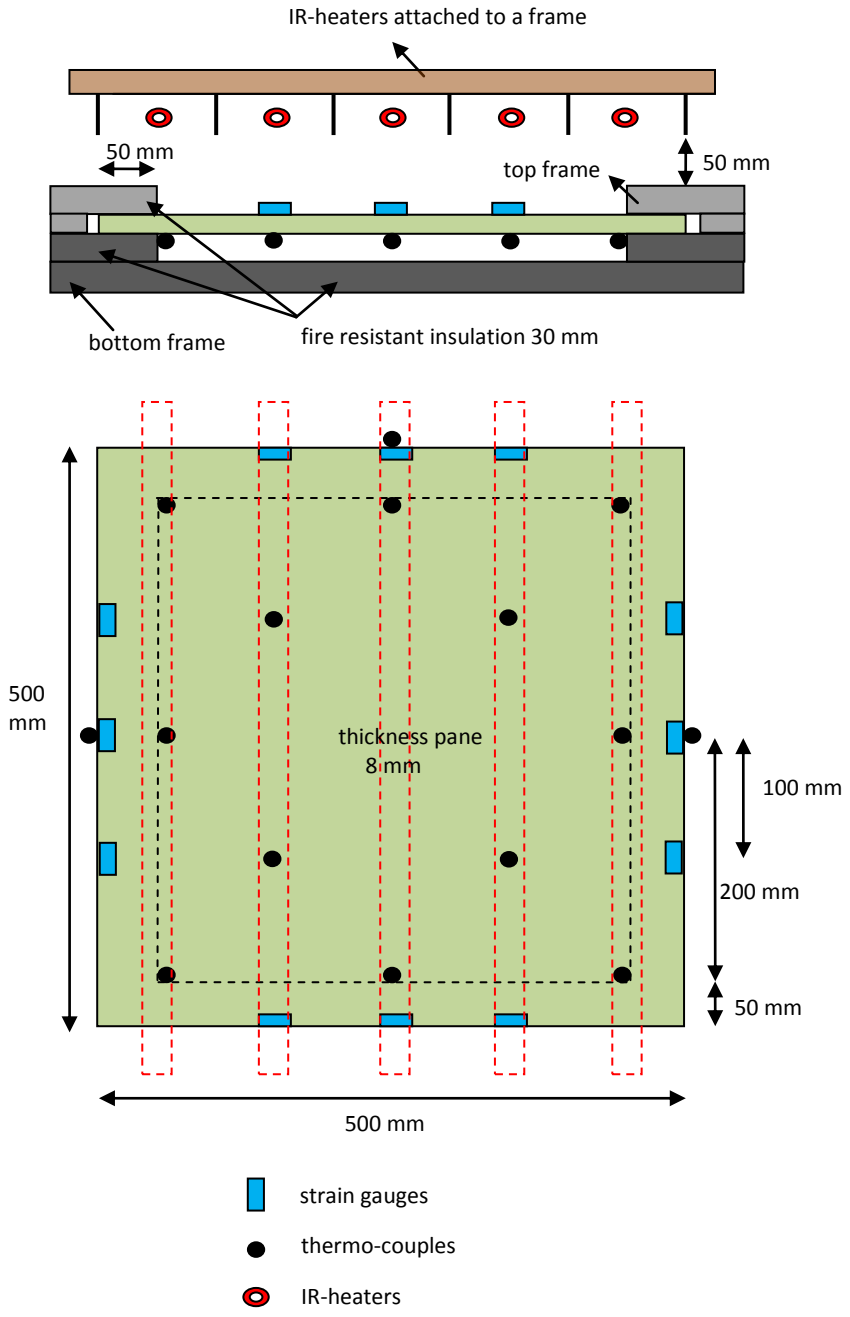

Figure 3.1: Temperature test setup, vertical view (above) and plan view.

3.2.3 Bending test setup

The specimens were subjected to in-plane 4PB tests using an Instron 3369 testing machine. The support span L and load span L_s (see Figures 3.2 and 3.3) were different for the different test programmes (see sections 3.3 to 3.8). For the supports and the loading, free rollers were applied with the use of a rubber intermediate. The specimens were supported laterally (mid-span) against buckling, in such a way that friction was minimized by the use of a Teflon interlayer between the specimen and the buckling support. Every test was executed at an actively controlled test temperature of 20 $\pm$ 2 °C and a relative humidity of 65 $\pm$ 4%, with the air (atmospheric) side of the glass always at the front side (see Figures 3.2 and 3.3). The testing machine enables two control modes: load and displacement control. For TP 1 a displacement rate was chosen, for the other TP's a load rate was chosen. Both rates can be transformed to a stress rate which is defined in the standard (EN 1288-1 2000; EN 1288-3 2000).

During testing, the load P was recorded in function of time. The specimens which failed outside the load span were excluded from the study.
From this, the stress at the bottom fibre σ_{4PB} was calculated in function of the load P by Eq. (3.1):

$$\sigma_{4PB} = \frac{(P/2).d}{(b.h^2)/6} = \frac{3.P.d}{b.h^2} \tag{3.1}$$

where σ_{4PB} [MPa] is the maximum tensile stress, constant within the load span, P [N] is the total load, d [mm] is the distance between the load and the support, b [mm] is the thickness of the specimen and h [mm] is the height of the specimen (Figure 3.2).

After testing, the failure stress values or tensile strength values $f_{eg,4PB}$ were calculated based on the failure loads P_f:

$$f_{eg,4PB} = \frac{3.P_f.d}{b.h^2} \tag{3.2}$$

where $f_{eg,4PB}$ [MPa] is the tensile edge strength corresponding to a linearly increased loading (experimental result: specimen loaded at a constant stress rate) and P_f [N] is the experimental failure load. In some literature, the strength value f is called the critical stress σ_c (Munz and Fett 1999).

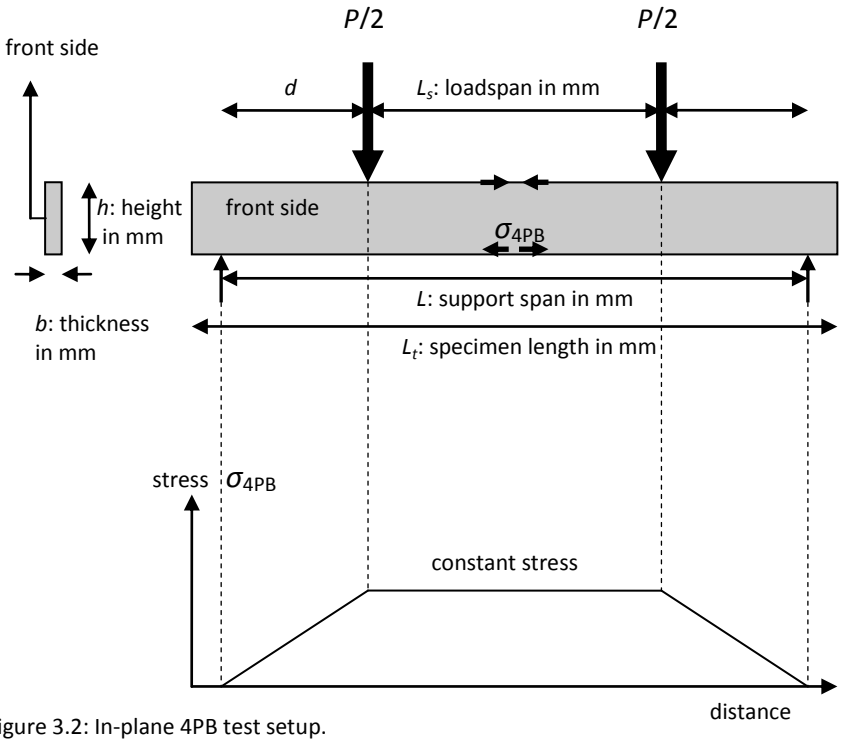

Figure 3.2: In-plane 4PB test setup.

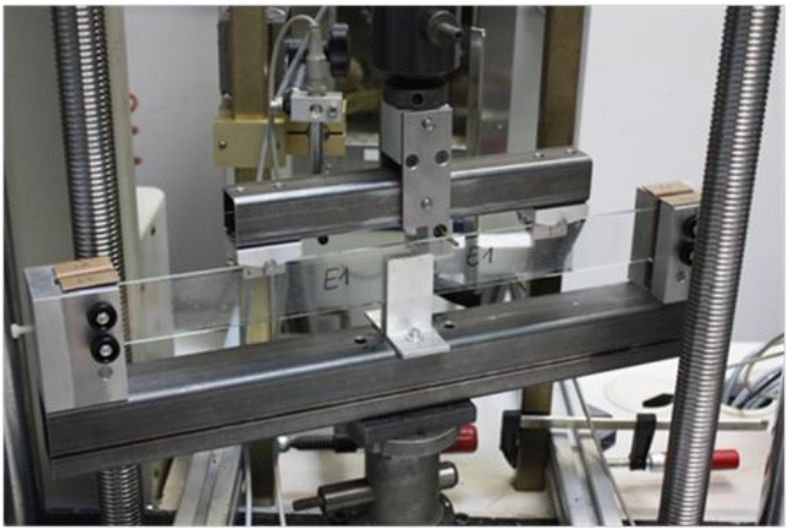

Figure 3.3: In-plane 4PB test setup.

Because of the 'Hertzian line contact' effect (Munz and Fett 1999), the predominance of failure directly below the inner rollers is more prevalent. To estimate this effect, the specimens of Figure 3.2 were simulated with the finite element (FE) software Abaqus. As illustrated in Figure 3.4, the stress σ_{4PB} near the loads $P/2$ deviate from the stress found theoretically by Eq. (3.1) because of the roller contacts. The ratio between the actual stress and the stress at the centre (which equals the result of Eq. (3.1)) in function of the distance from the centre of the specimen is shown in Figure 3.4. The load span is divided into 10 equal bins, from bin -v at the left-hand side to bin +v at the right-hand side of the centre of the specimen (marked above the horizontal axis).

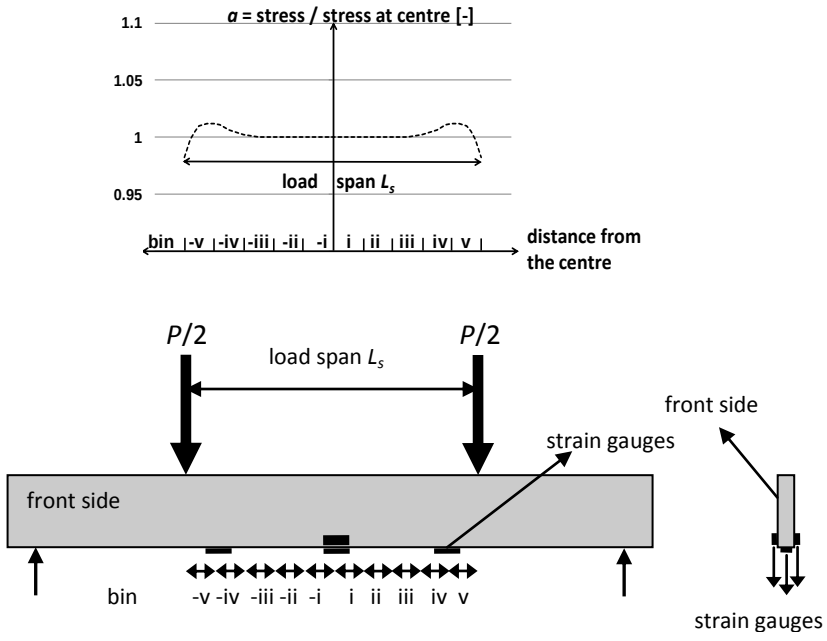

Figure 3.4: In-plane 4PB test setup.

In this study, all the calculated failure stresses were corrected according to this FE simulation, taking into account the measured location of the critical flaw along the load span. The corrected failure stresses are then given by:

$$f'_{eg,4PB} = a_{4PB}.\, f_{eg,4PB} \tag{3.3}$$

For the 4PB setup, the index 4PB was not used in chapter 3, only the index 3PB was used for the 3PB setup (see below).
The setup was monitored by means of strain gauges during TP 1 to ensure that the setup was symmetrical in the longitudinal and transversal direction. For that reason, strain gauges were applied at the centre, at the edge surface (bottom surface) and the front side and the other side, near the edge. Also at the maximum stresses (between bin -v and -iv and between bin iv and v), strain gauges at the edge surface (see Figure 2.1) were applied.

During TP 6, the specimens were also subjected to in-plane 3PB tests using the same testing machine to investigate the influence of the stress distribution. The specimens were supported in the same way as with the 4PB setup. Also, every test was executed at the same environmental conditions as during the 4PB test, with the air (atmospheric) side of the glass always at the front side (see Figure 3.5 and 3.6).

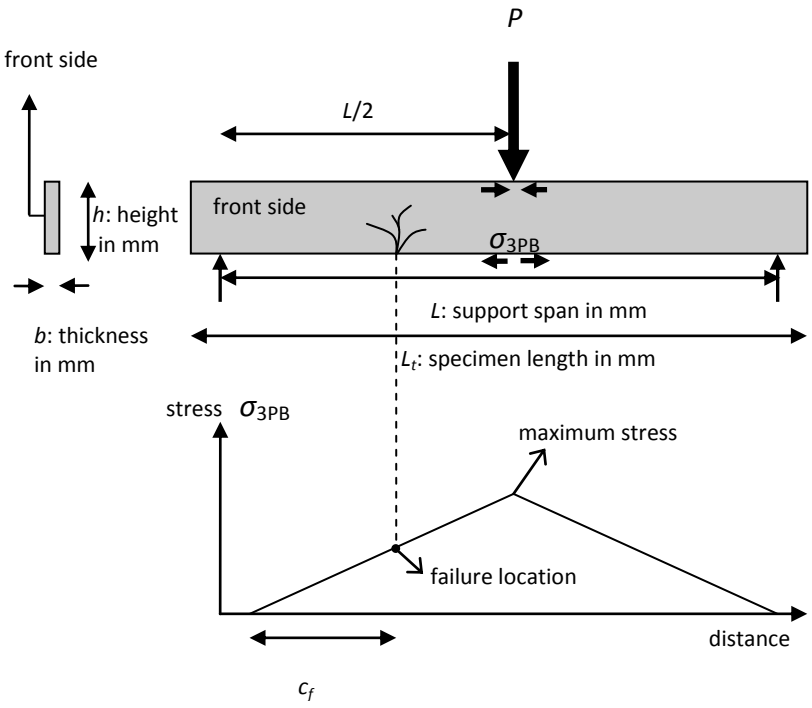

Figure 3.5: In-plane 3PB test setup.

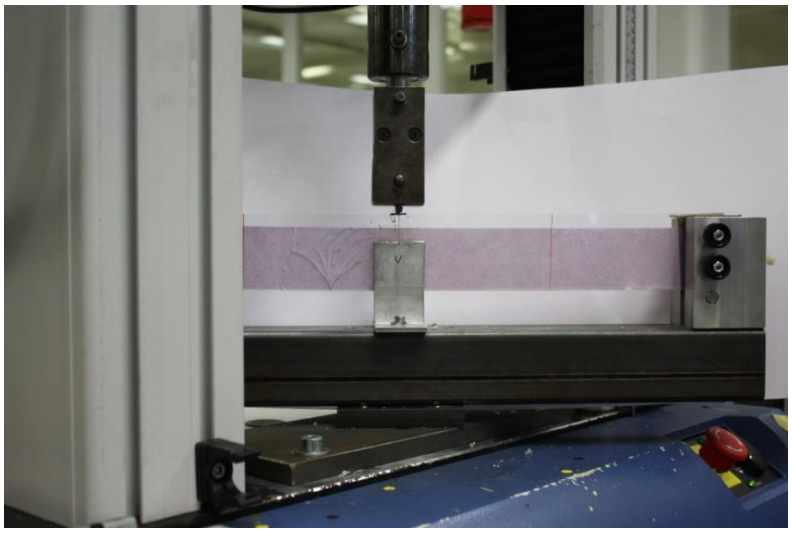

Figure 3.6: In-plane 3PB test setup.

During testing, the load P in function of the time was recorded. From this, the maximum stress at the bottom fibre σ_{3PB} was calculated in function of the load P by Eq. (3.4):

$$\sigma_{3PB} = \frac{(P/2).(L/2)}{(b.h^2)/6} = \frac{3.P.L}{2.b.h^2} \tag{3.4}$$

where σ_{3PB} [MPa] is the maximum tensile stress, in the middle of the support span L, P [N] is the total load, b [mm] is the thickness of the specimen and h [mm] is the height of the specimen (Figure 3.5).

After testing, the failure stress values or tensile strength values $f_{eg,3PB}$ were calculated based on the failure loads P_f and the failure location:

$$f_{eg,3PB} = \frac{c_f}{L/2}.\frac{3.P_f.L}{2.b.h^2} \tag{3.5}$$

where $f_{eg,3PB}$ [MPa] is the tensile edge strength corresponding to a linearly increased loading (experimental result: specimen loaded at a constant stress rate), c_f is the distance from the support to the failure origin and P_f [N] is the experimental failure load.

Because of the 'Hertzian line contact' effect (Munz and Fett 1999), the stress directly below the load is lower than the stress given by Eq. (3.4). In order to estimate this effect, the specimens of Figure 3.5 were simulated with the finite element (FE) software Abaqus. The ratio between the actual stress and the stress at Figure 3.5 (which equals the result of Eq. (3.4)) in function of the distance from the centre of the specimen was calculated.
In this study, all the calculated failure stresses were corrected according to this FE simulation, taking into account the measured location of the critical flaw along the length *L*. The corrected failure stresses are then given by:

$$f'_{eg,3PB} = a_{3PB}.\ f_{eg,3PB} \tag{3.6}$$

3.2.4 Analysis method of the test data

From the test data mean strength values or characteristic strength values can be derived. The reliability of these values depends on the specimen number of the series. Vandebroek *et al.* (2014a) conclude that, for the estimation of the characteristic strength value, 5 to 6 times more specimens are needed than for the estimation of the mean value, to provide the same reliability. For the estimation of the characteristic strength value, the study indicates that above 20 specimens the reliability does not increase significantly. Also, according to the standard prEN16612 (2013), the number of test specimens of a series to obtain a reliable mean value or characteristic value should be at least 10 or 20, respectively.

According to Gulvanessian *et al.* (2002), a confidence level γ of 0.95 is appropriate when a high level of structural reliability is required. Commonly, a confidence level γ of 0.75 is deemed acceptable (Caspeele, 2010; Caspeele and Taerwe, 2012). Consequently, the author proposes to apply a confidence level γ of 0.95 for structural elements of reliability class 3 (RC3) according to EN 1990 (2002). For structural elements of RC2 and RC1 (EN 1990 2002), a confidence level γ of 0.75 is suggested. Similarly, for non-structural elements and infill panels, a confidence level γ of 0.75 is proposed.

From the series of 20 to 30 specimens, it is difficult to predict which distribution the population follows. Fitting the data to different distributions was performed by several authors (Beason 1980; Beason and Morgan 1984; Fink 2001; Porter 2001; Haldimann 2006; Overend *et al.* 2007; Haldimann *et al.* 2008; Veer and Rodichev 2011; Overend and Zammit 2012; Morse and Norville 2013). The three most cited distributions are the normal distribution, the lognormal distribution and the Weibull distribution. Section 3.4 shows that some data fit better to one

distribution and other data better to another distribution. Applying the Coverage Method (EN 1990 2002; Caspeele, 2010; Caspeele and Taerwe, 2012; Zupan *et al.* 2007), the coefficients of the Weibull distribution deliver the highest values and are consequently more conservative.

In this study, the calculation of the characteristic strength values from a series of 20 specimens was performed with a confidence level γ of 0.75 for the infill panels. The Coverage Method starting from the Weibull distribution (Zupan *et al.* 2007) and starting from the normal distribution (ISO 12491 1997) were applied.

3.3 TP 1: Correlation temperature test and bending test

To investigate whether a temperature or a mechanical test delivers similar strength results, this test programme was set up. If the results correlate, mechanical testing can provide information about different influences on the strength values (e.g. environmental conditions, load history, size of the element, stress distribution along the element), during thermal loading.

3.3.1 Materials and testing details

In this programme, panes and beams with a cut edge finishing were tested. During the scoring process the wheel had an angle α_c of 154° (see Figure 2.2) and the cutting pressure amounted to 3 bar.
The temperature test setup described in section 3.2.2 was performed with 20 panes of 500 mm * 500 mm * 8 mm. Also, 20 specimens of 550 mm * 50 mm * 8 mm with the same edge finishing, cut on the same cutting table at the same moment were used to execute the in-plane 4PB test described in section 3.2.3. The bending tests were performed with a constant deformation rate of 0.009 mm/s and the load span L_s was 250 mm (see Figure 3.2). At least three weeks elapsed between processing the edge and testing the specimens. During the seven days before testing, the specimens were kept at a temperature of 20 °C $\pm$ 2 °C and a relative humidity of 65% $\pm$ 4%, the same as the test conditions. The actual thickness of the panes and the beams was close to 7.85 mm.

3.3.2 Results and discussion

During the temperature tests, the temperature of the thermo-couples was monitored (see Figure 3.8, thermo-couple number 5 and 16 did not function).

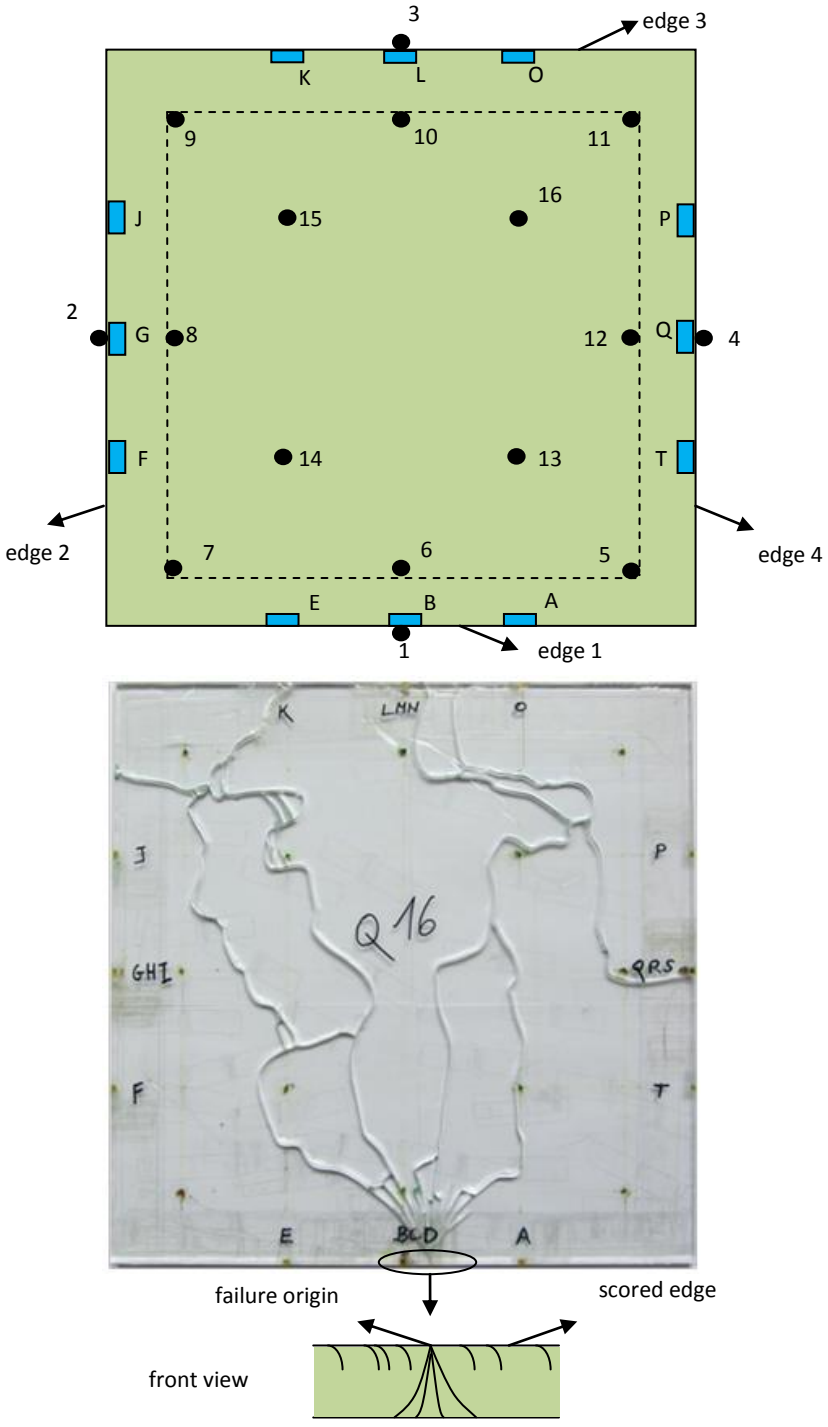

Figure 3.7: Temperature test: strain gauges and thermo-couples, failure origin.

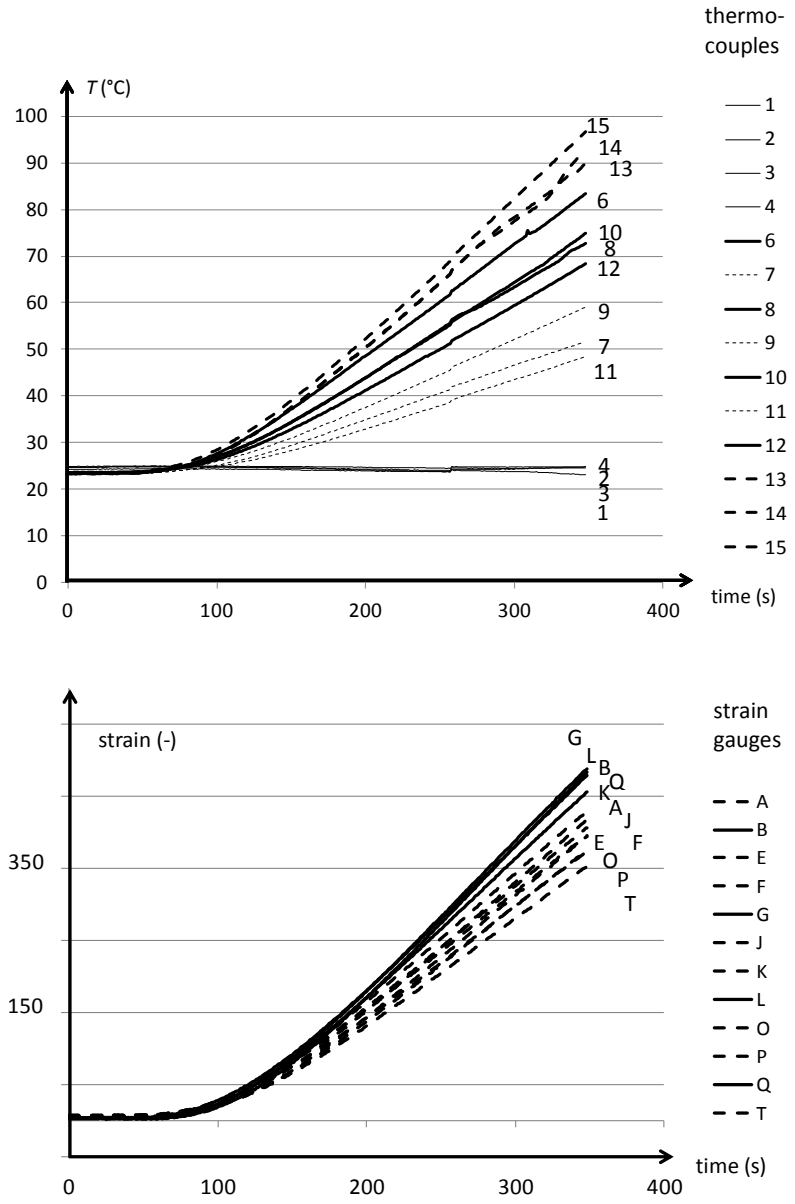

Figure 3.8: Temperature test: temperature and strain curves.

Also, the strain gauges (see Figure 3.8) were monitored and the strain at failure is presented in Table 3.3 (for every edge, the strain values at failure are given in Annex A, Tables A.1, A.2, A.3, A.4). After observation, all failures occurred at the scored edge as shown in Figure 3.7.

The strain was interpolated for the exact failure location between two adjacent strain gauges (see Annex A, Tables A.1 to A.4, presented in bold). Next, the edge at which the failure initiated is presented in Table 3.3. This indicates that the setup was rather symmetrical as only edge 1 had a few more failures and edge 2 a few less failures than the mean value of 5 failures. Finally, the failure stress was calculated with the module of elasticity of 68081 MPa, resulting from the bending test with an identical edge finishing (see Table 3.5). These strength values and the corresponding time to failure are provided in Table 3.3.
Finally, the sample standard deviation, the sample mean value and the coefficient of variation of the failure stress and the time to failure are presented in Table 3.3.

Table 3.3: the strain ε_s [10^{-6}] of the strain gauges.

Specimen number	ε_s [10^{-6}]	edge [-]	f_{eg} [MPa]	t_f [s]
1	548	1	37.3	284
2	476	4	32.4	270
3	510	4	34.7	270
4	542	1	36.9	269
5	480	2	32.7	292
6	526	3	35.8	268
7	542	1	36.9	304
8	447	1	30.5	244
9	505	4	34.4	258
10	542	3	36.9	299
11	529	4	36.0	273
12	494	4	33.6	275
13	548	1	37.3	289
14	530	1	36.1	273
15	515	1	35.1	281
16	475	1	32.3	256
17	534	2	36.3	274
18	461	3	31.4	259
19	461	3	31.4	260
20	492	2	33.5	264
s			2.2	15
$\bar{x}$			**34.6**	**273**
V			0.06	0.06

For the specimens tested in 4PB, the first 10 specimens (specimen numbers 1 to 10 in Table 3.5) were monitored by means of strain gauges. The strain values ε_s [10^{-6}] at failure are depicted in Table 3.4.
In Table 3.5, the corrected failure stresses f'_{eg} calculated by Eq. (3.3) and the time to failure t_f are presented. All failures occurred at the scored edge and inside the load span. A picture of a failed specimen is provided in Annex B (see Figure B.37).

Table 3.4: the strain values ε_s [10^{-6}] at failure.

Specimen number	left bottom	mid front	mid bottom	mid back	right bottom
1	620	519	626	583	607
2	**549**	**481**	**471**	**496**	**617**
3	551	503	539	471	545
4	530	478	532	472	522
5	603	537	620	545	599
6	614	543	601	541	613
7	**497**	**536**	**618**	**575**	**619**
8	557	485	556	526	554
9	584	515	577	525	575
10	**749**	**601**	**680**	**615**	**674**

At the right part of Table 3.5, the strain ε_s at failure location is presented for the first ten specimens (specimen numbers 1 to 10). The strains for the positions left bottom and right bottom are corrected according to Figure 3.5 by dividing the measured strain by α_{4PB} = 1.012 (Eq. 3.3). Then, the strains of left bottom, mid bottom and right bottom should be equal or almost equal. It can be noticed from Table 3.4 that the range between the three values amounts maximum to 21.10^{-6}, except for specimen number 2, 7 and 10 (bold in Table 3.4) with values of 146. 10^{-6}, 122. 10^{-6} and 75. 10^{-6}, respectively. Thus, the measurement of these three strain gauges is not considered as reliable. Only the seven reliable strain gauges were used to determine the module of elasticity $E = f'_{eg}/\varepsilon_s$ (MPa), resulting in a value of 68081 MPa (see Table 3.5). This value deviates 2.7% from the value of 70000 MPa according to the standards (prEN 16612 2013; DIN 18008-1 2010).
To evaluate the symmetry of the setup, the strains were compared both longitudinally and transversally.

Table 3.5: 4PB test results.

Specimen number	f'_{eg} [MPa]	t_f [s]	ε_s [10^{-6}]	E [MPa]
1	44.1	128	627	70336
2	38.3	98	-	-
3	37.4	102	558	67102
4	36.0	101	532	67584
5	41.2	116	620	66510
6	41.2	114	601	68545
7	42.8	108	-	-
8	38.2	97	556	68697
9	39.3	108	580	67795
10	46.6	119	-	-
11	36.1	108	-	-
12	41.1	105	-	-
13	41.4	112	-	-
14	39.5	101	-	-
15	39.2	103	-	-
16	40.7	109	-	-
17	41.6	116	-	-
18	40.9	107	-	-
19	40.8	106	-	-
20	42.0	111	-	-
s	2.6	8		1254
$\bar{x}$	**40.4**	**109**		**68081**
V	0.06	0.07		0.02

In longitudinal direction, the range between the strains of the left bottom and middle bottom strain as well as between the middle bottom and the right bottom strain was less than 21.10^{-6} with a mean value of the range which amounted to 0.2% between left bottom and middle bottom strain and 0.9% between middle bottom and right bottom strain.

In transversal direction, the range in the middle of the beam was maximum 39.10^{-6} except for the strain gauges of specimens number 1 and 8. The reliable ranges had a mean value of 0.8%, which is comparable to the 0.9% range in longitudinal direction. Nevertheless, in both directions, the ranges were very small which assured a symmetrical setup.

In conclusion, the maximum range in strains due to the setup was about 1% which is acceptable, as the accuracy of the strain gauges themselves is 1%.

To compare the strength results of the temperature test and the bending test, the values have to be corrected as they have a different load duration, size and stress distribution. These effects will be examined in detail in the next sections (3.4, 3.7 and 3.8). The loading rate of both tests, i.e. the temperature and the bending test was constant.

Applying Eq. (2.15) to the mean strength value of Table 3.5 with *n* equal to 16 yields:

$$40.4\,\mathrm{MPa} * (109\mathrm{s}/273\mathrm{s})^{1/16} = 38.15\mathrm{MPa} \tag{3.7}$$

The specimens of the 4PB test had a stressed length of 250 mm. During the temperature test, all failures occurred in the central length of 125 mm. Consequently, the stressed length of the temperature test amounts to
4 * 125 mm = 500 mm. Applying Eq. (2.40) to the mean sample values (which are close to the scale parameters), results with m'_0 equal to 7 (E2431-12 2012; Beason and Lingnell 2002) in a strength value of:

$$38.15\,\mathrm{MPa} * (250\,\mathrm{mm}/500\mathrm{mm})^{1/7} = 34.55\mathrm{MPa} \tag{3.8}$$

According to Beason and Lingnell (2002), the effective perimeter length or the stressed length is equal to 4 * (500 mm – 300 mm) = 800 mm instead of 500 mm, as the stresses decrease considerably close to the corners. This yields a corrected strength value of:

$$38.15\,\mathrm{MPa} * (250\,\mathrm{mm}/800\mathrm{mm})^{1/7} = 32.31\mathrm{MPa} \tag{3.9}$$

However, the correction according to Eq. (3.9) does not take the stress distribution into account, while the correction according to Eq. (3.8) implicitly does. Consequently, after the two corrections (Eq. (3.7) and Eq. (3.8)), the mean strength value of the bending test i.e. 34.55 MPa approaches the mean strength value of the temperature test i.e. 34.6 MPa.
Applying a value of *E* = 70000 MPa instead of 68081 MPa, yields values of
39.22 MPa and 35.52 MPa instead of 34.55 MPa and 32.31 MPa

3.3.3 Conclusion

A very good agreement was found between failure stresses induced by temperature loading and by mechanical loading. Thus, the subsequent test programmes to estimate the influence of the stress corrosion, of the load history, of the size and stress distribution can be executed with a bending set-up, which is considerably less time-consuming.

3.4 TP 2: Stress corrosion tests

The main goal of this programme was to examine the influence of the environmental conditions. To determine strength values, the data were fitted to different distribution functions. As two specimen sizes were used, the strength results were compared to find out whether a size effect could be noticed.

3.4.1 Materials and testing details

In this programme, 48 series of specimens, with either smooth ground (N1 for supplier 1, N2 for supplier 2), ground (G), arrissed (A) or cut (C1 for supplier 1, C2 for supplier 2) edge finishing and a nominal thickness of 4 or 8 mm were tested. The sizes of the specimens (see Figure 3.2) are presented in Table 3.6. For every edge finishing, specimens from two suppliers were provided. However, for the arrissed and ground edge finishings, which look similar, only the specimens of one supplier were tested. The bending tests were performed load controlled with a constant stress rate of 50 MPa/s $\pm$ 5 MPa/s, 2 MPa/s $\pm$ 0.2 MPa/s (corresponding to common testing procedures according to EN 1288-3 2000) or 0.08 MPa/s $\pm$ 0.008 MPa/s (corresponding to the load duration of wind actions according to EN 1991-1-4 2005). Only series 'N1-b1' was tested at a different stress rate i.e. 37 MPa/s $\pm$ 5 MPa/s instead of 50 MPa/s $\pm$ 5 MPa/s, because the specimens were performed displacement controlled instead of load controlled. An overview of the series is presented in Table 3.7.

During the cutting and grinding of the panels a strict protocol was applied. More specifically, the scoring of the specimens consistently occurred at the air side (i.e. the surface which is exposed to the air (atmosphere) during the float process). Furthermore, the cutting wheel had an angle α_c between 145° and 156° and the cutting pressure amounted from 0.7 bar to 2.1 bar. Arrissing or grinding was performed with a disc and not with an X-belt (see section 2.3). The anris varied between 0.9 mm and 1.1 mm for the 4 mm thick specimens and between 1.2 mm and 1.4 mm for the 8 mm thick specimens (Figures 2.1 to 2.4).

Table 3.6: overview of the specimen sizes of TP 2.

specimen geometry type	nominal thickness b [mm]	nominal height h [mm]	nominal specimen length L_t [mm]	nominal support span L [mm]	nominal load span L_s [mm]
a	4	12.5	110	100	40
b	4	62.5	550	500	200
c	8	18.8	170	150	60
d	8	62.5	550	500	200

Table 3.7: overview of the test series of TP 2.

edge finishing-supplier	specimen geometry type	stress rate 50 MPa/s	stress rate 2 MPa/s	stress rate 0.08 MPa/s
N1	a	N1-a1	N1-a2	N1-a3
N1	b	N1-b1	N1-b2	N1-b3
N1	c	N1-c1	N1-c2	N1-c3
N1	d	N1-d1	N1-d2	N1-d3
N2	b	N2-b1	N2-b2	-
N2	d	N2-d1	N2-d2	-
G	a	G-a1	G-a2	G-a3
G	b	G-b1	G-b2	G-b3
G	c	G-c1	G-c2	G-c3
G	d	G-d1	G-d2	G-d3
A	b	A-b1	A-b2	-
A	d	A-d1	A-d2	-
C1	a	C1-a1	C1-a2	C1-a3
C1	b	C1-b1	C1-b2	C1-b3
C1	c	C1-c1	C1-c2	C1-c3
C1	d	C1-d1	C1-d2	C1-d3
C2	b	C2-b1	C2-b2	-
C2	d	C2-d1	C2-d2	-

Finally, per glass thickness (4 or 8 mm) and per edge finishing, all panels were processed on the same day with the same machine and the same processing parameters, from which one can assume the same flaw population (section 2.3.4).
At least 90 days elapsed between processing the edge and testing the specimens. During the 14 days before testing, the specimens were kept at a temperature of 20 °C $\pm$ 2 °C and a relative humidity of 65% $\pm$ 4%, the same as the test conditions.

3.4.2 Results and discussion

Cross-sectional and longitudinal failure location

For the specimens of series N1, G and C1, the cross-sectional and longitudinal location of failure was determined from the mirror zone according to section 2.3.1 (see Figure 2.4). A picture of a failed specimen is provided in Annex B (see Figure B.37).

The **cross-sectional** location (0-5) could be determined (see Table 3.8), following the definitions as provided in Figures 3.9 and 3.10. The air side always corresponds to surface 0, edge 1 or edge 2 and the tin side corresponds to edge 3, edge 4 or surface 5. The longitudinal location was determined according to Figure 3.4 on which the load span L_s is divided into ten equal distances (bin -v to v). These locations were recorded in order to investigate the distribution of the strength values in both directions, cross-sectional and longitudinal.

It was observed that for the smooth ground edges (series N1) 84% of the failures occurred at the edges 1, 2, 3 or 4; 4% at the bevel surfaces between the edges 1 and 2 or 3 and 4; 0% at the surfaces 0 or 5 and 12% at the surface between the edges 2 and 3 (see Figure 3.9 and Table 3.8).

For the ground edges (series G), it was observed that 87% of the failures occurred at the edges 1, 2, 3 or 4; 0% at the bevel surfaces between the edges 1 and 2 or 3 and 4; 2% at the surfaces 0 or 5 and 0% at the surface between the edges 2 and 3 (see Figure 3.9 and Table 3.8).

Finally, for the cut edges (series C1), it was observed that 98% of the failures occurred at the edges 2 or 3; 0% at the bevel surfaces between the edges 1 and 2 or 3 and 4; 2% at the surfaces 0 or 5 and 0% at the surface between the edges 2 and 3 (see Figure 3.9 and Table 3.8).

It can be observed that for the smooth ground and the cut edge, significantly more failures occurred at edge 2 compared to edge 3. This was not the case for the ground edge. As edge 2 was the scored edge, this conclusion is obvious for the cut edge, but not for the smooth ground edge.

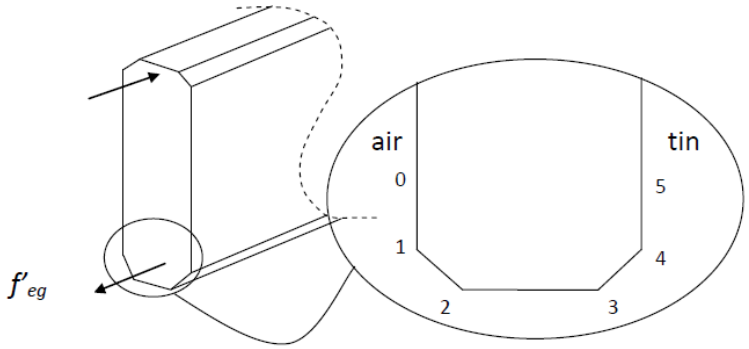

Figure 3.9: Schematic view of the edge of a smooth ground or ground specimen where f'_{eg} is the corrected strength value according to Eq. (3.3).

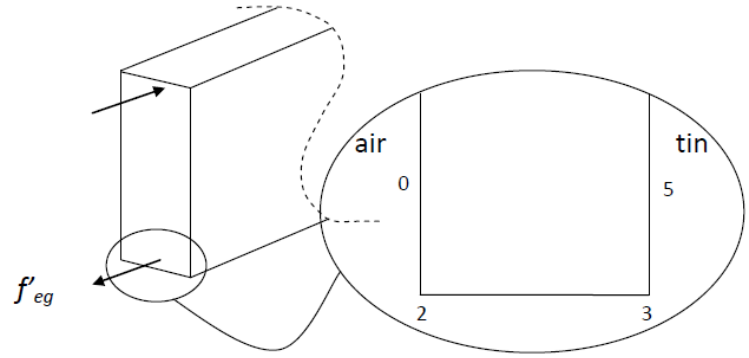

Figure 3.10: Schematic view of the edge of a cut specimen where f'_{eg} is the corrected strength value according to Eq. (3.3).

Table 3.8: Failure origins (%) at different edges (Figures 3.9 and 3.10).

Series	Surface 0	Edge 1	Surface between 1 and 2	Edge 2	Surface between 2 and 3	Edge 3	Surface between 3 and 4	Edge 4	Surface 5
	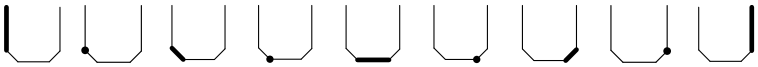								
N1-a/b	0	13	1	66	1	17	1	1	0
N1-c/d	0	3	5	38	23	27	1	3	0
N1-all	0	8	3	52	12	22	1	2	0
G-a/b	2	10	0	49	0	30	0	7	2
G-c/d	0	0	0	37	0	58	0	5	0
G-all	1	5	0	44	0	43	0	6	1
	Surface 0			Edge 2	Surface between 2 and 3	Edge 3			Surface 5
									
C1-a/b	0			56	0	41			3
C1-c/d	0			99	0	1			0
C1-all	0			77	0	21			2

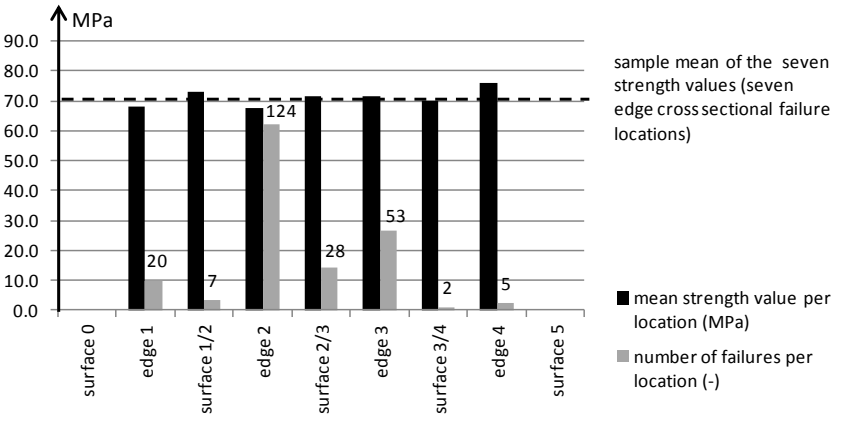

Figure 3.11: Failure origins and corresponding mean corrected strength values at the SMOOTH GROUND edges (4 mm and 8 mm thickness).

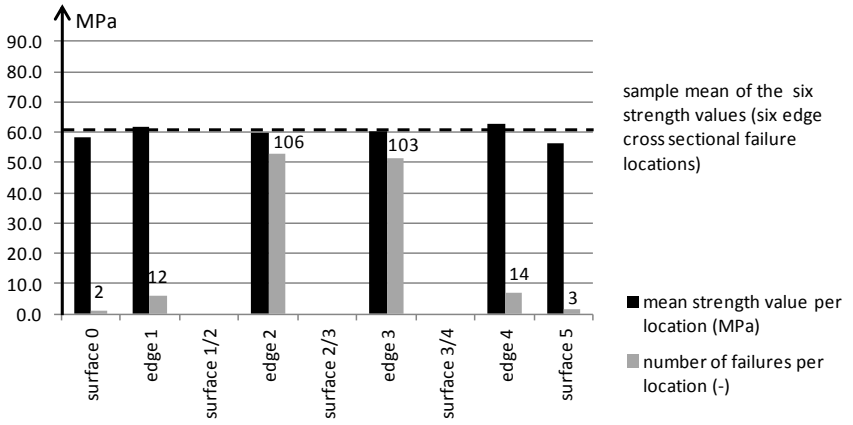

Figure 3.12: Failure origins and corresponding mean corrected strength values at the GROUND edges (4 mm and 8 mm thickness).

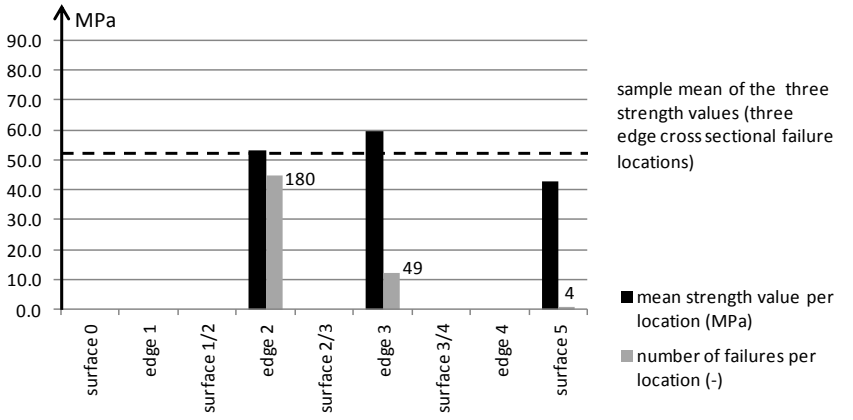

Figure 3.13: Failure origins and corresponding mean corrected strength values at the CUT edges (4 mm and 8 mm thickness).

For all the cross-sectional failure locations (7 in case of smooth ground specimens, 6 in case of ground specimens and 3 in case of cut specimens, see Table 3.8), the corresponding mean strength values (sample mean of the corrected strength values f'_{eg}) were calculated. To compare the results at different stress rates, they were first corrected to a stress rate of 2 MPa/s (see remark below). The results are depicted for all the smooth ground edges (4 mm and 8 mm) in Figure 3.11, for all the ground edges (4 mm and 8 mm) in Figure 3.12 and for all the cut edges (4 mm and 8 mm) in Figure 3.13.
Next, the sample mean, the sample standard deviation and the sample coefficient of variation in the number of failures (per cross sectional location) and in the mean strength values (per cross sectional location) were calculated (see Table 3.9).

Table 3.9: Distribution of the failure origins: location and corresponding strength values (sample mean of the corrected strength values f'_{eg}).

Specimens	number of failures per location			mean strength value per location		
	$\overline{x}$	s	V	$\overline{x}$	s	V
	[-]	[-]	[-]	[MPa]	[MPa]	[-]
Smooth ground	34	43	1.27	71.2	2.9	0.04
Ground	40	50	1.25	61.2	2.4	0.04
Cut	78	91	1.18	51.9	8.4	0.16

The corresponding strength values of all the edges and all the surfaces depended little on the cross-sectional failure location, as can be seen from Figures 3.11, 3.12 and 3.13. Indeed, Table 3.9 shows that the coefficients of variation in the number of failures per location range from 1.18 to 1.27, whereas the coefficients of variation in the corresponding mean strength values per location are much lower, i.e. from 0.04 to 0.16. Only the failures originating from surface 0 and 5 had lower strength values. Thus, these strength values were excluded from the further analysis (see Tables B.19 to B.26 of Annex B, and Figures 3.17 to 3.24).

For the smooth ground and ground edges, more failures occurred at the edges 2 and 3 compared to all the other failure locations (see Figures 3.11 and 3.12). A possible explanation can be found in the grinding process. The grinding of the edges was performed in four operations (see Figure 2.3). During the first

grinding operation, approximately 2 mm of the pane was removed by diamond discs (three discs), causing relatively large damage to the bottom surface (see Figure 2.3). Then, during the second and third grinding operation (see Figure 2.3), the bevel surfaces were processed by diamond discs, causing relatively large damage to the edges 1, 2, 3 and 4 and the surfaces 1/2 and 3/4. Finally, during the fourth grinding operation, approximately 0.1 mm of the bottom surface was removed by final grinding discs, causing smaller damage. It may be possible that the fourth grinding operation reduces the damage caused by the previous grinding operations. Further research is needed to investigate this assumption. As there occurred significantly more failures at the edges 2 or 3 (see Figure 3.11 and 3.12), the author assumes that the edges 2 and 3 were more frequently damaged because of two grinding operations causing serious damage (operation 1 and 2 or 3 according to Figure 2.3). All the other locations were assumedly only damaged during one grinding operation which caused serious damage. This indicates that edge 2 and 3 showed a larger number of critical flaws but as the strength values does not vary significantly, the critical flaw depth is not larger than at the other failure locations.

For the cut edges, significantly more failures originated from edge 2, compared to edge 3 (see Figure 3.13). Indeed, the scoring of the specimens consistently occurred at the air side (the edge 2 is situated at the air side). It can be concluded that the cutting wheel induces a larger number of critical flaws at this location, but the flaw depth is not larger than at edge 3.

Next, the **longitudinal** failure location was determined (see Figure 3.14 to 3.16). To investigate the spatial distribution of the strength values, the load span L_s was divided into 10 parts (10 bins, see Figure 3.4).

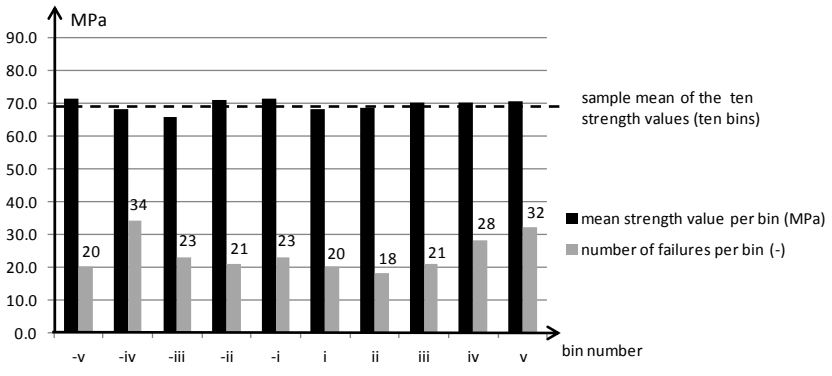

Figure 3.14: Failure origins and corresponding mean corrected strength values at the SMOOTH GROUND edges (4 mm and 8 mm thickness).

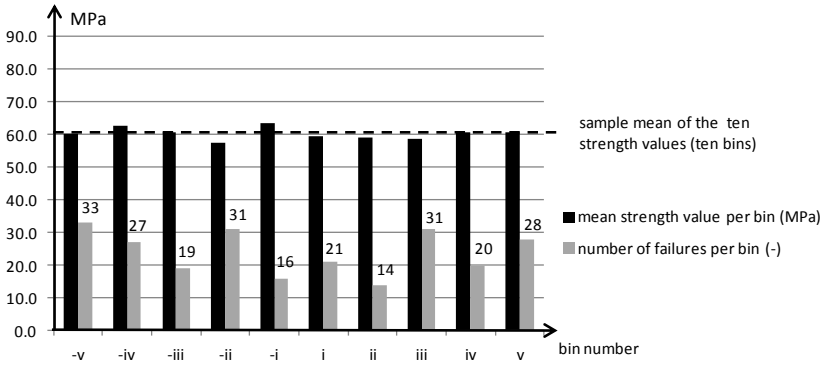

Figure 3.15: Failure origins and corresponding mean corrected strength values at the GROUND edges (4 mm and 8 mm thickness)

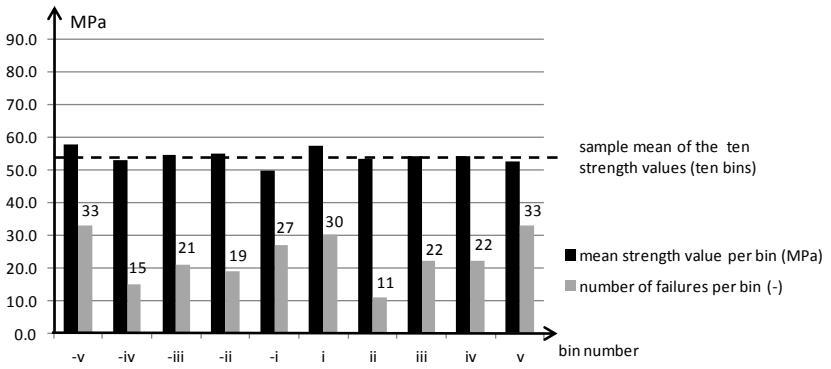

Figure 3.16: Failure origins and corresponding mean corrected strength values at the CUT edges (4 mm and 8 mm thickness).

The failure origins and corresponding mean strength values (sample means of the corrected strength values f'_{eg}) are depicted in function of the longitudinal failure location in Figures 3.14, 3.15 and 3.16 for all the smooth ground, ground and cut specimens, respectively.

Next, the sample mean, the sample standard deviation and the sample coefficient of variation in the number of failures (per bin) and in the mean strength values (per bin) were calculated (see Table 3.10).

Table 3.10: Distribution of the failure origins: location and corresponding strength values (sample mean of the corrected strength values f'_{eg}).

Specimens	Number of failures per location			Mean strength value per location		
	$\overline{x}$	s	V	$\overline{x}$	s	V
	[-]	[-]	[-]	[MPa]	[MPa]	[-]
Smooth ground	24	6	0.23	69.5	1.8	0.03
Ground	24	7	0.28	60.4	1.8	0.03
Cut	23	7	0.32	54.1	2.3	0.04

Because of the 'Hertzian line contact' effect (Munz and Fett 1999), the failure directly below the inner rollers is more predominant. This effect is larger for the smooth ground specimens (see Figure 3.14) than for the other specimens (see Figures 3.15 and 3.16). Although more failures occur at both ends of the load span, the corresponding strength values are similar to those in the middle of the load span, for all finishings. Indeed, Table 3.10 shows that the coefficients of variation in the number of failures per bin range from 0.23 to 0.32, whereas the coefficients of variation in the corresponding mean strength value per bin are much lower, i.e. from 0.03 to 0.04.

Remark: Figures 3.11 to 3.16 are based on the strength results of all series (at stress rates of 50 MPa/s, 2 MPa/s and 0.08 MPa/s). To compare these results, the value of the ratio 0.83 was used (see the mean value of Table B.24 or B.26 of Annex B).

Distribution fitting

All series were fitted to the Weibull distribution and the normal distribution. The distribution parameters were estimated by the least-squares method (LSM).

Linear regression is commonly used when all experimental data of one series result from one measurement method (e.g. the 4PB test) and one specimen size. However, if more than one measurement method and/or more than one specimen size is pooled in one series, the method of maximum likelihood is more appropriate (Wachtman *et al.* 2009). The latter method is required in the ASTM standard C 1239-07 (2007).

In this study, one series was performed with one measurement method and all specimens of one series had the same thickness, load span and edge finishing. Thus, both methods, the least-squares method and the method of maximum likelihood, are appropriate to use here.

For the least-squares method, the empirical failure probability usually assigned to the i^{th} strength value of n_s values (Munz and Fett 1999; ASTM C1239-07 2007) can be calculated as:

$$F_i = \frac{i - 0.5}{n_s} \tag{3.10}$$

where n_s is the specimen number of the series.

For all series (N1, N2, G, A, C1 and C2), the Weibull and normal plots are presented in Annex B (see Figures B.1 – B.36, corresponding data see Tables B.1 - B18). For the least-squares method, the estimation of the Weibull parameters ϑ'_0 and m'_0 (Eq. (2.41)), the estimation of the mean value $f'_{eg,m}$ and the standard deviation σ (normal distribution), as well as the coefficient of variation V and the coefficient of determination r^2, are presented in Annex B (Table B19, B20 and B21) for the stress rates of 50 MPa/s, 2 MPa/s and 0.08 MPa/s, respectively.

It can be concluded that the coefficient of determination r^2 is similar for fitting to the Weibull distribution and the normal distribution. The mean value of the coefficient of determination r^2 for all series amounts to 0.92 for the Weibull distribution and to 0.94 for the normal distribution. The mean value of the coefficient of variation V for all series amounts to 0.11 for the Weibull distribution and to 0.10 for the normal distribution.

Next, for all series (N1, N2, G, A, C1 and C2), the characteristic 5% strength value $f'_{eg,k}$ (with a confidence level of γ equal to 0.75), determined with the coverage method (section 3.2.4) is presented in Annex B (Table B22).

All the results are presented graphically in Figures 3.17 to 3.20 for the Weibull distribution and in Figures 3.21 to 3.24 for the normal distribution.

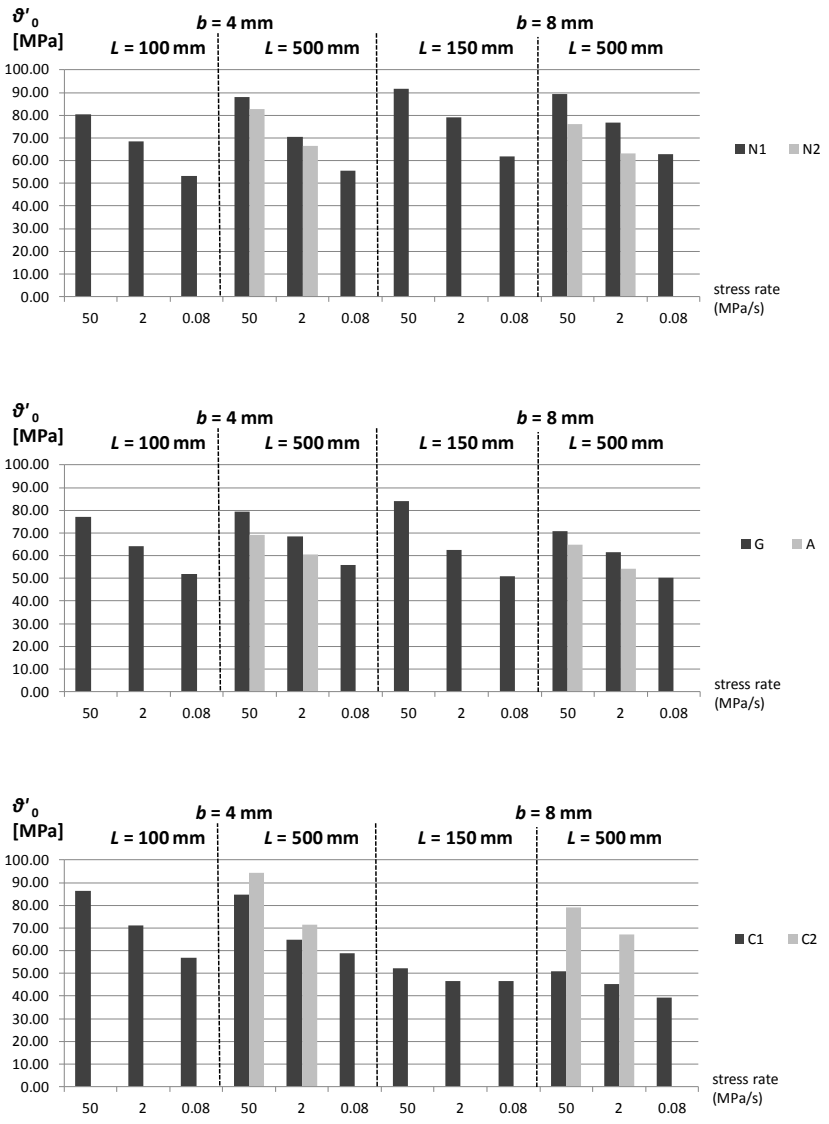

Figure 3.17: Weibull scale parameter ϑ'_0 for the smooth ground (N1, N2), ground (G), arrissed (A) and cut (C1,C2) specimens (Weibull distribution).

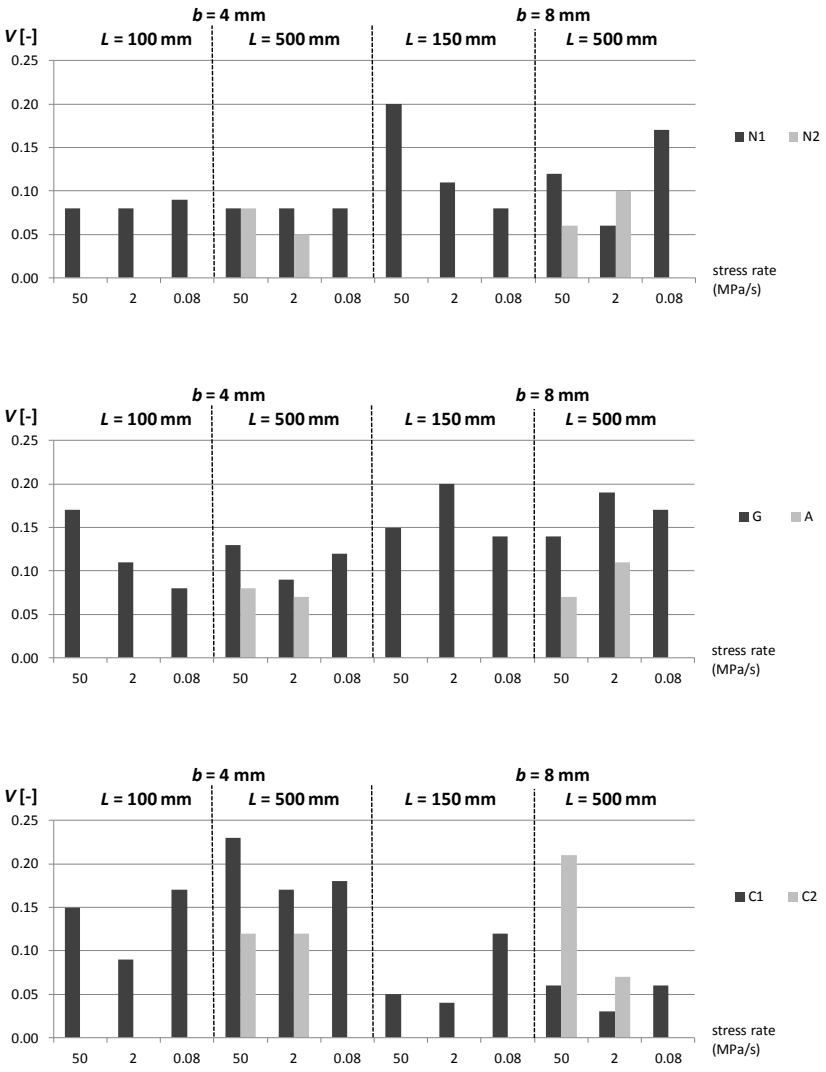

Figure 3.18: Coefficient of variation *V* for the smooth ground (N1, N2), ground (G), arrissed (A) and cut (C1,C2) specimens (Weibull distribution).

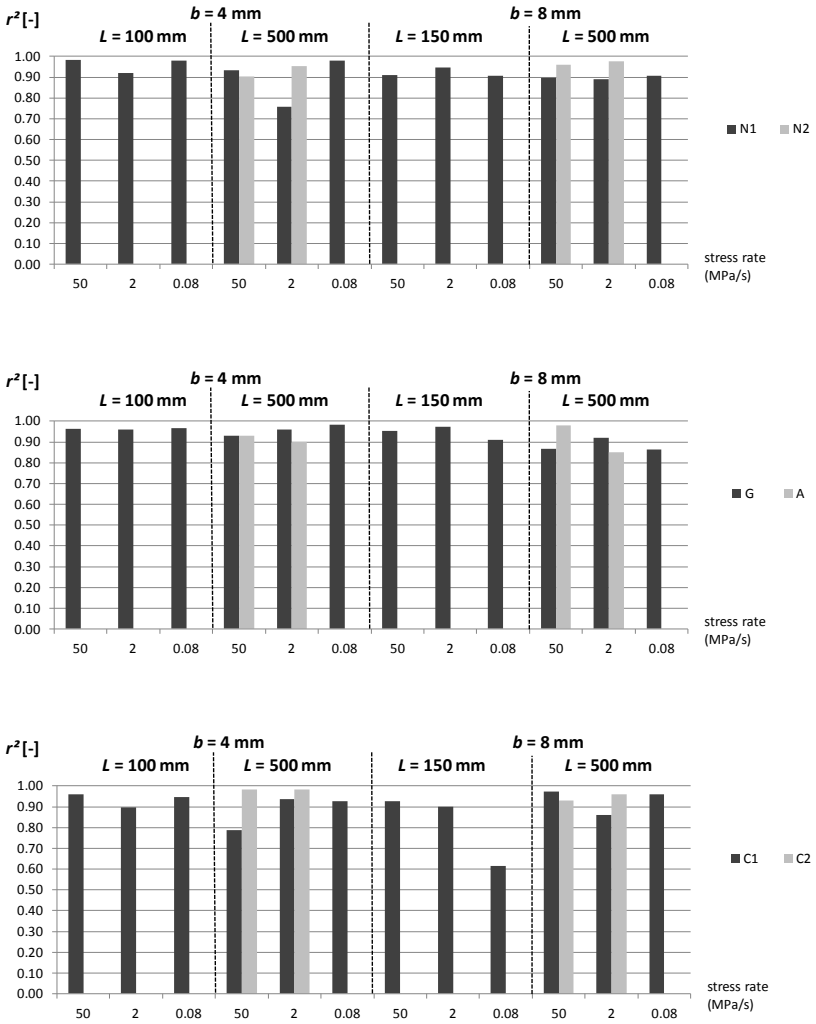

Figure 3.19: Coefficient of determination r^2 for the smooth ground (N1, N2), ground (G), arrissed (A) and cut (C1,C2) specimens (Weibull distribution).

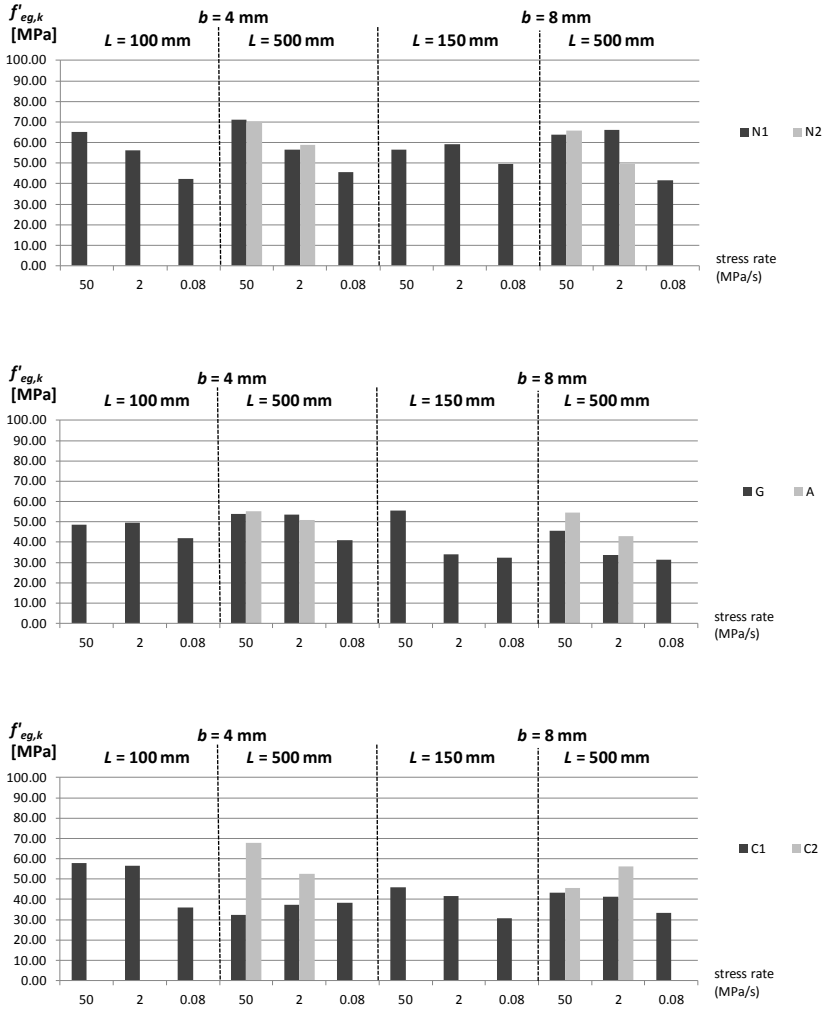

Figure 3.20: Characteristic strength value $f'_{eg,k}$ for the smooth ground (N1, N2), ground (G), arrissed (A) and cut (C1,C2) specimens (Weibull distribution).

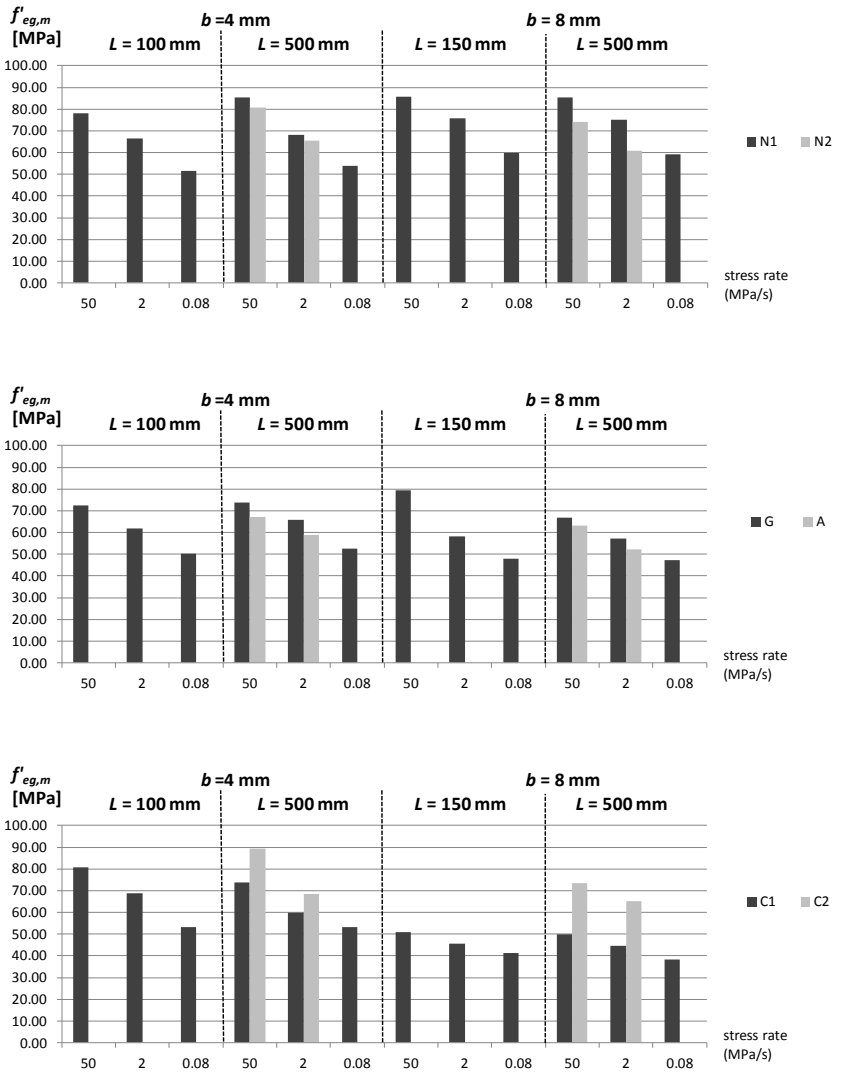

Figure 3.21: Mean strength value $f'_{eg,m}$ for the smooth ground (N1, N2), ground (G), arrissed (A) and cut (C1,C2) specimens (normal distribution).

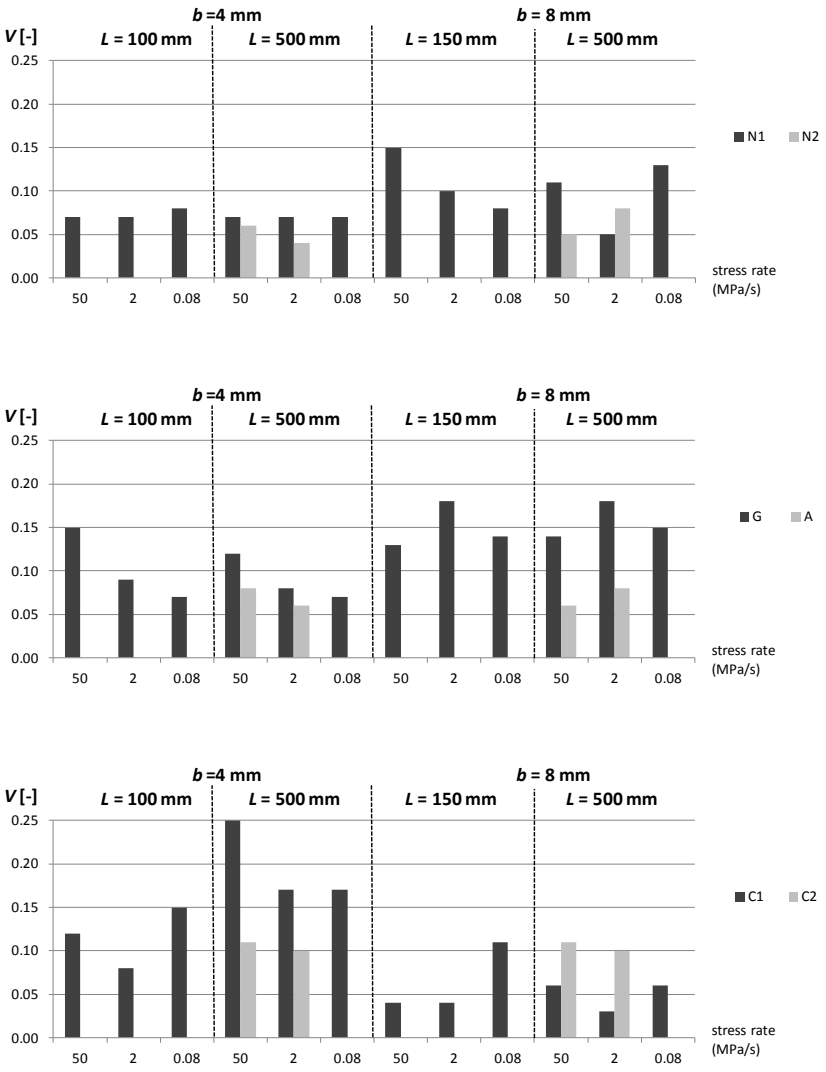

Figure 3.22: Coefficient of variation *V* for the smooth ground (N1, N2), ground (G), arrissed (A) and cut (C1,C2) specimens (normal distribution).

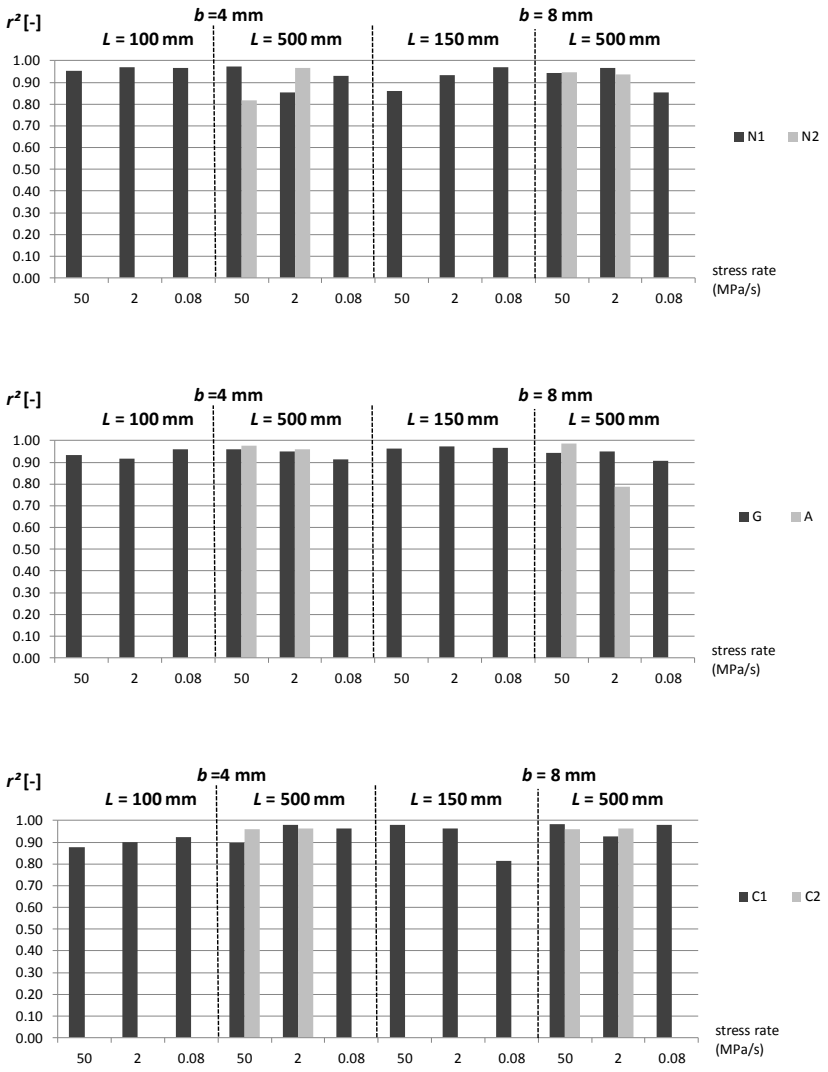

Figure 3.23: Coefficient of determination r^2 for the smooth ground (N1, N2), ground (G), arrissed (A) and cut (C1,C2) specimens (normal distribution).

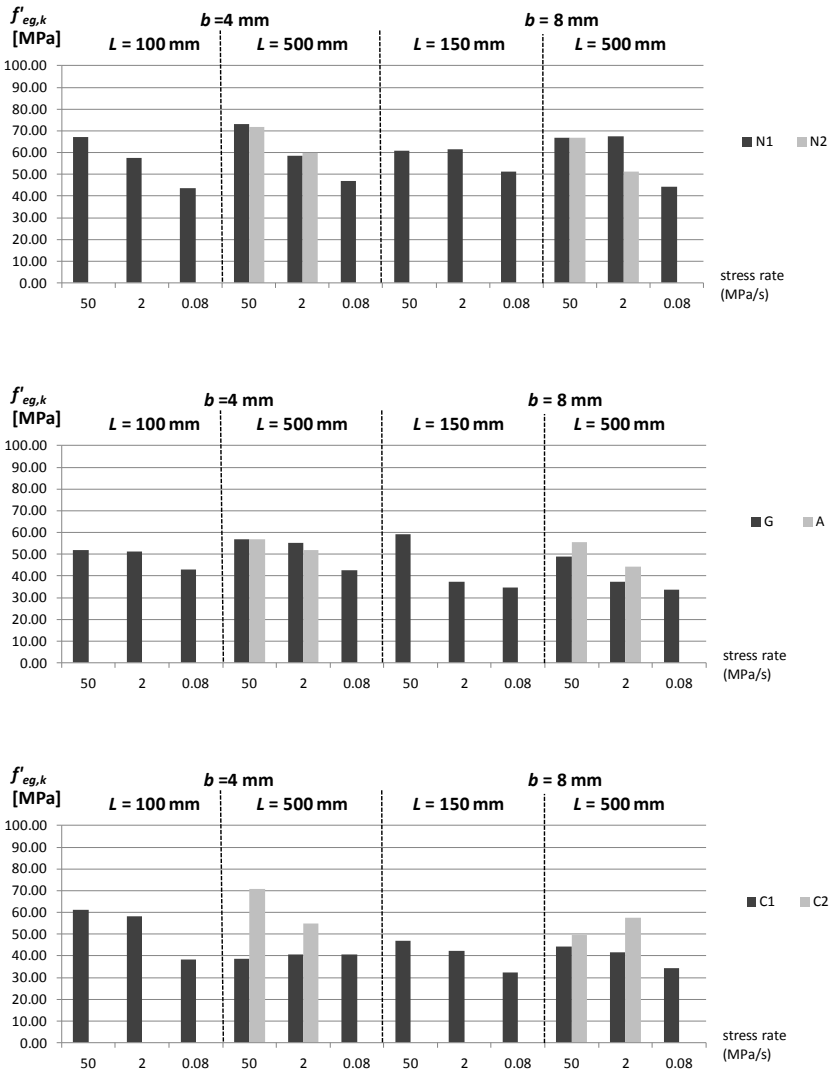

Figure 3.24: Characteristic strength value $f'_{eg,k}$ for the smooth ground (N1, N2), ground (G), arrissed (A) and cut (C1,C2) specimens (normal distribution).

From the values of Figure 3.17 (Weibull distribution) or Figure 3.21 (normal distribution), Eq. (2.15) was verified. To do so, the mean value of the times to failure for each series was calculated and presented in Table B.23 and B.25 of Annex B. The values of ϑ'_0 and $f'_{eg,m}$ were taken from Table B.19, B.20 and B.21 (see Annex B). In Tables B.23 to B.26, the index 1, 2, 3 was used for the stress rate of 50 MPa/s, 2 MPa/s and 0.08 MPa/s, respectively.

With the mean value of the ratios of the times to failure and the Weibull scale parameters (Table B.24 of Annex B), Eq. 2.15 yields the value of n = 16.5, while tested with 65% $\pm$ 4% RH. This value lies between the values of n = 16 for 100% RH and n = 18.1 for 50% RH according to the literature (Charles 1958; Blank 1993; Shen 1997; Fink 2000; Wörner 2001). The same conclusion can be drawn for the mean strength values (Table B.26 of Annex B). Thus, it can be concluded that the stress corrosion value of n = 16 for 100% RH and n = 18.1 for 50% RH is a good assumption for the equivalent stress verification (sections 4.3 to 4.6). In general, it can be assumed that the relative humidity near the middle pane of a double skin façade varies between 50% and 100%.

Characteristic and design values

Finally, all the values of Table B.22 (see Annex B) are corrected to a stress rate of 2 MPa/s (n = 16.5), which is the test procedure according to EN 1288-3 (2000). Thus, all these values can be compared to each other (see Table 3.11).

The extreme low characteristic strength value of series C1-b1 (26.9 MPa for the Weibull distribution and 32 MPa for the normal distribution) is due to the trilinearity of the regression (see Annex B, Figures B.27 and B.28). After eliminating these values, the lowest characteristic strength values for a specific edge finishing are presented in Table 3.12.

Applying γ_M = 1.8 (prEN 16612 2013; DIN 18008-1 2010), the design strength values $f'_{eg,d}$ are presented in Table 3.12.

From Table 3.12, it can be seen that the edge strength values of the smooth ground and the arrissed specimens are similar, as well as the edge strength values of the ground and the cut specimens. The latter are lower than the first. More testing is needed to investigate whether the arrissed specimens are always stronger than the ground specimens.

Table 3.11: Estimation of the characteristic 5% value of all series (confidence level γ of 0.75) with the coverage method, **corrected to a stress rate of 2 MPa/s (n = 16.5)**

Series*	LSM (Weibull distribution)			LSM (normal distribution)		
$f'_{eg,k}$ [MPa]	tested at 50 MPa/s	tested at 2 MPa/s	tested at 0.08 MPa/s	tested at 50 MPa/s	tested at 2 MPa/s	tested at 0.08 MPa/s
N1-a1,2,3	54.1	56.1	50.7	55.7	57.6	52.3
N1-b1,2,3	59.1	56.7	54.7	60.8	58.4	56.2
N1-c1,2,3	47.0	59.1	59.6	50.6	61.6	61.4
N1-d1,2,3	52.9	66.1	50.1	55.5	67.4	53.2
N2-b1,2	58.1	58.8	-	59.5	59.8	-
N2-d1,2	54.5	49.5	-	55.6	51.1	-
G-a1,2,3	40.3	49.4	50.2	43.2	51.2	51.7
G-b1,2,3	44.8	53.4	49.0	47.3	55.2	51.1
G-c1,2,3	46.1	33.9	38.8	49.0	37.4	41.6
G-d1,2,3	38.0	33.7	37.7	40.5	37.2	40.5
A-b1,2	45.8	50.8	-	47.2	52.0	-
A-d1,2	45.1	43.0	-	46.2	44.3	-
C1-a1,2,3	48.0	56.5	43.0	50.8	58.3	46.0
C1-b1,2,3	26.9	37.1	45.9	32.0	40.5	48.6
C1-c1,2,3	38.2	41.6	36.9	38.8	42.2	38.9
C1-d1,2,3	35.9	41.2	40.2	36.7	41.7	41.0
C2-b1,2	56.2	52.4	-	58.8	54.8	-
C2-d1,2	37.8	56.1	-	41.2	57.4	-

* Specimen name of all series, see Tables 3.1 and 3.2 of section 3.1

Table 3.12: Characteristic and design strength values for different edge finishings.

edge finishing	LSM (Weibull distribution)		LSM (normal distribution)	
	$f'_{eg,k}$ [MPa]	$f'_{eg,d}$ [MPa]	$f'_{eg,k}$ [MPa]	$f'_{eg,d}$ [MPa]
smooth ground	47.0	26.1	50.6	28.1
ground	33.7	18.7	37.2	20.7
arrissed	43.0	23.9	44.3	24.6
cut	35.9	19.9	36.7	20.4

Size effect

From Table B.23 (see Annex B), the strength values of geometry type a (4 mm * 12.5 mm * 110 mm) were compared to geometry type b (4 mm * 62.5 mm * 550 mm) and similarly, the strength values of geometry type c (8 mm * 18.8 mm * 170 mm) were compared to geometry type d (8 mm * 62.5 mm * 550 mm) (see Table 3.6). The results are presented in Table 3.13. The series of which one of the sizes had a coefficient of determination lower than 0.90, depicted bold in Table 3.13, were eliminated in the further analysis.

Table 3.13: Weibull scale parameter ϑ'_0 for different geometry types.

Series*	ϑ'_0 [MPa]		
	a	b	a/b
N1-a1,b1	80.5	88.2	0.91
G-a1,b1	77.0	79.2	0.97
C1-a1,b1	**86.3**	**84.7**	**1.02**
N1-a2,b2	**68.5**	**70.6**	**0.97**
G-a2,b2	64.2	68.6	0.94
C1-a2,b2	71.2	64.8	1.10
N1-a3,b3	53.3	55.6	0.96
G-a3,b3	52.0	55.8	0.93
C1-a3,b3	56.8	59.0	0.96
Series*	ϑ'_0 [MPa]		
	c	d	c/d
N1-c1,d1	91.8	89.3	1.03
G-c1,d1	**83.9**	**70.6**	**1.19**
C1-c1,d1	52.1	51.0	1.02
N1-c2,d2	**79.1**	**76.9**	**1.03**
G-c2,d2	62.6	61.5	1.02
C1-c2,d2	**46.4**	**45.3**	**1.02**
N1-c3,d3	61.8	62.9	0.98
G-c3,d3	**50.9**	**50.2**	**1.01**
C1-c3,d3	**46.6**	**39.2**	**1.19**

* Specimen name of all series, see Tables 3.1 and 3.2 of section 3.1

According to Eq. (2.40) with m'_0 = 12.3 (mean value of the series of 4 mm thickness):

$$\frac{\vartheta'_a}{\vartheta'_b} = \left(\frac{S_{s,b}}{S_{s,a}}\right)^{1/12.3} = \left(\frac{200\text{mm}}{40\text{mm}}\right)^{1/12.3} = 1.14 \tag{3.11}$$

which means that the geometry type a should be 14% stronger than the geometry type b (ratio of 1.14).

However, the mean value of the ratio a/b is 0.97.

Similarly, according to Eq. (2.40) with m'_0 = 12.8 (mean value of the series of 4 mm thickness)::

$$\frac{\vartheta'_c}{\vartheta'_d} = \left(\frac{S_{s,d}}{S_{s,c}}\right)^{1/12.8} = \left(\frac{200\text{mm}}{60\text{mm}}\right)^{1/12.8} = 1.10 \tag{3.12}$$

which means that the geometry type c should be 10% stronger than the geometry type d (ratio of 1.10).

However, the mean value of the ratio c/d is 1.01.

From this, it can be concluded that the geometry types a and b almost result in the same strength values (ratio of 0.97), as well as the geometry types c and d (ratio of 1.01). For this reason, the next extensive test programmes (TP 3 and TP 4) were executed with the small geometry types a and c. Indeed, the results are also applicable for the geometry types with a load span of 200 mm.

3.4.3 Conclusions

The cross-sectional and longitudinal failure location do not significantly influence the corresponding edge strength values. The value of the stress corrosion parameter *n* resulting from this study corresponds well to the literature. The characteristic edge strength values correspond well to the values of the standard NEN 2608+C1 (2012) and of the literature (Siebert 2011), in which no distinction was made between different edge finishings. However, it can be seen that the strength values of the smooth ground and arrissed specimens are considerably higher than the values of the ground and cut specimens. Finally, the different

geometry types of the bending tests in this TP do not influence the strength values significantly. The size effect will be further investigated with larger specimens in section 3.7.

3.5 TP 3: Influence of the load history

This programme examined the influence of the load history on the edge strength. Also, the influence of the number of specimens in a series was investigated, as the series for this programme consisted of a large number of specimens.

3.5.1 Materials and testing details

In this test programme, 17 series of specimens, with a smooth ground (N2 for supplier 2) edge finishing, an arrissed (A) edge finishing or a cut (C2 for supplier 2) edge finishing and a thickness of either 4 or 8 mm, were tested in a 4PB setup. First, six series were subjected to a linearly increased loading (constant stress rate, strength f). Then, six series of specimens, identical to the previous series, were tested under constant loading (constant stress, strength f_{ct}). Finally, six series, identical to the first six series, were tested under cyclic loading (cyclic constant stress, strength f_{cycl}). The sizes a and c of the specimens (see Figure 3.2) are presented in Table 3.14. The in-plane 4PB bending test setup is presented in Figure 3.25.

The specimens of 4 mm were loaded either at a stress rate of 2 MPa/s, a constant stress or a cyclic constant stress (Figure 3.26). For the cyclic constant stress, the holding phase amounted to 3 s and the time between the cycles amounted to 5 s. The transition between the constant stress and no stress was performed at a stress rate of 50 MPa/s. The specimens of 8 mm were loaded at a stress rate of 0.08 MPa/s, a constant stress or a cyclic constant stress (Figure 3.27). For the cyclic constant stress, the holding phase amounted to 3 s and the time between the cycles amounted to 20 s. The transition between the constant stress and no stress was performed at a stress rate of 50 MPa/s. An overview of the series is presented in Tables 3.15 and 3.16 and the loading histories are depicted in Figures 3.26 and 3.27. The number of specimens n_s for every series is indicated in the Tables 3.15 and 3.16.

Table 3.14: Overview of the specimen sizes of TP 3.

specimen size	nominal thickness b [mm]	nominal height h [mm]	nominal specimen length L_t [mm]	nominal support span L [mm]	nominal load span L_s [mm]
a	4	12.5	110	100	40
c	8	18.8	170	150	60

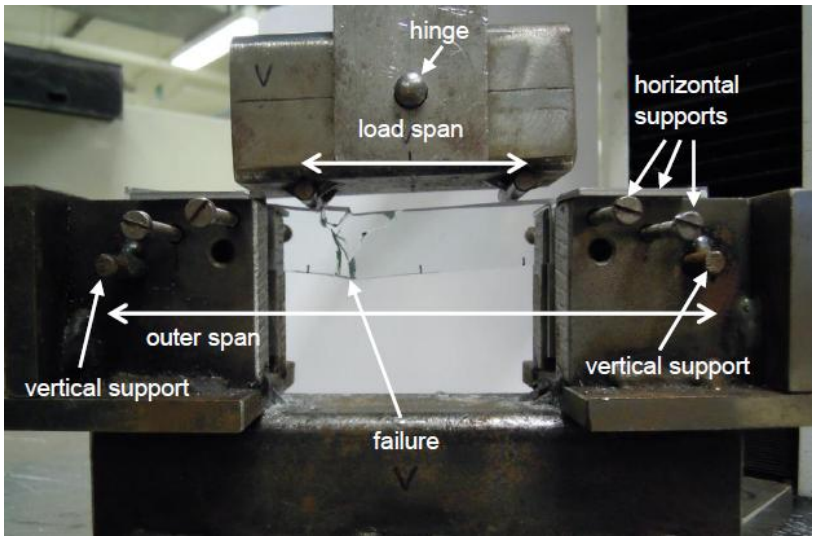

Figure 3.25: Detail of the in-plane 4PB test setup.

Table 3.15: Overview of the test series of TP 3: size a.

series	Stress rate 2 MPa/s	n_s	Constant stress (index 5)	n_s	Cyclic constant stress (index 6)	n_s
N2	N2-a2	60	N2-a5	30	N2-a6	30
A	A-a2	60	A-a5	30	A-a6	30
C2	C2-a2	100	C2-a5	40	-	-

Table 3.16: Overview of the test series of TP 3: size c.

series	Stress rate 0.08 MPa/s	n_s	Constant stress (index 5)	n_s	Cyclic constant stress (index 7)	n_s
N2	N2-c3	60	N2-c5	30	N2-c7	30
A	A-c3	60	A-c5	30	A-c7	30
C2	C2-c3	40	C2-c5	20	C2-c7	20

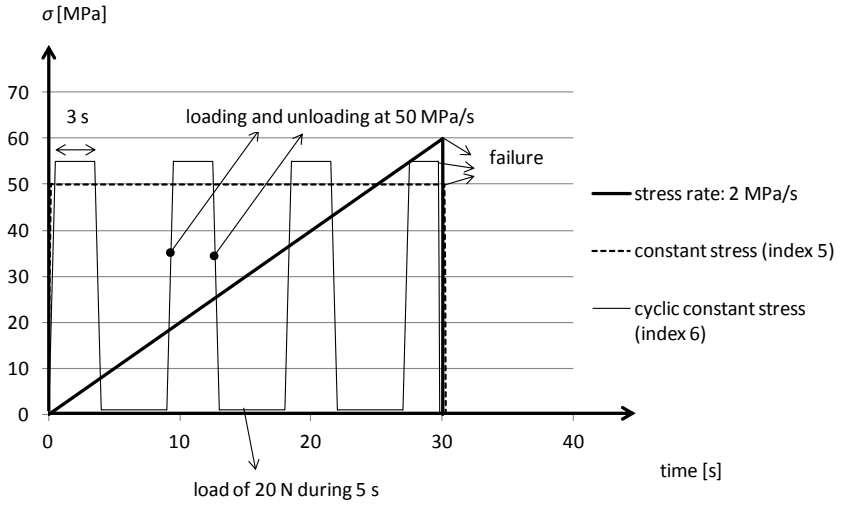

Figure 3.26: Loading at constant stress rate, constant stress and cyclic constant stress for the specimens of size a, 4 mm thick.

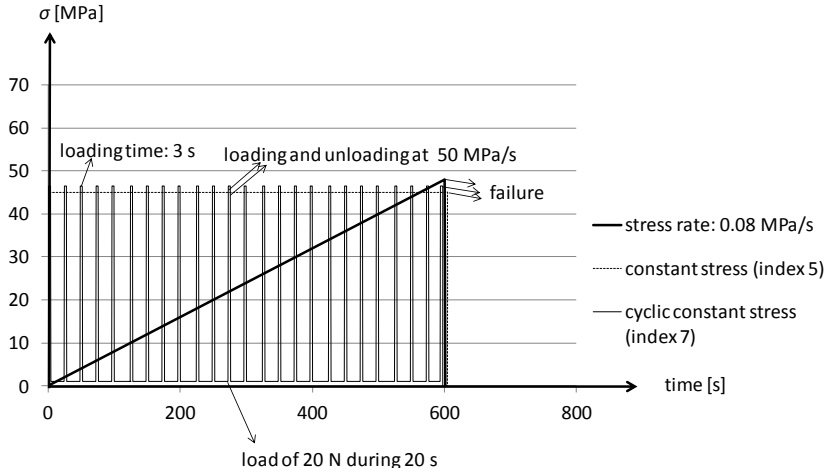

Figure 3.27: Loading at constant stress rate, constant stress and cyclic constant stress for the specimens of size c, 8 mm thick.

During the cutting, arrissing and grinding of the panels a strict protocol was applied. More specifically, the scoring of the specimens consistently occurred at the air side (i.e. the surface which is exposed to the air (atmosphere) during the float process). Furthermore, the cutting wheel had an angle α_c between 145° and 156° and the cutting pressure amounted from 0.7 bar to 1.8 bar for the 4 mm and 8 mm specimens, respectively. Arrissing or grinding was performed with a disc and not with an X-belt (see section 2.3).

The anris varied between 0.9 mm and 1.1 mm for the 4 mm thick specimens and between 1.2 mm and 1.4 mm for the 8 mm thick specimens (Figures 2.1 to 2.4). At least 90 days elapsed between processing the edge and testing the specimens. During the 14 days before testing, the specimens were kept at a temperature of 20 °C $\pm$ 2 °C and a relative humidity of 65% $\pm$ 4%, the same as the test conditions.

For a specific thickness and edge finishing, all the specimens of the three series (constant stress rate, constant stress and cyclic stress: see Tables 3.15 and 3.16) were prepared out of identical panes, of which the edge was processed on the same day with the same machine and the same processing parameters. Consequently, for the comparison of the three loading histories for a certain thickness and edge finishing, one can assume the same flaw population caused by processing the edge.

After testing at a constant stress rate, the failure stress values or tensile strength values f were calculated based on the failure loads P_f for series N2-a2, A-a2, C2-a2, N2-c3, A-c3, C2-c3 (Tables 3.15 and 3.16) with Eq. (3.2). The subscript *eg*, which means edge and glass, is omitted in this section. The correction according to Eq. (3.3) was not performed for this test programme as it is a very small correction. Also, the different load histories are only compared relatively to each other and no characteristic strength values are estimated in this section.

To compare theoretical and experimental strength values for the three different load histories, two different approaches were considered (Vandebroek *et al.* 2013):

- In the first approach testing is conducted at a constant stress rate at inert conditions (high stress rate and no influence of humidity). Using Eq. (2.2), the distribution of the initial critical flaw depth a_{ci} can be determined if the geometry factor Y is well known. However, in literature, the value of Y is not given for an edge flaw population. This is achieved by measuring the initial critical flaw depth a_{ci} by means of microscopy. Unfortunately, this measurement is difficult to carry out (Lindqvist 2013). Next, using Eq. (2.3) or (2.11), failure times and their distribution for the specific loading history (constant stress rate) can be calculated, taking into account slow crack growth. However, the values of the stress corrosion parameters n and v_0 must be known in order to calculate the failure times. The parameter n is well known but v_0 is not well known in literature for laboratory conditions. Again, this parameter v_0 can be assessed by testing at ambient conditions (at a constant stress rate i.e. linearly increased loading) by applying Eq. (2.11). The calculated failure time distributions can then be compared with failure time distributions measured under constant load or cyclic load experiments.
- In the second approach testing is conducted at ambient conditions (at a constant stress rate i.e. linearly increased loading). Next, the measured failure time distributions of this linearly increased loading at ambient conditions are compared to those of the constant load or cyclic load experiments. All three load histories are executed under the same ambient conditions (temperature of 20 °C $\pm$ 2 °C and relative humidity of 65% $\pm$ 4%), without assessment of the stress corrosion parameters.

Summarizing, for this TP 3, the second approach was followed because:

a. For the first approach, the geometry factor Y is not well known, and consequently the initial critical flaw depth a_{ci} of each specimen has to be measured by means of microscopy, which is very difficult.

b. Testing with a linearly increased loading at ambient conditions is needed for both approaches. However, for the first approach this is needed additionally to the inert testing to determine the stress corrosion parameter v_0. Consequently, twice the number of tests would be required to obtain the same goal.

c. In both approaches, the assumption of the same flaw distribution for the three load histories has to be made, even if one of them is measured (see point a above related) and the other two are implicitly reflected in the strength values and time to failure values (first approach). Also in the second approach, the same flaw distribution is reflected in the strength values and the failure time values for the three load histories, as they are cut out of identical glass panes. More precisely, the assumption which is made in the second approach is that the mean value of the distribution of a_{ci} is identical for the three load histories (which are compared to each other). This assumption is reasonable, as the specimens are prepared from identical panes. Individual specimens are not compared between two load histories, as the initial critical flaw depth a_{ci} can vary considerably between individual specimens in one series or in the other.

Applying the second approach, first, the series N2-a2, A-a2, C2-a2 were tested at a constant stress rate of 2 MPa/s at ambient laboratory conditions. Similarly, the series N2-c3, A-c3, C2-c3 were tested at a constant stress rate of 0.08 MPa/s at ambient laboratory conditions. These tests resulted in the experimental strength value f. Then the series N2-a5, A-a5, C2-a5, N2-c5, A-c5, C2-c5 were tested at a constant stress (load controlled testing). Theoretically, the magnitude of this constant stress was determined by means of Eq. (2.12). Therefore, experiments were first executed under the latter constant stress, aiming at the same time to failure as the test with a constant stress rate, see Figure 3.26 and 3.27. If the mean failure time of a certain number of specimens was higher than the mean value of the corresponding series, tested at a constant stress rate, the level of the constant stress was increased, and vice versa. In this way, the experimental strength f_{ct} was determined.

As the height of the individual specimens varied, the corresponding constant stress varied accordingly when a constant load was applied for one series.

However, as the variation of the height was similar for each load history and only the mean value of the strength values and failure time values of all specimens of one series was compared between different load histories, the followed procedure does not influence the accuracy.
Finally, the same procedure was followed for series N2-a6, A-a6, N2-c7, A-c7, C2-c7, which determined the experimental strength f_{cycl}.

3.5.2 Results and discussion

Influence of the load history

For all specimens, the failure origin was determined from the mirror zone according to section 2.3 (see Figure 2.4).
It was observed that for the smooth ground edges 79% of the failures occurred at the edges, 21% at the bevel surfaces (bevel surface between two edges). For the three different load histories this ratio was similar (failures at the edge: constant stress rate: 81%, constant stress: 79%, cyclic constant stress: 75%). For the arrissed edges 74% of the failures occurred at the edges, 26% at the bevel surfaces. For the three different load histories this ratio was similar (failures at the edge: constant stress rate: 69%, constant stress: 78%, cyclic constant stress: 75%). Finally, for the cut specimens, all failures were initiated at the edge.

For every series, the sample mean $\bar{x}$ of the strength and the time to failure and the corresponding sample standard deviation s are listed in Table 3.17 and 3.18.

Table 3.17: Sample mean value and standard deviation of f, f_{ct} , f_{cycl} and t_f, $t_{f,ct}$, $t_{f,cycl}$ for the series with thickness 4 mm.

series	f or f_{ct} or f_{cycl}		t_f or $t_{f,ct}$ or $t_{f,cycl}$	
	$\bar{x}$ [MPa]	s [MPa]	$\bar{x}$ [s]	s [s]
N2-a2	64.9	7.3	32.0	4.1
N2-a5	54.5	0.9	37.8	48.0
N2-a6	61.9	1.5	32.9	35.3
A-a2	47.7	5.2	23.4	2.9
A-a5	40.4	1.0	25.7	26.7
A-a6	45.5	1.3	28.3	22.1
C2-a2	58.0	5.4	28.6	2.9
C2-a5	48.3	1.5	34.0	49.2

Table 3.18: Sample mean value and standard deviation of f, f_{ct} , f_{cycl} and t_f, $t_{f,ct}$, $t_{f,cycl}$ for the series with thickness 8 mm.

series	f or f_{ct} or f_{cycl}		t_f or $t_{f,ct}$ or $t_{f,cycl}$	
	$\bar{x}$ [MPa]	s [MPa]	$\bar{x}$ [s]	s [s]
N2-c3	49.9	3.2	616	38
N2-c5	41.8	0.9	632	300
N2-c7	49.8	1.0	645	307
A-c3	45.1	3.6	559	49.0
A-c5	37.8	0.8	581	408
A-c7	45.1	0.7	571	274
C2-c3	59.6	5.9	736	68.0
C2-c5	50.0	0.5	757	487
C2-c7	59.7	0.8	826	693

Theoretically, the magnitude of the constant strength value f_{ct} was calculated from Eq. (2.12) ($\sigma_{n1}(t)$ being the stress history, testing under constant stress rate, failing after a period of time t_{f1}; $\sigma_{n2}(t)$ being the constant stress history by which the specimens fail after the same period of time $t_{f,ct,2} = t_{f1}$). The value of K_{th} was taken equal to 0.25 MPa.m$^{1/2}$ and the inert strength is considered to be 60% higher than the strength value tested with a stress rate of 2 MPa/s. For the strength value tested at 0.08 MPa/s, the value of n = 16.5 was used (see section 3.4) when applying Eq. (2.13). Thus, the theoretical ratio f_{ct}/f was calculated. This ratio was compared to the experimental ratio. In the same way, the theoretical ratio f_{cycl}/f, by using Eq. (2.12), was compared to the corresponding experimental ratio.

Table 3.19: Theoretical and experimental ratio of f_{ct}/f and f_{cycl}/f for the series with thickness 4 mm.

series	theoretical		experimental		
	f_{ct}/f [-]	f_{cycl}/f [-]	f_{ct}/f [-]	f_{cycl}/f [%]	dev. [%]
N2-a5/N2-a2	0.842	-	0.840	-	**-0.3**
N2-a6/N2-a2	-	0.907	-	0.954	+5.2
A-a5/A-a2	0.842	-	0.847	-	**+0.6**
A-a6/A-a2	-	0.888	-	0.954	+7.4
C2-a5/C2-a2	0.842	-	0.833	-	**-1.1**

Table 3.20: Theoretical and experimental ratio of f_{ct}/f and f_{cycl}/f for the series with thickness 8 mm.

series	theoretical		experimental		
	f_{ct}/f [-]	f_{cycl}/f [-]	f_{ct}/f [-]	f_{cycl}/f [%]	dev. [%]
N2-c5/N2-c2	0.841	-	0.838	-	**-0.4**
N2-c7/N2-c2	-	0.955	-	0.998	+4.5
A-c5/A-c2	0.841	-	0.838	-	**-0.3**
A-c7/A-c2	-	0.954	-	1.000	+4.8
C2-c5/C2-c2	0.841	-	0.839	-	**-0.2**
C2-c7/C2-c2	-	0.955	-	1.002	+4.9

The results of this comparison are provided in Table 3.19 and 3.20. The deviation between the experimental ratio and the theoretical ratio was calculated:
dev. = 100 * (experimental ratio – theoretical ratio) / theoretical ratio

It can be concluded from Table 3.19 and 3.20 that Eq. (2.12) yields a ratio of f_{ct} / f which is only 1.1% less to 0.6% more conservative than the experimental values (bold values of the dev.). Both the theoretical and experimental values of f_{ct} / f are all very close to the value found by Mencik (1992), i.e. $(1/(n+1))^{1/n}$ = 0.841 (Eq. (2.14) with n = 16.5). The deviation between the values calculated with Eq. (2.12) (see Tables 3.20 and 3.21, n = 16.5; i.e. 0.842 and 0.841, respectively) and the value calculated with Eq (2.14) (i.e. 0.841) is maximum 0.1%. However, Eq. (2.12) yields a ratio f_{cycl} / f which is 5.2% to 7.4% more conservative than the experimental values, tested with 3 to 4 cycles (Table 3.19). Tested with about 25 cycles (Table 3.20), Eq. (2.12) yields a ratio f_{cycl} / f which is 4.5% to 4.9% more conservative than the experimental values. For the latter deviations (f_{ct} / f and f_{cycl} / f), little difference was found between the smooth ground, arrissed and cut edge finishing.

According to prEN 16612 (2013), the design strength is calculated using k_{mod} , which considers the load duration of an action (e.g. for wind loads i.e. 600 s) and is given by Eq. (3.13), which is basically derived from Eq. (2.13):

$$k_{mod} = \left(\frac{t_{test}}{t_{load}}\right)^{1/n} \tag{3.13}$$

where k_{mod} [-] is the factor for the load duration, t_{test} [s] is the load duration of the test and t_{load} [s] is the load duration of the action.

In case these guidelines are used for incorporating the effects of cyclic loading, a discrepancy occurs.
Applying Eq. (2.13) or Eq. (3.13), the strength $f_{ct,1\ cycle}$ which corresponds to the time of one cycle equals: $f_{ct,1\ cycle} = f_{ct} * (t_{f,ct} / t_{f,ct,1cycle})^{1/n}$ and delivers the values listed in Table 3.21 and 3.22.

Consequently, the deviation between f_{cycl} and $f_{ct,1\ cycle}$ was calculated and listed in Tables 3.21 and 3.22:
dev. = $100*(f_{cycle} - f_{ct,1\ cycle}) / f_{ct,1\ cycle}$

Table 3.21 shows that the approach used in the standards is slightly non-conservative (dev. of 0.3% to 0.9%), as the cyclic load is considered with a few cycles (3 to 4). However, when the number of cycles is about 25 (Table 3.22), the guidelines in the standard overestimates the strength by 12.4% to 13.4%, compared to the experimental values.

Next, the experimental values of f_{cycl} are compared to the values $f_{ct,all\ cycles}$ considering all cycles.
Applying Eq. (2.13) or Eq. (3.13), the strength $f_{ct,all\ cycles}$ which corresponds to the total time of all cycles together is given by $f_{ct,all\ cycles} = f_{ct} * (t_{f,ct} / t_{f,ct,all\ cycles})^{1/n}$. The values are presented in Tables 3.23 and 3.24. Consequently, the deviation between f_{cycl} and $f_{ct,all\ cycles}$ was calculated and listed:
dev. = $100*(f_{cycle} - f_{ct,all\ cycles}) / f_{ct,all\ cycles}$

Table 3.21: Estimated mean experimental values for f_{ct}, $f_{ct,1cycle}$ *and* f_{cycl} for the series with thickness 4 mm.

series	f_{ct} [MPa]	$f_{ct,\ 1\ cycle}$ [MPa]	f_{cycl} [MPa]	dev. [%]
N2-a5/ N2-a6	54.5	62.4	61.9	-0.9
A-a5/ A-a6	40.5	45.6	45.5	-0.3

Table 3.22: Estimated mean experimental values for f_{ct}, $f_{ct,1cycle}$ *and* f_{cycl} for the series with thickness 8 mm.

series	f_{ct} [MPa]	$f_{ct,\ 1\ cycle}$ [MPa]	f_{cycl} [MPa]	dev. [%]
N2-c5/N2-c7	41.8	57.1	49.8	-12.9
A-c5/A-c7	37.8	51.5	45.1	-12.4
C2-c5/C2-c7	50.0	69.0	59.7	-13.4

Table 3.23: Estimated mean experimental values for f_{ct}, $f_{ct,1cycle}$ *and* f_{cycl} for the series with thickness 4 mm.

series	f_{ct} [MPa]	$f_{ct,\ all\ cycles}$ [MPa]	f_{cycl} [MPa]	dev. [%]
N2-a5/ N2-a6	54.5	58.4	61.9	6.0
A-a5/ A-a6	40.5	42.8	45.5	6.4

Table 3.24: Estimated mean experimental values for f_{ct}, $f_{ct,1cycle}$ *and* f_{cycl} for the series with thickness 8 mm.

series	f_{ct} [MPa]	$f_{ct,\ all\ cycles}$ [MPa]	f_{cycl} [MPa]	dev. [%]
N2-c5/N2-c7	41.8	47.0	49.8	5.9
A-c5/A-c7	37.8	42.6	45.1	6.0
C2-c5/C2-c7	50.0	55.9	59.7	6.8

Tables 3.23 and 3.24 present values for which the standard is in all cases conservative (dev. of 5.9% to 6.8%), on condition that all cycles are considered instead of one cycle. The deviation does not vary significantly, neither with the edge finishing, nor with the time between two cycles or the number of cycles. Thus, considering the number of cycles will be a good basis for a strength calculation method for cyclic loading in future standards.

According to the literature (Haldimann 2006), the crack healing is a consequence of two phenomena, the crack threshold and the hysteresis effect, i.e. an aged crack will not repropagate immediately on reloading (Lawn 1993). A non-coplanar re-propagation was directly observed by atomic force microscopy (Hénaux and Creuzet 1997; Wiederhorn *et al.* 2002 2003). However, the crack growth threshold was first explained by rounding of the crack tip (blunting), observed by transmission electron microscopy (Charles and Hilling 1962; Bando *et al.* 1984). More recent research revealed a chemical process at the crack tip (Gehrke *et al.* 1991; Nghiem 1998; Guin and Wiederhorn 2003).

In this test programme, the crack healing varies between 5.9% and 6.8% if the load history is cyclic constant, compared to the edge strength induced by a constant load history (both considered during the same load duration). The conclusions from the test programme are also valid both when the experimental data are fitted to a 2p-Weibull and to a 2p-lognormal distribution (Vandebroek *et al.* 2013).

Number of specimens in a series

As the series N2-a2, A-a2, C2-a2 of this test programme consisted of a large number of specimens (60 to 100, see Table 3.15), these series were used to verify whether the number of specimens of 20 in a series (applied in TP 1 and TP 2) was reliable enough for the estimation of edge strength values (Vandebroek *et al.* 2014a).

Starting from the strength values f_{eg} (60 or 100 test results) calculated according to Eq. (3.2), the estimated mean value $\hat{f}_{eg,m}$ and the standard deviation s was computed (see Tables 3.25, 3.26 and 3.27). The estimation of the lower 5%-fractile characteristic value $\hat{f}_{eg,k}$ for a confidence level γ equal to 0.75 was calculated according to ISO 12491 (1997), assuming that the population standard deviation is not known (see Table 3.28):

$$\hat{f}_{eg,k} = \hat{f}_{eg,m} - k_s.s \tag{3.15}$$

Hereby, k_s was taken equal to 1.76 and 1.80 in case of a sample of 100 specimens and 60 specimens, respectively (ISO 12491, 1997).

Table 3.25: Experimental results of f_{eg} [MPa] of series N2-a2.
$\hat{f}_{eg,m}$ is the estimated mean value [MPa] and s the standard deviation [MPa].

62.4	62.1	72.1	79.6	64.8	58.9	60.9	70.5	62.3	62.3
57.1	62.4	72.9	53.1	68.0	73.7	64.3	63.0	73.1	61.1
54.1	60.3	76.6	62.3	64.4	71.5	58.6	64.3	69.8	63.4
60.1	63.6	75.3	62.6	66.8	70.5	58.6	**41.3**	61.9	65.0
60.7	72.9	68.9	63.5	71.1	60.5	54.8	71.0	62.1	62.3
53.9	78.2	77.5	58.5	72.3	73.9	65.7	74.2	57.8	58.9
mean value*		$\hat{f}_{eg,m}$	64.9		standard deviation			s	7.3

*the small deviation in the value of $\hat{f}_{eg,m}$ from Table 3.17 is caused by the correction due to the experimental stress rate of 2.03 MPa/s instead of the nominal stress rate of 2 MPa/s

Table 3.26: Experimental results of f_{eg} [MPa] of series A-a2.
$\hat{f}_{eg,m}$ is the estimated mean value [MPa] and s the standard deviation [MPa].

47.6	51.9	51.1	42.8	54.1	45.6	49.9	52.6	53.5	46.7
41.3	43.3	51.9	47.6	47.1	39.6	44.1	53.3	49.4	44.6
44.1	51.5	33.1	45.1	50.4	54.7	51.2	53.0	56.7	48.6
45.9	48.4	48.3	42.8	53.4	45.8	48.9	54.0	34.7	52.0
47.2	35.7	45.3	49.5	48.6	47.6	43.8	51.8	57.5	53.9
47.5	47.8	43.6	42.3	38.6	48.8	44.7	50.0	49.1	53.0
mean value*		$\hat{f}_{eg,m}$	47.8		standard deviation			s	5.2

*the small deviation in the value of $\hat{f}_{eg,m}$ from Table 3.17 is caused by the correction due to the experimental stress rate of 2.05 MPa/s instead of the nominal stress rate of 2 MPa/s

Then, the Nonparametric Bootstrap Method was applied (Hedderich and Sachs 2012; Higgens 2004). Random re-sampling (1000 samples) with replacement was performed with samples of 10, 20, 30, …. to 100 specimens. Then, the mean value, the standard deviation and the coefficient of variation of the estimated mean strength values (1000 values) and estimated 5% characteristic strength values (1000 values) were calculated.

For the different sample sizes, which were analyzed with the Bootstrap Method (Hedderich and Sachs, 2012; Higgens, 2004), the values of k_s according to ISO 12491 (1997) are presented in Table 3.29. Tables 3.30, 3.31 and 3.32 show the characteristics of the Bootstrap distributions (mean value $\bar{x}$, standard deviation s and the coefficient of variation V) for the 5% characteristic strength value (for a confidence level γ equal to 0.75). Similarly, Tables 3.33, 3.34 and 3.35 show these characteristics in case the mean strength value is estimated. Finally, Figure 3.28, shows the coefficient of variation V in function of the number of specimens n_s of the sample for the series N2-a2, A-a2 and C2-a2.

Table 3.27: Experimental results of f_{eg} [MPa] of series C2-a2.
$\hat{f}_{eg,m}$ is the estimated mean value [MPa] and s the standard deviation [MPa].

53.9	60.5	62.9	54.9	55.8	59.7	62.5	52.5	60.9	60.5
56.0	50.8	52.4	57.0	59.0	56.2	62.5	51.1	55.3	53.2
61.4	56.2	66.8	52.9	55.3	69.2	59.2	52.9	59.3	53.3
68.1	56.0	63.1	62.1	66.3	59.1	60.5	55.7	63.9	58.5
66.9	52.9	57.8	49.9	58.0	59.9	62.6	54.8	57.3	56.1
62.0	54.7	62.1	57.5	56.9	52.3	57.7	52.9	60.8	55.1
65.7	54.7	61.2	63.3	57.6	54.9	63.2	56.1	57.7	53.5
63.1	54.8	55.7	63.0	61.6	56.3	52.4	50.0	58.5	52.0
55.5	57.7	51.5	58.8	69.7	75.6	67.5	62.5	38.3	53.8
66.6	52.8	52.1	60.5	66.1	60.0	53.2	51.5	56.6	56.3
mean value*		$\hat{f}_{eg,m}$	58.1		standard deviation			s	5.4

*the small deviation in the value of $\hat{f}_{eg,m}$ from Table 3.17 is caused by the correction due to the experimental stress rate of 2.02 MPa/s instead of the nominal stress rate of 2 MPa/s

Table 3.28: Estimated values of $f_{eg,k}$ [MPa].

series	k_s [-]	$\hat{f}_{eg,k}$ [MPa]
N2-a2	1.80	51.8
A-a2	1.80	38.5
C2-a2	1.76	48.6

Table 3.29: Values of k_s according to ISO 12491 (1997).

n_s [-]	k_s [-]
10	2.10
20	1.93
30	1.86
40	1.83
50	1.81
60	1.80
70	1.79
80	1.78
90	1.77
100	1.76

Table 3.30: Characteristics of the Bootstrap distribution of $f_{eg,k}$ (γ = 0.75) for series N2-a2.

sample size	$\bar{x}$ [MPa]	s [MPa]	V [-]
10	50.2	4.5	0.090
20	51.1	3.1	0.060
30	51.5	2.5	0.048
40	51.8	2.1	0.041
50	51.9	1.9	0.037
60	52.0	1.7	0.033
70	52.0	1.6	0.031
80	52.1	1.5	0.029
90	52.2	1.4	0.027
100	52.2	1.3	0.026

Table 3.31: Characteristics of the Bootstrap distribution of $f_{eg,k}$ (γ = 0.75) for series A-a2.

sample size	$\bar{x}$ [MPa]	s [MPa]	V [-]
10	37.3	3.7	0.100
20	37.9	2.6	0.068
30	38.2	2.1	0.054
40	38.3	1.7	0.044
50	38.5	1.5	0.038
60	38.5	1.3	0.034
70	38.5	1.2	0.032
80	38.6	1.2	0.030
90	38.7	1.1	0.028
100	38.7	1.0	0.026

Table 3.32: Characteristics of the Bootstrap distribution of $f_{eg,k}$ (γ = 0.75) for series C2-a2.

sample size	$\bar{x}$ [MPa]	s [MPa]	V [-]
10	47.2	3.4	0.073
20	47.8	2.3	0.049
30	48.1	1.9	0.039
40	48.3	1.6	0.033
50	48.4	1.4	0.029
60	48.4	1.3	0.027
70	48.5	1.2	0.025
80	48.5	1.1	0.023
90	48.5	1.1	0.022
100	48.6	1.0	0.020

Table 3.33: Characteristics of the Bootstrap distribution of $f_{eg,m}$ (γ = 0.75) for series N2-a2.

sample size	$\bar{x}$ [MPa]	s [MPa]	V [-]
10	64.9	2.2	0.033
20	64.9	1.6	0.024
30	64.9	1.3	0.020
40	64.9	1.1	0.017
50	64.9	1.0	0.016
60	64.9	0.9	0.014
70	64.9	0.9	0.013
80	64.9	0.8	0.012
90	64.9	0.8	0.012
100	64.9	0.7	0.011

Table 3.34: Characteristics of the Bootstrap distribution of $f_{eg,m}$ (γ = 0.75) for series A-a2.

sample size	$\bar{x}$ [MPa]	s [MPa]	V [-]
10	47.8	1.7	0.035
20	47.8	1.2	0.025
30	47.8	1.0	0.020
40	47.8	0.8	0.017
50	47.8	0.7	0.015
60	47.8	0.6	0.014
70	47.8	0.6	0.012
80	47.8	0.6	0.012
90	47.8	0.5	0.011
100	47.8	0.5	0.011

Table 3.35: Characteristics of the Bootstrap distribution of $f_{eg,m}$ (γ = 0.75) for series C2-a2.

sample size	$\bar{x}$ [MPa]	s [MPa]	V [-]
10	58.1	1.6	0.028
20	58.1	1.2	0.021
30	58.1	1.0	0.017
40	58.1	0.9	0.015
50	58.1	0.8	0.013
60	58.1	0.7	0.012
70	58.1	0.6	0.011
80	58.1	0.6	0.010
90	58.1	0.6	0.010
100	58.1	0.5	0.009

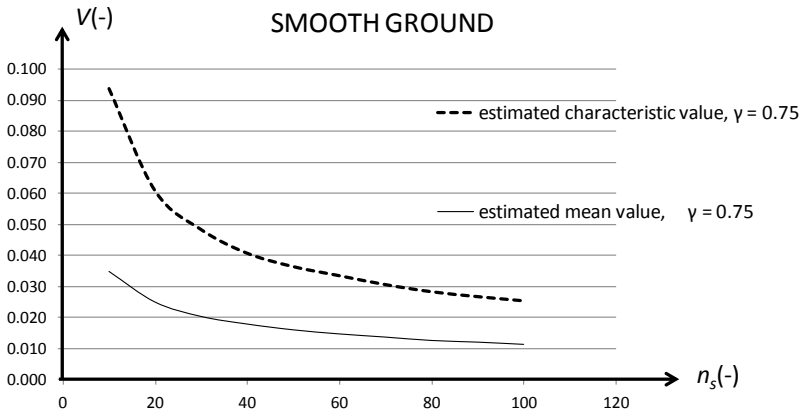

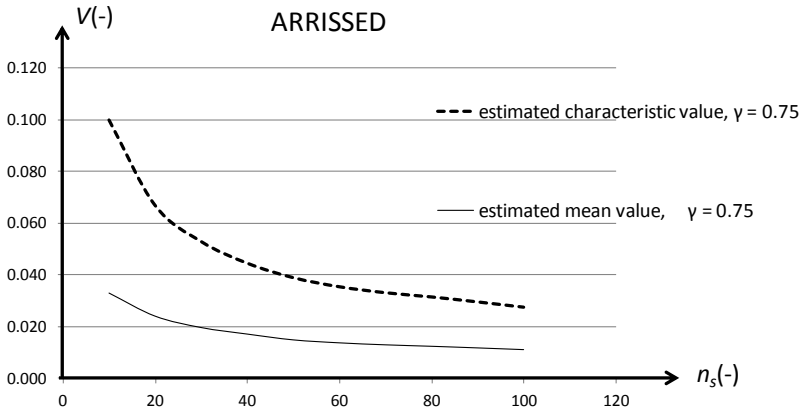

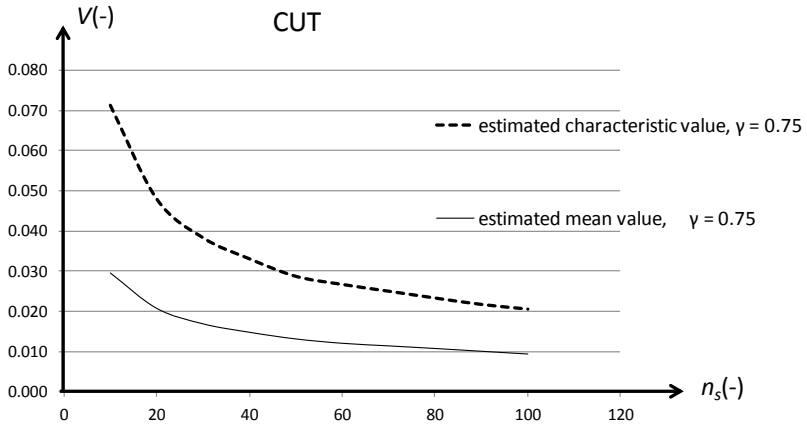

Figure 3.28: Coefficient of variation V in function of the number of specimens n_s of the sample.

According to ISO 12491 (1997), the estimation of the lower 5%-fractile shall be calculated according to Eq. (3.14). To verify the basic assumption of a Normal distribution of glass strength as inherently assumed by Eq. (3.14), the parameters of the Normal distribution were estimated by means of the least-squares method. The coefficient of determination r^2 was found to be 0.96, 0.95 and 0.96 for the series N2-a2, A-a2, C2-a2, respectively, which justifies the assumption of the Normal distribution. The corresponding probability plots are presented in Figure C.1, C.2 and C.3 (see Annex C). The variation coefficient V amounts to 0.10, 0.10 and 0.09 for the series N2-a2, A-a2, C2-a2, respectively, which is in good agreement with the mean coefficient of variation V = 0.10 of all the series of TP 2 (see section 3.4). Figure 3.28 shows that the coefficient of variation drops significantly between n_s = 10 and n_s = 20. For n larger than 20, the decrease of the coefficient of variation is less significant. This phenomenon is visible for all series. Finally, Figure 3.28 indicates that for the estimation of the mean strength value, five times fewer specimens are required to achieve the same coefficient of variation, compared to the estimation of the characteristic strength value.

3.5.3 Conclusions

The influence of the load history was investigated. For the cyclic loading, similar to the thermal stress loading, a crack healing effect could be estimated (6%, see Tables 3.23 and 3.24). However, the time between two cycles was only 5 s and does not correspond to the real time between two thermal stress loadings. Therefore, TP 4 was executed to estimate the crack healing with a time of one week between two subsequent loading cycles. Also, the influence of the number of specimens in a series was examined. A number of 20 specimens in a series seems acceptable for this study. Also, according to the standard prEN16612 (2013), the number of test specimens of a series to obtain a reliable mean value or characteristic value should be at least 10 or 20, respectively.

3.6 TP 4: Influence of the load history (one week)

This test programme was set up to estimate the influence of the time period between two sequential cycles on the crack healing.

3.6.1 Materials and testing details

In this test programme, six series of specimens, with a cut edge finishing (series C3 for supplier 3) and a thickness of either 4 or 8 mm, were tested in a 4PB setup. First, two series were subjected to a linearly increased loading (constant stress rate, strength *f*). Then, two series, identical to the first series, were tested under cyclic loading with a period of 5 s between two sequential cycles (see Figure 3.26, cyclic constant stress, strength f_{cycl}). Finally, two series, identical to the first series, were tested under cyclic loading with a period of one week between two sequential cycles (cyclic constant stress, strength $f_{cycl,week}$). The sizes a and c of the specimens according to Figure 3.2 are presented in Table 3.36. The in-plane 4PB test setup is presented in Figure 3.25.

The specimens were loaded at a stress rate of 1 MPa/s and a cyclic constant stress (similar to Figure 3.26). For the cyclic constant stress, the holding phase amounted to 3 s and the time between the cycles amounted to 5 s or one week. The transition between the constant stress and no stress was performed at a stress rate of 50 MPa/s. Furthermore, the testing method of TP3 was followed.
An overview of the series is presented in Tables 3.37 and 3.38 and the loading histories are similar to those of Figure 3.26 (the time between two cycles amounted to 5 s or one week). The number of specimens n_s for every series is indicated.

Table 3.36: overview of the specimen sizes of TP 4.

specimen size	nominal thickness *b* [mm]	nominal height *h* [mm]	nominal specimen length L_t [mm]	nominal support span *L* [mm]	nominal load span L_s [mm]
a	4	12.5	110	100	40
c	8	18.8	170	150	60

Table 3.37: overview of the test series of TP 4: size a.

series	n_s	load history
C3-a4	40	stress rate 1 MPa/s (index 4)
C3-a6	40	cyclic constant stress (index 6: 5 seconds between two cycles
C3-a8	77	cyclic constant stress (index 8: 1 week between two cycles

Table 3.38: overview of the test series of TP 4: size c.

series	n_s	load history
C3-c4	40	stress rate 1 MPa/s (index 4)
C3-c6	38	cyclic constant stress (index 6: 5 seconds between two cycles
C3-c8	40	cyclic constant stress (index 8: 1 week between two cycles

3.6.2 Results and discussion

For every series, the sample mean $\bar{x}$ of the strength and the time to failure and the corresponding sample standard deviation *s* are listed in Table 3.39 and 3.40.

Table 3.39: Sample mean value and standard deviation of f, f_{cycl}, $f_{cycl,week}$ and t_f, $t_{f,cycl}$, $t_{f,cycl,week}$ for the series with thickness 4 mm.

series	f or f_{cycl} or $f_{cycl,week}$		t_f or $t_{f,cycl}$ or $t_{f,cycl,week}$	
	$\bar{x}$ [MPa]	s [MPa]	$\bar{x}$ [s]	s [s]
C3-a4	59.7	10.1	59.3	9.9
C3-a6	59.7	1.3	56.8	105
C3-a8	60.6	2.4	71.9	98.7

Table 3.40: Sample mean value and standard deviation of f, f_{cycl} , $f_{cycl,week}$ and t_f, $t_{f,cycl}$, $t_{f,cycl,week}$ for the series with thickness 8 mm.

series	f or f_{cycl} or $f_{cycl,week}$		t_f or $t_{f,cycl}$ or $t_{f,cycl,week}$	
	$\bar{x}$ [MPa]	s [MPa]	$\bar{x}$ [s]	s [s]
C3-c4	63.1	8.5	63.0	8.6
C3-c6	62.1	1.8	59.2	105
C3-c8	62.7	1.7	66.5	75.3

From Tables 3.39 and 3.40, it can be derived that f_{cycl} /$f_{cycl,week}$ = 0.99 for the specimens of 4 mm and f_{cycl} /$f_{cycl,week}$ = 1.01 for 8 mm thickness. Consequently, the crack healing effect can be considered independent of the time between two sequential cycles for the cut edge finishing.

As the testing was only performed with a CUT edge finishing, more research is needed to investigate whether this conclusion is also valid for other edge finishings. However, from Tables 3.23 and 3.24, it can be noticed that the crack healing only varies from 5.9% to 6.8% between the different edge finishings, i. e. smooth ground, arrissed and cut. Consequently, the author assumes that also with one week between the cycles, the conclusion applies to the different edge finishings.

3.6.3 Conclusion

The time between two subsequent cycles of a cyclic loading does not seem to have an influence on the crack healing effect. Consequently, the crack healing effect, estimated in TP 3 can be used for the ultimate limit verification of sections 4.3 to 4.6.

3.7 TP 5: Influence of the size

This test programme focused on the estimation of the influence of the size of a glass element on the edge strength.

3.7.1 Materials and testing details

In this programme (Vandebroek *et al.* 2014b), eight series of beam specimens, with either smooth ground or cut edge finishing, a thickness of either 4 or 8 mm, and a length of either 550 or 1100 mm (see Table 3.41) were tested in a 4PB setup described in section 3.2.3. All series were subjected to a linearly increased loading (constant stress rate) until failure.

The objective of this investigation is to assess the strength reduction between the different beam sizes and to compare these experimental values with the probabilistic formulas available in the literature (Shen 1997; Munz and Fett 1999; Wachtman *et al.* 2009; Haldimann 2006; Haldimann *et al.* 2008; Weller *et al.* 2010; Overend and Zammit 2012) and in the standard E2431-12 (2012).

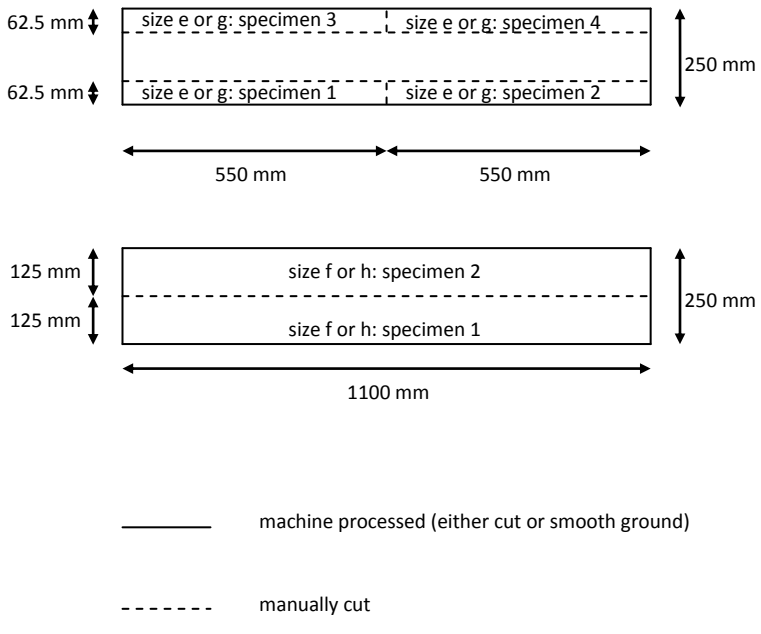

Figure 3.29: Overview of the small specimens (size e or g, see Table 3.41) and the large specimens (size f or h, see Table 3.41) out of a large pane.

For this test programme, panels of 1100 mm * 250 mm with a nominal thickness of 4 or 8 mm and either smooth ground or simple cut edges, were obtained from a qualified glass processor. During the machine cutting and grinding of the panels a strict protocol was applied. More specifically, the scoring of the specimens consistently occurred at the air side (i.e. the surface which is exposed to the air (atmosphere) during the float process). Furthermore, the cutting wheel had an angle α_c of 145° (pressure of 0.7 bar) for the 4 mm specimens and 154° (pressure of 1.8 bar) for the 8 mm specimens. In addition, for the smooth ground specimens, the grinding was done with a diamond-grit disc (D151, D91). The anris varied between 0.9 mm and 1.1 mm for the 4 mm thick specimens and between 1.2 mm and 1.4 mm for the 8 mm thick specimens (Figures 2.1 to 2.4). Finally, per glass thickness (4 or 8 mm) and per edge finishing (cut or smooth ground) all panels were processed on the same day with the same machine and the same processing parameters, from which one can assume the same flaw population between the series with the small (length of 550 mm) and the large specimens (length of 1100 mm).

Subsequently, these panels were manually cut in to eight different specimen series with final nominal specimen dimensions of 550 mm * 62.5 mm or 1100 mm * 125 mm as indicated in Figure 3.29 and listed in Tables 3.41 and 3.42. The specimens were cut such that the edge which was exposed to tensile stresses during the bending tests always corresponded to the machined cut or smooth ground edge (instead of to the manually cut edge). Both the small and large specimens of one thickness and one edge finishing originated from the same large 6 m * 3.21 m standard size float glass panel.

Table 3.41: overview of the specimen sizes of TP 5.

specimen size	nominal thickness *b* [mm]	nominal height *h* [mm]	nominal specimen length L_t [mm]	nominal support span *L* [mm]	nominal load span L_s [mm]
e	4	62.5	550	500	250
f	4	125	1100	1000	500
g	8	62.5	550	500	250
h	8	125	1100	1000	500

The support span L and load span L_s were 500 mm and 250 mm, respectively, for the 550 mm specimens and 1000 mm and 500 mm, respectively, for the 1100 mm specimens (see Figure 3.2 and Table 3.41). All specimens were loaded at a constant stress rate of 2 $\pm$ 0.06 MPa/s. The small variation in stress rate of 0.06 MPa/s, due to the variability in specimen height in one series, is well within the allowable variation of 0.4 MPa/s according to the standard EN1288-3 (2000). At least 30 days elapsed between processing the edge (i.e. the machined edge) and testing the specimens (i.e. the machined edge). During the 7 days before testing, the specimens were kept at a temperature of 20°C $\pm$ 2°C and a relative humidity of 65% $\pm$ 4%, the same as the test conditions.

After eliminating the out-of-load-span failures (23 out of 250 specimens), 227 valid specimens remained. An overview of the test series is given in Table 3.42.

Table 3.42: overview of the test series of TP 5.

series	nominal thickness [mm]	nominal load span L_s [mm]	number of specimens
N4-e2	4	250	30
N4-f2	4	500	30
N4-g2	8	250	29
N4-h2	8	500	28
C4-e2	4	250	28
C4-f2	4	500	30
C4-g2	8	250	28
C4-h2	8	500	24

3.7.2 Results and discussion

In this test programme, the strength values are first corrected according to Eq. (3.3). Then, the cross-sectional and the longitudinal failure locations are examined as well as the corresponding corrected strength values (see Figure B.37 of Annex B). Finally, the corrected strength values estimated by the least-squares method and the method of maximum likelihood are presented as well as the corresponding Weibull plots (Figures D.1 to D.4, Annex D).

For most of the specimens (85%), the **cross-sectional** location (0-5) could be determined (see Table 3.43), following the definitions as provided in Figures 3.9 and 3.10. The air side always corresponds to surface 0, edge 1 or edge 2 and the tin side corresponds to edge 3, edge 4 or surface 5.

It was observed that for the ground edges 58% of the failures occurred at the edges 1, 2, 3 or 4; 14% at the bevel surface between the edges 1 and 2 or 3 and 4; 13% at the surfaces 0 or 5 and 15% at the surface between the edges 2 and 3 (see Figure 3.9 and Table 3.43).
Also, it was observed that for the cut edges 79% of the failures occurred at the edges 2 or 3; 20% at the surfaces 0 or 5 and only 1% at the surface between the edges 2 and 3 (see Figure 3.10 and Table 3.43).

Table 3.43: Failure origins (%) at the different edges (see Figures. 3.9 and 3.10).

Series	Surface 0	Edge 1	Surface between 1 and 2	Edge 2	Surface between 2 and 3	Edge 3	Surface between 3 and 4	Edge 4	Surface 5
									
N4-e2	0	0	4	30	18	26	15	0	7
N4-f2	10	3	3	17	7	37	10	3	10
N4-g2	0	9	9	48	4	4	0	13	13
N4-h2	0	0	14	27	32	18	0	0	9
	Surface 0			Edge 2	Surface between 2 and 3	Edge 3			Surface 5
									
C4-e2	0			62	4	19			15
C4-f2	14			32	0	32			22
C4-g2	0			82	0	12			6
C4-h2	11			68	0	16			5

For all the cross-sectional failure locations (9 in case of ground specimens, 5 in case of cut specimens, see Table 3.43), the corresponding mean strength values (sample mean of the corrected strength values f'_{eg}) were calculated. The results are depicted for all the ground edges (small and large specimens) in Figure 3.31 and for all the cut edges (small and large specimens) in Figure 3.32.

Next, the sample mean, the sample standard deviation and the sample coefficient of variation in the number of failures (per cross sectional location) and in the mean strength values (per cross sectional location) were calculated (see Table 3.44).

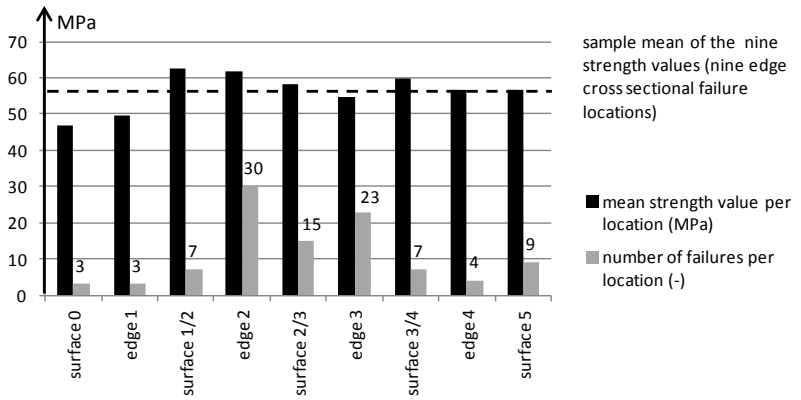

Figure 3.31: Failure origins and corresponding mean corrected strength values at the SMOOTH GROUND edges (small and large specimens).

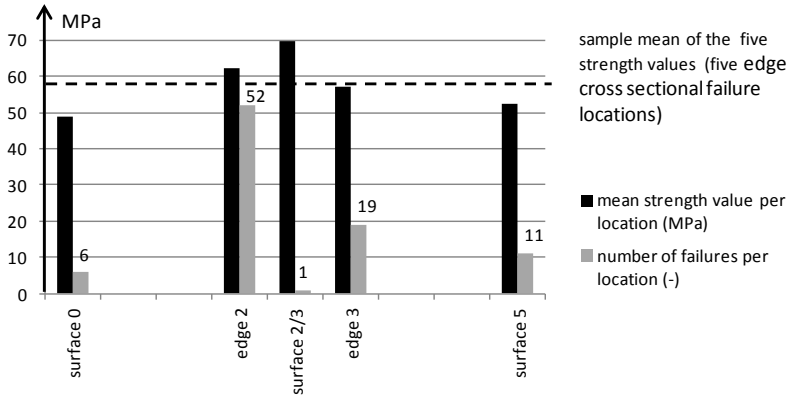

Figure 3.32: Failure origins and corresponding mean corrected strength values at the CUT edges (small and large specimens).

Table 3.44: Distribution of the failure origins: location and corresponding strength values.

Specimens	Number of failures per location			Mean strength value per location		
	$\bar{x}$ [-]	s [-]	V [-]	$\bar{x}$ [MPa]	s [MPa]	V [-]
Smooth Ground	11	10	0.85	56.3	5.2	0.09
Cut	18	20	1.14	58.1	8.3	0.14

For the smooth ground edges, more failures occurred at the edges 2 and 3 compared to all the other failure locations (see Figure 3.31). A possible explanation was given in section 3.4.2. However, the corresponding strength values of all the edges and all the surfaces depended little on the cross-sectional failure location, as can be seen from Figure 3.31. Only the failures originating from edge 1 and surface 0 had lower strength values. Thus, these strength values were excluded from the further analysis (see Table 3.46).

For the cut edges, significantly more failures originated from edge 2, compared to edge 3 (see Figure 3.32). Indeed, the scoring of the specimens consistently occurred at the air side (the edge 2 is situated at the air side). It can be concluded that the cutting wheel induces a larger number of critical flaws at this location. Again, the corresponding strength values were mostly independent of the cross sectional failure location, as shown in Figure 3.32. Only the failures originating from surface 0 and 5 had lower strength values (see Figure 3.32). Thus, these strength values were excluded from the further analysis (see Table 3.46).

Indeed, Table 3.44 shows that the coefficients of variation in the number of failures per location amount from 0.85 (smooth ground) to 1.14 (cut), whereas the coefficients of variation in the corresponding mean strength values per location are much lower, i.e. from 0.09 (smooth ground) to 0.14 (cut).

Next, for all specimens, the **longitudinal** location of failure was determined (see Figures 3.33, 3.34 and 3.35). In order to investigate the spatial distribution of the strength values, the load span L_s was divided into 10 parts (10 bins, see Figure 3.4).

The failure origins and corresponding mean strength values (sample means of the corrected strength values f'_{eg}) are depicted in Figure 3.33 for all the small specimens, in Figure 3.34 for all the large specimens and finally in Figure 3.35 for all the specimens (small and large together) in function of the longitudinal failure location.

Next, the sample mean, the sample standard deviation and the sample coefficient of variation in the number of failures (per bin) and in the mean strength values (per bin) were calculated (see Table 3.45).

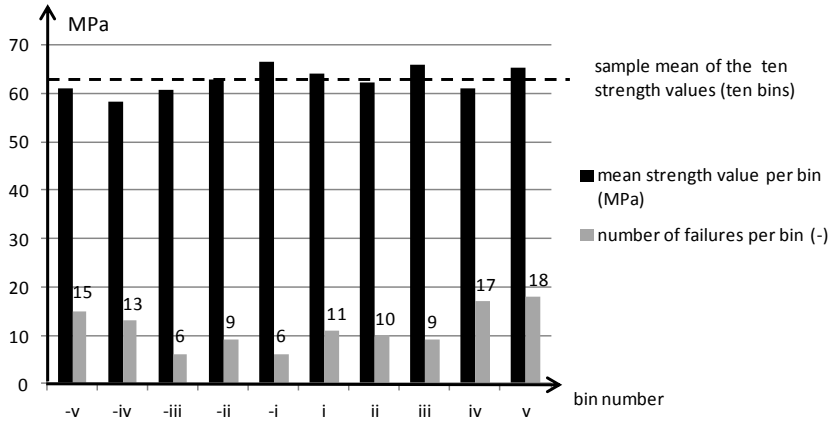

Figure 3.33: Failure origins and corresponding mean corrected strength values at the edges of the SMALL specimens (load span of 250 mm).

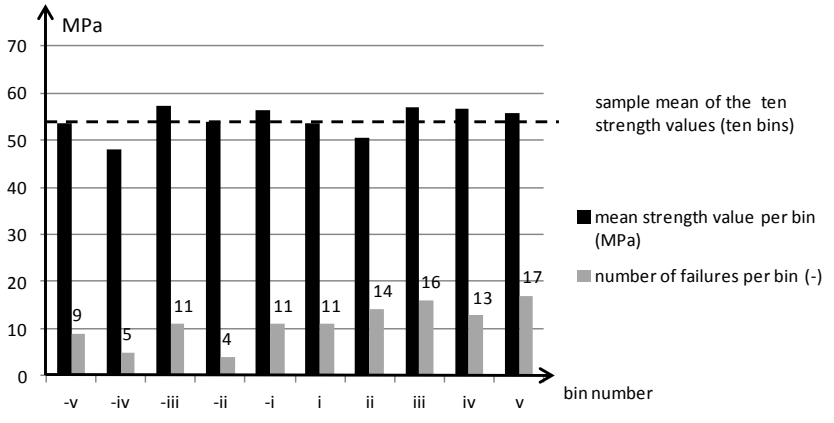

Figure 3.34: Failure origins and corresponding mean corrected strength values at the edges of the LARGE specimens (load span of 500 mm).

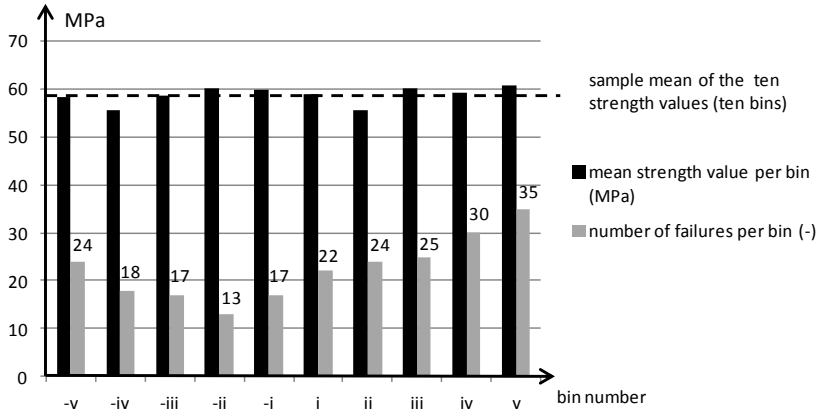

Figure 3.35: Failure origins and corresponding mean corrected strength values at the edges of ALL specimens (the small and the large specimens).

Table 3.45: Distribution of the failure origins: location and corresponding strength values.

Specimens	Number of failures per bin			Mean strength value per bin		
	$\bar{x}$	s	V	$\bar{x}$	s	V
	[-]	[-]	[-]	[MPa]	[MPa]	[-]
Small	11	4	0.37	62.9	2.6	0.04
Large	11	4	0.38	54.3	3.0	0.06
All	23	7	0.29	58.7	1.9	0.03

Figures 3.33, 3.34 and 3.35 provide the distribution along the load span for the small specimens (see Figure 3.33), for the large specimens (see Figure 3.34) and for all specimens (see Figure 3.35). Because of the 'Hertzian line contact' effect (Munz and Fett 1999), the failure directly below the inner rollers is more predominent. This effect is larger for the small specimens (see Figure 3.33, bin numbers –v, -iv, iv and v) than for the large specimens (see Figure 3.34, bin numbers –v, -iv, iv and v). Although, more failures occur at both ends of the load span, the corresponding strength values are similar to those in the middle of the load span, for both the small and the large specimens. Indeed, Table 3.45 shows that the coefficients of variation in the number of failures per bin amount from 0.29 to 0.38, whereas the coefficients of variation in the corresponding mean strength values per bin are much lower, i.e. from 0.03 to 0.06.

For the least-squares method, the estimation of the Weibull parameters ϑ'_0 and m'_0, as well as the coefficient of determination r^2, is presented in Table 3.46 (the estimator function according to Eq. (2.42) or Eq. (2.43)). For the method of maximum likelihood, the estimates of the Weibull parameters ϑ'_0 and m'_0 (Eq. (2.44) and (2.45)), as well as the corrected shape parameter m_{corr} according to Eq. (2.46) and (2.47) is given in Table 3.46. As could be expected, the influence of Eq. (2.42) or Eq. (2.43) is negligible and, due to the high number of specimens considered, m_{corr} is approximately equal to m'_0. In Table 3.46, the strength values corresponding to the failures at surface 0 and edge 1 for the smooth ground specimens and of the failures at surface 0 and 5 for the cut specimens have been eliminated.

Table 3.46: Estimation of the Weibull parameters.

Series	LSM Eq. (2.42)			LSM Eq. (2.43)			MLE		
	ϑ'_0 [MPa]	m'_0 [-]	r^2 [-]	ϑ'_0 [MPa]	m'_0 [-]	r^2 [-]	ϑ'_0 [MPa]	m'_0 [-]	m_{corr} [-]
N4-e2	62.2	14.5	0.94	62.3	13.2	0.96	62.2	14.2	13.5
N4-f2	53.7	12.3	0.88	53.9	10.7	0.83	53.1	17.7	16.7
N4-g2	68.8	13.8	0.98	69.0	12.3	0.96	68.7	15.2	14.4
N4-h2	60.5	14.0	0.85	60.7	12.2	0.81	59.9	21.0	20.0
C4-e2	72.7	11.0	0.97	72.9	9.7	0.96	72.4	12.7	12.0
C4-f2	60.6	21.9	0.81	60.7	19.3	0.82	60.7	18.1	16.9
C4-g2	61.1	11.4	0.96	61.3	10.1	0.94	61.0	11.9	11.3
C4-h2	56.7	10.3	0.92	56.9	9.2	0.95	56.7	10.8	10.1

The values in Table 3.46 do not account for the effect of the stress history. Indeed, as the small and the large specimens fail after different load durations, the strength values cannot be compared without correcting them.
To do so, the strength values of the small and the large specimens were converted to a reference time period of 60 s and also to a constant stress value (see the next two paragraphs).

To convert the strength values with the actual load duration to a reference time period of 60 s, Eq. (2.15) was applied:

$$\frac{\vartheta'_{0,60}}{\vartheta'_0} = \left(\frac{t_f}{60}\right)^{1/n} \tag{3.22}$$

$\vartheta'_{0,60}$ is the Weibull scale parameter corresponding to a reference period of 60 s (constant stress rate and corrected for the Hertzian line contact effect), ϑ'_0 is the tested value (constant stress rate and corrected for the Hertzian line contact effect) and n = 16 is a conservative estimate of the crack velocity parameter (see section 3.4.3).

To convert the strength value from a linearly increasing loading (constant stress rate) to a constant loading (constant stress), Mencik (1992) introduces a correcting factor, i.e. $(1/(n+1))^{1/n}$ = 0.838. This factor was validated by Vandebroek *et al.* (2013) and for ground specimens a deviation of only 0.6% was found.

After the elimination of the failures at surface 0 and edge 1 for the ground specimens and of the failures at surface 0 and 5 for the cut specimens and the stress corrosion corrections above, Table 3.46 resulted in Table 3.47. Also, for all series, the Weibull plots are presented in Figures D.1, D.3, D.5 and D.6 of Annex D (according to Eq. (2.42)). Also, the sample mean value and the sample coefficient of variation are provided (see Table 3.48).

Table 3.47: Estimation of the corrected Weibull parameters.

Series	LSM Eq. (2.42)			LSM Eq. (2.43)			MLE		
	ϑ'_0 [MPa]	m'_0 [-]	r^2 [-]	ϑ'_0 [MPa]	m'_0 [-]	r^2 [-]	ϑ'_0 [MPa]	m'_0 [-]	m_{corr} [-]
N4-e2	50.0	13.6	0.94	50.1	12.4	0.96	50.1	13.4	12.7
N4-f2	42.8	11.5	0.88	42.9	10.1	0.83	42.3	16.7	15.8
N4-f2*	42.5	20.3	0.99	42.6	18.1	0.99	42.6	20.0	18.9
N4-g2	55.7	12.9	0.98	55.9	11.5	0.96	55.7	14.2	13.5
N4-h2	48.6	13.2	0.85	48.8	11.5	0.81	48.1	19.8	18.8
N4-h2*	48.3	23.8	0.98	48.4	21.3	0.98	48.3	23.7	22.5
C4-e2	59.0	10.4	0.97	59.2	9.2	0.96	58.8	12.0	11.3
C4-f2	48.7	20.7	0.81	48.8	18.2	0.82	48.7	17.1	15.9
C4-g2	49.1	10.7	0.96	49.3	9.5	0.94	49.0	11.2	10.6
C4-h2	45.4	9.7	0.92	45.5	8.7	0.95	45.4	10.2	9.5

* after elimination of the outliers, one in series N4-f2 and one in series N4-h2 (see next)

Table 3.48: Estimation of the Weibull parameters.

series	SAMPLE	
	$\bar{x}$	V
	[MPa]	[-]
N4-e2	48.1	0.09
N4-f2	40.9	0.09
N4-f2*	41.5	0.06
N4-g2	53.6	0.09
N4-h2	46.7	0.08
N4-h2*	47.3	0.05
C4-e2	56.2	0.11
C4-f2	47.4	0.06
C4-g2	46.9	0.11
C4-h2	43.1	0.12

* after elimination of the outliers,
one in series N4-f2 and one in series N4-h2 (see next)

Based on Table 3.47, Table 3.49 presents the ratio of the estimated Weibull scale parameters (experimental values in the first column, application of Eq. (2.41) with the LSM according to Eq. (2.42) in the next columns). Similarly, Table 3.50 presents the ratio of the estimated Weibull scale parameters (experimental values, application of Eq. (2.41) with the LSM according to Eq. (2.43)). Finally, Table 3.51 presents the ratio of the estimated Weibull scale parameters (experimental values, application of Eq. (2.41) with the MLE). For the three methods, the ratios are calculated for m'_0 equal to the minimum, maximum and mean value for the specific series involved in the determination of the size effect (e.g. N4-e2/ N4-f2, N4-g2/ N4-h2, C4-e2/ C4-f2 etc.).
The error caused by the shift of the roller contact lines is not taken into account (Munz and Fett 1999). In case of large deflections, the inner roller contact lines shift outwards and the outer roller contact lines move inwards. The estimated error is about 0.4% for the small specimens and 0.3% for the large specimens (Munz and Fett 1999). However, while comparing the strength values of the small and large specimens in the current test programme, the relative error of only 0.1% is negligible.

The application of Eq. (2.41) in Tables 3.49, 3.50 and 3.51 implies that:

$$\left(\frac{L_{s,2}}{L_{s,1}}\right)^{1/m'_0} = \left(\frac{L_{s,small}}{L_{s,large}}\right)^{1/m'_0} = (0.5)^{1/m'_0} \tag{3.24}$$

Table 3.49: Estimation of the Weibull parameters with LSM using Eq. (2.42).

Series	Application of Eq. (2.43) with the LSM according to Eq.(2.42)						
	$\frac{\vartheta'_{exp,large}}{\vartheta'_{exp,small}}$	m_{min}	$(0.5)^{\frac{1}{m_{min}}}$	m_{max}	$(0.5)^{\frac{1}{m_{max}}}$	m_{mean}	$(0.5)^{\frac{1}{m_{mean}}}$
N4-e2/ N4-f2	0.86	11.5	0.94	13.6	0.95	12.6	0.95
N4-e2/ N4-f2*	0.85	13.6	0.95	20.3	0.97	16.9	0.96
N4-g2/ N4-h2	0.87	12.9	0.95	13.2	0.95	13.1	0.95
N4-g2/ N4-h2*	0.87	12.9	0.95	23.8	0.97	18.4	0.96
C4-e2/ C4-f2	0.83	10.4	0.94	20.7	0.97	15.5	0.96
C4-g2/ C4-h2	0.92	9.7	0.93	10.7	0.94	10.2	0.93

* after elimination of the outliers, one in series N4-f2 and one in series N4-h2

From Tables 3.49, 3.50 and 3.51, it can be observed that the approach in the literature with Eq. (2.41) is in most cases unsafe for the edge strength. Only for the series C4-g2/C4-h2, a conservative value was observed. The experimental ratio was up to 14% lower than the ratio according to Eq. (2.41), for the series N4-e2/N4-f2, N4-g2/N4-h2 and C4-e2/C4-f2. Series C4-g2/C4-h2 had a CUT 8 mm thick edge. The angle during cutting was 154° and the pressure 1.8 bar. As the angle and the pressure are quite high for common practice, the damage is larger than for the other series. This may explain why the strength values of the 8 mm cut specimens are lower than the corresponding values of the 4 mm cut specimens. For the 4 mm thick specimens, the angle (145°) and the pressure (0.9 bar) are common practice. The opposite is true for the GROUND specimens, where the 8 mm thick specimens are stronger than the 4 mm thick specimens. After grinding, one can assume that the damage caused by cutting has vanished. Consequently, the unsafe values of the ratio for the series N4-e2/N4-f2, N4-g2/N4-h2 and C4-e2/C4-f2 can be assumed to be the general rule and the series C4-g2/C4-h2 the exception.

It can be noticed that the reduction is hardly dependent of the followed method LSM Eq. (2.42), LSM Eq. (2.43) or MLE and of the type of edge finishing i.e. smooth ground or cut.

Table 3.50: Estimation of the Weibull parameters with LSM using Eq. (2.43).

Series	Application of Eq. (2.41) with the LSM according to Eq.(2.43)						
	$\frac{\vartheta'_{exp,large}}{\vartheta'_{exp,small}}$	m_{min}	$(0.5)^{\frac{1}{m_{min}}}$	m_{max}	$(0.5)^{\frac{1}{m_{max}}}$	m_{mean}	$(0.5)^{\frac{1}{m_{mean}}}$
N4-e2/ N4-f2	0.86	10.1	0.93	12.4	0.95	11.2	0.94
N4-e2/ N4-f2*	0.85	12.4	0.95	18.1	0.96	15.2	0.96
N4-g2/ N4-h2	0.87	11.5	0.94	11.5	0.94	11.5	0.94
N4-g2/ N4-h2*	0.87	11.5	0.94	21.3	0.97	16.4	0.96
C4-e2/ C4-f2	0.82	9.2	0.93	18.2	0.96	13.7	0.95
C4-g2/ C4-h2	0.92	8.7	0.92	9.5	0.93	9.1	0.93

* after elimination of the outliers, one in series N4-f2 and one in series N4-h2

Table 3.51: Estimation of the Weibull parameters with MLE.

Series	Application of Eq. (2.41) with the MLE						
	$\frac{\vartheta'_{exp,large}}{\vartheta'_{exp,small}}$	m_{min}	$(0.5)^{\frac{1}{m_{min}}}$	m_{max}	$(0.5)^{\frac{1}{m_{max}}}$	m_{mean}	$(0.5)^{\frac{1}{m_{mean}}}$
N4-e2/ N4-f2	0.85	12.7	0.95	15.8	0.96	14.2	0.95
N4-e2/ N4-f2*	0.85	12.7	0.95	18.9	0.96	15.8	0.96
N4-g2/ N4-h2	0.86	13.5	0.95	18.8	0.96	16.1	0.96
N4-g2/ N4-h2*	0.87	13.5	0.95	22.5	0.97	18.0	0.96
C4-e2/ C4-f2	0.83	11.3	0.94	15.9	0.96	13.6	0.95
C4-g2/ C4-h2	0.93	9.5	0.93	10.6	0.94	10.1	0.93

* after elimination of the outliers, one in series N4-f2 and one in series N4-h2

In Figures D.1 and D.3 of Annex D, for the large specimens, two statistical outliers (one in each Figure) can be noticed but could not be explained after observation of the specimens during and after testing. After elimination of these two results, the adapted values are also presented in Tables 3.47 to 3.51 and the corrected Weibull plots of series N4-f2 and N4-h2 are presented in Figures D.2 and D.4 (see Annex D), respectively. It can be noticed that the coefficient of determination r^2 for the series N4-f2 and N4-h2 increases considerably after elimination of the outliers. Only the coefficient of determination is much lower for the series C4-f2 compared to all the other series, which could be caused by the bi-linearity of the regression line (see Figure D.5 of Annex D).

The reduction in the strength based on the statistical approach of Eq. (2.41) is not satisfactory and other phenomena might be involved such as the effect of the absolute dimensions of the specimens (Veer and Riemslag 2009).

According to section 2.3.5, residual compressive stresses are common in as-received annealed glass. However, as the series which were compared in this study (for example series N4-e2 and N4-f2) originated from the same large 6 m * 3.21 m standard size float glass panel and were cut and processed at the same moment, the potential compressive stresses caused by manufacturing the plates or cutting and processing the specimens were the same for each two series which were compared to each other in this study. However, if series should originate from different manufacturers or should be processed at different moments or in different factories, this issue becomes very important.

E2431-12 (2012) provides curves for the reduction of the edge strength in function of the perimeter. According to Beason and Lingnell (2002; 2003), the underlying influence of the size on the curves is given by:

$$k_A = \left(\frac{L_{small}}{L_{large}}\right)^{1/7} = (0.5)^{1/7} = 0.91 \tag{3.24}$$

Thus, Eq. (3.24) according to Beason and Lingnell (2002; 2003), is also unsafe compared to the relevant edge strength test results (N4-e2/N4-f2, N4-g2/N4-h2 and C4-e2/C4-f2) presented in this study.

Finally, observing the relevant data of Tables 3.49, 3.50 and 3.51, the experimental strength reduction does not depend significantly on the Weibull shape parameter, which stands for the scatter of the results. Assuming the value of 0.25 instead of 1/7 according to Beason and Lingnell (2002; 2003) delivers a value of 0.84 for the value of k_A:

$$k_A = \left(\frac{L_{small}}{L_{large}}\right)^{0.25} = (0.5)^{0.25} = 0.84 \tag{3.25}$$

in which the coefficient of 0.25 is independent of the scatter of the data, analogue to the code E2431-12 (2012). This coefficient of 0.25 delivers a safe estimation of the size effect compared to the experimental data.

3.7.3 Conclusion

It can be concluded that the results of TP 5 demonstrate that there is a considerable size effect, which can only partly be explained by the theory described in the literature. The theoretical approach was up to 14% unsafe compared to the test results of this study. Possibly, larger specimens fail differently from smaller specimens (Veer and Riemslag 2009). However, the study was performed with only as-received glass. The results do not represent the performance of weathered glass or glass damaged during handling or transport or by other in-service events that induce further flaws on the glass edge surface.

3.8 TP 6: Influence of the stress distribution

The objective of this test programme was to assess the influence of the stress distribution along the considered element on the glass edge strength and to compare these experimental values with the probabilistic formulas available in the literature (Munz and Fett 1999; Wachtman *et al.* 2009; Haldimann 2006; Haldimann *et al.* 2008; Overend and Zammit 2012; Feldmann *et al.* 2014).

3.8.1 Materials and testing details

In this test programme, 8 series of beam specimens, with either smooth ground or cut edge finishing, a thickness of either 4 or 8 mm, and a length of 550 mm (see Table 3.53) were tested in a 4PB and a 3PB setup as described in section 3.2.3. All series were subjected to a linearly increased loading (constant stress rate of 2 MPa/s) until failure.

For this test programme, panels of 1100 mm * 250 mm with a thickness of 4 or 8 mm and either smooth ground or simple cut edges, were obtained from a qualified glass processor. During the machine cutting and grinding of the panels a strict protocol was applied. More specifically, the scoring of the specimens consistently occurred at the air side (i.e. the surface which is exposed to the atmosphere during the float process), which corresponds to location 2 according to Figure 3.10. Furthermore, the cutting wheel had an angle α_c of 145° (pressure of 0.6 bar) for the 4 mm specimens and 158° (pressure of 0.6 bar) for the 8 mm specimens. In addition, for the smooth ground specimens, the grinding was done with a diamond-grit disc (D151, D91, D64). The anris varied between 0.9 mm and 1.1 mm for the 4 mm thick specimens and between 1.2 mm and 1.4 mm for the 8 mm thick specimens (Figures 2.1 to 2.4). Finally, per glass thickness (4 or 8 mm) and per edge finishing (cut or smooth ground), all panels were processed on the same day with the same machine and the same processing parameters, from which one can assume the same flaw population between the series tested with a 4PB setup and a 3PB setup.

Subsequently, these panels were manually cut in to 8 different specimen series with final nominal specimen dimensions of 550 mm * 62.5 mm as indicated in Figure 3.29 (at the upper end) and listed in Tables 3.52 and 3.53. The specimens were cut such that the edge which was exposed to tensile stresses during the bending tests always corresponded to the machined cut or smooth ground edge

(instead of to the manually cut edge). Moreover, from one specific pane of 1100 mm * 250 mm, specimen 1 and 3 were tested in 4PB and specimen 2 and 4 were tested in 3PB (see Figure 3.29, at the upper end). Consequently, differences between the edge finishing of the different panels were excluded completely. All series were tested in identical laboratory conditions (the same stress corrosion parameters). In conclusion, the corresponding series which were tested in the 4PB setup and the 3PB setup, which are compared to each other, were tested in identical environmental conditions and had the same flaw population.

Table 3.52: overview of the specimen sizes of TP 6.

specimen size	nominal thickness *b* [mm]	nominal height *h* [mm]	nominal specimen length L_t [mm]	nominal support span *L* [mm]
e	4	62.5	550	500
g	8	62.5	550	500

Table 3.53: overview of the test series of TP 6.

series	thickness [mm]	Bending setup 4PB or 3PB	number of specimens
N5-e2	4	4PB	33
N5-e9	4	3PB	36
N5-g2	8	4PB	31
N5-g9	8	3PB	35
C5-e2	4	4PB	32
C5-e9	4	3PB	34
C5-g2	8	4PB	32
C5-g9	8	3PB	35

The load span L_s was 250 mm for the 4PB setup (see Figure 3.2). The specimens for the 4PB test were loaded at a constant stress rate of 2 $\pm$ 0.06 MPa/s. The small variation in stress rate of 0.06 MPa/s, due to the variability in specimen height in one series, stays well within the allowable variation of 0.4 MPa/s according to the standard EN1288-3 (2000). The specimens for the 3PB test were loaded at a constant stress rate of 2 MPa/s, assumed that the mean location of the failures should be at 30 mm away from the centre of the beam. After testing and determining the failure locations, this mean value was 14 mm, 17 mm, 18 mm and 18 mm instead of 30 mm for the series N5-e9, N5-g9, C5-e9,and C5-g9, respectively. Consequently, a correction for the strength values had to be made according to Eq. (2.15), which delivered a correction factor of 0.995 for the series N5 and 0.996 for the series C5.

At least 30 days elapsed between processing the edge (i.e. the machined edge) and testing the specimens (i.e. the machined edge). During the 7 days before testing, the specimens were kept at a temperature of 20°C $\pm$ 2°C and a relative humidity of 65% $\pm$ 4%, the same as the test conditions.

3.8.2 Results and discussion

After eliminating the out-of-load-span failures (21 out of 268 specimens), 247 valid specimens remained. An overview of the test series is given in Table 3.53. A picture of a failed specimen in the 4PB test and the 3PB test is provided in Annex B (see Figure B.37 and B.38).

According to the literature (Munz and Fett 1999; Wachtman *et al.* 2009; Haldimann 2006; Haldimann *et al.* 2008; Overend and Zammit 2012; Feldmann *et al.* 2014), a non-uniform stress distribution has the same effect as an equivalent uniform stress distribution when:

$$\int_A \sigma^{m'0} .dA = A.\sigma_{eq}^{m'0} \tag{3.26}$$

or

$$\sigma_{eq} = (\frac{1}{A}. \int_A \sigma^{m'0} .dA)^{1/m'0} \tag{3.27}$$

where A is the stressed area of the element.

In this test programme the strength values were first corrected according to Eq. (3.3) and Eq. (3.6). Then, the cross-sectional locations were examined. It was observed that the majority of the failures occurred at locations 2 and 3 (see Figures 3.9 and 3.10). After elimination of the failures for which the origin could not be determined, because of the damage after failure, the number of failure locations at position 2 and 3 are presented in Table 3.54. As the series C5-e2 had only 2 failures at location 2, no reliable conclusion can be made from this series.

The sample mean strength values and the corresponding standard deviation and coefficient of variation are provided in Table 3.55. It was noticed that the coefficient of variation *V* was significantly higher for the failure location 3 than for the location 2. Next, the ratio of the sample mean value of the 3PB and the 4P bending test was presented in Table 3.56. It was noticed that the ratio for series C5-e9/C5-e2 i.e. 1.82 was not reliable as explained before. For the smooth ground specimens, the experimental ratio was very similar for the failure locations 2 and 3. However, for the cut specimens of series C5-g9/C5-g2, the ratio was very different for the failure locations 2 and 3.

Table 3.54: overview of the failure locations 2 and 3 of TP 6.

series	number of specimens	failures at location 2 or 3	failures at location 2	failures at location 3
N5-e2	33	19	6	13
N5-e9	36	34	7	27
N5-g2	31	20	6	14
N5-g9	35	30	10	20
C5-e2	32	19	2	17
C5-e9	34	26	16	10
C5-g2	32	17	9	8
C5-g9	35	34	25	9

Table 3.55: location and corresponding strength values.

series	strength values location 2			strength values location 3		
	$\bar{x}$	s	V	$\bar{x}$	s	V
	[MPa]	[MPa]	[-]	[MPa]	[MPa]	[-]
N5-e2	65.6	5.2	0.08	60.9	8.1	0.13
N5-e9	69.4	4.7	0.07	65.1	8.9	0.14
N5-g2	63.8	5.0	0.08	57.9	9.5	0.16
N5-g9	62.5	6.7	0.11	56.5	11.0	0.19
C5-e2	49.9	4.8	0.10	69.6	16.0	0.23
C5-e9	90.8	14.8	0.16	66.6	13.1	0.20
C5-g2	66.3	9.1	0.14	62.3	8.9	0.14
C5-g9	73.2	9.0	0.12	59.2	12.6	0.21

Table 3.56: ratio of strength values of the 3PB and the 4PB test.

series	ratio strength values 3PB/4PB location 2		ratio strength values 3PB/4PB location 3	
	experiment	Eq. (3.27)	experiment	Eq. (3.27)
	[-]	[-]	[-]	[-]
N5-e9/N5-e2	1.06	1.16	1.07	1.21
N5-g9/N5-g2	0.98	1.18	0.98	1.23
C5-e9/C5-e2	**1.82**	1.25	0.96	1.25
C5-g9/C5-g2	1.10	1.23	0.95	1.26

Table 3.57: Weibull shape parameters for the failure locations 2 and 3 for the 3PB test.

series	location 2	location 3
	m'_0	m'_0
	[-]	[-]
N5-e9	13.26	7.83
N5-g9	9.92	6.06
C5-e9	4.96	5.06
C5-g9	6.33	4.28

Next, Eq. (3.27) was applied to the sample mean strength value of the 3PB test. For that, the strength values were fitted to the Weibull distribution to estimate the Weibull shape parameter, presented in Table 3.57.

Table 3.57 shows that the Weibull shape parameter is significantly lower for the cut specimens compared to the smooth ground specimens. From these shape parameters, Eq. (3.27) was applied over the central area of 250 mm. The theoretical ratio of the 3PB strength to the 4PB strength is provided in Table 3.56. It can be concluded that the application of Eq. (3.27) is unsafe compared to the experimental data. The difference ranges from 9% to 33%, if series C5-e9/C5-e2 (location 2) is disregarded.

The experiments should be repeated on specimens with a larger load span. In this study, the failure locations were concentrated in the central 200 mm for the 4PB tests and in the central 50 mm for the 3PB tests. Indeed, also in TP 2, no size effect was noticed between the small specimens (load span of 40 mm or 60 mm) and the large specimens (load span of 200 mm).

In this TP, the strength values were not corrected regarding the influence of stress corrosion, as the strength values of the 3PB and the 4PB tests were very similar, and thus the ratio would not change significantly.

3.8.3 Conclusion

It can be concluded that the relevant data indicate that the stress distribution in the 3PB test does not increase the strength values according to Eq. (3.27) and that this equation cannot be applied for the estimation of the thermal stresses (see chapter 4). However, more experiments are needed to investigate this issue thoroughly, as the series with the cut edge finishing are not statistically reliable enough. Also, the tests should be repeated with larger specimens (load span of 500 mm instead of 250 mm for the 4PB tests).

3.9 Highlights of this chapter

3.9.1 Temperature test, bending test and analysis

- The procedures for the temperature testing and bending testing, applied for this study, are explained.
- From the test data, characteristic values were determined according to the Coverage Method with a confidence level γ of 0.75 for infill panels.

3.9.2 Correlation temperature tests and bending tests

- A very good correlation was found between failure stresses induced by temperature loading and by mechanical loading.
- Consequently, the testing to estimate the influence of the stress corrosion, the load history, the size and stress distribution could be executed with a bending setup, which was considerably less time-consuming.

3.9.3 Stress corrosion tests

- It can be concluded that the edge strength values of the specimens for a specific edge finishing were mostly independent of the cross-sectional failure location or the longitudinal failure location, although some locations showed significantly more failures than other locations.
- The experimental determined value of the stress corrosion parameter n corresponded well to the values, found in literature.
- Also, the characteristic and design edge strength values were comparable to those found in literature and standards.
- The strength values found by testing beams of 100 mm or 150 mm length were similar to those of beams of 500 mm length, and consequently, the influence of the load history could be performed with the small beam sizes.

3.9.4 Influence of the load history

- The influence of a load history, similar to the thermal stress history of an actual pane was simulated in the 4PB test setup.
- For a constant load history, the theoretical approach from literature was very accurate.
- For a cyclic constant stress history, the theoretical approach considering the number of cycles involved was about 6% too conservative. Consequently, the crack healing effect amounted to 6%.
- For the cut edge finishing, the time between two cycle sequences, 5 seconds or 1 week, had no influence on the crack healing. More experiments with different edge finishings must be performed to generalize this conclusion.

3.9.5 Influence of the size

- The test results demonstrate that there is a considerable size effect for the edge strength of glass. For design purposes, one should take this effect into account in a conservative way.
- This effect was assessed on a theoretical basis according to the literature. However, the theoretical approach is not safe enough when applying it to the current test results. More specifically, the experimental results showed that the actual reduction in strength was 14% larger than the predicted strength reduction according to the theoretical approach in literature. Possibly, larger specimens fail differently from smaller specimens. More research is needed to clarify this.
- E2431-12 (2012) estimates the size effect, although in an unsafe way. The relevant results of this study showed that the reduction in strength was 9% larger compared to the reduction proposed in the standard E2431-12 (2012).
- Eq. (3.25) is proposed as a safe estimation of the size effect for the edge strength of glass.

3.9.6 Influence of the stress distribution

- It can be concluded that for the smooth ground edge finishing the stress distribution (4PB or 3PB) has almost no influence on the experimental strength values. However, for the cut edge finishing, the scored side of the pane showed an influence of the stress distribution on the experimental strength values whereas the other side did not.
- The theoretical approach in literature is an unsafe approach compared to the experimental data of this test programme. However, more experiments are needed to investigate this issue thoroughly.

4. Numerical investigations

In this age of specialization men who thoroughly know one field are often incompetent to discuss another. The great problems of the relations between one and another aspect of human activity have for this reason been discussed less and less in public. When we look at the past great debates on these subjects we feel jealous of those times, for we should have liked the excitement of such argument. The old problems, such as the relation of science and religion, are still with us, and I believe present as difficult dilemmas as ever, but they are not often publicly discussed because of the limitations of specialization.

Richard Feynman (1918-1988)

4.1 Introduction

In this section, the calculation method of the thermal stresses for a double skin façade is presented. First, the temperature gradients were calculated with a transient finite element programme, starting from real climate data (section 4.2.1). Second, the stresses due to these gradients were estimated with another finite element programme (section 4.2.2). Finally, the ultimate limit state method according to EN1990 (2002) is presented (section 4.2.3). The maximum stress method and the equivalent lifetime stress method are described. The first method does not account for damage accumulation, while the latter takes into account the influence of reloading during the lifetime of the pane. For the calculations of the design strength values and design stress values, the results of chapter 3 (TP 2 to TP6) were used. A flow chart of the procedure is presented in Figure E.1 (see annex E).

4.2 Method

4.2.1 Action model

The examined double skin façade was chosen in dialogue with an industrial partner and is depicted in Figure 4.1 (horizontal section). At the interior, the insulating glass unit (IGU) is composed of an inner laminated pane 44.2 PVB (reflectance: ρ_s = 0.069, transmittance: τ_s = 0.795) and a single outer 8 mm pane (ρ_s = 0.069, τ_s = 0.795), connected by a stainless steel spacer. The 15 mm thick sealed space is filled with air. On position 3 (Figure 4.2) a low-E coating (emissivity: ε = 0.04) was applied.
Between the IGU and the additional pane of 6 mm (ρ_s = 0.069, τ_s = 0.795), there is a cavity of 105 mm (Figure 4.1), which is not ventilated, but in which a dry air supply prevents condensation (Closed Cavity Façade or CCF). The additional pane is adhesively bonded to the aluminium frame. The width of the window is 1000 mm (see Figure 4.1, the left and right side looking from the exterior side is marked). All panes are smooth ground.
The thermal analysis programme Bistra (Physibel 2011) used in this study is a transient two-dimensional programme which calculates the heat transfer in two-dimensional free form objects. The time-dependent boundary conditions are described with external real climate functions (for an example, see Figures E.2 and E.3 of Annex E). The programme contains a solar processor based on direct and diffuse radiation climate files. Radiation, convection and conduction are calculated separately.

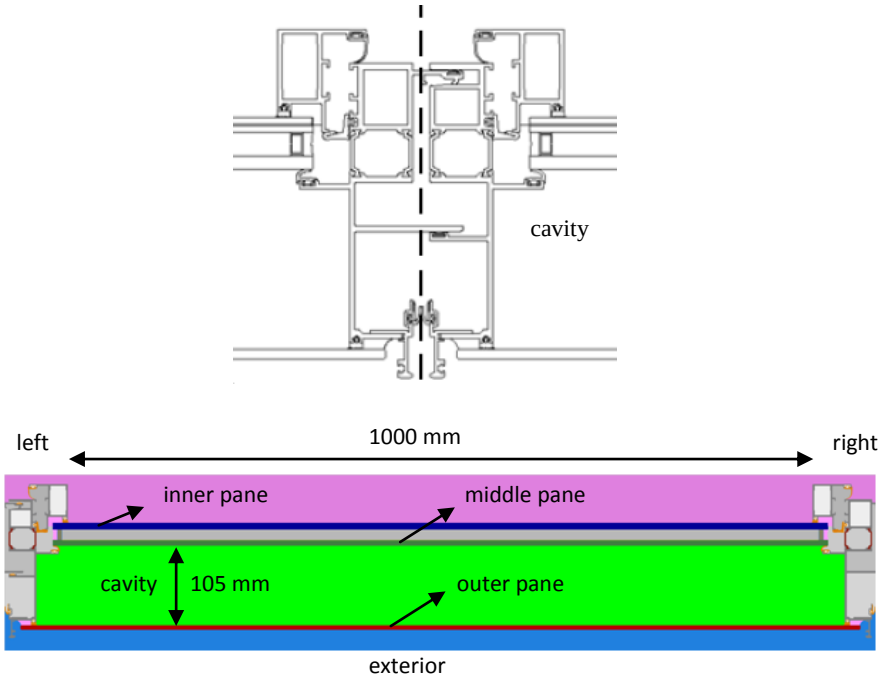

Figure 4.1: Schematic view of the double skin façade (horizontal section, every material has a colour code) (Vanden Poel 2010; Balcaen 2013).

First, the frame was simplified to reduce the calculation time as the temperature gradients were calculated over the lifetime of the glass construction (twenty years). This simplification was performed in a way that the heat flux through and the temperature change in the frame did not change significantly (see Figure 4.2; Vanden Poel 2010). Then, the temperature at every point of the three panes during the lifetime of the pane was calculated. The calculation was performed for different locations, orientations of the façade and different twenty-year periods, with the real climate data functions of the location (for an example, see Figures E.2 and E.3 of Annex E). First, the horizontal section with a south orientation at Maastricht during the time period 1991-2010 was simulated (basic case, see section 4.3). Then, the same configuration was treated but for the period 1971-1990 or for another location, i.e. Leeuwarden (see section 4.4). The location Maastricht was chosen as it is situated close to France, to compare the results with the results using the climatic data of the French standard NF P 78-201-1/A1(DTU39) (1998). Next, the horizontal section with an east orientation at Maastricht for the time period 1991-2010 was investigated (see section 4.4). Finally, the vertical section was simulated with a south and east

orientation at Maastricht for the time period 1991-2010 (see section 4.6). The indicated orientations were chosen as the west and the north orientation were not relevant and the time frames were chosen as the climatic data were available.

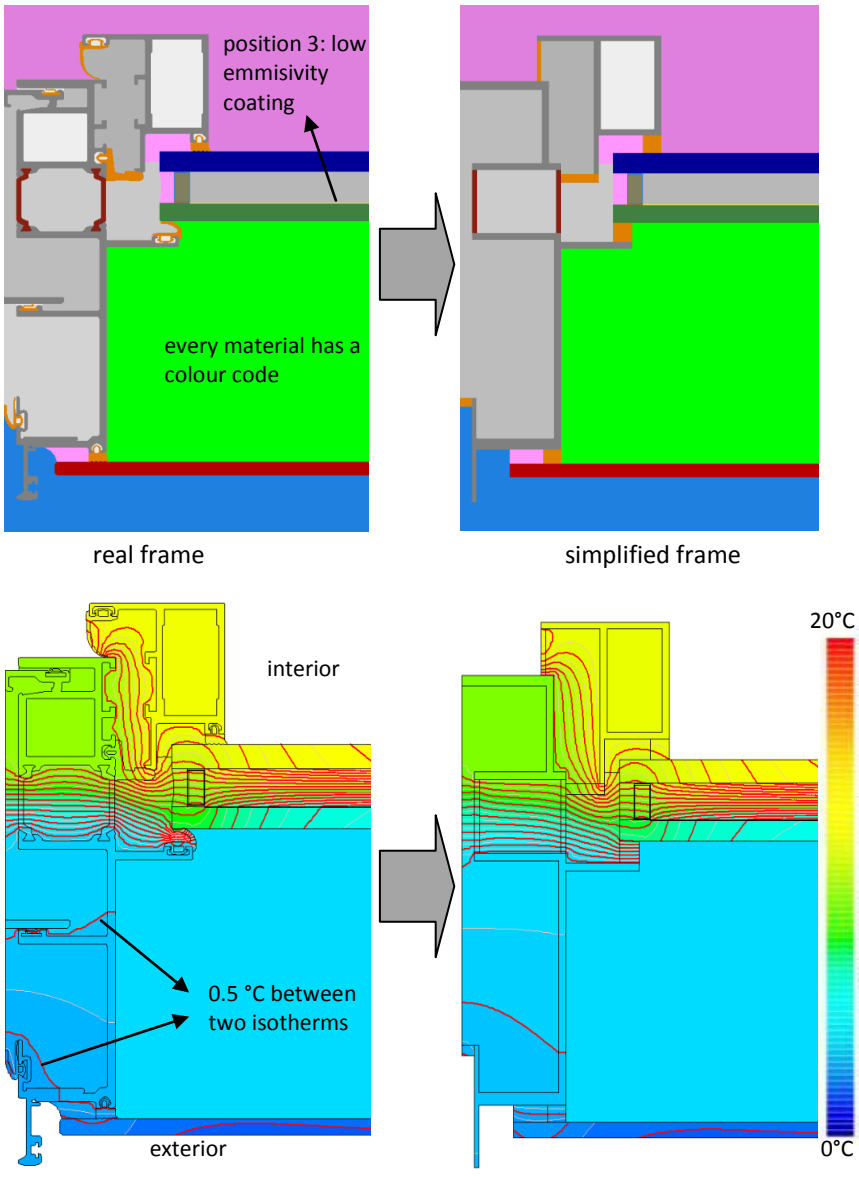

Figure 4.2: Simplification of the frame for the thermal analysis in Bistra (Vanden Poel 2010; Balcaen 2013).

4.2.2 Structural model

Next, the output of the finite element programme Bistra was used to calculate the stresses at the edge of the panes. This was performed with the finite element programme Abaqus (DS Simulia 2010). The grid for the stress calculation was 10 mm (see Figure 4.3, right side). This calculation resulted in the thermal stress history at the edge of the three glass panes over a period of twenty years (intended lifetime of the panes).

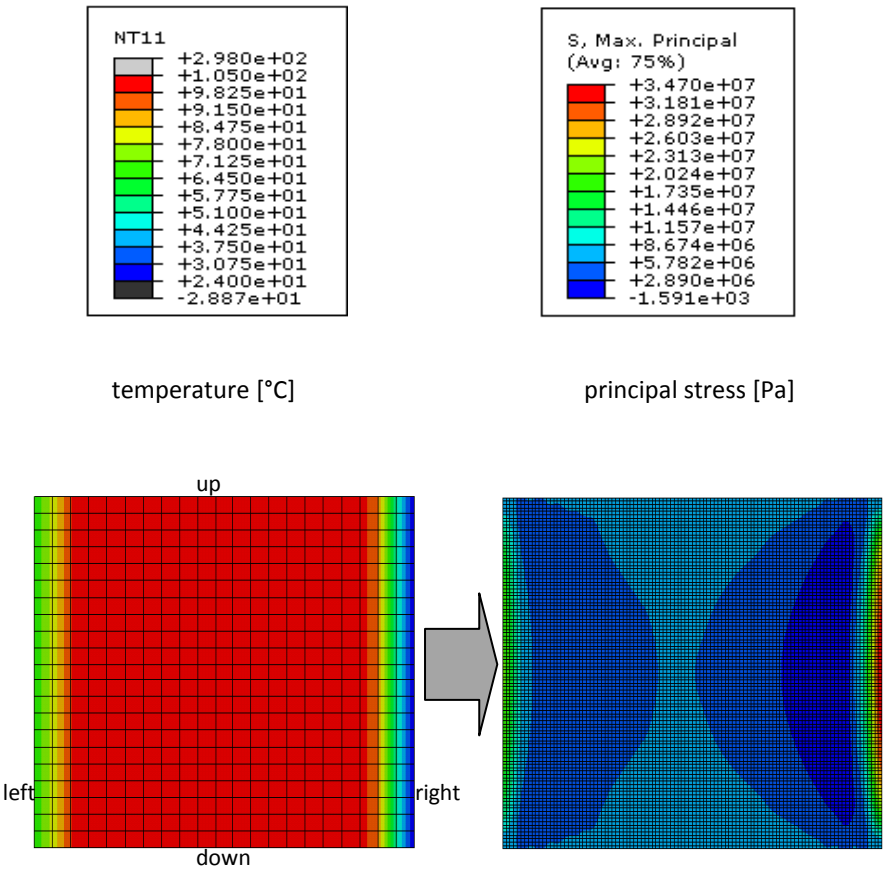

Figure 4.3: Input temperature history and output thermal stress history in Abaqus (of which one critical time step is depicted, Vansteenbrugge 2012) on a 1000 mm by 1000 mm glass panel.

4.2.3 Ultimate limit state method

Maximum stress method

The calculated stress history during the lifetime of the panes (section 4.2.2) was simulated. From this stress history, the maximum yearly values were selected. Then, the yearly maximum equivalent constant stress $\sigma_{eq,yearly}$ was derived from Eq. (2.12) after substitution of $\sigma_{n1}(t) = \sigma_{eq,yearly}$:

$$\sigma_{eq,yearly} = \left(\frac{1}{t_{f2} - t_{th}} . \int_{t_{th}}^{t_{f2}} \sigma_{n2}^{n}(t).dt\right)^{1/n} \quad (4.1)$$

The integration was performed for values of $K_I > K_{th}$, K_{th} being the crack growth threshold (Fink 2000; Haldimann 2006; Haldimann *et al.* 2008). Thus, the value of $t = t_{th}$ corresponds to the moment where $\sigma_{n2}(t)$ equals the threshold stress and the value of t_{f2} corresponds to the moment where the stress reaches its maximum value (Overend & Zammit 2012).

The partial safety coefficient for the material glass was considered: γ_M = 1.8 (prEN 16612 2013; DIN 18008-1 2010). This coefficient was used for the calculation of the threshold stress (section 4.3.3).

The partial safety coefficient for the stress at the edge was taken equal to γ_F = 1.1 (prEN 16612 2013) for infill panels (class of consequence lower than CC1).

Consequently, the yearly maximum equivalent constant design stress $\sigma_{d,eq,yearly}$ equals:

$$\sigma_{d,eq,yearly} = \gamma_F * \sigma_{eq,yearly} = 1.1 * \sigma_{eq,yearly} \quad (4.2)$$

The 20 yearly maximum equivalent design stress values $\sigma_{d,eq,yearly}$ were fitted to a Gumbel distribution to estimate the characteristic 5% maximum value $\sigma_{d,5\%,eq,yearly}$.
During the calculations, both the stress and strength values were considered for a load duration of 3600 s by applying Eq. (2.15). In that case, stress and strength values were compared correctly.

Finally, the stress value $\sigma_{d,5\%,eq,yearly}$ was compared to the design strength value f_d , according to the German standard (DIN 18008-1 2010) and the experimental values (see section 3.4).

Equivalent lifetime stress method

Considering the calculated lifetime stress history of the panes, the equivalent lifetime constant stress $\sigma_{eq,lifetime}$ was derived from Eq. (2.12) after substitution of $\sigma_{n1}(t) = \sigma_{eq,lifetime}$:

$$\sigma_{eq,lifetime} = \left(\frac{1}{\Sigma(t_{th,2} - t_{th,1})} \cdot \int_{t_{th,1}}^{t_{th,2}} \sigma_{n2}^{n}(t).dt\right)^{1/n} \tag{4.3}$$

The integration was performed for values of $K_I > K_{th}$, K_{th} being the crack growth threshold (Fink 2000; Haldimann 2006; Haldimann *et al.* 2008). Thus, the value of $t = t_{th,1}$ corresponds to every moment during the lifetime where $\sigma_{n2}(t)$ equals the threshold stress and the value of $t = t_{th,2}$ corresponds to every moment where the stress reaches again the threshold stress (Overend & Zammit 2012). In between two moments of threshold stress, a maximum value is reached.

However, the partial safety coefficient for the stress (effect of the actions) at the edge was taken equal to: $\gamma_F = 1.05$. Indeed, in section 4.4, the stress history was calculated during two twenty-year periods, i.e. 1971-1990 and 1991-2010 and the difference in $\sigma_{eq,lifetime}$ was less than 5% (about 2%). In the future, this coefficient has to be determined more precisely by comparing several twenty-year periods.

Consequently, the equivalent lifetime constant design stress $\sigma_{d,eq,lifetime}$ equals:

$$\sigma_{d,eq,lifetime} = \gamma_F * \sigma_{eq,lifetime} = 1.05 * \sigma_{eq,lifetime} \tag{4.4}$$

During the calculations, both the stress and strength values were considered for a load duration of 3600 s by applying Eq. (2.15). In that case, stress and strength values were compared correctly.

Finally, the stress value $\sigma_{d,eq,lifetime}$ was compared to the design strength value f'_d, according to the German standard (DIN 18008-1 2010) and the experimental values (section 3.4), but for this method the strength increase due to crack healing was considered (sections 3.5 and 3.6).

4.3 Results: basic case (south orientation and horizontal section)

4.3.1 Temperature gradient results

The model described in section 4.2.1 was used to perform calculations over a twenty-year period from 1991 to 2010 at a location in The Netherlands (Maastricht). The double skin façade was oriented to the south. This configuration is referred to as 'basic case'. The outcome of these simulations was the temperature history over the total area of the different panes in the investigated configuration.

4.3.2 Thermal stress history

The output of the simulations of section 4.3.1 was used as input for the simulation of the model as described in section 4.2.2, which resulted in the thermal stress history of the three panes. Only the stress history at the middle pane was relevant for further analysis, as the stresses at the edges of the other panes were smaller than the threshold stress $\sigma_{d,th}$ (see Table 4.1).

4.3.3 Ultimate limit state verification

For the maximum stress verification and equivalent stress verification, section 4.2.3 was applied with the values of $\sigma_{d,th}$ according to Table 4.1. The calculations were executed with the stress corrosion parameter n = 16 or n = 18.1 corresponding to 100% RH and 50% RH, respectively (Charles 1958; Blank 1993; Shen 1997; Fink 2000; Wörner 2001). The 5% characteristic strength value of the German standard DIN 18008-1 (2010) $f'_{eg,k}$ = 36 MPa (Siebert and Seel 2011) or the experimental value from Table 3.12 for the smooth ground edge finishing $f'_{eg,k}$ = 47 MPa (section 3.4) were considered.

Table 4.1: values of $\sigma_{d,th}$.

	n = 16	n = 18.1
$f'_{eg,k}$ [MPa]	$\sigma_{d,th}$ [MPa]	$\sigma_{d,th}$ [MPa]
36	5.34	5.62
47	7.09	7.44

Table 4.2: simulated stresses and strength values [MPa] (horizontal section directed to the south orientation), the ratios in bold are non-dimensional and ΔT in °C.

	$f'_{eg,k}$ = 36 MPa				$f'_{eg,k}$ = 47 MPa			
$\sigma_{d,eq,yearly}$	n=16		n=18.1		n=16		n=18.1	
year	left	right	left	right	left	right	left	right
1991	7.6	9.4	7.6	9.4	7.5	9.4	7.5	9.4
1992	6.3	8.9	6.3	8.9	-	8.9	-	8.9
1993	6.2	8.5	6.2	8.5	-	8.5	-	8.5
1994	8.2	10.7	8.2	10.7	8.2	10.6	8.2	10.7
1995	9.2	11.3	9.3	11.4	9.2	11.3	9.3	11.4
1996	9.4	12.8	9.4	12.9	9.4	12.8	9.4	12.9
1997	6.8	8.3	6.8	8.3	-	8.3	-	8.3
1998	9.2	13.5	9.2	13.6	9.2	13.5	9.2	13.6
1999	6.7	8.5	6.7	8.5	-	8.5	-	8.5
2000	7.8	11.0	7.8	11.0	7.8	11.0	7.7	11.1
2001	6.6	9.1	6.6	9.1	-	9.1	-	9.1
2002	7.8	11.2	7.8	11.2	7.8	11.2	7.8	11.2
2003	6.9	8.6	7.0	8.6	-	8.6	-	8.6
2004	7.7	9.2	7.7	9.2	7.7	9.2	7.7	9.2
2005	6.9	9.0	7.0	9.0	6.6	9.0	-	9.0
2006	6.6	9.0	6.6	9.0	-	9.0	-	9.0
2007	7.1	9.7	7.1	9.8	7.0	9.7	-	9.8
2008	8.9	13.1	8.9	13.1	8.9	13.1	8.9	13.1
2009	7.8	9.7	7.9	9.8	7.8	9.8	7.8	9.8
2010	8.5	10.7	8.8	10.7	8.8	10.7	8.8	10.7
$\sigma_{d,5\%,eq,yearly}$	9.5	13.1	9.6	13.2	9.8	13.1	9.8	13.2
f_d	10.0	10.0	10.5	10.5	13.3	13.3	14.0	14.0
$r_1=\sigma_{d,5\%,eq,yearly} / f_d$	**0.95**	**1.31**	**0.91**	**1.25**	**0.74**	**0.99**	**0.70**	**0.94**
$\sigma_{d,eq,lifetime}$	10.3	14.1	10.0	13.9	10.1	14.1	9.9	13.9
$f'_d = 1.06 * f_d$	10.6	10.6	11.2	11.2	14.1	14.1	14.8	14.8
$r_2=\sigma_{d,eq,lifetime} / f'_d$	**0.97**	**1.33**	**0.89**	**1.25**	**0.72**	**1.00**	**0.67**	**0.94**
r_2/r_1	**1.02**	**1.02**	**0.99**	**1.00**	**0.97**	**1.02**	**0.96**	**1.00**
$\sigma_{d,eq,NF}$	8.8	8.3	8.8	8.3	8.8	8.3	8.8	8.3
f_d	10.0	10.0	10.5	10.5	13.3	13.3	14.0	14.0
$r_3=\sigma_{d,eq,NF} / f_d$	**0.88**	**0.83**	**0.83**	**0.79**	**0.66**	**0.63**	**0.63**	**0.60**
ΔT (°C)	14.5	13.4	14.5	13.4	14.5	13.4	14.5	13.4
$\sigma_{\Delta T,NF}$	8.5	7.8	8.5	7.8	8.5	7.8	8.5	7.8
f_{NF}	24.0	24.0	24.0	24.0	24.0	24.0	24.0	24.0
$r_4=\sigma_{\Delta T,NF} / f_{NF}$	**0.35**	**0.33**	**0.35**	**0.33**	**0.35**	**0.33**	**0.35**	**0.33**

The yearly maximum equivalent constant design stress values $\sigma_{d,eq,yearly}$ [MPa] are presented in Table 4.2 for every year from 1991 to 2010 (for the different values of $f'_{eg,k}$ and n according to Table 4.1). At the left side (of the pane) for $f'_{eg,k}$ = 47 MPa, the value of $\sigma_{d,eq,yearly}$ was lower than the corresponding value of the threshold stress during several years (no value is presented in the column).

Then these 20 design stress values were fitted to the Gumbel maximum distribution and the 5% maximum value $\sigma_{d,5\%,eq,yearly}$ was calculated (see Table 4.2). Next, the equivalent lifetime constant design stress $\sigma_{d,eq,lifetime}$ was calculated according to section 4.2.3 (see Table 4.2).

The stress values $\sigma_{d,5\%,eq,yearly}$ and $\sigma_{d,eq,lifetime}$ were compared with the strength values f_d (without crack healing) and f'_d (with crack healing), respectively. Concerning the strength increase due to the crack healing, the value of 6% was assumed according to the conclusions of section 3.5.

The design strength value f_d was calculated with Eq. (4.5):

$$f_d = \frac{f'_{eg,k} * k_{mod} * k_A}{\gamma_M} \tag{4.5}$$

with k_{mod} equal to:

$$k_{mod} = (1/(n+1))^{1/n} . (\frac{f'_{eg,k}/2\,\mathrm{MPa/s}}{3600\,\mathrm{s}})^{1/n} \tag{4.6}$$

The first part of Eq. (4.6) corrects the load history from a constant stress rate of 2 MPa/s (testing according to DIN18008-1 2010 or TP2 of this study) to a constant stress history, as the stresses are also calculated as constant stresses. This correction was validated in section 3.5 and the deviation was only 0.1%. The value of 3600 s in Eq. (4.6) was chosen as the mean value of the actual load duration (FE simulations) was close to this value. Also E2431-12 (2012) considers a load duration of 3600 s. The same value of 3600 s was chosen for the calculation of the stress and strength values to compare them correctly (see section 4.2.3).
For k_A the value of 0.84 was chosen, according to Eq. (3.25) of section 3.7. The value of γ_M was taken equal to 1.8 according to DIN 18008-1 (2010) or prEN 16612 (2013).
Eq. (4.5) yields values of the strength f_d which are presented in Table 4.3. The values of f'_d = 1.06 f_d are provided in Table 4.3 as well.

Table 4.3: values of f_d and f'_d.

	n = 16	n = 18.1	n = 16	n = 18.1
$f'_{eg,k}$ [MPa]	f_d [MPa]	f_d [MPa]	f'_d [MPa]	f'_d [MPa]
36	10.0	10.5	10.6	11.2
47	13.3	14.0	14.1	14.8

Next, the ratios $r_1 = \sigma_{d,5\%,eq,yearly} / f_d$ and $r_2 = \sigma_{d,eq,lifetime} / f'_d$ were calculated and presented in Table 4.2. These ratios indicate the degree of utilization of the strength. Also, the ratio r_2/r_1 was calculated, indicating which method is more conservative.
It can be noticed that there is a considerable difference between the stresses at the left side and the right side of the pane. There are small deviations between the values for n = 16 (100% RH) and n = 18.1 (50% RH). The left side with $f'_{eg,k}$ = 47 MPa is not considered as the stress in this case is below the threshold stress during half the lifetime and thus not relevant (see Table 4.2).
For the right side, which determines the risk of thermal fracture, the value of r_2/r_1 varies between 1.00 (50% RH) and 1.02 (100% RH), which means that the equivalent lifetime stress method is little more conservative than the maximum stress method for the investigated configuration.

Next, the climate data of NF P 78-201-1/A1(DTU39) (1998), extrapolated to the site 'Maastricht' were considered and the maximum equivalent constant stress $\sigma_{d,eq,NF}$ was calculated (Vansteenbrugge 2012). Also the ratio $r_3 = \sigma_{d,eq,NF} / f_d$ was calculated and presented in Table 4.2. The subscript *NF* indicates the French standard NF P 78-201-1/A1(DTU39) (1998).
Finally, the method of NF P 78-201-1/A1(DTU39) (1998) was applied, although the standard is not applicable for double skin façades. The temperature gradient ΔT from the finite element simulation was used to calculate the stress according to the standard NF P 78-201-1/A1(DTU39) (1998):

$$\sigma_{\Delta T,NF} = k_t . E.\alpha.\Delta T \tag{4.7}$$

where k_t = 0.9 for the aluminium frame of this configuration; E = 72000 MPa (module of elasticity) and $\alpha = 9.10^{-6}$ °C^{-1} (dilatation coefficient).
The allowable stress according to NF P 78-201-1/A1(DTU39) (1998) is equal to
f_{NF} = 1.2 * 20 MPa = 24 MPa
The values of $\sigma_{\Delta T,NF}$ and $r_4 = \sigma_{\Delta T,NF} / f_{NF}$ are presented in Table 4.2.

The ratio r_3 is considerably lower and the ratio r_4 is much lower than the ratios r_1 and r_2, which indicates that the method, calculating with the actual climate data is more conservative than the calculation with the climate data of the French standard or much more conservative than the method of the French standard NF P 78-201-1/A1(DTU39) (1998).

The cause of the very large difference between r_3 and r_4 can be found in the high allowable strength value (24 MPa) according to the standard NF P 78-201-1/A1(DTU39) (1998), as the values of $\sigma_{d,eq,NF}$ and $\sigma_{\Delta T,NF}$ are almost equal. The design strength according to E2431-12 (2012) for a pane with a perimeter of 4 m is equal to 12.7 MPa, 9.4 MPa and 6.8 MPa for a probability of failure of 0.008, 0.001 and 0.0001, respectively. Assuming a probability of failure of 0.008 delivers a design strength of 12.7 MPa, which is comparable to the design strength values f_d of Table 4.3. These values are much lower than the strength value of 24 MPa according to the standard NF P 78-201-1/A1(DTU39) (1998).

Comparing the ratio r_3 to the ratio r_1, indicates that for the left side, the difference is much smaller than for the right side. The climate data of the standard NF P 78-201-1/A1(DTU39) (1998) do not seem to induce the same stress values at the right side of the frame, compared to the real climate data.
Both transient calculations were compared for the left and the right side of the pane and presented in Figures 4.4 and 4.5.
On the horizontal axis, the time of the day is depicted in hours. The global radiation on a horizontal plane (after division by 10) is presented on the vertical axis, as well as the temperature and the stress history. The maximum stresses according to the standard NF P 78-201-1/A1(DTU39) (1998) occurred for both sides during the autumn. These maximum stresses amounted to 8.3 MPa and 7.9 MPa for the left and the rights side, respectively. Based on the real climate data, the maximum stress at the left side occurred at day 361 of 1996 and at the right side at day 325 of 1998. The corresponding global radiation values on a horizontal plane amounted to 383 W/m² and 467 W/m² and the corresponding maximum stresses to 8.9 MPa and 12.8 MPa. It is also noticed that at the right side, the maximum stress occurs a few hours earlier. In conclusion, this comparison demonstrates the important influence of the global radiation, more than the temperature history.

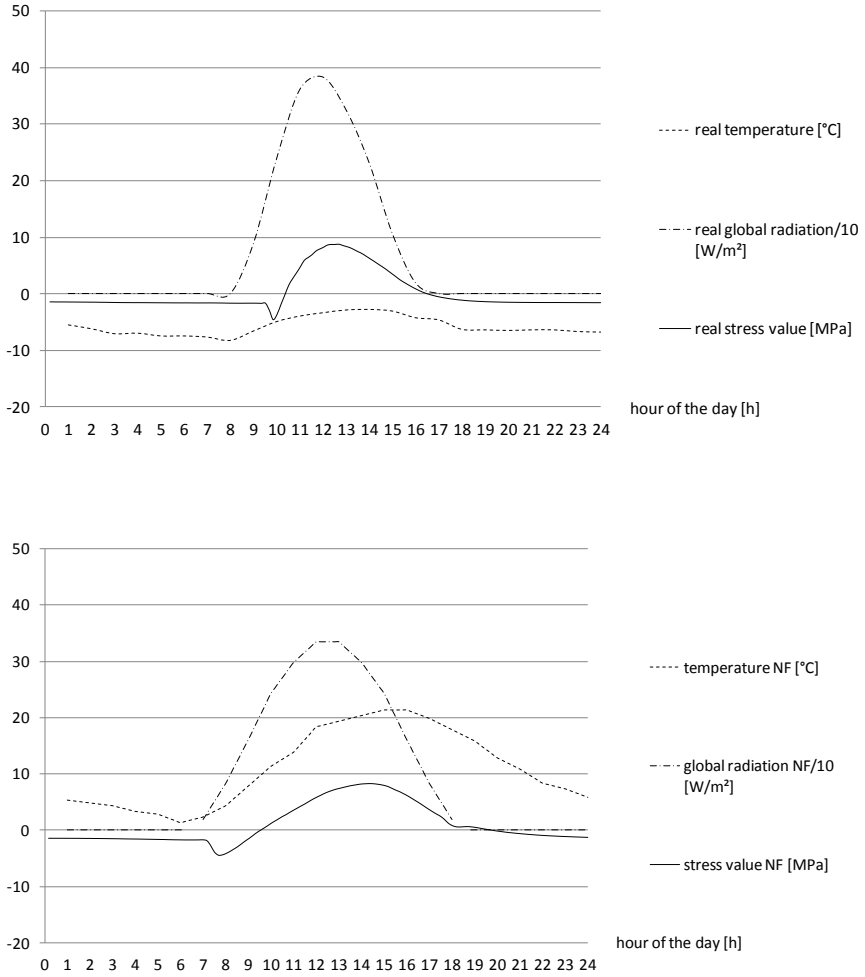

Figure 4.4: climate data and stresses at the left side edge (first real climate data, then French standard climate data: NF)

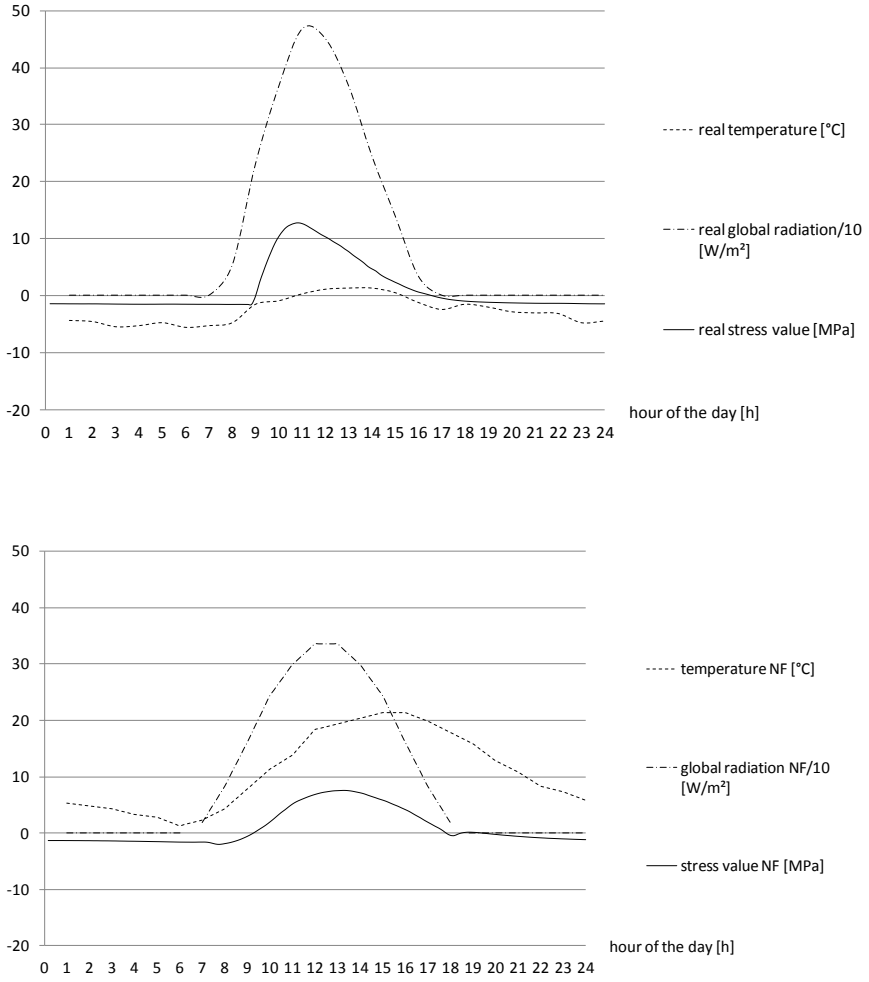

Figure 4.5: climate data and stresses at the right side edge (first real climate data, then French standard climate data: NF)

4.4 Results of another twenty-year period and another location

4.4.1 Temperature gradient results and thermal stress history

The same model simulated in section 4.3 was used to perform calculations over another twenty-year period from 1971 to 1990 at the same location in The Netherlands (Maastricht) and another location in the Netherlands (Leeuwarden) over the same period from 1991 to 2010. The double skin façade was oriented to the south in both cases. The outcome of these simulations was the temperature history over the total area of the different panes in the investigated configurations, which was used to calculate the stress history (see section 4.3.2).

4.4.2 Ultimate limit state verification

For the maximum stress verification and equivalent stress verification, the stress corrosion parameter *n* was taken equal to 16 corresponding to 100% RH (Charles 1958; Blank 1993; Shen 1997; Fink 2000; Wörner 2001). The 5% characteristic strength value of the German standard DIN 18008-1 (2010) $f'_{eg,k}$ = 36 MPa (Siebert and Seel 2011) was considered.

The yearly maximum equivalent constant design stress values $\sigma_{d,eq,yearly}$ [MPa] are presented in Table 4.4 for every year from 1971 to 1990 and in Table 4.5 for the other location in the Netherlands (Leeuwarden). Also, the corresponding values of the period from 1991 to 2010 for the location Maastricht are presented in Tables 4.4 and 4.5 (two right columns).

Then these 20 design stress values were fitted to the Gumbel maximum distribution and the 5% maximum value $\sigma_{d,5\%,eq,yearly}$ was calculated (see Tables 4.4 and 4.5). Next, the equivalent lifetime constant design stress $\sigma_{d,eq,lifetime}$ was calculated according to section 4.2.3 (see Tables 4.4 and 4.5).

The stress values $\sigma_{d,5\%,eq,yearly}$ and $\sigma_{d,eq,lifetime}$ were compared with the strength values and the ratios r_1, r_2 and r_2/r_1 were calculated and presented in Tables 4.4 and 4.5, similar to section 4.3.3.

It can be concluded that the difference between the sample means of the twenty values $\sigma_{d,eq,yearly}$ for the periods 1971-1990 and 1991-2010 amounts to a maximum of 2% (see Table 4.4). Consequently, the climatic conditions did not change significantly over two sequential time periods of 20 years.

Table 4.4: simulated stresses and strength values [MPa] (horizontal section directed to the south orientation), the ratios in bold and the values of *V* are non-dimensional.

year	left	right	year	left	right
	$\sigma_{d,eq,yearly}$			$\sigma_{d,eq,yearly}$	
1971	7.6	10.4	1991	7.6	9.4
1972	6.2	7.8	1992	6.3	8.9
1973	6.2	7.8	1993	6.2	8.5
1974	6.4	8.2	1994	8.2	10.7
1975	8.4	10.4	1995	9.2	11.3
1976	8.3	12.2	1996	9.4	12.8
1977	7.1	9.2	1997	6.8	8.3
1978	7.2	10.1	1998	9.2	13.5
1979	8.7	12.6	1999	6.7	8.5
1980	8.3	11.7	2000	7.8	11.0
1981	7.2	10.5	2001	6.6	9.1
1982	8.3	11.9	2002	7.8	11.2
1983	7.7	9.5	2003	6.9	8.6
1984	7.3	8.5	2004	7.7	9.2
1985	7.2	8.6	2005	6.9	9.0
1986	7.9	10.6	2006	6.6	9.0
1987	8.2	11.7	2007	7.1	9.7
1988	7.0	8.3	2008	8.9	13.1
1989	8.0	11.3	2009	7.8	9.7
1990	6.8	8.5	2010	8.5	10.7
$\bar{x}$	7.5	10.0	$\bar{x}$	7.6	10.1
s	0.76	1.55	s	1.01	1.61
V	0.10	0.16	V	0.13	0.16
$\sigma_{d,5\%,eq,yearly}$	8.9	12.9	$\sigma_{d,5\%,eq,yearly}$	9.5	13.1
f_d	10.0	10.0	f_d	10.0	10.0
$r_1=\sigma_{d,5\%,eq,yearly} / f_d$	**0.89**	**1.29**	$r_1=\sigma_{d,5\%,eq,yearly} / f_d$	**0.95**	**1.31**
$\sigma_{d,eq,lifetime}$	10.0	13.7	$\sigma_{d,eq,lifetime}$	10.3	14.1
$f'_d = 1.06 * f_d$	10.6	10.6	$f'_d = 1.06 * f_d$	10.6	10.6
$r_2=\sigma_{d,eq,lifetime} / f'_d$	**0.94**	**1.29**	$r_2=\sigma_{d,eq,lifetime} / f'_d$	**0.97**	**1.33**
r_2/r_1	**1.05**	**1.00**	r_2/r_1	**1.02**	**1.02**

However, the difference between the sample means of the twenty values $\sigma_{d,eq,yearly}$ of the same period for the locations Maastricht and Leeuwarden amounts to 20% (see Table 4.5). The distance between Maastricht and Leeuwarden is only 320 km and according to prEN thstr (2004), the same climate data should be considered. Thus, the climate can change significantly over a small distance. For the right side, which determines the risk of thermal fracture,

the value of r_2/r_1 varies between 1.00 and 1.03, which means that the equivalent lifetime stress method is little more conservative than the maximum stress method for the investigated configurations.

Table 4.5: simulated stresses and strength values [MPa] (horizontal section directed to the south orientation), the ratios in bold and the values of *V* are non-dimensional.

$\sigma_{d,eq,yearly}$	Leeuwarden		Maastricht	
year	left	right	left	right
1991	5.8	7.0	7.6	9.4
1992	5.6	6.9	6.3	8.9
1993	6.0	7.8	6.2	8.5
1994	5.9	7.8	8.2	10.7
1995	6.4	9.9	9.2	11.3
1996	7.2	9.9	9.4	12.8
1997	6.3	7.7	6.8	8.3
1998	5.6	8.6	9.2	13.5
1999	6.8	9.5	6.7	8.5
2000	6.1	6.7	7.8	11.0
2001	5.6	6.9	6.6	9.1
2002	6.0	7.5	7.8	11.2
2003	6.0	8.9	6.9	8.6
2004	5.7	6.9	7.7	9.2
2005	5.8	7.1	6.9	9.0
2006	6.1	6.7	6.6	9.0
2007	6.0	8.1	7.1	9.7
2008	6.2	8.0	8.9	13.1
2009	7.9	11.0	7.8	9.7
2010	6.8	8.1	8.5	10.7
$\bar{x}$	6.2	8.0	7.6	10.1
s	0.59	1.24	1.01	1.61
V	0.10	0.15	0.13	0.16
$\sigma_{d,5\%,eq,yearly}$	7.3	10.4	9.5	13.1
f_d	10.0	10.0	10.0	10.0
$r_1=\sigma_{d,5\%,eq,yearly} / f_d$	**0.73**	**1.03**	**0.95**	**1.31**
$\sigma_{d,eq,lifetime}$	8.4	11.3	10.3	14.1
$f'_d = 1.06 * f_d$	10.6	10.6	10.6	10.6
$r_2=\sigma_{d,eq,lifetime} / f'_d$	**0.80**	**1.06**	**0.97**	**1.33**
r_2/r_1	**1.09**	**1.03**	**1.02**	**1.02**

4.5 Results of the east orientation

4.5.1 Temperature gradient results and thermal stress history

The same model simulated in section 4.3 was used to perform calculations for the double skin façade, oriented to the east instead of to the south. The outcome of these simulations was the temperature history over the total area of the different panes in the investigated configuration, which was used to calculate the stress history (see section 4.3.2).

4.5.2 Ultimate limit state verification

The yearly maximum equivalent constant design stress values $\sigma_{d,eq,yearly}$ [MPa] are presented for the east orientation for every year from 1991 to 2010 at the location Maastricht (see Table 4.6). Also, the values of the south orientation are provided for the same location and time period (two right columns). In both cases, the stress corrosion parameter n = 16 and the 5% characteristic strength value of the German standard DIN 18008-1 (2010) $f'_{eg,k}$ = 36 MPa were considered.

Then these 20 design stress values were fitted to the Gumbel maximum distribution and the 5% maximum value $\sigma_{d,5\%,eq,yearly}$ was calculated (see Table 4.6). Next, the equivalent lifetime constant design stress $\sigma_{d,eq,lifetime}$ was calculated according to section 4.2.3 (see Table 4.6).

The stress values $\sigma_{d,5\%,eq,yearly}$ and $\sigma_{d,eq,lifetime}$ were compared with the strength values and the ratios r_1, r_2 and r_2/r_1 were calculated and presented in Table 4.6, similar to section 4.3.3.

It can be noticed that for the east orientation, the difference between the sample means of the left and the right side is smaller than for the south orientation (see Table 4.6). However, the value of r_2/r_1 amounts to 1.20 and 1.22 for the left and the right side, respectively. This is considerably higher than for the south orientation, for which the ratio was only 1.02. This indicates that the equivalent lifetime stress method is much more conservative than the maximum stress method for the east orientation. Consequently, it would be unsafe to consider only the maximum stress method.

Table 4.6: simulated stresses and strength values [MPa] (horizontal section directed to the east and south orientation), the ratios in bold and the values of *V* are without dimension.

$\sigma_{d,eq,yearly}$	east		south	
year	left	right	left	right
1991	12.1	11.1	7.6	9.4
1992	11.3	11.1	6.3	8.9
1993	11.7	11.3	6.2	8.5
1994	12.2	11.6	8.2	10.7
1995	11.6	12.2	9.2	11.3
1996	12.3	11.7	9.4	12.8
1997	12.3	11.7	6.8	8.3
1998	11.6	12.0	9.2	13.5
1999	12.3	11.8	6.7	8.5
2000	12.3	12.3	7.8	11.0
2001	12.7	12.0	6.6	9.1
2002	12.7	11.5	7.8	11.2
2003	12.9	12.5	6.9	8.6
2004	12.7	12.9	7.7	9.2
2005	13.6	13.0	6.9	9.0
2006	13.0	13.0	6.6	9.0
2007	12.9	12.4	7.1	9.7
2008	13.0	12.8	8.9	13.1
2009	13.0	12.3	7.8	9.7
2010	14.4	12.1	8.5	10.7
$\bar{x}$	12.5	12.1	7.6	10.1
s	0.87	0.60	1.01	1.61
V	0.07	0.05	0.13	0.16
$\sigma_{d,5\%,eq,yearly}$	13.9	13.2	9.5	13.1
f_d	10.0	10.0	10.0	10.0
$r_1=\sigma_{d,5\%,eq,yearly} / f_d$	**1.39**	**1.32**	**0.95**	**1.31**
$\sigma_{d,eq,lifetime}$	17.9	17.1	10.3	14.1
$f'_d = 1.06 * f_d$	10.6	10.6	10.6	10.6
$r_2=\sigma_{d,eq,lifetime} / f'_d$	**1.68**	**1.61**	**0.97**	**1.33**
r_2/r_1	**1.21**	**1.22**	**1.02**	**1.02**

4.6 Results of the vertical section

4.6.1 Temperature gradient results and thermal stress history

The same model from section 4.3 was simulated but in vertical position, oriented to the east and to the south at the location Maastricht for the time period 1991-2010. The outcome of these simulations was the temperature history over the total area of the different panes in the investigated configurations, which was used to calculate the stress history (see section 4.3.2).

4.6.2 Ultimate limit state verification

The yearly maximum equivalent constant design stress values $\sigma_{d,eq,yearly}$ [MPa] are presented for the east and south oriented vertical position for every year from 1991 to 2010 at the location Maastricht (see Table 4.7). Also, the values of the horizontal position is provided for the same location, orientation and time period. In all cases, the stress corrosion parameter n = 16 and the 5% characteristic strength value of the German standard DIN 18008-1 (2010) $f'_{eg,k}$ = 36 MPa were considered.

Then these 20 design stress values were fitted to the Gumbel maximum distribution and the 5% maximum value $\sigma_{d,5\%,eq,yearly}$ was calculated (see Tables 4.7). Next, the equivalent lifetime constant design stress $\sigma_{d,eq,lifetime}$ was calculated according to section 4.2.3 (see Table 4.7).

The stress values $\sigma_{d,5\%,eq,yearly}$ and $\sigma_{d,eq,lifetime}$ were compared with the strength values and the ratios r_1, r_2 and r_2/r_1 were calculated and presented in Table 4.7, similar to section 4.3.3.

It can be concluded that for the south orientation, stresses at the top side are less critical than the right side. However, for the east orientation, the opposite is observed. Furthermore, the ratio r_2/r_1 is little higher for the vertical position than for the horizontal position for the critical side, for both orientations.

Table 4.7: simulated stresses and strength values [MPa] (vertical and horizontal section directed to the east and south orientation), the ratios in bold and the values of *V* are without dimension.

	south				east			
$\sigma_{d,eq,yearly}$	vertical		horizontal		vertical		horizontal	
year	down	up	left	right	down	up	left	right
1991	6.6	9.3	7.6	9.4	9.4	12.7	12.1	11.1
1992	-	9.0	6.3	8.9	8.4	12.5	11.3	11.1
1993	5.6	8.0	6.2	8.5	8.9	13.0	11.7	11.3
1994	7.9	10.1	8.2	10.7	8.9	12.6	12.2	11.6
1995	8.6	10.9	9.2	11.3	9.0	12.5	11.6	12.2
1996	9.0	11.3	9.4	12.8	9.6	12.9	12.3	11.7
1997	5.8	8.3	6.8	8.3	9.3	12.9	12.3	11.7
1998	9.0	12.3	9.2	13.5	8.9	13.0	11.6	12.0
1999	5.6	8.5	6.7	8.5	8.5	12.7	12.3	11.8
2000	7.6	10.3	7.8	11.0	9.4	13.5	12.3	12.3
2001	6.4	8.5	6.6	9.1	9.5	13.4	12.7	12.0
2002	7.7	9.6	7.8	11.2	9.1	12.8	12.7	11.5
2003	5.6	8.5	6.9	8.6	9.9	13.8	12.9	12.5
2004	6.5	8.9	7.7	9.2	9.6	14.0	12.7	12.9
2005	6.2	8.7	6.9	9.0	9.9	13.9	13.6	13.0
2006	6.1	8.2	6.6	9.0	9.7	14.0	13.0	13.0
2007	6.7	8.5	7.1	9.7	9.8	13.9	12.9	12.4
2008	9.2	11.3	8.9	13.1	10.1	13.9	13.0	12.8
2009	6.9	9.4	7.8	9.7	9.8	13.5	13.0	12.3
2010	8.0	10.3	8.5	10.7	9.7	13.7	14.4	12.1
$\bar{x}$	7.1	9.5	7.6	10.1	9.4	13.3	12.5	12.1
s	1.23	1.23	1.01	1.61	0.47	0.55	0.87	0.60
V	0.17	0.13	0.13	0.16	0.05	0.04	0.07	0.05
$\sigma_{d,5\%,eq,yearly}$	9.4	11.8	9.5	13.1	10.2	14.3	13.9	13.2
f_d	10.0	10.0	10.0	10.0	10.0	10.0	10.0	10.0
$r_1=\sigma_{d,5\%,eq,yearly} / f_d$	**0.94**	**1.18**	**0.95**	**1.31**	**1.02**	**1.43**	**1.39**	**1.32**
$\sigma_{d,eq,lifetime}$	10.0	13.0	10.3	14.1	13.3	19.0	17.9	17.1
$f'_d = 1.06 * f_d$	10.6	10.6	10.6	10.6	10.6	10.6	10.6	10.6
$r_2=\sigma_{d,eq,lifetime} / f'_d$	**0.95**	**1.22**	**0.97**	**1.33**	**1.25**	**1.79**	**1.68**	**1.61**
r_2/r_1	**1.01**	**1.04**	**1.02**	**1.02**	**1.22**	**1.26**	**1.21**	**1.22**

4.7 Highlights of this chapter

4.7.1 Method

- The principles for the calculation of the temperature gradients (action model) and the thermal stresses (structural model) are presented
- The approach of the ultimate limit state method is provided

4.7.2 Verifications

- For a specific façade configuration, a finite element simulation was performed over a twenty-year period to determine the temperature gradients in the panes and the corresponding stress history.
- For the south oriented façade configuration (horizontal section), the equivalent stress method was little more conservative compared to the maximum stress method (0% to 2% for the largest stresses). However, the humidity (50% or 100%) and the characteristic strength value ($f'_{eg,k}$ = 36 MPa or $f'_{eg,k}$ = 47 MPa) had a minor influence on the difference between both calculation methods.
- Although the French standard (NF P 78-201-1/A1(DTU39) 1998) is strictly not applicable, the calculations demonstrate that the climate data which are used in the standard or the proposed method of the standard are unsafe compared to the simulations of this study.
- Compared to the period of 1991 to 2010, the period of 1971 to 1990 provides results for the stresses which only differ 2%. However, the location of Leeuwarden, only 320 km away from Maastricht results in stresses which are about 20% lower, simulated with the real climate data. According to prEN thstr (2004), the same climate data should be used for the simulations of the two locations.
- For the east orientation, the equivalent stress method was much more conservative compared to the maximum stress method (22% for the largest stresses), compared to the south orientation.
- Similar conclusions can be drawn for the vertical section as well as for the horizontal section.

5. Conclusions and recommendations

My mind seems to have become a kind of machine for grinding general laws out of large collections of facts.

Charles Darwin (1809-1882)

5.1 Conclusions

The existing calculation methods to evaluate thermal fracture of glass differ considerably. As thermal stresses are mainly influenced by solar radiation and diurnal temperature change and the edge strength is determined by numerous processing and environmental parameters, a verifiable calculation method for thermal fracture remains a challenge. This study aimed at clarifying the environmental influences on both the action side (stresses) and the resistance side (strength). Indeed, the stresses are caused by radiation and temperature, while the strength is influenced by humidity, causing stress corrosion. Because of the influence of humidity and the fact that the strength is governed by defects due to the edge processing procedures, load duration and load history as well as size and stress distribution effects become important when designing glass elements which have to withstand thermal actions.

The issues mentioned in the previous paragraph were introduced by the principles of the theory of LEFM and the principles of probability theory (see section 2.3). Then, a comprehensive experimental (chapter 3) and numerical (chapter 4) investigation was performed. Finally, the semi-probabilistic method according to EN1990 (2002) was applied.

Multiple conclusions are drawn, amongst which the most important are:

- temperature loading and mechanical loading resulted in similar edge strength values (TP 1)
- the influence of stress corrosion on strength values is accurately described in the literature and the standards and is in good agreement with the results found in the current study (TP 2)
- the characteristic edge strength values found in this study have the same magnitude as the values provided in the literature and the standards (TP 2)
- the edge strength values of the specimens for a specific edge finishing, were mostly independent of the cross-sectional failure location or the longitudinal failure location, although some locations showed significantly more failures than other locations (TP 2 and TP 5)
- the influence of the load history corresponds well to the approach found in the literature for a constant load history, but not for a cyclic load history (TP 3 and TP 4)
- for the cyclic load history, a crack healing effect was estimated at 6% (TP 3 and TP 4)

- concerning the influence of the size effect, the approach in the literature is unsafe (TP 5)
- the influence of the stress distribution on the strength values does not follow the theoretical approach found in the literature for the tested edge finishing and the tested size (TP 6)
- for the ultimate limit state verification, stress corrosion has to be considered as well as the entire load history during the lifetime of the element, and not only the maximum value during the lifetime
- the climate data which are used for the verification have a very significant influence on the safety assessment

For a more detailed overview of the conclusions, the reader can consult the detailed highlights of chapters 2, 3 and 4 (section 2.6, 3.9 and 4.7).

Consequently, this study fulfilled the objective to provide a better fundamental insight in the mechanisms of glass failure caused by thermal actions. Based on this insight, a methodology according to the semi-probabilistic safety format provided in EN1990 (2002) has been developed, to avoid possible failures and to avoid imposing tempered glass products in cases where they are not necessary. The proposed method provides the probability of failure and accounts for stress corrosion and damage accumulation due to cyclic loading. Stress corrosion and crack healing effects were quantified in a very accurate manner by testing at different stress rates and different load histories in a 4PB setup. Also, the size effect and stress distribution effect was thoroughly examined by testing. All these effects were not yet quantified before for the edge strength of glass in actively controlled laboratory conditions on such a large scale.

5.2 Recommendations

Future work could focus on:

- performing a parametric study, varying the geometrical and material properties of the façade configuration and estimating the influence of climatic conditions with execution of a precise validation;
- estimating the influence of ventilation in a double skin façade and performing a precise validation;
- optimizing the cutting and processing parameters (cutting wheel, cutting pressure, cutting speed, grinding discs, …) resulting in higher edge strength values;
- introducing an appropriate conformity system for the edge strength;
- applying both methods, the maximum stress method and the equivalent stress method, to several façade configurations to determine more accurately the partial safety coefficients for both methods;
- proposing a simplified calculation method based on the findings of the previous paragraph.

BIBLIOGRAPHY

ASTM C 1239-07 (2007) *Standard Practice for Reporting Uniaxial Strength Data and Estimating Weibull Distribution Parameters for Advanced Ceramics*. ASTM, USA.

ASTM C1678-10 (2010) *Standard Practice for Fractographic Analysis of Fracture Mirror Sizes in Ceramics and Glasses.* ASTM, USA.

Auradou H, Vandembroucq D, Guillot C, Bouchaud E (2001) *A probabilistic model for the stress corrosion fracture of glass.* Transactions, SMiRT 16, Washington DC.

Balcaen N (2013). *Thermische breuk van dubbele glazen gevels: parameterstudie.* Masterthesis, Ghent University, Ghent, Belgium.

Bando Y, Ito S, Tomozawa M (1984) *Direct Observation of Crack Tip Geometry of SiO2 Glass by High-Resolution Electron Microscopy.* Journal of the American Ceramic Society, 67(3): C36-C37.

Beason W L (1980). A failure prediction model for window glass. Dissertation, Institute for Disaster Research, Texas, USA.

Beason W L, Morgan J R (1984). *Glass failure prediction model.* Journal Structural Engineering, 11:2, p 197 – 212.

Beason W L, Lingnell A W (2002) *A Thermal Stress Evaluation Procedure for Monolithic Annealed Glass.* The use of Glass in Buildings, p. 105 – 118, ASTM, PA, USA.

Beason W L, Lingnell A W (2003) *A Method of Evaluation for Thermal Stress in Monolithic Annealed Glass.* Proc. of GPD, p. 291 – 293, Tampere, Finland.

Belis J (2005) *Kipsterkte van monolithische en gelamineerde glazen liggers.* PhD thesis, Ghent University, Ghent, Belgium.

Belgian Glass (1997) *Evaluation des contraintes thermiques dans les vitrages.* Federation de l'industrie du verre a.s.b.i., Belgium.

Blank K (1993) *Dickenbemessung von vierseitig gelagerten rechteckigen Glasscheiben unter gleichförmiger Flächenlast.* Institut für konstruktiven Glasbau, Gelsenkirchen.

Blomsterberg Å (2007) *Best Practice for Double Skin Façades.* University of Lund, Sweden.

Caspeele R (2010) *Probabilistic Evaluation of Conformity Control and the Use of Bayesian Updating Techniques in the Framework of Safety Analyses of Concrete Structures.* PhD thesis, Ghent University, Ghent, Belgium.

Caspeele R and Taerwe L (2012) *Quantitative Comparison of Estimation Methods for Determining the in Situ Characteristic Concrete Compressive Strength.* Structural Engineering International, 2012/2, 215-222.

Charles R J (1958) *Static Fatigue of Glass II.* J Appl Phys, 29, Number 11: 1554-1560.

Charles R J, Hilling W B (1962) *The kinetics of glass failure by stress corrosion.* Symposium on Mechanical Strength of Glass and Ways of Improving it. Charleroy, Belgium.

Conway J C and Mecholsky JJ (1989) *Use of crack branching data for measuring near surface residual stresses in tempered glass.* Journal of the American Ceramic Society, Vol. 72, No (9), pp. 1584-1587.

DIN 1249-11 (1986) *Flachglas im Bauwesen, Glaskanten.* Beuth, Berlin, Germany.

DIN 18008-1 (2010) *Glas im Bauwesen – Bemessings- und Konstruktionsregeln – Teil 1: Begriffe und allgemeine Grundlagen.* Beuth, Berlin, Germany.

Dassault Systèmes Simulia Corp. (2010). Abaqus: Standard user's manual version 6.10, Providence, RI, USA.

E2431-12 (2012) *Standard practice for Determining the Resistance of Single Glazed Annealed Architectural Flat Glass to Thermal Loadings.* ASTM, USA.

EN 1288-1 (2000). *Glass in buildings – Determination of the bending strength of glass – Part 1: Introduction to testing glass.* European standard, CEN.

EN 1288-3 (2000) *Glass in building – Determination of the bending strength of glass – Part 3: Test with specimen supported at two points (four point bending).* European standard, CEN.

EN 1863-1 (2000) *Glass in building – Heat strengthened soda lime silicate glass – Part 1: Definition and description.* European standard, CEN.

EN 1990 (2002) *Eurocode – Basis of structural design.* European standard, CEN.

EN 1991-1-4 (2005) *Eurocode 1: Actions on structures – Part 1-4: General actions – Wind actions.* European standard, CEN.

EN 12150-1 (2000) *Glass in building – Thermally toughened soda lime silicate safety glass – Part 1: Definition and description.* European standard, CEN.

EN 14179-1 (2005) *Glass in building – Heat soaked thermally toughened soda lime silicate safety glass – Part 1: Definition and description.* European standard, CEN.

Feldmann M, Kasper R, Abeln B, Cruz P, Belis J, Beyer J, Colvin J, Ensslen F, Eliasova M, Galuppi L, Geßler A, Grenier C, Haese A, Hoegner H, Kruijs R, Langosch K, Louter C, Manara G, Morgan T, Neugebauer J, Rajcic V, Royer-Carfagni G, Schneider J, Schula S, Siebert G, Sulcova Z, Wellershoff F, Zarnic R (2014) *Guidance for European Structural Design of Glass Components, report EUR 26439 EN.* European Union, Luxembourg.

Feryn D (2012). *Spanningsopbouw in beglazing onder invloed van een thermische belasting.* Masterthesis, Ghent University, Ghent, Belgium.

Fink A (2000) *Dissertation D17: Ein Beitrag zum Einsatz von Floatglas als Dauerhaft tragender Konstruktionswerkstoff im Bauwesen.* Technische Universität Darmstadt, Institut für Statik, Bericht Nr. 21.

Gehrke E, Ullner C, Hähnert M (1987) *Correlation between multistage crack growth and time-dependent strength in commercial silicate glasses, part 1.* Glastechnische Berichte 60, Nr. 8. S 268 ff.

Gehrke E, Ullner C, Hähnert M (1991) *Fatigue limit and crack arrest in alkali-containing silicate glasses.* Journal of Material Science, 26: 5445-5455.

Griffith A A (1920) *The Phenomena of Rupture and Flow in Solids.* Philosophical Transactions, Series A, 221: 163-198.

Guin J P, Wiederhorn S (2003) Crack growth threshold in soda lime silicate glass: role of hold time. Journal of Non-Crystalline Solids, 316(1): 12-20.

Gulvanessian H, Calgaro J-A, Holický M (2002). *Designers' Guide to EN 1990 Eurocode: Basis of structural design.* Thomas Telford, London.

Güsgen J (1998). *Bemessung tragender Bauteile aus Glas.* Aachen: Shaker Verlag. Schriftenreihe Stahlbau – RWTH Aachen, Heft 42, D82, Aachen, Germany.

Haldimann M (2006) *Fracture strength of structural glass elements – analytical and numerical modelling, testing and design.* Dissertation, EPFL, Lausanne, Switserland.

Haldimann M, Luible A, Overend M (2008) *Structural Engineering Document 10: Structural use of glass.* IABSE / ETH Zürich, Zürich, Switserland.

Hedderich J, Sachs, L (2012) *Angewandte Statistik*. Berlin/Heidelberg: Springer Verlag.

Hénaux S, Creuzet F (1997) *Kinetic fracture of glass at the nanometer scale.* Journal of Materials Science Letters, 16(12): 1008-1011.

Hess R (2000) *Glasträger.* Forschungsbericht Nr. 20. ETH Zürich. Institut für Hochbautechnik, Zürich, Switserland.

Higgins J (2004) *An Introduction to Modern Nonparametric Statistics*. Thomson Learning, USA.

Irwin G (1957) *Analysis of Stresses and Strains near the End of a Crack Traversing a Plate.* J Appl Mech, 24: 361-364.

ISO 12491 (1997) *Statistical methods for quality control of building materials and components.* International Organisation for Standardisation, Geneve, Switzerland.

Lawn B R (1993) *Fracture of Brittle solids, 2nd edition.* Cambridge University Press, Cambridge, UK.

Lindqvist M (2013) *Structural Glass Strength Prediction Based on Edge Flaw Characterisation.* Dissertation, EPFL, Lausanne, Switserland.

Makkonen L (2008) *Problems in the extreme value analysis.* Structural Safety, 30, 405-419.

Mencik J (1992) *Strength and Fracture of Glass and Ceramics.* Glass Science and Technology, 12.

Morse S M, Norvill H S 2013. *Method to Determine the Probability of Failure for Annealed Monolithic Window Glass Loaded with a Uniform Wind Load.* Journal of Archit. Eng. DOI: 10.1061/(ASCI)AE.1943-5568.0000128.

Munz D, Fett T (1999) *Ceramics: mechanical properties, failure behaviour, materials selection.* Springer, Germany.

NEN 2608 + C1 (2012) Glass in building – Requirements and determination method. NEN, Delft.

NF P 78-201-1/A1(DTU39) (1998) *Travaux de miroiterie-vitrerie – Partie 1 : Cahier des clauses techniques – Amendement 1.* CEBTP, France.

Nghiem B (1998) *Fracture du verre et heterogeneites à l'echelle sub-micronique.* Ph.D Thesis Nr 98 PA06 6260, Université Paris-VI.

Overend M, Parke G, Buhagiar D (2007) *Predicting Failure in Glass – A General Crack Growth Model.* Journal of Structural Engineering, august, p. 1146 – 1155.

Overend M, De Gaetano S, Haldimann M (2007) *Diagnostic interpretation of glass failure.* Structural Engineering International, Vol. 2, pp. 151-158.

Overend M, Zammit K (2012) *A computer algorithm for determining the tensile strength of float glass.* Engineering Structures, 45, p. 68 – 77.

Physibel (2011) *Bistra v3.1w: manual.* Maldegem.

Pilette C F, Taylor D A (1988) *Thermal Stresses in Double-Glazed Windows.*Canadian Journal of Civil Engineering, Vol. 15, No. 5, p. 807-814.

Porter M (2001) *Aspects of Structural Design with Glass.* Dissertation, Trinity, Oxford, UK.

prEN thstr (2004) *Glass in building – Thermal Stress Calculation Method.* Draft European standard, CEN.

prEN 16612 (2013) *Glass in building – Determination of the load resistance of glass panes by calculation and testing.* Draft European standard, CEN.

Rodichev Y, Maslov V, Netychuk A, Bodunov V, Yevplov Y (2007) *Bending strength and fracture of glass materials under the different loading conditions.* Proc. of GPD, p. 615 – 618.

Saelens D (2002) *Energy performance assessment of single storey multiple-skin façades.* Dissertation, KUL, Leuven, Belgium.

Shen X (1997) *Entwicklung eines Bemessings- und Sicherheitskonzeptes für den Glasbau.* Fortschritt-Berichte VDI, Reihe 4, Nr. 138.

Simmons C J, Freiman S W (1981) *Effect of corrosion processes on subcritical crack growth in glass.* Journal of The American Ceramic Society, Vol. 64.

Siebert G, Seel M (2011) *New German DIN Standard DIN 18008 for design of glass elements.* Proc. of GPD, p. 465 – 467, Tampere, Finland.

Sglavo V, Müller C, Righetti F (2007) *Influence of edge finishing on the resistence to thermal stresses of float glass.* Proc. of GPD, p. 668 – 672, Tampere, Finland.

Thoman D, Bain I, Antle C (1969) *Inferences on the parameters of the Weibull distribution*. Technometrics 11, 445-460.

TV 214 (1999) *Glas en glasproducten, functies van beglazing.* WTCB, Brussels, Belgium.

Vandebroek M, Belis J, Louter C, Van Tendeloo G (2012) *Experimental validation of edge strength model for glass with polished and cut edge finishing.* Engineering Fracture Mechanics, 96, 480-489.

Vandebroek M, Belis J, Louter C, Caspeele R (2013) *Influence of the load history on the edge strength of glass with arrised and ground edge finishing.* Engineering Fracture Mechanics, 104, 29-40.

Vandebroek M, Louter C, Caspeele R, Belis J (2014a) *Influence of the number of test specimens on glass strength estimates.* Proc. Of Challenging Glass 4 and COST Action TU0905 Final Conference, p. 725 – 730.

Vandebroek M, Louter C, Caspeele R, Ensslen F, Belis J (2014b) *Size effect model for the edge strength of glass with cut and ground edge finishing.* Engineering Structures, 79, 96-105.

Vandenpoel M (2010). *Thermische belasting en breuk bij glazen gevels.* Masterthesis, Ghent University, Ghent, Belgium.

Vansteenbrugge D (2012). *Klimaatbelasting en breuk bij glazen gevels.* Masterthesis, Ghent University, Ghent, Belgium.
Veer F, Riemslag A (2009) *The strength of glass, size effects.* Proc. of GPD, p. 851 – 853.

Veer F, Rodichev Y (2011) *The structural strength of glass: hidden damage.* Strength of Materials, Vol. 43, No. 3, 302 – 315.

Wachtman J B, Cannon W R, Matthewson M J (2009) *Mechanical properties of ceramics, 2nd edition.* A John Wiley & Sons, Inc., USA.

Weller B, Nicklisch S, Thieme T, Weimar T (2010) *Glasbau-Praxis: Konstruktion und Bemessung, 2 Aufl.* Bauwerk, Berlin, Germany.

Wiederhorn S M, Bolz L H (1970) *Stress corrosion and static fatigue of glass.* J Am Ceram Soc, Vol. 53, p. 543 – 548.

Wiederhorn S M, Dretzke A, Rödel J (2002) *Crack growth in soda-lime-silicate glass near the static fatigue limit.* Journal of the American Ceramic Society, 85(9): 2287-2292.

Wiederhorn S M, Dretzke A, Rödel J (2003) Near the fatigue limit in glass. International Journal of Fracture, 121(1-2): 1-7.

Wörner J-D, Schneider J, Fink A (2001) *Glasbau: Grundlagen, Berechnung, Konstruktion.* ISBN 3-540-66881-0 Springer-Verlag Berlin Heidelberg New York.

Yingzhi L, Hills D A (1990) *Stress intensity factor solutions for kinked surface cracks.* Journal of Strain Analysis, Vol. 25, No. 1.

Zaccaria M and Overend M (2012) Validation of a simple relationship between the fracture pattern and the fracture state of glass. Proc. of the International Conference Engineered Transparency, p. 179-187, Düsseldorf, Germany.

Zupan D, Srpčič J, Turk G (2007) *Characteristic value determination from small samples.* Structural Safety, 29, 268 – 278.

ANNEX A:

Table A.1: the strain $\varepsilon_s[10^{-6}]$ at failure for edge 1.

Specimen number	gauge A	gauge B	gauge E
1	539	**567**	**486**
2	461	563	471
3	455	467	426
4	**406**	**557**	448
5	525	605	489
6	468	545	432
7	**475**	**597**	473
8	**429**	**469**	386
9	406	533	409
10	493	568	465
11	442	519	418
12	437	510	409
13	457	**576**	**467**
14	**441**	**547**	452
15	**445**	**553**	445
16	**421**	**491**	398
17	424	549	461
18	398	502	432
19	434	532	448
20	425	534	455

Table A.2: the strain $\varepsilon_s[10^{-6}]$ at failure for edge 2.

Specimen number	gauge F	gauge G	gauge J
1	453	529	409
2	405	501	402
3	418	482	380
4	440	510	408
5	460	**530**	**442**
6	427	505	395
7	467	553	416
8	356	431	338
9	371	498	335
10	416	497	403
11	389	467	372
12	406	480	381
13	420	558	467
14	400	533	448
15	387	511	436
16	377	495	410
17	409	**550**	**450**
18	395	521	427
19	424	550	435
20	420	**549**	**445**

Table A.3: the strain $\varepsilon_s[10^{-6}]$ at failure for edge 3.

Specimen number	gauge K	gauge L	gauge O
1	450	521	390
2	463	530	416
3	456	516	385
4	449	508	381
5	468	538	410
6	**482**	**547**	422
7	525	596	455
8	386	454	357
9	389	467	401
10	**483**	**557**	441
11	452	527	405
12	449	527	409
13	463	543	432
14	454	524	412
15	452	531	420
16	434	485	376
17	475	525	396
18	**436**	**491**	373
19	**432**	**493**	358
20	417	482	362

Table A.4: the strain $\varepsilon_s[10^{-6}]$ at failure for edge 4.

Specimen number	gauge P	gauge Q	gauge T
1	435	582	449
2	**447**	**559**	435
3	369	**521**	**423**
4	395	477	397
5	423	552	450
6	410	594	482
7	440	632	507
8	367	523	412
9	359	**537**	**429**
10	429	589	461
11	**388**	**545**	438
12	431	**524**	**373**
13	432	517	409
14	417	494	384
15	441	525	401
16	398	462	354
17	405	475	375
18	362	437	347
19	357	441	342
20	359	440	354

ANNEX B

Table B.1: failures stresses f'_{eg} [MPa] of series N1-a1,a2,a3.

Specimen number	N1-a1 50 MPa/s	N1-a2 2 MPa/s	N1-a3 0.08 MPa/s
1	81.1	67.1	42.4
2	71.6	62.0	49.9
3	73.2	74.5	55.5
4	70.5	71.5	43.9
5	64.1	64.0	48.1
6	71.2	65.4	48.3
7	78.8	59.4	51.9
8	77.1	61.2	55.3
9	81.4	67.9	56.0
10	80.0	64.8	49.7
11	79.7	66.8	56.1
12	78.9	70.2	54.0
13	81.5	71.4	53.9
14	80.4	61.4	50.8
15	86.9	67.0	52.5
16	74.8	71.3	53.4
17	82.8	63.8	49.0
18	84.7	73.7	58.6
19	84.5	59.6	49.6
20	77.1	65.8	52.0

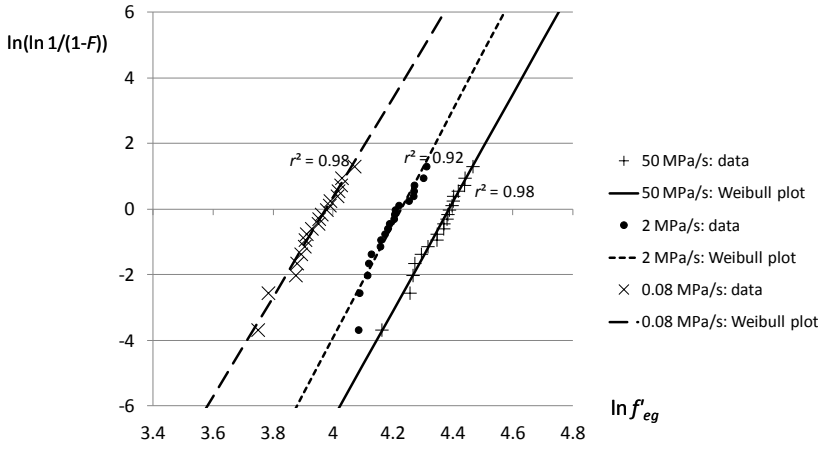

Figure B.1: Weibull plot for the series N1-a1,a2,a3.

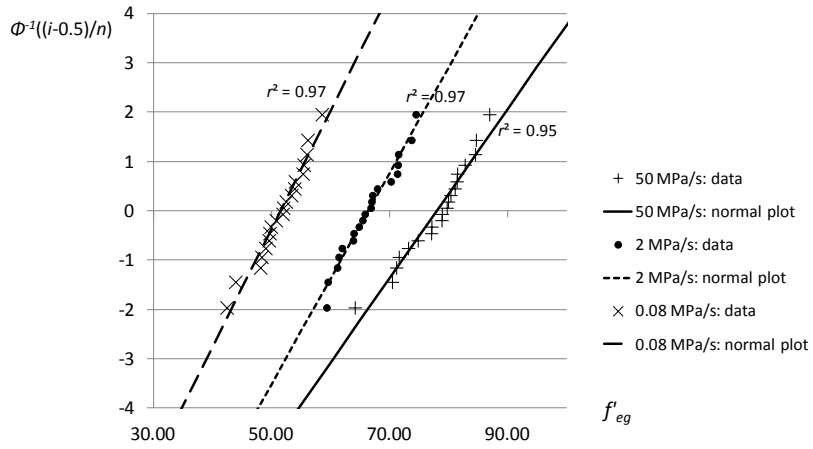

Figure B.2: normal plot for the series N1-a1,a2,a3.

Table B.2: failures stresses f'_{eg} [MPa] of series N1-b1,b2,b3.

Specimen number	N1-b1 50 MPa/s	N1-b2 2 MPa/s	N1-b3 0.08 MPa/s
1	82.3	67.2	56.1
2	81.8	67.2	56.1
3	81.2	70.3	58.2
4	75.0	64.1	52.8
5	77.8	67.2	55.3
6	85.5	67.3	56.5
7	82.8	63.7	58.9
8	86.3	66.5	44.2
9	83.0	77.1	50.6
10	90.4	64.6	53.6
11	82.6	64.7	55.5
12	87.6	70.8	51.3
13	93.7	81.2	55.9
14	91.0	77.3	51.0
15	74.6	67.8	53.9
16	81.0	68.2	58.5
17	96.3	65.9	53.5
18	96.0	64.2	47.7
19	89.6	67.5	56.6
20	89.5	60.4	51.9

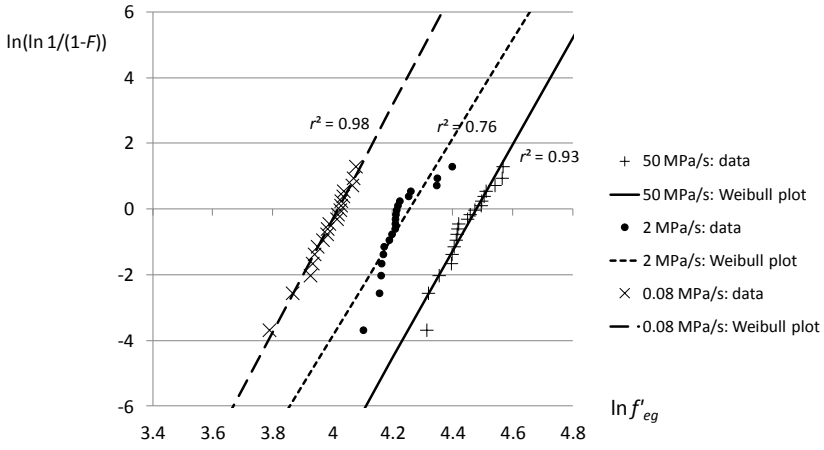

Figure B.3: Weibull plot for the series N1-b1,b2,b3.

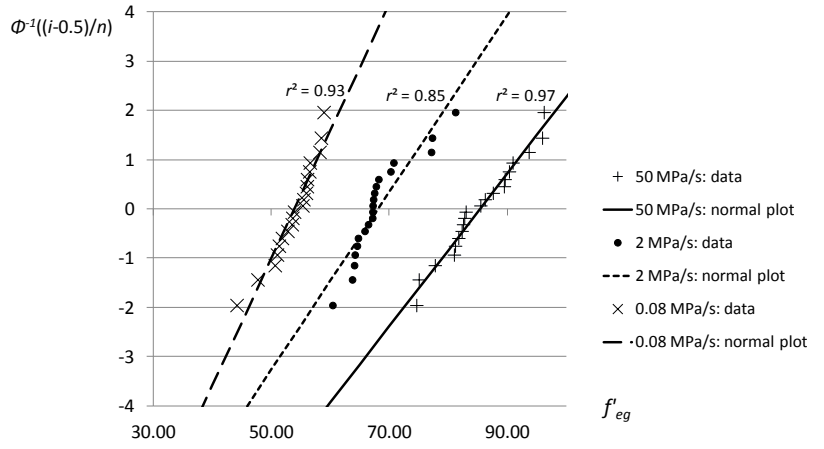

Figure B.4: normal plot for the series N1-b1,b2,b3.

Table B.3: failures stresses f'_{eg} [MPa] of series N1-c1,c2,c3.

Specimen number	N1-c1 50 MPa/s	N1-c2 2 MPa/s	N1-c3 0.08 MPa/s
1	79.2	73.2	65.5
2	87.1	81.3	60.5
3	84.9	79.5	62.4
4	95.6	76.1	57.4
5	96.4	60.7	56.7
6	93.9	74.7	57.4
7	78.2	80.5	61.0
8	57.7	73.3	59.9
9	84.1	73.7	53.4
10	91.1	79.3	58.4
11	90.3	73.8	63.6
12	93.5	73.6	57.1
13	100.8	78.0	69.9
14	94.4	80.4	52.8
15	100.8	82.5	59.0
16	86.7	88.6	58.5
17	90.9	87.0	67.1
18	76.2	59.6	52.9
19	80.8	74.0	61.7
20	51.1	67.3	61.6

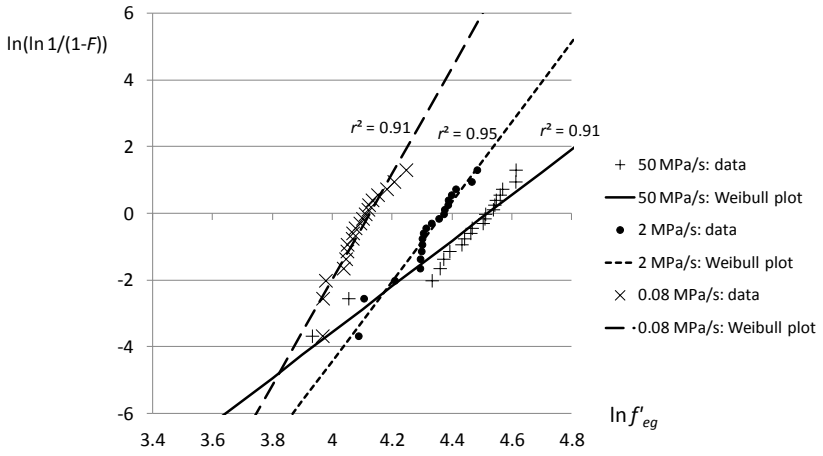

Figure B.5: Weibull plot for the series N1-c1,c2,c3.

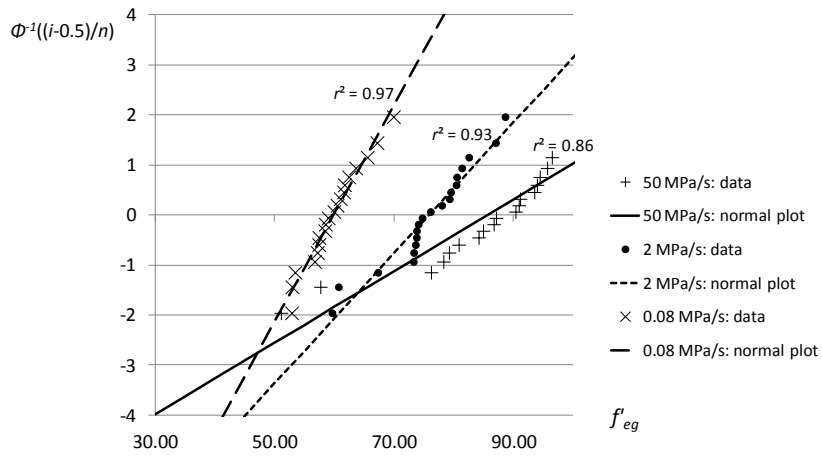

Figure B.6: normal plot for the series N1-c1,c2,c3.

Table B.4: failures stresses f'_{eg} [MPa] of series N1-d1,d2,d3.

Specimen number	N1-d1 50 MPa/s	N1-d2 2 MPa/s	N1-d3 0.08 MPa/s
1	98.5	73.7	64.2
2	99.8	81.1	65.0
3	81.0	76.2	57.5
4	71.5	75.9	57.4
5	92.0	71.4	58.7
6	85.6	82.5	61.3
7	80.8	76.1	67.5
8	87.0	73.0	41.8
9	93.0	78.9	62.6
10	87.9	80.4	60.9
11	80.7	69.2	59.6
12	77.5	73.4	65.1
13	95.2	74.1	70.1
14	97.4	80.1	38.6
15	72.4	70.2	61.0
16	72.0	71.8	64.8
17	95.6	75.2	59.9
18	80.7	77.3	52.0
19	71.8	70.0	60.9
20	82.4	70.9	55.1

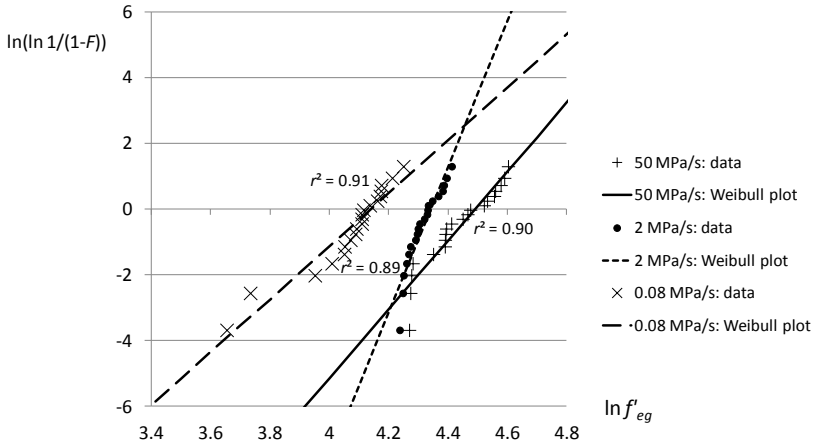

Figure B.7: Weibull plot for the series N1-d1,d2,d3.

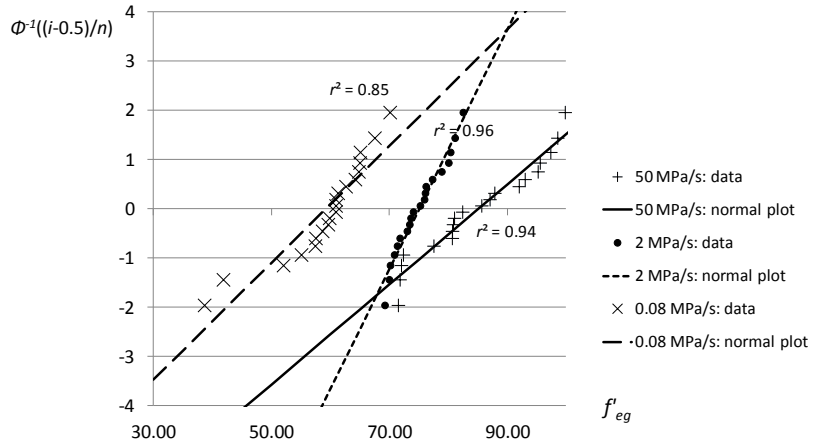

Figure B.8: normal plot for the series N1-d1,d2,d3.

Table B.5: failures stresses f'_{eg} [MPa] of series N2-b1,b2.

Specimen number	N2-b1 50 MPa/s	N1-b2 2 MPa/s
1	**44.2**	60.5
2	**51.2**	68.0
3	76.5	***47.6***
4	81.7	68.2
5	82.1	63.8
6	76.1	67.3
7	82.0	69.1
8	81.8	66.3
9	85.7	64.5
10	84.2	60.3
11	85.7	66.4
12	82.4	65.3
13	66.4	64.5
14	80.3	66.0
15	79.7	**67.4**
16	80.4	**70.4**
17	78.2	61.0
18	**61.4**	63.6
19	84.7	65.7
20	82.7	70.0

results in bold: failures at surface 0 or 5, excluded from the study
results in italic and bold: statistical outliers, excluded from the study

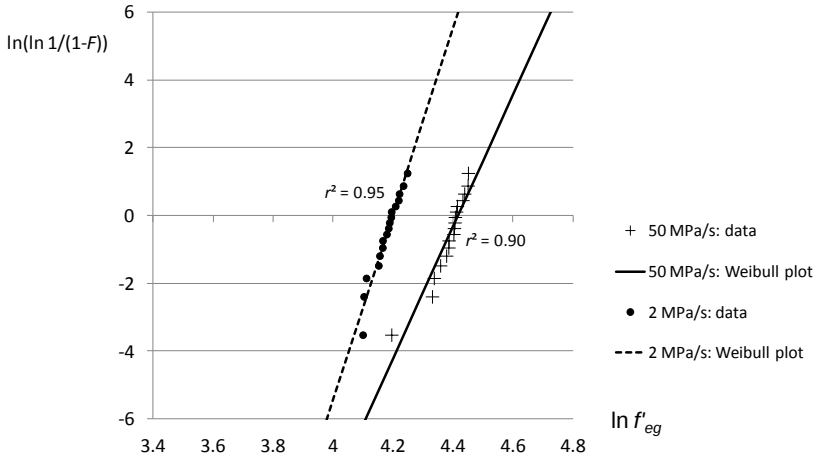

Figure B.9: Weibull plot for the series N2-b1,b2.

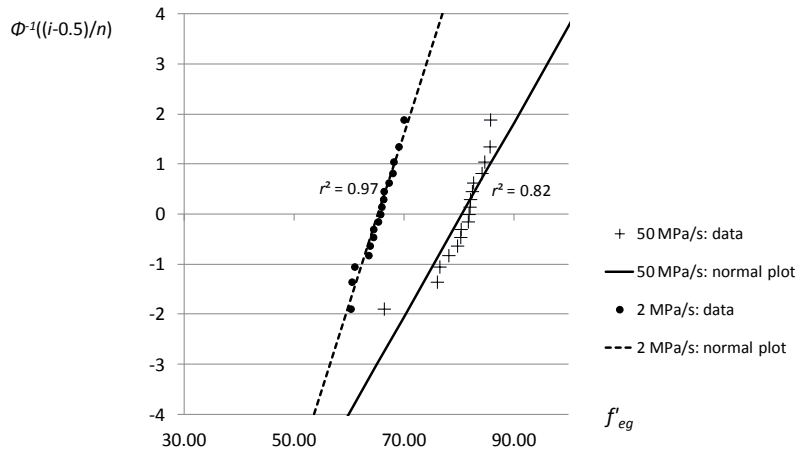

Figure B.10: normal plot for the series N2-b1,b2.

Table B.6: failures stresses f'_{eg} [MPa] of series N2-d1,d2.

Specimen number	N2-d1 50 MPa/s	N1-d2 2 MPa/s
1	73.7	64.0
2	76.3	65.7
3	71.0	53.8
4	67.2	62.1
5	73.2	61.8
6	76.7	63.5
7	72.1	59.6
8	72.9	59.7
9	76.3	68.2
10	75.8	65.3
11	75.9	55.6
12	69.4	49.5
13	76.1	61.7
14	77.2	64.6
15	66.9	52.5
16	79.0	66.9
17	79.8	63.4
18	77.0	64.5
19	71.1	55.9
20	***39.1***	60.6

results in italic and bold: statistical outliers, excluded from the study

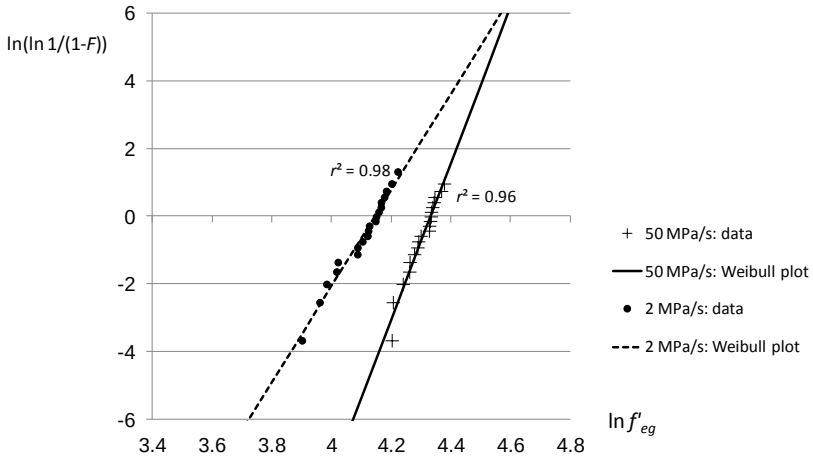

Figure B.11: Weibull plot for the series N2-d1,d2.

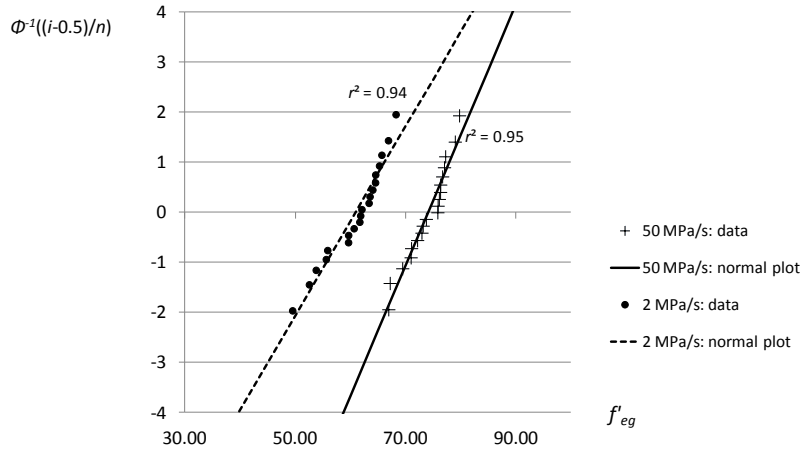

Figure B.12: normal plot for the series N2-d1,d2.

Table B.7: failures stresses f'_{eg} [MPa] of series G-a1,a2,a3.

Specimen number	G-a1 50 MPa/s	G-a2 2 MPa/s	G-a3 0.08 MPa/s
1	83.4	59.9	44.3
2	73.2	66.0	51.4
3	75.1	57.4	51.2
4	80.0	56.8	48.3
5	52.8	59.0	51.9
6	71.7	70.4	48.6
7	85.3	63.9	50.0
8	75.6	59.5	48.7
9	87.8	64.4	44.0
10	83.4	54.3	42.5
11	75.0	59.3	57.3
12	76.2	65.5	50.6
13	67.5	63.8	54.7
14	76.5	62.6	54.6
15	77.3	46.3	54.1
16	73.0	62.4	49.3
17	56.7	68.7	52.3
18	61.1	64.5	48.8
19	67.2	64.5	52.5
20	49.4	65.4	52.1

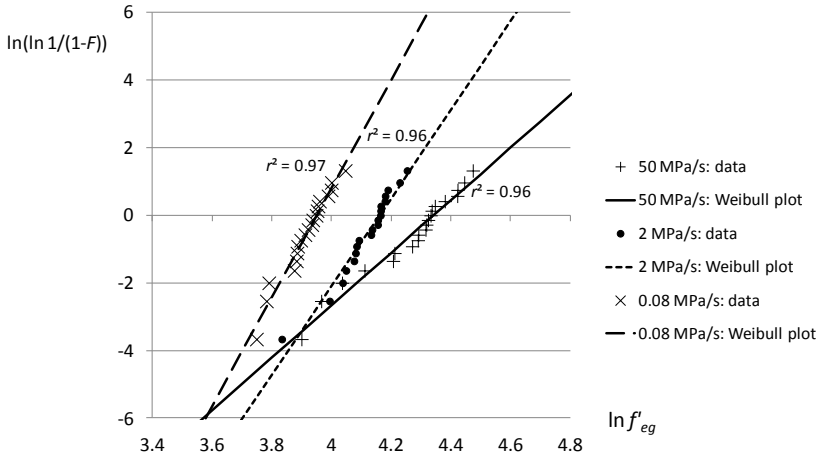

Figure B.13: Weibull plot for the series G-a1,a2,a3.

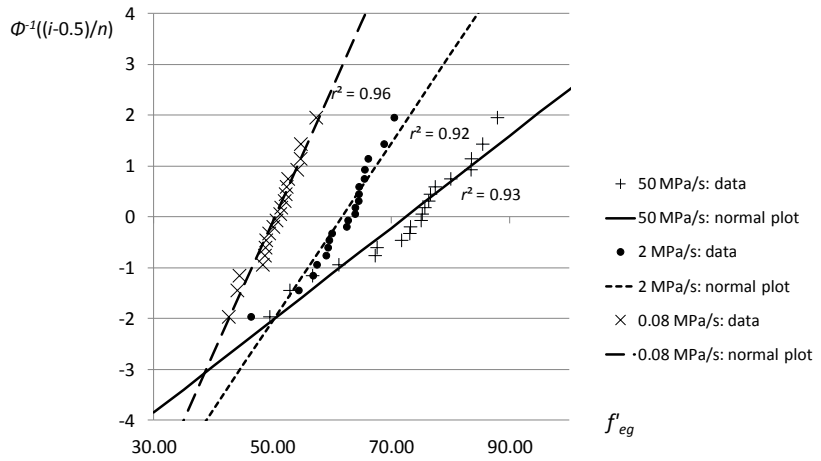

Figure B.14: normal plot for the series G-a1,a2,a3.

Table B.8: failures stresses f'_{eg} [MPa] of series G-b1,b2,b3.

Specimen number	G-b1	G-b2	G-b3
	50 MPa/s	2 MPa/s	0.08 MPa/s
1	80.2	**59.4**	56.6
2	69.4	53.9	57.2
3	82.7	69.7	54.2
4	79.4	71.3	**48.1**
5	74.0	66.6	56.5
6	65.1	64.5	**53.2**
7	82.8	67.7	53.1
8	87.2	61.1	57.9
9	**69.0**	61.6	54.6
10	63.3	66.0	48.2
11	76.5	67.5	54.0
12	64.3	66.3	50.4
13	80.3	65.4	50.4
14	**56.2**	62.9	43.6
15	58.1	68.7	53.1
16	66.2	68.3	54.9
17	65.0	63.3	53.5
18	75.6	54.7	47.0
19	84.6	71.3	59.2
20	71.1	75.8	39.9

results in bold: failures at surface 0 or 5, excluded from the study

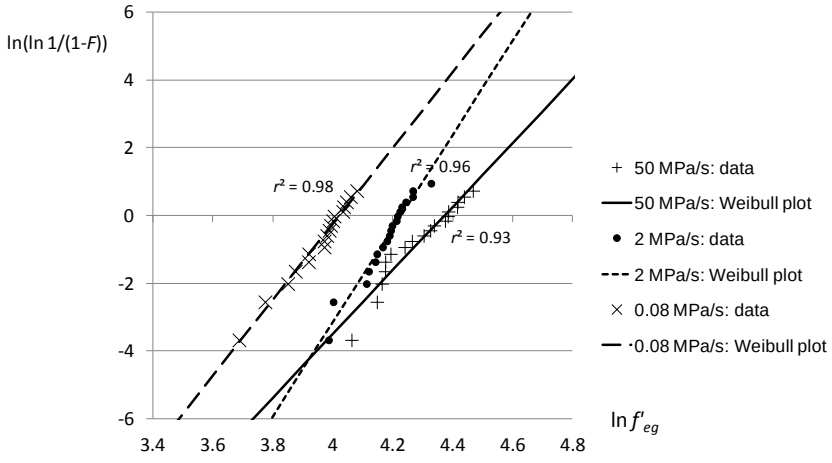

Figure B.15: Weibull plot for the series G-b1,b2,b3.

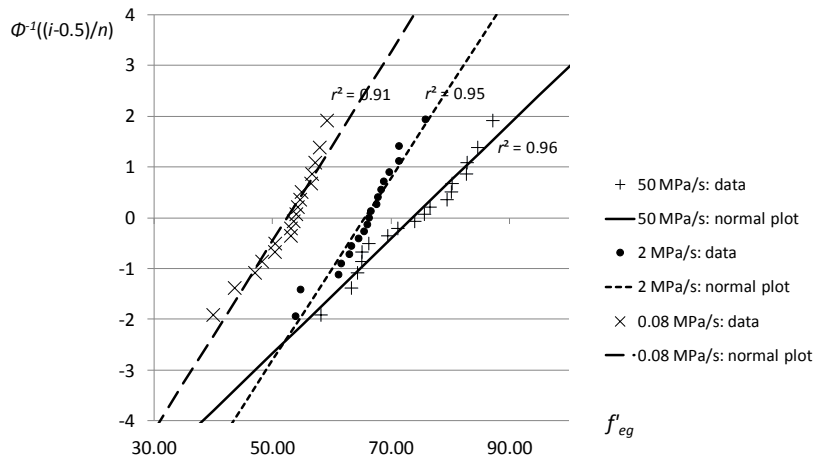

Figure B.16: normal plot for the series G-b1,b2,b3.

Table B.9: failures stresses f'_{eg} [MPa] of series G-c1,c2,c3.

Specimen number	G-c1 50 MPa/s	G-c2 2 MPa/s	G-c3 0.08 MPa/s
1	63.7	42.9	48.1
2	74.5	51.1	43.8
3	70.4	49.8	51.3
4	82.5	66.9	40.3
5	80.5	71.4	46.3
6	91.3	41.4	50.3
7	65.2	65.4	54.6
8	72.3	69.4	58.1
9	61.0	50.6	55.5
10	76.6	50.6	49.4
11	90.3	54.6	40.3
12	66.2	55.3	39.9
13	82.8	66.9	46.6
14	78.5	60.4	54.0
15	82.6	65.0	39.0
16	92.1	60.5	46.6
17	92.4	37.6	46.7
18	96.3	62.3	37.6
19	89.9	77.6	48.6
20	79.9	65.1	64.1

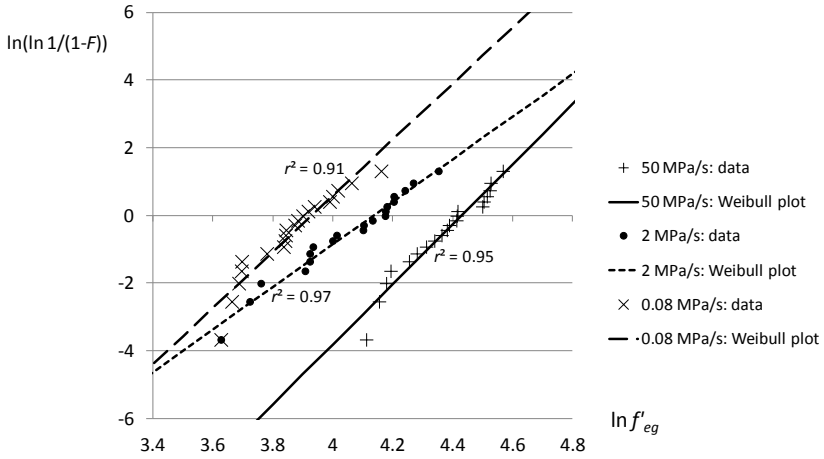

Figure B.17: Weibull plot for the series G-c1,c2,c3.

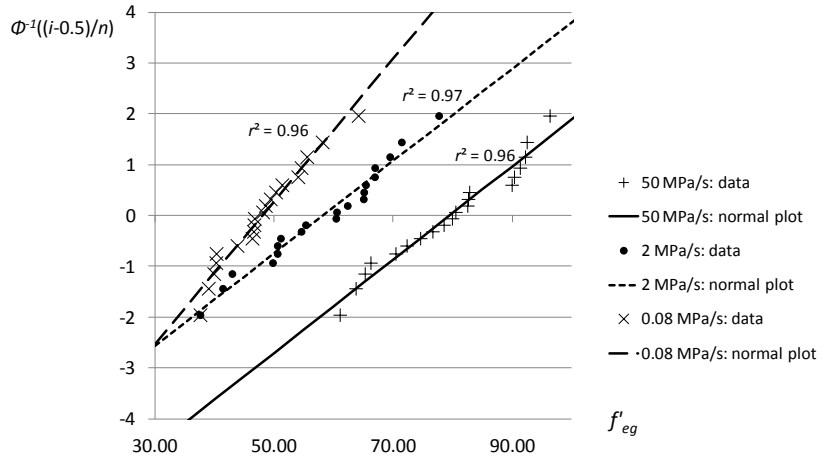

Figure B.18: normal plot for the series G-c1,c2,c3.

Table B.10: failures stresses f'_{eg} [MPa] of series G-d1,d2,d3.

Specimen number	G-d1 50 MPa/s	G-d2 2 MPa/s	G-d3 0.08 MPa/s
1	60.5	52.6	37.5
2	82.9	73.5	56.2
3	68.7	44.6	51.0
4	63.6	53.8	39.6
5	59.8	56.6	40.1
6	70.6	53.9	54.9
7	56.3	69.9	39.6
8	65.9	48.0	50.0
9	56.2	53.5	46.7
10	72.3	75.7	56.7
11	55.2	48.3	49.4
12	69.2	47.3	51.8
13	70.5	61.2	38.3
14	80.3	74.7	55.7
15	65.1	39.4	50.1
16	73.0	66.0	38.2
17	54.7	54.5	39.4
18	87.2	65.6	55.8
19	60.1	51.5	45.8
20	61.7	56.6	46.0

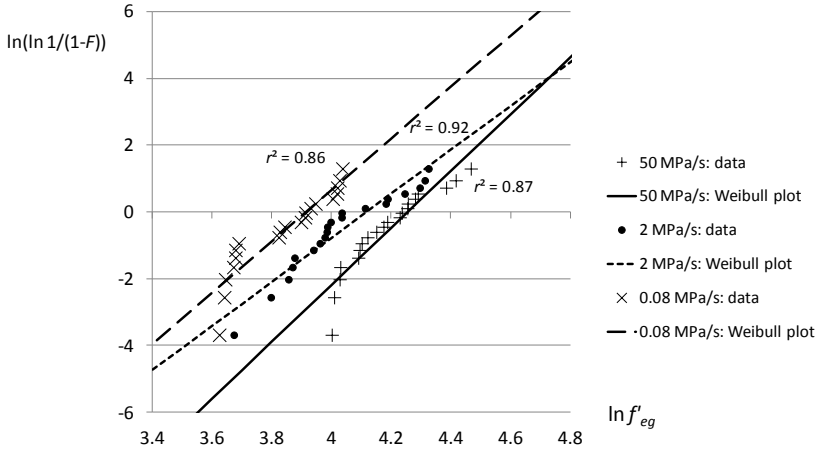

Figure B.19: Weibull plot for the series G-d1,d2,d3.

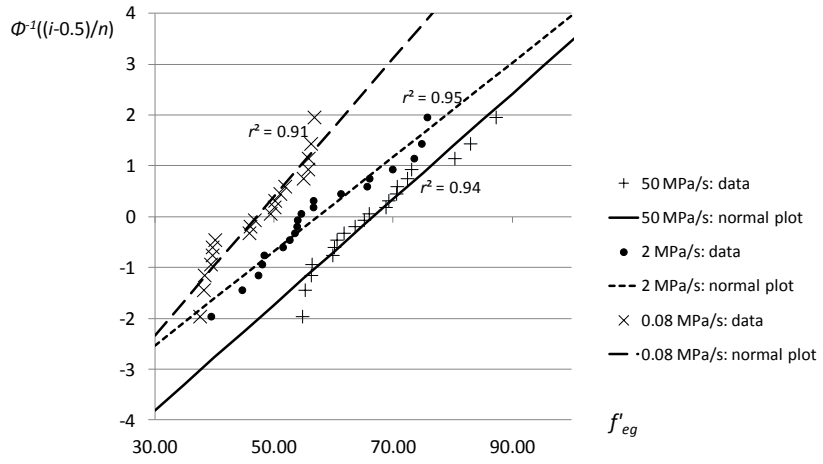

Figure B.20: normal plot for the series G-d1,d2,d3.

Table B.11: failures stresses f'_{eg} [MPa] of series A-b1,b2.

Specimen number	A-b1 50 MPa/s	A-b2 2 MPa/s
1	60.6	55.8
2	58.2	61.1
3	69.2	65.1
4	70.8	54.1
5	60.9	54.4
6	64.6	60.1
7	69.9	63.9
8	69.1	62.7
9	63.3	56.5
10	62.7	56.8
11	72.8	60.9
12	73.2	62.0
13	67.6	54.9
14	65.1	57.3
15	63.7	57.5
16	74.0	60.8
17	60.2	57.8
18	65.7	53.8
19	76.8	64.4
20	71.0	60.0

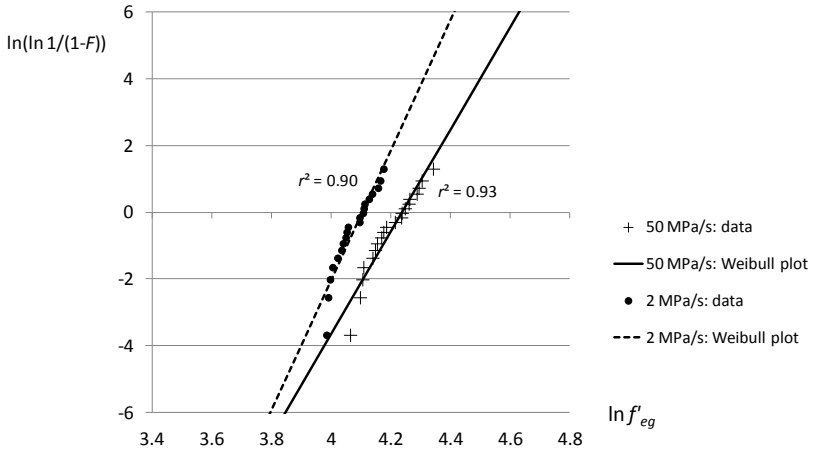

Figure B.21: Weibull plot for the series A-b1,b2.

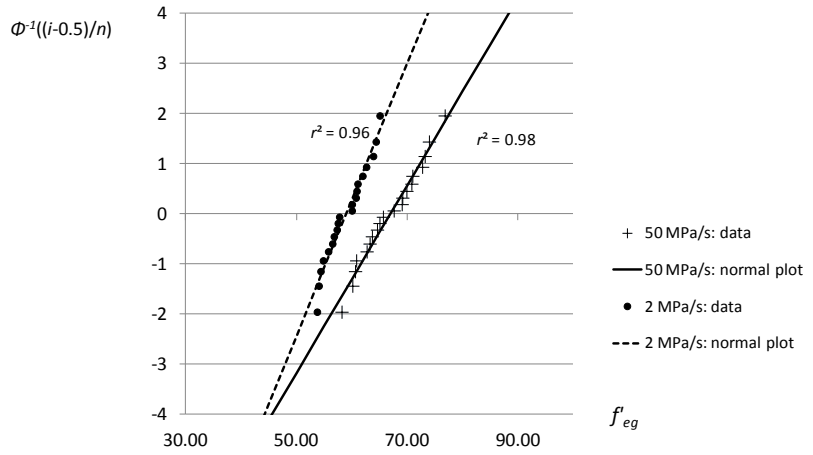

Figure B.22: normal plot for the series A-b1,b2.

Table B.12: failures stresses f'_{eg} [MPa] of series A-d1,d2.

Specimen number	A-d1 50 MPa/s	A-d2 2 MPa/s
1	69.0	53.0
2	65.3	53.4
3	61.3	50.6
4	69.5	53.8
5	67.1	38.1
6	62.8	49.7
7	62.3	54.4
8	63.0	55.6
9	63.8	51.1
10	60.8	54.8
11	65.4	52.1
12	55.4	51.9
13	64.6	57.8
14	66.8	47.4
15	58.8	56.0
16	59.8	52.4
17	59.4	52.7
18	63.9	53.6
19	66.0	51.0
20	56.4	55.3

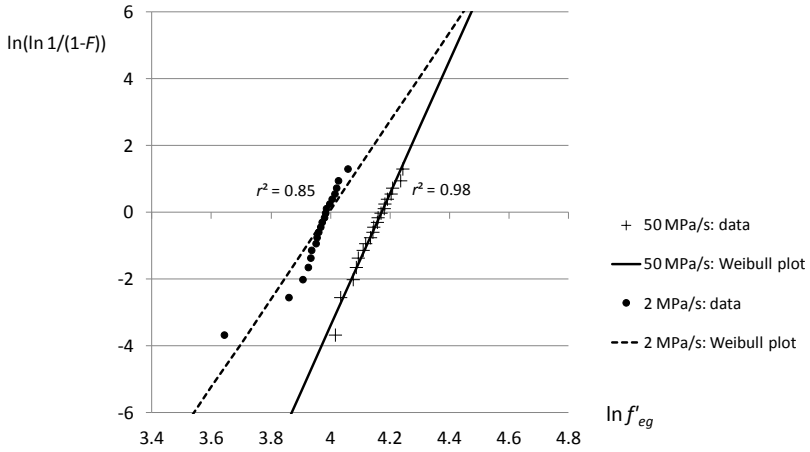

Figure B.23: Weibull plot for the series A-d1,d2.

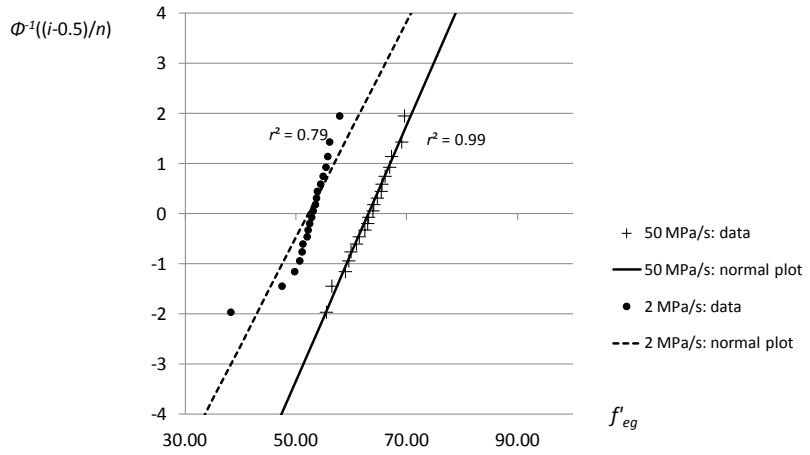

Figure B.24: normal plot for the series A-d1,d2.

Table B.13: failures stresses f'_{eg} [MPa] of series C1-a1,a2,a3.

Specimen number	C1-a1 50 MPa/s	C1-a2 2 MPa/s	C1-a3 0.08 MPa/s
1	82.2	66.1	55.8
2	84.5	74.8	55.7
3	78.4	65.9	54.9
4	85.4	68.1	36.9
5	89.6	66.7	51.0
6	83.8	74.3	59.6
7	55.5	77.4	52.1
8	88.7	70.0	55.1
9	72.6	67.0	61.7
10	90.5	65.8	36.2
11	60.9	68.3	49.2
12	71.6	77.2	60.3
13	73.4	67.0	53.9
14	85.8	76.6	56.0
15	80.6	69.8	54.7
16	88.2	66.4	55.4
17	90.9	54.8	66.8
18	90.6	62.3	44.5
19	78.4	67.9	60.8
20	-	68.1	46.4

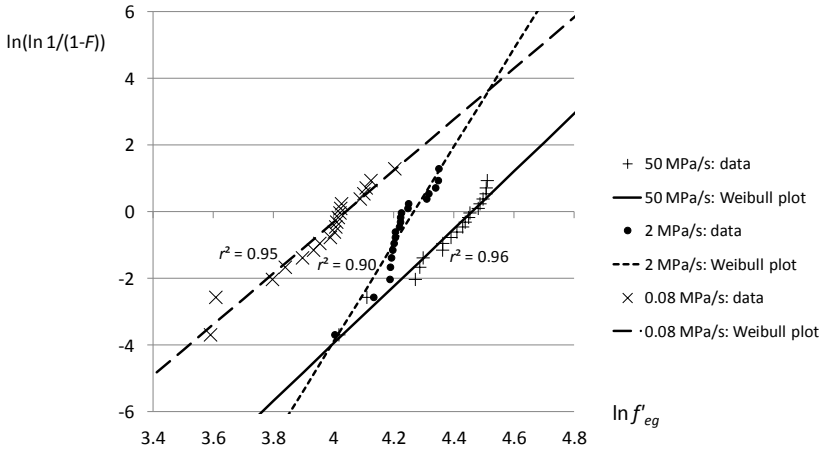

Figure B.25: Weibull plot for the series C1-a1,a2,a3.

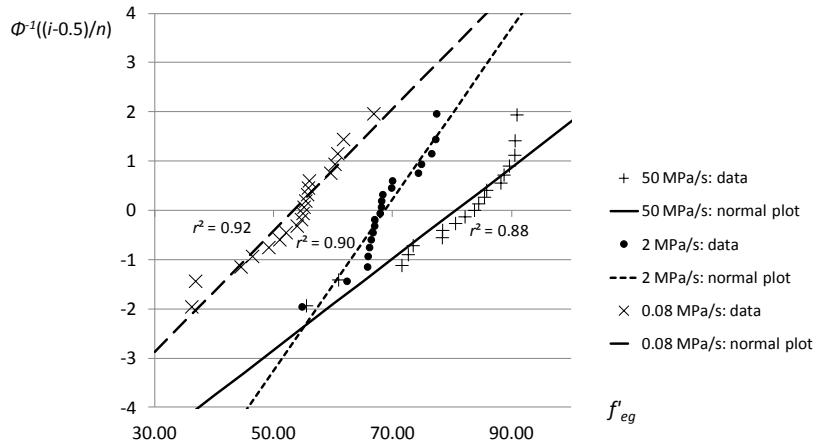

Figure B.26: normal plot for the series C1-a1,a2,a3.

Table B.14: failures stresses f'_{eg} [MPa] of series C1-b1,b2,b3.

Specimen number	C1-b1 50 MPa/s	C1-b2 2 MPa/s	C1-b3 0.08 MPa/s
1	**48.8**	67.8	52.9
2	**48.5**	**45.3**	**38.1**
3	77.5	61.8	50.0
4	81.0	67.1	36.4
5	60.7	70.7	49.3
6	70.5	56.9	49.4
7	63.3	51.1	49.7
8	55.6	56.3	56.0
9	80.2	52.4	58.1
10	58.1	74.9	55.1
11	116.0	55.4	58.9
12	107.6	53.5	44.0
13	53.0	69.2	60.9
14	66.9	55.9	57.9
15	77.5	79.0	38.5
16	68.8	58.8	72.4
17	55.4	64.0	49.1
18	57.6	42.3	51.0
19	95.6	51.1	68.1
20	79.0	45.1	-

results in bold: failures at surface 0 or 5, excluded from the study

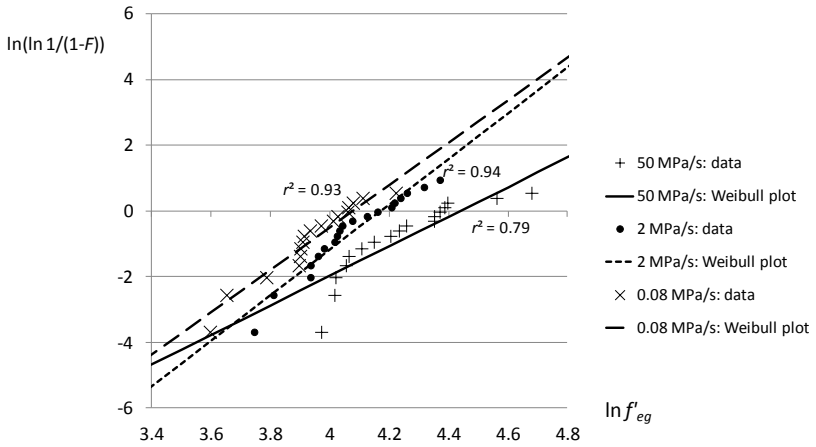

Figure B.27: Weibull plot for the series C1-b1,b2,b3.

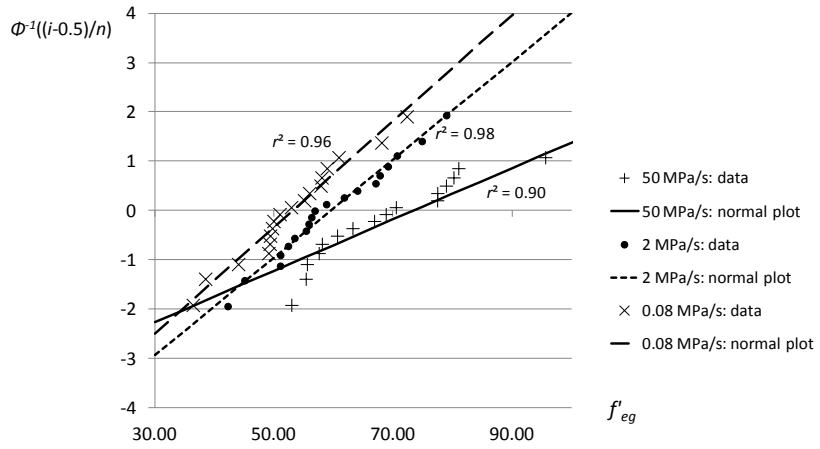

Figure B.28: normal plot for the series C1-b1,b2,b3.

Table B.15: failures stresses f'_{eg} [MPa] of series C1-c1,c2,c3.

Specimen number	C1-c1 50 MPa/s	C1-c2 2 MPa/s	C1-c3 0.08 MPa/s
1	47.3	46.6	39.3
2	50.6	44.3	41.9
3	47.9	48.1	38.1
4	52.4	43.0	37.3
5	49.1	46.9	48.7
6	48.1	44.9	42.9
7	51.0	44.6	41.9
8	50.7	43.1	40.0
9	49.8	46.5	39.0
10	52.7	48.7	49.4
11	51.5	46.1	38.8
12	49.5	46.3	37.2
13	51.3	46.9	50.1
14	54.5	48.5	37.5
15	53.5	46.3	38.5
16	53.2	43.2	-
17	48.7	45.4	-
18	51.2	44.1	-
19	***65.1***	43.9	-
20	54.1	44.8	-

results in italic and bold: statistical outliers, excluded from the study

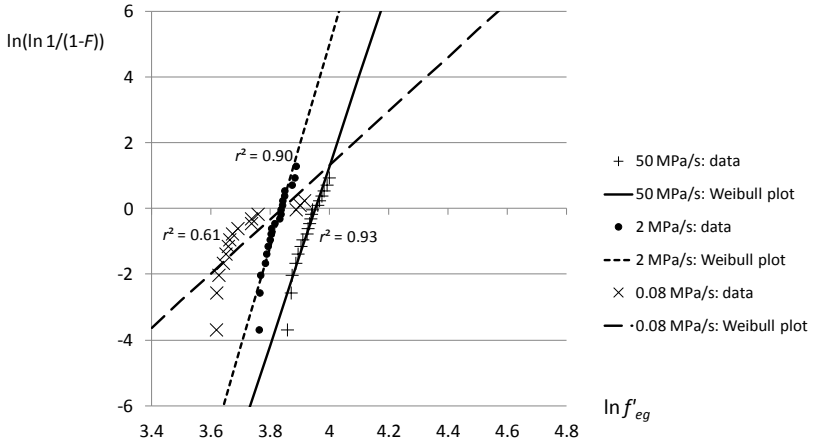

Figure B.29: Weibull plot for the series C1-c1,c2,c3.

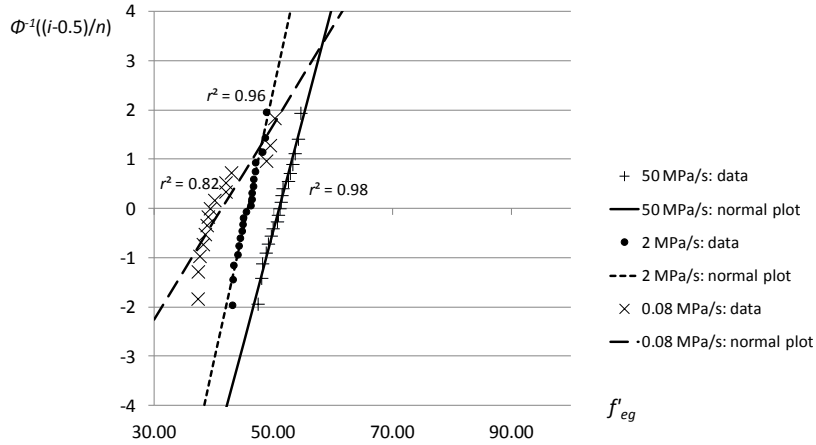

Figure B.30: normal plot for the series C1-c1,c2,c3.

Table B.16: failures stresses f'_{eg} [MPa] of series C1-d1,d2,d3.

Specimen number	C1-d1 50 MPa/s	C1-d2 2 MPa/s	C1-d3 0.08 MPa/s
1	49.4	44.1	38.7
2	47.9	44.4	34.3
3	48.1	42.1	38.0
4	47.6	45.1	40.4
5	49.9	44.1	37.4
6	52.4	44.1	38.2
7	46.7	44.6	37.7
8	50.4	44.9	35.2
9	51.0	44.1	37.1
10	53.1	41.9	38.6
11	50.8	46.1	39.7
12	55.0	44.1	39.8
13	46.8	45.4	35.7
14	48.0	48.4	37.5
15	43.5	46.8	39.2
16	50.0	44.0	34.9
17	45.8	46.0	41.0
18	52.9	44.5	42.5
19	51.3	43.2	38.9
20	53.0	44.0	40.3

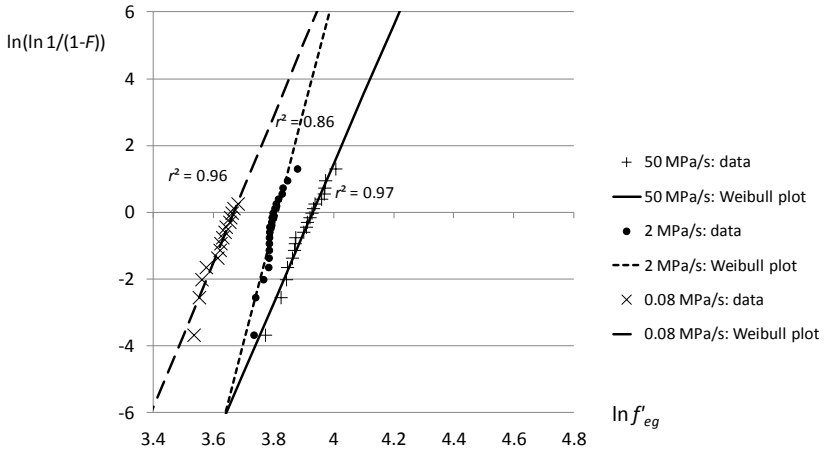

Figure B.31: Weibull plot for the series C1-d1,d2,d3.

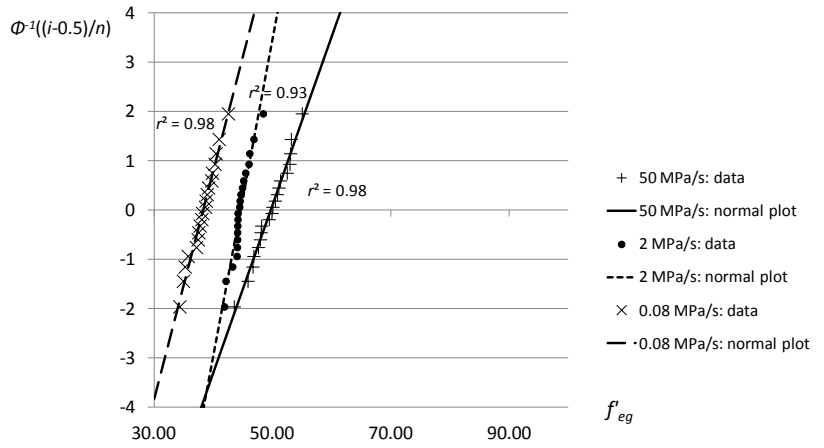

Figure B.32: normal plot for the series C1-d1,d2,d3.

Table B.17: failures stresses f'_{eg} [MPa] of series C2-b1,b2.

Specimen number	C2-b1 50 MPa/s	C2-b2 2 MPa/s
1	86.1	66.8
2	88.6	67.9
3	98.2	78.3
4	103.0	52.9
5	92.4	68.1
6	76.7	78.2
7	85.8	71.8
8	96.3	78.4
9	80.5	64.3
10	69.4	65.4
11	86.7	73.2
12	100.3	63.5
13	92.7	61.6
14	73.1	71.8
15	91.6	73.6
16	89.5	74.2
17	99.9	72.8
18	***46.7***	70.1
19	85.0	58.4
20	100.3	58.5

results in italic and bold: statistical outliers, excluded from the study

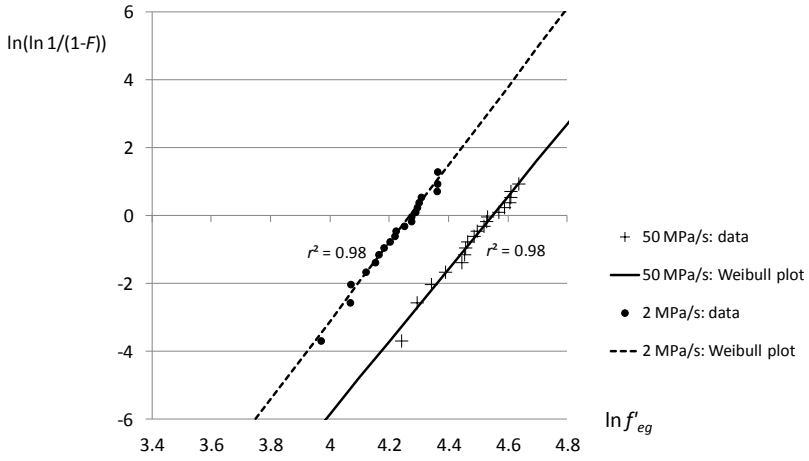

Figure B.33: Weibull plot for the series C2-b1,b2.

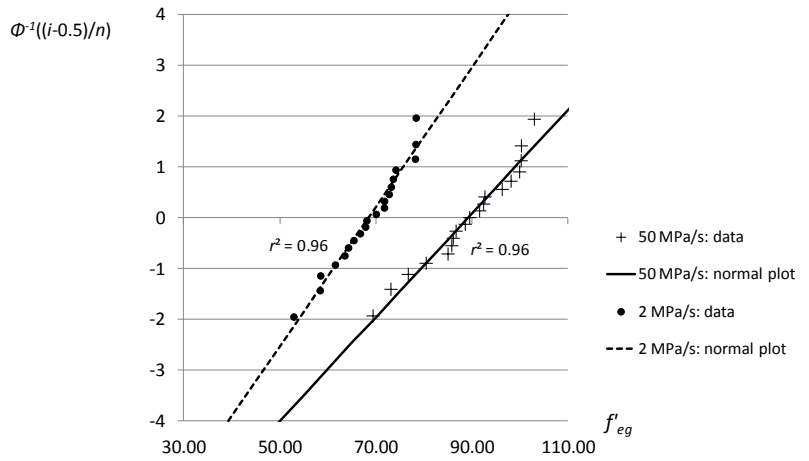

Figure B.34: normal plot for the series C2-b1,b2.

Table B.18: failures stresses f'_{eg} [MPa] of series C2-d1,d2.

Specimen number	C2-d1 50 MPa/s	C2-d2 2 MPa/s
1	56.5	69.1
2	81.4	69.7
3	75.8	63.3
4	86.5	62.3
5	73.4	54.5
6	47.9	68.8
7	80.7	62.8
8	84.3	60.8
9	85.6	66.6
10	61.6	68.0
11	86.6	68.3
12	81.9	67.3
13	74.8	70.3
14	48.3	67.9
15	74.4	69.5
16	77.4	64.5
17	78.2	65.3
18	58.8	61.7
19	85.6	61.0
20	70.6	63.1

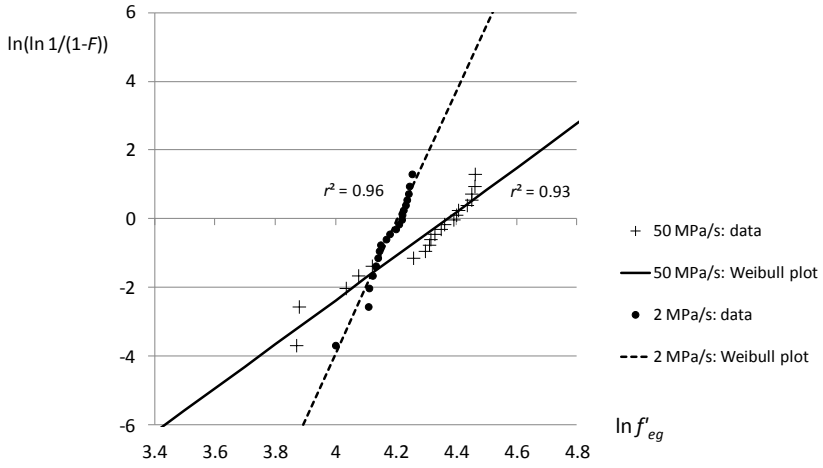

Figure B.35: Weibull plot for the series C2-d1,d2.

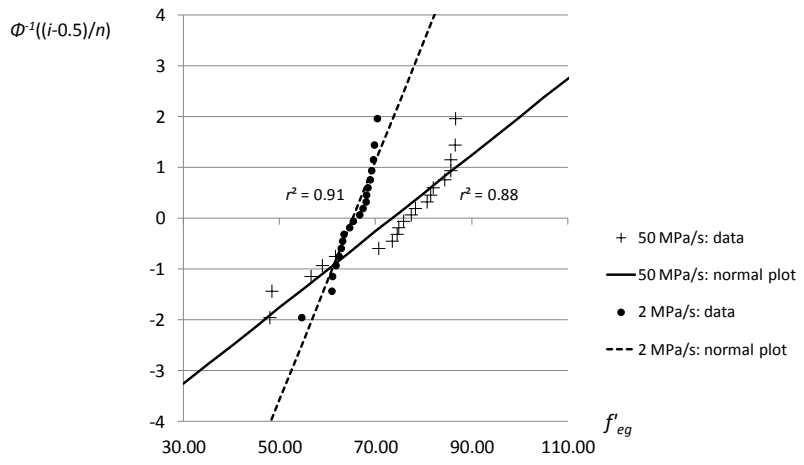

Figure B.36: normal plot for the series C2-d1,d2.

Table B.19: Estimation of the Weibull and normal parameters of all series (50 MPa/s).

Series	LSM (Weibull distribution)				LSM (normal distribution)			
	ϑ'_0	m'_0	V	r^2	$f'_{eg,m}$	σ	V	r^2
	[MPa]	[-]	[-]	[-]	[MPa]	[MPa]	[-]	[-]
N1-a1	80.5	16.5	0.08	0.98	78.0	5.7	0.07	0.95
N1-b1	88.2	16.2	0.08	0.93	85.4	6.3	0.07	0.97
N1-c1	91.8	6.9	0.20	0.91	85.7	12.9	0.15	0.86
N1-d1	89.3	10.5	0.12	0.90	85.1	9.5	0.11	0.94
N2-b1	82.8	19.4	0.08	0.90	80.6	4.6	0.06	0.82
N2-d1	76.1	23.1	0.06	0.96	74.1	3.7	0.05	0.95
G-a1	77.0	7.8	0.17	0.96	72.4	10.6	0.15	0.93
G-b1	79.2	9.4	0.13	0.93	73.7	8.6	0.12	0.96
G-c1	83.9	8.9	0.15	0.95	79.5	10.6	0.13	0.96
G-d1	70.6	8.5	0.14	0.87	66.7	9.3	0.14	0.94
A-b1	69.3	15.3	0.08	0.93	67.0	5.2	0.08	0.98
A-d1	64.8	19.9	0.07	0.98	63.1	3.9	0.06	0.99
C1-a1	86.3	8.6	0.15	0.96	80.6	10.0	0.12	0.88
C1-b1	84.7	4.5	0.23	0.79	73.6	18.0	0.25	0.90
C1-c1	52.1	27.3	0.05	0.93	50.9	2.1	0.04	0.98
C1-d1	51.0	20.9	0.06	0.97	49.7	2.9	0.06	0.98
C2-b1	94.4	10.7	0.12	0.98	89.3	9.5	0.11	0.96
C2-d1	79.0	6.4	0.21	0.93	73.5	12.4	0.17	0.88

Table B.20: Estimation of the Weibull and normal parameters of all series (2 MPa/s).

Series	LSM (Weibull distribution)				LSM (normal distribution)			
	ϑ'_0	m'_0	V	r^2	$f'_{eg,m}$	σ	V	r^2
	[MPa]	[-]	[-]	[-]	[MPa]	[MPa]	[-]	[-]
N1-a2	68.5	17.3	0.08	0.92	66.4	4.6	0.07	0.97
N1-b2	70.6	15.0	0.08	0.76	68.2	5.1	0.07	0.85
N1-c2	79.1	12.0	0.11	0.95	75.8	7.4	0.10	0.93
N1-d2	76.9	22.2	0.06	0.89	75.1	4.0	0.05	0.96
N2-b2	66.6	27.5	0.05	0.95	65.3	2.9	0.04	0.97
N2-d2	63.2	14.2	0.10	0.98	60.9	5.1	0.08	0.94
G-a2	64.2	13.0	0.11	0.96	61.7	5.4	0.09	0.92
G-b2	68.6	13.8	0.09	0.96	65.6	5.4	0.08	0.95
G-c2	62.6	6.3	0.20	0.97	58.2	10.8	0.18	0.97
G-d2	61.5	6.6	0.19	0.92	57.4	10.4	0.18	0.95
A-b2	60.6	19.5	0.07	0.90	59.0	3.6	0.06	0.96
A-d2	54.3	13.3	0.11	0.85	52.2	4.1	0.08	0.79
C1-a2	71.2	14.6	0.09	0.90	68.7	5.4	0.08	0.90
C1-b2	64.8	6.9	0.17	0.94	59.7	9.9	0.17	0.98
C1-c2	46.4	30.8	0.04	0.90	45.6	1.8	0.04	0.96
C1-d2	45.3	34.8	0.03	0.86	44.6	1.5	0.03	0.93
C2-b2	71.5	11.5	0.12	0.98	68.5	7.1	0.10	0.96
C2-d2	67.1	19.1	0.07	0.96	65.3	4.0	0.06	0.91

Table B.21: Estimation of the Weibull and normal parameters of all series (0.08 MPa/s).

Series	LSM (Weibull distribution)				LSM (normal distribution)			
	ϑ'_0	m'_0	V	r^2	$f'_{eg,m}$	σ	V	r^2
	[MPa]	[-]	[-]	[-]	[MPa]	[MPa]	[-]	[-]
N1-a3	53.3	15.1	0.09	0.98	51.6	4.1	0.08	0.97
N1-b3	55.6	17.2	0.08	0.98	53.9	3.7	0.07	0.93
N1-c3	61.8	15.8	0.08	0.91	59.8	4.5	0.08	0.97
N1-d3	62.9	8.1	0.17	0.91	59.2	7.7	0.13	0.85
G-a3	52.0	16.1	0.08	0.97	50.4	3.7	0.07	0.96
G-b3	55.8	11.2	0.12	0.98	52.5	5.1	0.07	0.91
G-c3	50.9	8.3	0.14	0.91	48.1	6.9	0.14	0.96
G-d3	50.2	7.7	0.17	0.86	47.1	7.0	0.15	0.91
C1-a3	56.8	7.7	0.17	0.95	53.4	7.8	0.15	0.92
C1-b3	59.0	6.5	0.18	0.93	53.2	9.1	0.17	0.96
C1-c3	46.6	8.2	0.12	0.61	41.4	4.5	0.11	0.82
C1-d3	39.2	21.8	0.06	0.96	38.3	2.1	0.06	0.98

Table B.22: Estimation of the characteristic 5 % value of all series (confidence level γ of 0.75) with the coverage method.

Series*	LSM (Weibull distribution)			LSM (normal distribution)		
$f'_{eg,k}$	50	2	0.08	50	2	0.08
[MPa]	MPa/s	MPa/s	MPa/s	MPa/s	MPa/s	MPa/s
N1-a1,2,3	65.2	56.1	42.2	67.1	57.6	43.6
N1-b1,2,3	71.2	56.7	45.6	73.2	58.4	46.8
N1-c1,2,3	56.7	59.1	49.6	60.9	61.6	51.1
N1-d1,2,3	63.7	66.1	41.8	66.9	67.4	44.3
N2-b1,2	70.5	58.8	-	71.6	59.8	-
N2-d1,2	65.7	49.5	-	67.0	51.1	-
G-a1,2,3	48.5	49.4	41.8	52.0	51.2	43.1
G-b1,2,3	54.0	53.4	40.8	56.9	55.2	42.5
G-c1,2,3	55.5	33.9	32.3	59.0	37.4	34.6
G-d1,2,3	45.7	33.7	31.4	48.8	37.2	33.7
A-b1,2	55.2	50.8	-	56.9	52.0	-
A-d1,2	54.4	43.0	-	55.7	44.3	-
C1-a1,2,3	57.8	56.5	35.8	61.2	58.3	38.4
C1-b1,2,3	32.4	37.1	38.3	38.5	40.5	40.5
C1-c1,2,3	46.1	41.6	30.8	46.8	42.2	32.4
C1-d1,2,3	43.2	41.2	33.5	44.2	41.7	34.2
C2-b1,2	67.7	52.4	-	70.9	54.8	-
C2-d1,2	45.5	56.1	-	49.6	57.4	-

*index 1, 2, 3 indicates a stress rate of 50 MPa/s, 2 MPa/s and 0.08 MPa/s, respectively

Table B.23: Time to failure and Weibull scale parameter for all series.

Series*	time to failure (s)			ϑ'_0 (MPa)		
	t_{f1}	t_{f2}	t_{f3}	ϑ_1'	ϑ_2'	ϑ_3'
N1-a1,2,3	1.57	32.7	621	80.5	68.5	53.3
N1-b1,2,3	1.68	34.5	684	88.2	70.6	55.6
N1-c1,2,3	1.76	37.4	748	91.8	79.1	61.8
N1-d1,2,3	1.73	38.0	749	89.3	76.9	62.9
N2-b1,2	1.65	33.0	-	82.8	66.6	-
N2-d1,2	1.50	30.3	-	76.1	63.2	-
G-a1,2,3	1.45	30.8	611	77.0	64.2	52.0
G-b1,2,3	1.51	33.1	658	79.2	68.6	55.8
G-c1,2,3	1.61	28.7	597	83.9	62.6	50.9
G-d1,2,3	1.35	28.5	586	70.6	61.5	50.2
A-b1,2	1.37	28.7	-	69.3	60.6	-
A-d1,2	1.27	25.7	-	64.8	54.3	-
C1-a1,2,3	1.63	34.2	659	86.3	71.2	56.8
C1-b1,2,3	1.52	30.2	673	84.7	64.8	59.0
C1-c1,2,3	1.03	22.6	510	52.1	46.4	46.6
C1-d1,2,3	1.01	22.1	477	51.0	45.3	39.2
C2-b1,2	1.83	34.5	-	94.4	71.5	-
C2-d1,2	1.49	32.5	-	79.0	67.1	-

*index 1, 2, 3 indicates a stress rate of 50 MPa/s, 2 MPa/s and 0.08 MPa/s, respectively

Table B.24: ratios of the times to failure and the Weibull scale parameters for all series.

Series*	ratio of times to failure (-)		ratio of ϑ'_0 (-)	
	t_{f2}/t_{f1}	t_{f3}/t_{f2}	$\vartheta_2'/\vartheta_1'$	$\vartheta_3'/\vartheta_2'$
N1-a1,2,3	20.85	18.99	0.85	0.78
N1-b1,2,3	20.54	19.82	0.80	0.79
N1-c1,2,3	21.25	20.01	0.86	0.78
N1-d1,2,3	22.01	19.70	0.86	0.82
N2-b1,2	20.06	-	0.80	-
N2-d1,2	20.23	-	0.83	-
G-a1,2,3	21.27	19.87	0.83	0.81
G-b1,2,3	21.98	19.88	0.87	0.81
G-c1,2,3	17.82	20.77	0.75	0.81
G-d1,2,3	21.07	20.57	0.87	0.82
A-b1,2	20.98	-	0.87	-
A-d1,2	20.23	-	0.84	-
C1-a1,2,3	21.03	19.28	0.82	0.80
C1-b1,2,3	19.86	22.33	0.76	0.91
C1-c1,2,3	22.01	22.58	0.89	1.00
C1-d1,2,3	21.79	21.60	0.89	0.87
C2-b1,2	18.91	-	0.76	-
C2-d1,2	21.78	-	0.85	-
mean value	20.61		0.83	

*index 1, 2, 3 indicates a stress rate of 50 MPa/s, 2 MPa/s and 0.08 MPa/s, respectively

Table B.25: Time to failure and mean strength value $f'_{eg,m}$ for all series.

Series*	time to failure (s)			$f'_{eg,m}$ (MPa)		
	t_{f1}	t_{f2}	t_{f3}	$f'_{eg,m,1}$	$f'_{eg,m,2}$	$f'_{eg,m,3}$
N1-a1,2,3	1.57	32.7	621	78.0	66.4	51.6
N1-b1,2,3	1.68	34.5	684	85.4	68.2	53.9
N1-c1,2,3	1.76	37.4	748	85.7	75.8	59.8
N1-d1,2,3	1.73	38.0	749	85.1	75.1	59.2
N2-b1,2	1.65	33.0	-	80.6	65.3	-
N2-d1,2	1.50	30.3	-	74.1	60.9	-
G-a1,2,3	1.45	30.8	611	72.4	61.7	50.4
G-b1,2,3	1.51	33.1	658	73.7	65.6	52.5
G-c1,2,3	1.61	28.7	597	79.5	58.2	48.1
G-d1,2,3	1.35	28.5	586	66.7	57.4	47.1
A-b1,2	1.37	28.7	-	67.0	59.0	-
A-d1,2	1.27	25.7	-	63.1	52.2	-
C1-a1,2,3	1.63	34.2	659	80.6	68.7	53.4
C1-b1,2,3	1.52	30.2	673	73.6	59.7	53.2
C1-c1,2,3	1.03	22.6	510	50.9	45.6	41.4
C1-d1,2,3	1.01	22.1	477	49.7	44.6	38.3
C2-b1,2	1.83	34.5	-	89.3	68.5	-
C2-d1,2	1.49	32.5	-	73.5	65.3	-

*index 1, 2, 3 indicates a stress rate of 50 MPa/s, 2 MPa/s and 0.08 MPa/s, respectively

Table B.26: ratios of the times to failure and the mean strength values for all series.

Series*	ratio of times to failure (-)		ratio of $f'_{eg,m}$ (-)	
	t_{f2}/t_{f1}	t_{f3}/t_{f2}	$f'_{eg,m,2}/f'_{eg,m,1}$	$f'_{eg,m,3}/f'_{eg,m,2}$
N1-a1,2,3	20.85	18.99	0.85	0.78
N1-b1,2,3	20.54	19.82	0.80	0.79
N1-c1,2,3	21.25	20.01	0.89	0.79
N1-d1,2,3	22.01	19.70	0.88	0.79
N2-b1,2	20.06	-	0.81	-
N2-d1,2	20.23	-	0.82	-
G-a1,2,3	21.27	19.87	0.85	0.82
G-b1,2,3	21.98	19.88	0.89	0.80
G-c1,2,3	17.82	20.77	0.73	0.83
G-d1,2,3	21.07	20.57	0.86	0.82
A-b1,2	20.98	-	0.88	-
A-d1,2	20.23	-	0.83	-
C1-a1,2,3	21.03	19.28	0.85	0.78
C1-b1,2,3	19.86	22.33	0.81	0.89
C1-c1,2,3	22.01	22.58	0.90	0.91
C1-d1,2,3	21.79	21.60	0.90	0.86
C2-b1,2	18.91	-	0.77	-
C2-d1,2	21.78	-	0.77	-
mean value	20.61		0.83	

*index 1, 2, 3 indicates a stress rate of 50 MPa/s, 2 MPa/s and 0.08 MPa/s, respectively

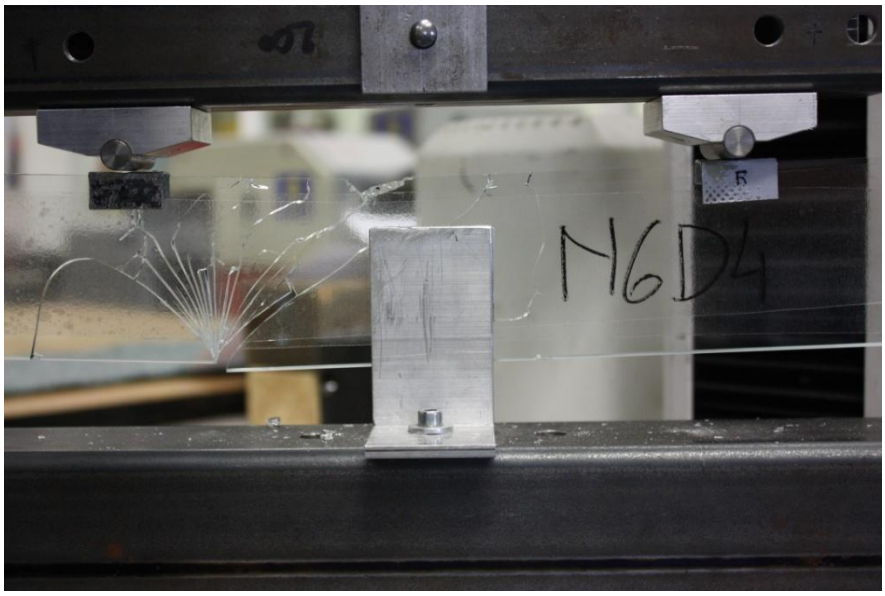

Figure B.37: failure after a 4PB test.

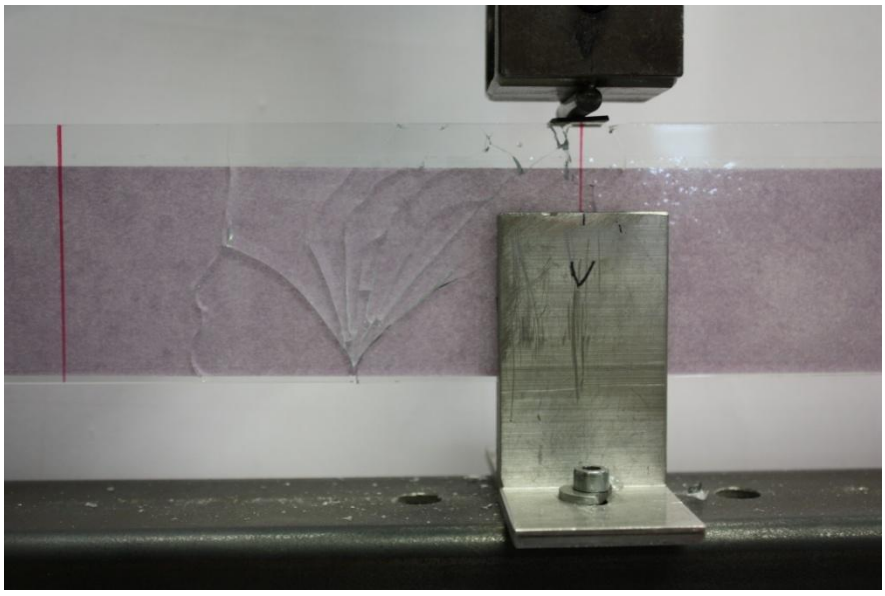

Figure B.38: failure after a 3PB test.

ANNEX C:

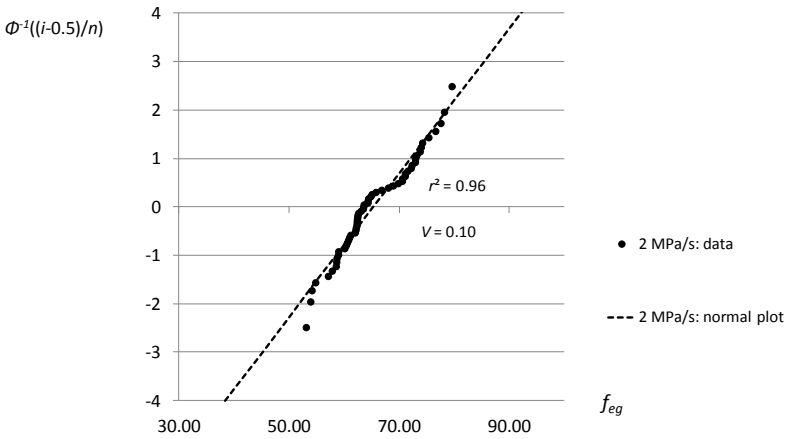

Figure C.1: normal plot for the series N2-a2.

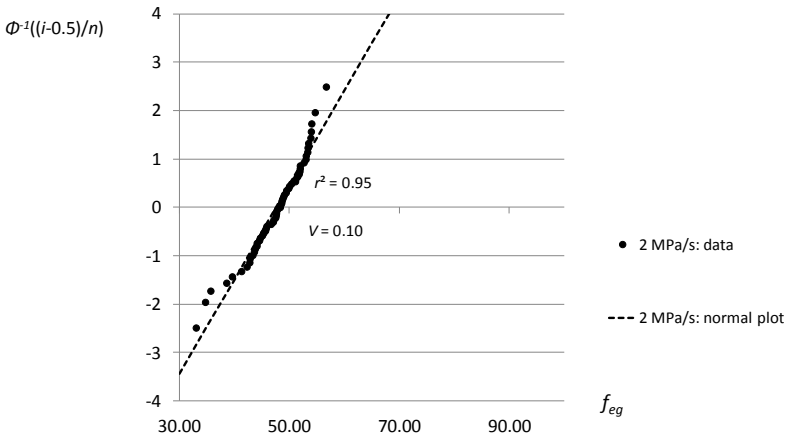

Figure C.2: normal plot for the series A-a2.

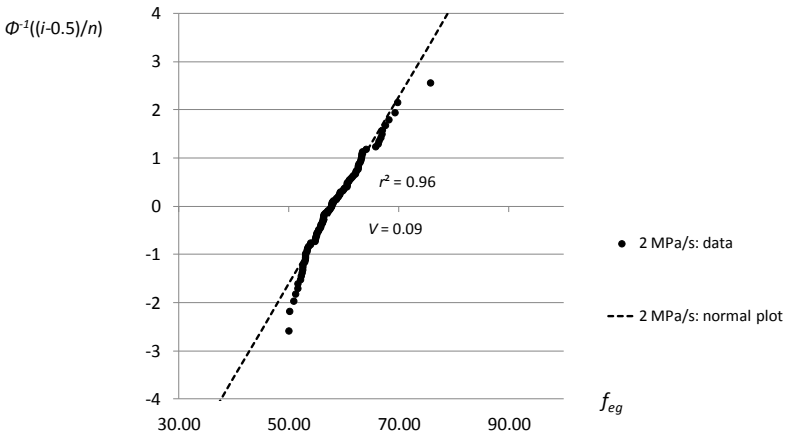

Figure C.3: normal plot for the series C2-a2.

ANNEX D

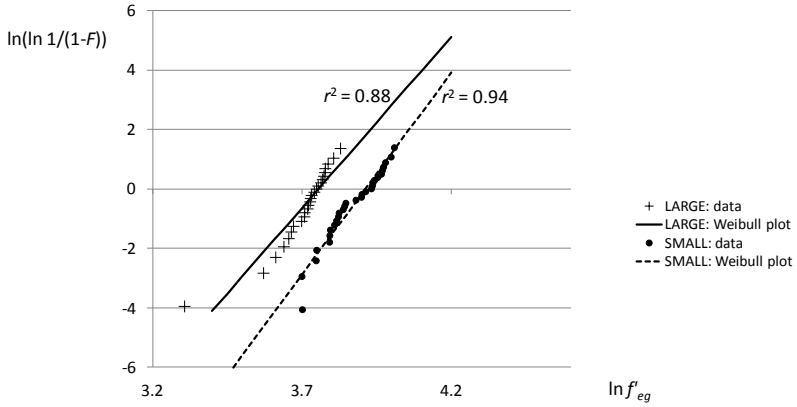

Figure D.1: Weibull plot for the series N4-e2, N4-f2.

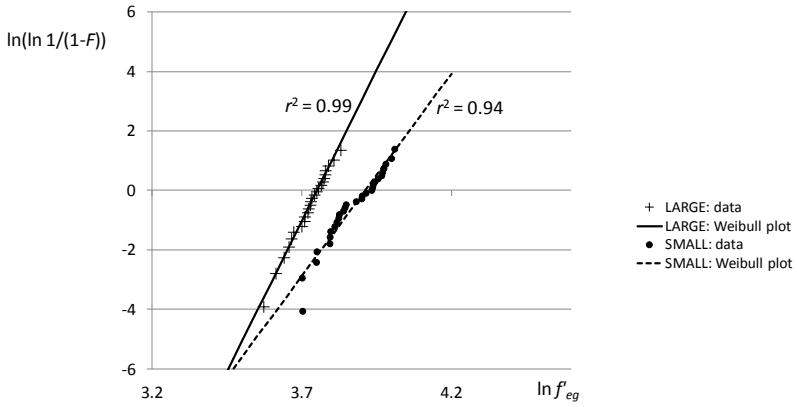

Figure D.2: Weibull plot for the series N4-e2, N4-f2*.

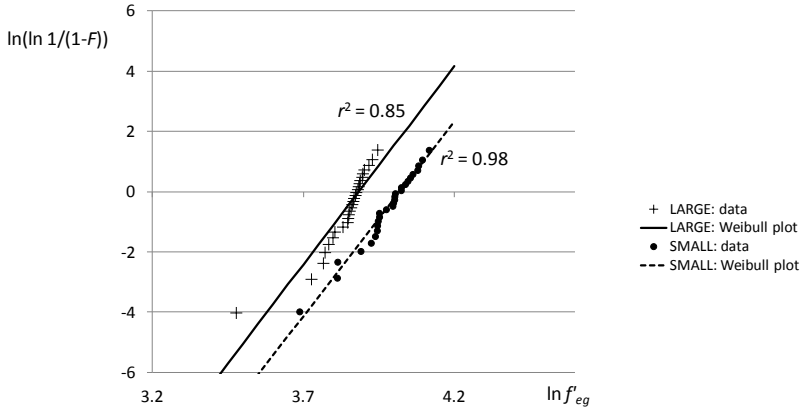

Figure D.3: Weibull plot for the series N4-g2, N4-h2.

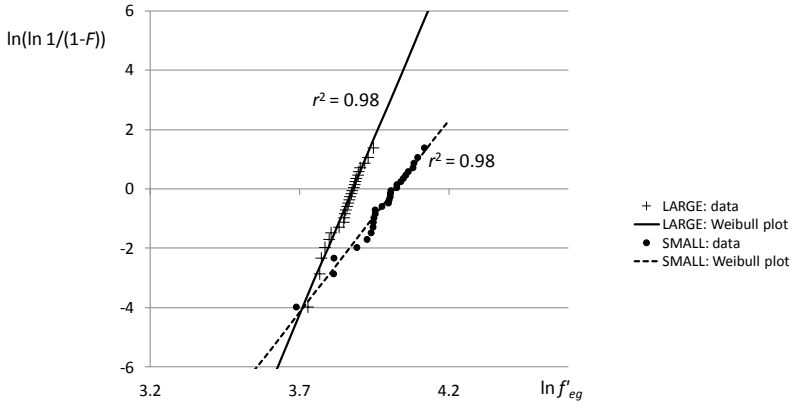

Figure D.4: Weibull plot for the series N4-g2, N4-h2*.

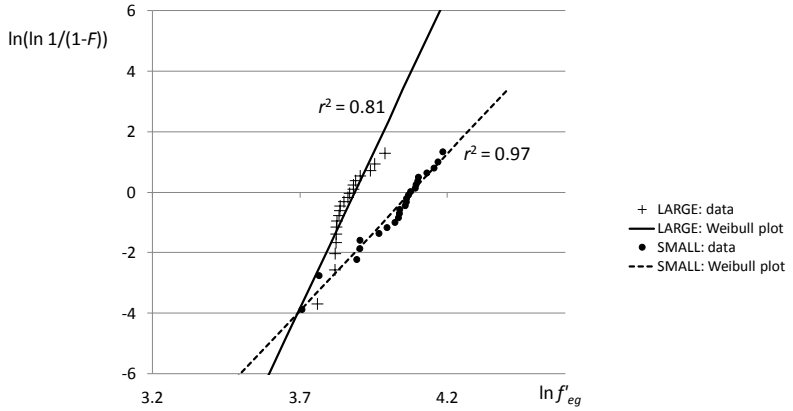

Figure D.5: Weibull plot for the series C4-e2, C4-f2.

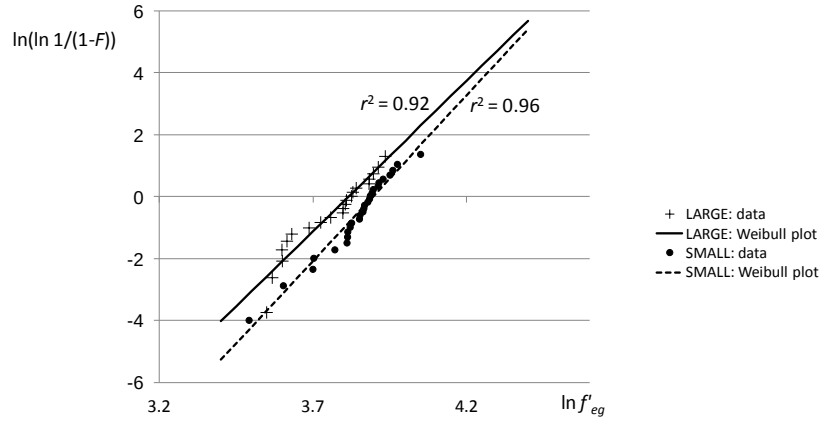

Figure D.6: Weibull plot for the series C4-g2, C4-h2.

ANNEX E

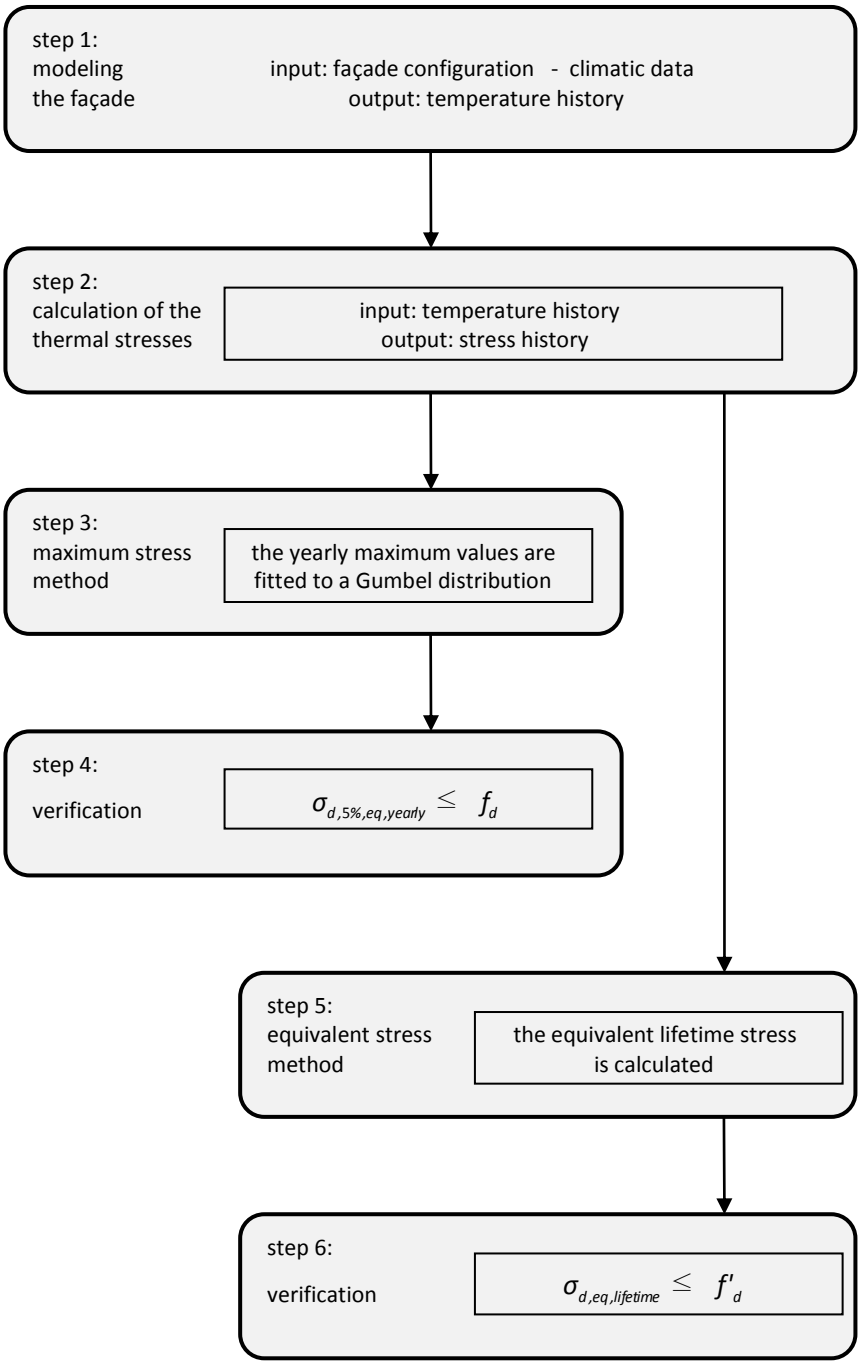

Figure E.1: flow-chart.

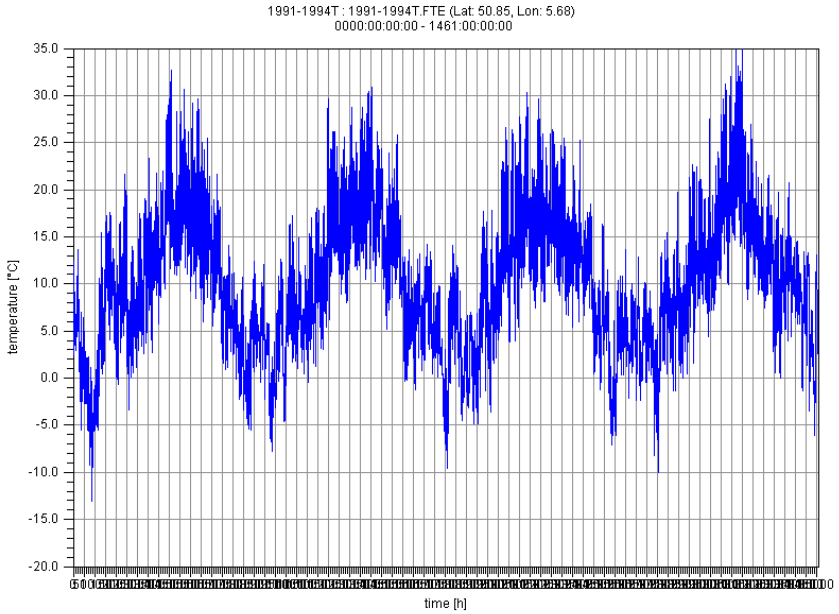

Figure E.2: example climate function: temperature data (°C) at Maastricht during the period 1991-1994.

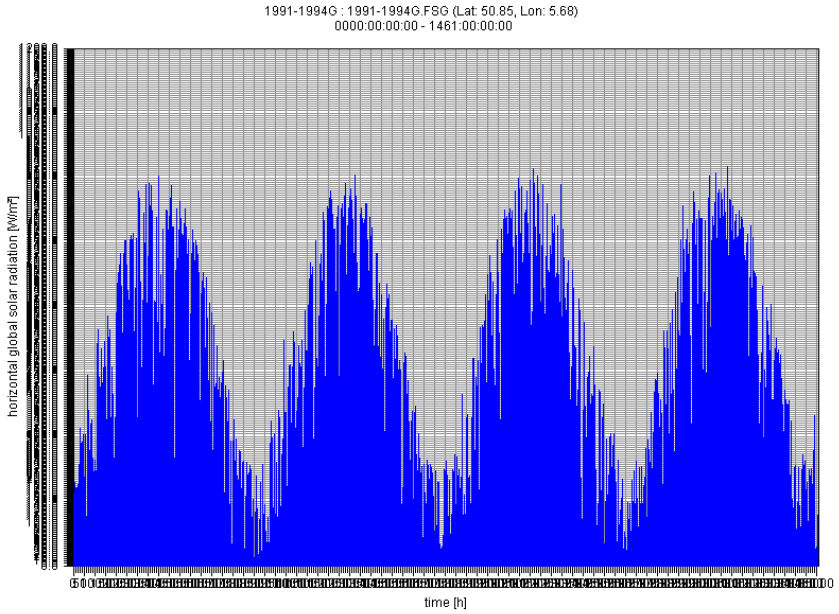

Figure E.3: example climate function: global radiation data (W/m²) at Maastricht during the period 1991-1994.